

Investigations of Cloud Altering Effects of Atmospheric Aerosols using a New Mixed Eulerian-Lagrangian Aerosol Model

Henry Donnan Steele

Center for Global Change Science
Department of Earth, Atmospheric and Planetary Sciences
MIT, Cambridge, MA 02139-4307 USA



**Report No. 74
September 2004**

The Earth's unique environment for life is determined by an interactive system comprising the atmosphere, ocean, land, and the living organisms themselves. Scientists studying the Earth have long known that this system is not static but changing. As scientific understanding of causal mechanisms for environmental change has improved in recent years there has been a concomitant growth in public awareness of the susceptibility of the present environment to significant regional and global change. Such change has occurred in the past, as exemplified by the ice ages, and is predicted to occur over the next century due to the continued rise in the atmospheric concentrations of carbon dioxide and other greenhouse gases.

The *Center for Global Change Science* at MIT was established to address long-standing scientific problems that impede our ability to accurately predict changes in the global environment. The Center is interdisciplinary and involves both research and education.

This report is one of a series of preprints and reprints from the Center intended to communicate new results or provide useful reviews and commentaries on the subject of global change. See the inside back cover of this report for a complete list of the titles in this series.

Ronald G. Prinn, *Director*
Rafael L. Bras, *Associate Director*
MIT Center for Global Change Science

For more information contact the Center office.

LOCATION:
Center for Global Change Science
Massachusetts Institute of Technology
Building 54, Room 1312
77 Massachusetts Avenue
Cambridge, MA 02139-4307 USA

ACCESS:
Tel: (617) 253-4902
Fax: (617) 253-0354
E-mail: cgcs@mit.edu
Website: <http://mit.edu/cgcs/>

Investigations of Cloud Altering Effects of Atmospheric Aerosols using a New Mixed Eulerian-Lagrangian Aerosol Model

by

Henry Donnan Steele

B.S. Physics and Computer Science
Yale University, 1998

Submitted to the Department of Earth, Atmospheric, and Planetary Sciences
in partial fulfillment of the requirements for the degree of

Doctor of Philosophy in Atmospheric Chemistry

at the

MASSACHUSETTS INSTITUTE OF TECHNOLOGY

September 2004

© Massachusetts Institute of Technology 2004. All rights reserved.

Author
Department of Earth, Atmospheric, and Planetary Sciences
August 17, 2004

Certified by
Ronald G. Prinn
TEPCO Professor of Atmospheric Chemistry
Thesis Supervisor

Accepted by
Maria Zuber
E. A. Griswold Professor of Geophysics
Head of the Department

Investigations of Cloud Altering Effects of Atmospheric Aerosols using a New Mixed Eulerian-Lagrangian Aerosol Model

by

Henry Donnan Steele

Submitted to the Department of Earth, Atmospheric, and Planetary Sciences
on August 17, 2004, in partial fulfillment of the
requirements for the degree of
Doctor of Philosophy in Atmospheric Chemistry

Abstract

Industry, urban development, and other anthropogenic influences have substantially altered the composition and size-distribution of atmospheric aerosol particles over the last century. This, in turn, has altered cloud albedo, lifetime, and patterns which together are thought to exert a negative radiative forcing on the climate; these are the indirect effects of atmospheric aerosols. The specifics of the process by which aerosol particles seed cloud particles are complex and highly uncertain. The goal of this thesis is to refine understanding of the role of various aerosol types in determining cloud properties. We approach this goal by constructing a new highly detailed aerosol-cloud process model that is designed to simulate condensation upon complex aerosol populations. We use this model to investigate the microphysics of aerosol-cloud interactions, specifically considering the role of cloud dynamics and of the ubiquitous mixed soot / sulfate aerosols.

We describe the Mixed Eulerian-Lagrangian Aerosol Model (MELAM). This new computer model of aerosol microphysics is specifically tailored to simulate condensation and activation as accurately as possible. It specifically calculates aerosol thermodynamics, condensation, coagulation, gas and aqueous phase chemistry, and dissolution. The model is able to consider inorganic aerosols and aerosols with both inorganics and insoluble cores; the specific chemical system to be considered is specified by the user in text input files. Aerosol particles may be represented using “sectional distributions” or using a “representative sample” distribution which tracks individual particles. We also develop a constant updraft speed, adiabatic parcel model and a variable updraft speed, episodically entraining parcel model to provide boundary conditions to MELAM and allow simulations of aerosol activation in cloud updrafts.

Using MELAM and the parcel models, we demonstrate that aerosol activation depends on the composition and size distribution of the sub-cloud aerosol population, on the updraft speed through a parcel’s lifting condensation level, on the vertical profile of the updraft speed, and on entrainment. We use a convective parameterization that was developed for use in global or regional models to drive the episodically entraining, variable updraft speed parcel model. Ultimately, reducing the uncertainty of the global impact of the indirect effects of aerosols will depend on successfully linking cloud parameterizations to models of aerosol activation; our work represents a step in that direction.

We also consider the activation of mixed soot / sulfate particles in cloud updrafts. We constrain for the first time a model of condensation onto these mixed particles that incorporates the contact angle of the soot / solution interface and the size of the soot core. We find that as soot ages and its contact angle with water decreases, mixed soot / sulfate aerosols activate more readily than the equivalent sulfate aerosols that do not have soot inclusions. We use data from the Aerosol Characterization Experiments (ACE) 1 and 2, and from the Indian Ocean Experiment (INDOEX) to define representative aerosol distributions for clean, polluted, and very polluted marine environ-

ments. Using these distributions, we argue that the trace levels of soot observed in clean marine environments do not substantially impact aerosol activation, while the presence of soot significantly increases the number of aerosol that activate in polluted areas.

Thesis Supervisor: Ronald G. Prinn

Title: TEPCO Professor of Atmospheric Chemistry

Acknowledgments

I am fortunate to have spent my graduate school years here at M.I.T.; I found everything here that I had hoped to find, and oftentimes much more. This thesis is the culmination of many stages of learning and discovery and marks the end of an important stage of my life. I did not make it through these six years on my own. Throughout the past six years, I have leaned on many teachers, advisors, colleagues, friends, and on my family; I am very grateful to each of them.

My advisor Ron Prinn provided countless lessons in the classroom and in his office, and showed by example what it is to do science well. He was always generous with his time, advice, confidence, and support. And he tolerated my pursuit of many non-scientific interests with patience and grace. I am fortunate to have worked with him over these past several years. The other members of my committee – Greg McRae, Mario Molina, and Kerry Emanuel – have each contributed time, expertise, and encouragement. I very much appreciate their efforts. This thesis also benefited enormously from discussions with Don Lucas, Yu-Han Chen, Chien Wang, Greg Lawson, Ico San Martini, Bill Boos, Rob Korty, Zan Stine, Sam Arey, Gary Kleiman, and many others. I have always appreciated the quality of the scientific community I found here, and will always appreciate the collaborations I began here and the friendships I formed here.

I owe a great debt to my friends and family for their love, encouragement, and support over the past few years. I am blessed to have so many wonderful people in my life.

This thesis research was supported by the Federal and Industry Sponsors of the MIT Joint Program on the Science and Policy of Global Change (U.S. Department of Energy, U.S. National Science Foundation, Alstom Power (France), American Electric Power (USA), BP p.l.c. (UK/USA), ChevronTexaco Corporation (USA), DaimlerChrysler AG (Germany), Duke Energy (USA), J-Power (Electric Power Development Co., Ltd.) (Japan), Electric Power Research Institute (USA), Electricité de France, ExxonMobil Corporation (USA), Ford Motor Company (USA), General Motors (USA), Mirant (USA), Murphy Oil Corporation (USA), Oglethorpe Power Corporation (USA), RWE/Rheinbraun (Germany), Shell International Petroleum (Netherlands/UK), Statoil (Norway), Tennessee Valley Authority (USA), Tokyo Electric Power Company (Japan), TotalFinaElf (France), Vetlesen Foundation (USA), We Energies (USA)). It was also supported by NASA Grant NAG-5-12099.

Contents

1	Introduction	23
1.1	Motivation	23
1.2	The Role of Aerosols in the Climate System	25
1.2.1	The Effects of Aerosols on the Global Climate	25
1.2.2	The Scale Problem	30
1.2.3	Microphysical Scale Modeling of Aerosol / Cloud Interaction	34
1.3	Goals and Outline of the Thesis	37
2	Overview of the Mixed Eulerian-Lagrangian Aerosol Model	41
2.1	Introduction	41
2.2	Aerosol Size Representation	44
2.3	Chemical Continuity	46
2.4	Gas-Phase and Aqueous-Phase Chemistry	48
2.5	Aerosol Chemical Thermodynamics	49
2.6	Gas-Aerosol Transfer: Condensation and Dissolution	51
2.7	Aerosol Dynamics	53
2.8	Boundary Conditions for Microphysical Studies of Aerosol Activation: Updraft Models	58
2.9	Summary	59
3	Representation of Aerosols and Droplets	61
3.1	Introduction	61
3.2	Functional Representations of Observed Aerosol Size Distributions	62
3.3	Representing Size Distributions in Models	65
3.3.1	Bulk	65
3.3.2	Method of Moments	65
3.3.3	Modal Representations	66

3.3.4	Sectional Representations	66
3.3.5	Continuous and Lagrangian Representations	71
3.3.6	Mixed Sectional and Lagrangian Representations	74
3.4	Representation of Aerosol Composition and Mixing State	76
3.5	Summary	80
4	Aerosol Chemical Thermodynamics	81
4.1	Introduction	81
4.2	Chemical Continuity	83
4.3	Equilibrium Dissociation of Electrolytes and Acids	84
4.3.1	Equilibrium Coefficients for Dissociating Species	85
4.3.2	Solving for Equilibrium Concentrations	86
4.4	Thermodynamic Activities	90
4.4.1	Calculating Binary Activity Coefficients when Binary Data is Available . . .	91
4.4.2	Calculating Binary Activity Coefficients when Binary Data is Not Available .	98
4.4.3	Calculating Activity Coefficients and Equilibrium for Partially Dissociating Species: Sulfuric Acid	99
4.4.4	Calculating Activity Coefficients in Mixtures	106
4.5	Mixing Rules for Other Thermodynamic Properties	109
4.6	Surface Tension	110
4.6.1	Surface Tension of Flat Surfaces of Pure Water	111
4.6.2	Surface Tension of Flat Surfaces of Electrolytic Solutions	111
4.6.3	Surface Tensions Calculated Using the Gibbs Dividing Surface for Electrolytic Solutions	112
4.6.4	Influence of Soluble and Slightly Soluble Organic Species	114
4.7	Solution Density	115
4.8	Summary	117
5	Mass Transfer to and from Particles: Condensation and Dissolution	119
5.1	Introduction	119
5.2	Continuity Between Phases	120
5.3	Coupling between Condensation and Aqueous Chemistry and Thermodynamics . . .	121
5.4	Equilibrium and Non-Equilibrium Across the Gas and Aerosol Phases	122
5.4.1	The Equilibration of Water	123

5.4.2	The Equilibration of Trace Species	124
5.5	Equilibrium Water Content	126
5.5.1	The Zdanovskii-Stokes-Robinson Approximation	127
5.5.2	Calculating the Water Activity in Single Salt Solutions	128
5.5.3	Mixing Single Salt Water Activities to Estimate Water Activity for a Multi- Component System	130
5.5.4	Equilibrating Particle Water Content	131
5.5.5	Comparison of Water Equilibration Methods	134
5.6	Trace Gas - Aerosol Equilibrium	135
5.6.1	Activity Coefficients	137
5.6.2	Solving for Gas-Particle Equilibrium	138
5.6.3	Model Comparison for Urban Aerosol Case	139
5.7	The Diffusion Limited Aerosol Growth Model	143
5.7.1	The Quasi-Stationary Equation	144
5.7.2	Mass-Flux Model for Multi-Component Aerosol Growth	144
5.7.3	Corrections to Condensation Rate Constant Terms	145
5.8	Water Condensation	149
5.8.1	Condensational Growth of Soluble Aerosol Particles	151
5.8.2	Droplet Formation on Mixed Soluble-Insoluble Aerosol Particles	154
5.8.3	The Role of Soluble Organic Species	159
5.8.4	Activation: A Definition	160
5.9	Non-Equilibrium between Trace Gases and Aerosol: Dissolution	161
5.10	Numerical Solution to Time-Dependent Gas-Aerosol Transfer	163
5.10.1	Sparse Matrix Solution Method	164
5.10.2	Integration of Operator-Split Condensation and Dissolution Equations	166
5.11	Comparison of Equilibrium and Non-Equilibrium Prediction of Aerosol Water Content	170
5.12	Conclusion	173
6	Aerosol Activation within 1-D Updraft Models	175
6.1	Introduction	175
6.2	Constant Updraft Parcel Model	176
6.2.1	Non-Entraining and Continuously Entraining Parcel Models	177
6.2.2	Pressure Equation	179

6.2.3	Temperature Equation	179
6.2.4	Water Condensation and Aerosol Dynamics Equations	181
6.2.5	Volume Equation	182
6.2.6	Summary and Example	183
6.2.7	Problems with the Constant Updraft Model	187
6.3	A New Entraining, Variable-Updraft-Speed Parcel Model	191
6.3.1	The Episodically Entraining Plume and the Buoyancy Sorting Hypothesis . .	192
6.3.2	Framework for an Episodically Entraining, Variable-Updraft-Speed Parcel Model	195
6.3.3	Vertical Velocities	197
6.3.4	Lateral Mixing of Environmental Air	203
6.3.5	Vertical Distribution of Aerosol	205
6.3.6	Example	205
6.3.7	Sensitivities of the Updraft Parcel Models to Minimum Updraft Speed . . .	215
6.3.8	Summary and Discussion	218
6.4	Conclusions	219
7	Aerosol Activation in Sooty Environments	221
7.1	Introduction	221
7.2	Soot Data	226
7.2.1	Chemical Aging, Hygroscopic Properties, and Contact Angle of Soot Aerosols	227
7.2.2	Measurements in the Ambient Environment	228
7.2.3	Field Campaigns	230
7.2.4	Overview of Observed Aerosol Mixing State	232
7.3	Effect of Contact Angle on Aerosol Activation for Internally Mixed Soot / Sulfate Particles in Heavily Polluted Regions	235
7.3.1	Aerosol Distributions	235
7.3.2	Results	237
7.3.3	Summary	242
7.4	The Role of Soot in Cloud Formation in the Clean Marine Atmosphere	244
7.4.1	Aerosol Populations	244
7.4.2	Sea Salt	247
7.4.3	Black Carbon: Concentrations and Mixing State	248

7.4.4	Results	250
7.4.5	Summary and Discussion	253
7.5	The Relationship Between the Size of the Soot Core and Aerosol Activation	254
7.6	Overview	257
8	Conclusion	261
8.1	Summary and Conclusions	261
8.2	Limitations of Data and Theory	265
8.3	Future Directions	267
A	Definition of a Simplified Inorganic Aerosol System	269

List of Figures

1-1	Estimates of the radiative forcing of various climate-altering effects, as a differential between the radiative forcing in 1750 and 2000	29
1-2	Schematic of the necessary components in a model of the role of indirect radiative forcing in the global climate system	31
1-3	Several parameterizations of $N_c(N_a)$ and $N_c(\mathbf{m}_a)$ relationships	32
1-4	Schematic of several aerosol types	35
2-1	Schematic of the microphysical processes included in the MELAM microphysics model	42
3-1	Example observed bimodal log-normal aerosol number distribution from ACE-2 . . .	64
3-2	Sectional representation of the number concentration of an example bimodal, log-normal distribution of aerosol	69
3-3	Inversion of a cumulative distribution function for an example log-normal aerosol distribution	73
3-4	Schematic of several aerosol types	75
3-5	Schematic of one way to represent multiple aerosol types in a sectional distribution; there are three aerosol populations, each divided into four separate size bins; populations 1 and 2 include a single type of aerosol (homogeneous in composition, but not necessarily single-component), while the third distribution is “internally mixed” such that each aerosol in each bin is comprised of partially of the components of population 1 and partially of the components of population 2	78
4-1	Variation of Γ° against l in the Kusik-Meissner formulation	94
4-2	γ_{NaCl}° calculated as a function of l at several temperatures using the Kusik-Meissner formulation and compared to data	95
4-3	γ_{HCl}° calculated as a function of l at several temperatures using the Kusik-Meissner formulation and compared to data	96

4-4	$\gamma_{\text{H}_2\text{SO}_4}^\circ$ calculated as a function of l at several temperatures using the Kusik-Meissner formulation and compared to data	97
4-5	$\gamma_{\text{HNO}_3}^\circ$ calculated as a function of l at 25° C using the Kusik-Meissner formulation and compared to data	97
4-6	Comparison of the dissociation quotients, Q , of several models to a parameterization of data	105
4-7	Schematic of the Gibbs dividing surface approach to surface tension calculation . . .	113
4-8	Variation of parameterized binary densities of several electrolytes with molality shown next to data	116
5-1	Equilibration time-scales for a range of accommodation coefficient values for NaCl and $(\text{NH}_4)_2\text{SO}_4$ particles at 80% \mathcal{RH}	125
5-2	Examples of Na_2SO_4 aerosols equilibrated at several \mathcal{RH} using MELAM	133
5-3	Comparison of water content using ISORROPIA, MIT-IAM, MELAM, and AIM III	134
5-4	Comparison of aerosol liquid water content for the urban aerosol example as predicted by MELAM and ISORROPIA	141
5-5	Comparison of electrolyte partitioning for urban aerosol by MELAM and ISORROPIA	142
5-6	Schematic of four theoretical targets of water condensation	150
5-7	Equilibrium saturation vapor pressure curve as a ratio to a flat surface	154
5-8	Schematic of the contact angle in a mixed soluble / insoluble aerosol	156
5-9	Variation of equilibrium saturation with contact angle	158
5-10	Comparison of aerosol water content predicted by equilibrium and kinetic approaches	171
5-11	Characteristic water equilibration times	172
6-1	Schematic of the constant-velocity updraft parcel model	177
6-2	Non-entraining parcel model used to calculate the activation of a simple $(\text{NH}_4)_2\text{SO}_4$ distribution	184
6-3	Distributions of a ammonium sulfate aerosol population adiabatically lifted at three different updraft velocities	186
6-4	The ratio of observed mean liquid water content to the value expected were cloud base air adiabatically lifted	188
6-5	Diagram of the lagrangian episodically entraining, variable-speed parcel updraft model	196

6-6	Calculated CAPE_i and minimum updraft vertical velocity through the depth of an example cloud	201
6-7	Parcel dilution, environmental temperature, and environmental relative humidity in the E91 model for an example cloud	204
6-8	Relative humidity and aerosol activation fraction, shown as a function of altitude, for a simple $(\text{NH}_4)_2\text{SO}_4$ distribution adiabatically lifted using four updraft models .	208
6-9	Comparison of parcel liquid water content for four updraft models	210
6-10	Aerosol size spectra at various altitudes in the entraining and adiabatic variable-updraft-speed parcel models	212
6-11	Sensitivity of the variable-updraft-speed and constant speed updraft models to minimum updraft speed	214
6-12	Sensitivity of the aerosol size distributions for the entraining and adiabatic variable-updraft-speed parcel models to minimum updraft speed	217
7-1	Schematics of the known mechanisms by which soot aerosols may become involved in aerosol activation and cloud formation	225
7-2	Activation fraction as a function of updraft velocity and the cosine of the contact angle for the three Polluted Marine distributions	238
7-3	Maximum \mathcal{RH} reached during adiabatic lifting as a function of updraft velocity and the cosine of the contact angle for the three Polluted Marine distributions	239
7-4	Activation fraction as a function of updraft velocity and the cosine of the contact angle for the four Maldives aerosol distributions	241
7-5	Activation fraction as a function of updraft speed for each of six remote marine case-study environments	251
7-6	Schematic of mixed soot / sulfate aerosols	254

List of Tables

4.1	Kusik-Meissner Parameters for Several Equilibrium Reactions	94
7.1	Observed Aerosol Size Distributions from INDOEX Campaigns	236
7.2	Observed aerosol size distributions from the ACE field campaigns	245
7.3	Aerosol SO_4^{2-} mass implied by observed size distributions compared to observed values	246
7.4	O'Dowd Parameterization of Sea Salt Distributions	247
7.5	Mass Loadings of Sea Salt Aerosols: Observations and Fit to Observations	247
7.6	Mode-by-Mode Soot Inclusion Rates	248
7.7	Summary of Calculated Soot Size and Mass Loadings for the Marine Environment .	249
7.8	The Relationship Between the Radius of the Solution Embryo and of the Insoluble Core in a Mixed Soluble / Insoluble Particle	256
A.1	Chemical Species	270
A.2	Aqueous Phase Equilibrium Reactions	271
A.3	Equilibrium Reactions	272
A.4	Kusik-Meissner Parameters for Selected Electrolytes	272
A.5	Surface Tension and Density Parameters	273

List of Symbols

Symbol	Description
$A_{a/s}, A_{s/sd}$	Area of the air-solution and solution-solid interfaces of a mixed-phase particle (cm^2)
a_i	Empirical regression coefficients used in the definition equation (4.40) ($\text{J cm}^{-2} \text{K}^{-1}$)
a_w	Water activity (–)
a_x	Thermodynamic activity of species x (mol kg^{-1})
$c_{a,i}$	Aqueous phase concentration of species i in aerosol a (mol cm^{-3})
C_i	Gas phase concentration of species i (mol cm^{-3})
c_p^o	Standard molal heat capacity at constant temperature ($\text{J mole}^{-1} \text{K}^{-1}$)
D_i	Molecular diffusion coefficient of vapor i in air ($\text{cm}^2 \text{s}^{-1}$)
e_n	n^{th} edge in a sectional distribution (–)
$e_{s,water}$	Saturation vapor pressure of water (mbar)
F_x	Ionic strength fraction defined in (4.31) (–)
$\Delta_f G^o$	Standard molal Gibbs free energy of formation (J mole^{-1})
h	Time step (s)
H_i	Henry’s Law Coefficient for species i ($\text{mol kg}^{-1} \text{mbar}^{-1}$)
ΔH_0^o	Standard molal enthalpy of formation (J mole^{-1})
I	Ionic strength (mol kg^{-1})
I	The identity matrix (–)
J	The Jacobian matrix defined in equation (5.72)
$K_{eq}, K_{eq,i}$	Equilibrium coefficient, in general and for reaction i (various)
k_i	Condensational rate constant of species i , defined in equation (5.34) (mol s^{-1})
k_x	In the definition of K_{eq} in equation (4.4), this is +1 if species x is a product

Symbol	Description
	and -1 if it is a reactant $(-)$
Kn_i	Knudsen number $(-)$
L_i	Latent heat of species i (J kg^{-1})
$m_i, m_i^{(\text{vapor})}, m_{i,\text{p}}^{(\text{aqueous})}, m_{i,\text{p}}^{(\text{solid})}$	Total, vapor phase, aqueous particle phase, and solid particle phase mass of species i (g)
\mathbf{m}_i	Molality of species i (mol kg^{-1})
M_i	Molecular mass of species i (g mol^{-1})
M_w	Molecular mass of water (g mol^{-1})
N_a	Aerosol number concentration (particles cm^{-3})
N_{gp}	Number of aerosols or bins of aerosols at a particular grid point $(-)$
N_a	Number concentration of a log-normal distribution of aerosols (particles cm^{-3})
N_B	Nuber of bins in a sectional distribution $(-)$
N_c	Cloud drop concentration (particles cm^{-3})
N_A	Avogadro's number ($\text{molecules mole}^{-1}$)
n_w, n_s	Number of water and solute molecules in a solution droplet (mol)
p	Atmospheric pressure (mbar)
$\mathcal{P}(r)$	Particle distribution function $(-)$
\mathbf{p}_i	Partial pressure of species i (mbar)
$\wp_{IJ}^{(0)}, \wp_{IJ}^{(1)}$	Zeroth and first density regression parameters as used in (4.46) ($\text{g cm}^{-3}, \text{kg mol}^{-1}$ respectively)
\mathbf{p}_v	partial pressure of water vapor (mbar)
$\mathbf{p}_{v,s}$	Saturation partial pressure of water vapor (mbar)
\mathbf{p}_{water}	Internal pressure along a water surface (mbar)
Pr	Prandtl Number $(-)$
Q	Dissociation quotient of sulfate, defined in (4.29) (mol kg^{-1})
$Q_{\text{electrolytes}}, Q_{\text{ions}}$	Scaled limiting concentrations for the electrolyte-to-ion and ion-to-electrolyte pathways, respectively defined in equation (4.12)
q, q_r, q_T	Kusik-Meissner coefficients as defined in (4.19) $(-)$
\mathcal{R}	Ratio of the largest possible aerosol in a bin to the smallest aerosol in a bin in a sectional representation of aerosols $(-)$
R^*	Universal gas constant (e.g., $\text{kg m}^2 \text{s}^{-1} \text{mole}^{-1} \text{K}^{-1}$)

Symbol	Description
r_a	The radius of particle a (cm)
\bar{r}_a	Mean radius of a log-normal distribution of aerosols (cm)
r_a^*	Critical radius at which a particle activates (cm)
r_w	Difference between the water activity of an aerosol and local relative humidity, defined in equation (5.19) (–)
Re_a	Reynolds Number of particle a (–)
\mathcal{RH}	Relative Humidity (–)
S^*	Critical saturation at which a particle activates, defined in equation (5.54) (–)
S'	The ratio of the modified saturation vapor pressure to the saturation vapor pressure over a flat surface of pure water (–)
$S'_{a,i}$	Dimensionless equilibrium saturation ratio of the particle-specific near-surface saturation concentration to the saturation concentration over a flat interface of an equivalent solution (–)
Sc_i	Schmidt Number of species i (–)
T	Temperature (K)
T_0	Reference temperature (K)
v_p	Volume of particle p (cm^3)
\vec{x}_t	State vector containing gas and aerosol phase concentrations of a particular specie defined in equation (5.71) (cm^{-3})
Δx_t	Mass flux parameter for time t defined in (4.14)
y_{ij}	The fractional contribution of a single electrolyte toward the total ionic strength, defined in (4.37) (–)
\vec{y}_t	Rate vector used for LSODES in equation (5.71) (cm^{-3})
z_i	Charge of species i (–)
Z_t	Tracking parameter for time t defined in (4.13) (–)
Z_x	Charge fraction, defined in (4.38) (–)
α, α_i	Mass accommodation coefficient for i (–)
$\beta_{1,2}$	Coagulation kernel for particles 1 and 2 ($\text{cm}^3 \text{ particle}^{-1} \text{ s}^{-1}$)
β, β_{IJ}°	Regression coefficient for determining the surface tension of a mixed and binary electrolytic solution, respectively, as defined in (4.41) and (4.42) ($\text{mol}^{-1} \text{ g K}^{-i}$)

Symbol	Description
γ_{ij}, γ_{ij}	The mean activity coefficient of cation i and anion j and, interchangeably, of electrolyte ij , defined in (4.16) (–)
$\Gamma_{ij}, \Gamma_{ij}^\circ$	Reduced mean activity coefficient, in general and for a binary electrolytic solution, defined in (4.17) (–)
ζ_i	Surface excess of species i (mole m ⁻²)
η_{air}	Dynamic Viscosity of Air (kg cm ⁻¹ s ⁻¹)
θ	Contact angle (degrees)
κ_d	Thermal conductivity (J cm ⁻¹ s ⁻¹ K ⁻¹)
λ_i	Mean free path of a molecule of species i in air (cm)
μ_i	Chemical potential of species i (J mol ⁻¹)
μ^i	Chemical potential in the interfacial region, as used in (4.44) (J mol ⁻¹)
μ_n	n^{th} aerosol moment (cm ⁿ cm ⁻³)
ν_x	Stoicheometric coefficient of species x in an equilibrium reaction (–)
ξ	Absolute value of fractional distance from equilibrium defined in (4.15) (–)
ρ	Density of a solution (g cm ⁻³)
ρ_a	Air density (g cm ⁻³)
$\rho_{v,i}, \rho_{v,a,i}$	Vapor density of species i , in the environment and at the surface of particle a (g cm ⁻³)
$\rho_{\text{water}}, \rho_{ij}^\circ$	Densities of water and of a pure solution of electrolyte ij (g cm ⁻³)
σ_a	Geometric standard deviation of a log-normal distribution of aerosols (–)
$\sigma_{\text{w/a}}, \sigma_{\text{s/a}}$	Surface tension along a flat water/air and solution/air interfaces, respectively (J cm ⁻²)
$\varsigma_{c,a}^D, \varsigma_{c,a}^{\kappa_d}$	Correction of D and κ_d for collisional geometry and sticking probability (–)
$\varsigma_{V,a}^D, \varsigma_{V,a}^{\kappa_d}$	Correction of D and κ_d for ventilation (–)
Φ_{ln}	Cumulative distribution function of a log-normal distribution (–)
ψ_{ij}	Density mixing parameter, as used in (4.47) (–)

Chapter 1

Introduction

1.1 Motivation

The pollution that attends industrialization and population growth is changing the Earth’s radiative balance and climate. Recent assessments of the state of predictive climate science conclude that the largest uncertainties in the impact of human activity on global mean radiative forcing are due to the lack of understanding of how pollution influences cloud patterns and the attributes of individual clouds (*Houghton et al.*, 2001). It is known that cloud droplet number concentrations rise with increasing aerosol loading (*Pueschel et al.*, 1986), but neither the specific microphysical processes that control this behavior nor its implications are well understood. In this thesis, we will develop a new numerical model that simulates, at the smallest scales, the formations of clouds in various polluted environments; and we will use the model to address several outstanding questions related to aerosol / cloud interaction. The amount of work to do on these topics is vast, and an increasingly important sub-field of atmospheric chemistry has emerged as a result. Our work represents a step towards understanding the relationship between particulate pollution and cloud behavior, and towards reducing the uncertainty of predictions of global mean radiative forcing overall; the model we present will be used in studies beyond this thesis to take additional steps towards these goals.

The largest anthropogenic increases in aerosol concentrations are due to the direct emission of elemental carbon and organic aerosol from incomplete combustion of carbonaceous fuels, and the nucleation of primary emissions of ammonia, nitrate, sulfate, and condensable organic species. For example, the flux of anthropogenic sulfur to the atmosphere has accelerated at a rate similar to that of CO₂ since industrialization and has eclipsed natural fluxes since 1960 (*Penner et al.*, 1994;

Seinfeld and Pandis, 1998). Aerosols evolve after their emission or nucleation, and observations reveal that aerosol populations are frequently inhomogeneous mixtures of complex multi-component aerosols. Our ability to measure ambient aerosol distributions and to identify the constituents of the particles has, until recently, been rudimentary. Advances in measurement techniques now allow much greater insight into aerosol composition, mixing state, size distribution, and other characteristics that are essential for unraveling the intricacies of the impact of aerosols on cloud development and therefore on the climate. The data from these new measurement techniques assures a very promising next decade of research into aerosol chemistry and the impact of aerosols on the climate.

Clouds play vital roles in: regulating the hydrologic cycle; atmospheric pollutant redistribution and removal (*Flossmann et al., 1985, 1987; Flossmann and Pruppacher, 1988; Chen, 1992; Flossmann, 1993; Wang and Chang, 1993b; Wang and Prinn, 1998*); global energetics (*Hartmann et al., 1993*); and atmospheric chemistry (*Pruppacher and Klett, 1997; Bott, 1999; Wang and Prinn, 2000*). The potential alteration of cloud behavior due to increasing levels of particulate pollution has vast and complex implications for the global climate. Two primary cloud-altering “indirect effects” of aerosols on climate have been observed: clouds that form in polluted environments are optically thicker and reflect more inbound sunlight back to space before it can warm the lower atmosphere and surface; and clouds that form in polluted environments are less likely to precipitate, which increases the lifetime of individual clouds and shifts rainfall patterns.

Published estimates of the magnitude of the indirect effects generally disagree except in that they all expect a net cooling of the earth’s surface (e.g., *Jones et al., 1994; Jones and Slingo, 1996; Boucher and Lohmann, 1995; Lohmann and Feichter, 1997; Boucher, 1999; Roeckner et al., 1999; Rotstajn et al., 2000; Houghton et al., 2001; Lohmann and Lesins, 2002*). Much of the disagreement may be traced to differences in the microphysical schemes that relate aerosol loading to cloud drop concentrations and cloud properties overall. Given that aerosols from two distinct sources will certainly differ in concentration, composition, optical properties, solubility, activity as ice formation nuclei, and shape (*Toon, 2000*), correct dependencies of bulk cloud properties on aerosol composition and distribution, cloud dynamics, and larger scale meteorology are incredibly difficult to calculate.

The fundamental concern of models of the indirect effects of aerosols is the relationship between sub-cloud aerosol populations and the properties of cloud droplets that form upon them. The specific objective of this thesis is to extend the microphysical understanding of the interaction between atmospheric aerosol and cloud droplets through development of a sophisticated microphysical model

that fully accounts for variation in aerosol and cloud droplet composition and size. This model will back away from methods of approximation developed for the aerosol modules of air quality and chemical engineering reactor models and employ the most realistic and basic physical assumptions possible. It is intentionally flexible such that it is easily reconfigured to address particular issues related to the aerosol / cloud transition or to include future extensions of theory and modeling methods.

In Section 1.2, we will discuss the various ways aerosols alter the climate system, and discuss how models may be used to understand these alterations. Then, in Section 1.3 we will present the specific goals and outline of the thesis.

1.2 The Role of Aerosols in the Climate System

The composition of the atmosphere is changing due to pollution from anthropogenic sources, and these changes have impacted the climate both regionally and in the global mean. Some of the impacts of this pollution on the climate are well understood, such as warming due to radiative forcing by greenhouse gases; others are poorly understood, such as the impact of aerosols on cloud formation and behavior. The latter is the subject of this thesis.

In Section 1.2.1, we will summarize what is known about the role of aerosols in the global climate. In Section 1.2.2, we will discuss the difficulty of linking the properties of microscopic aerosol particles to changes in the global climate. Finally, in Section 1.2.3 we will consider some of the behaviors of aerosols during cloud formation and discuss how the model presented in this thesis can be used to study the aerosol / cloud droplet transition.

1.2.1 The Effects of Aerosols on the Global Climate

The atmospheric concentrations of long-lived greenhouse gases, including CO₂, CH₄, N₂O, SF₆, and the various chlorofluorocarbons (CFCs), have greatly increased since industrialization, as have those of many atmospheric aerosols (*Hartmann, 1994; Seinfeld and Pandis, 1998*). Because of their relatively long atmospheric residence times, localized greenhouse gas emissions are small with respect to the total atmospheric burden. Long chemical lifetimes allow these gases to mix and circulate away from their sources, yielding nearly uniform mixing ratios throughout the atmosphere. These gases serve as an insulating blanket around the globe that traps outgoing thermal radiation and so exerts a warming force on the Earth of approximately $+2.4 \text{ W m}^{-2}$ (*Charlson et al., 1992; Kiehl and Briegleb, 1993; Houghton et al., 2001*) and an associated warming of approximately

0.9 ± 0.24 K/century (*Tett et al.*, 2002).

Unlike greenhouse gases, aerosol particles have extremely short atmospheric lifetimes, remaining aloft several to many days rather than several to many years. As a result, aerosol concentrations are spatially inhomogeneous, distributed with industry and biomass-burning populations and varying in time (*Penner et al.*, 1994; *Toon*, 2000). Aerosol particles range in size from molecular clusters, nanometers wide, to much larger spores, sea salt particles, and grains of dirt which may be $10\text{ }\mu\text{m}$ in diameter or larger. Theory and observation suggest that aerosol particles perturb local climates by direct clear-sky scattering and absorption of incoming radiation (this is direct radiative forcing, or the direct effect of aerosols), by changing the thermal structure of the atmosphere (this is the semi-direct effect of aerosols), and by changing the microphysical character of clouds, which affects clouds' mean lifetime, spatial coverage, precipitation efficiency, and albedo (this is known as indirect radiative forcing, or the first and second indirect effects of aerosols). In aggregate, these aerosol effects cool the Earth, speckling a countervailing cooling-pattern above a nearly uniform greenhouse-related warming (*Wigley*, 1991; *Houghton et al.*, 2001; *Jacobson*, 2001b; *Rotstayn and Penner*, 2001; *Penner et al.*, 2004). We will next briefly introduce and discuss each of these four climate-altering aerosol effects.

The Direct Effect of Aerosols

In sub-saturated air, particulate and gas-phase pollution results in broad layers of high aerosol concentrations in the lower troposphere near emission sources that interact with radiation in three primary ways. First, aerosols scatter incoming sunlight, some of which is reflected back to space and so never reaches the surface. Second, some aerosols absorb incoming sunlight and then re-emit the energy as thermal radiation; this has the effect of preventing sunlight from reaching the surface, a cooling effect, and also of warming the atmosphere near the absorbing aerosols. Third, aerosols may absorb a fraction of the outgoing thermal radiation and re-emit some of the energy back towards the earth, thus trapping heat near the surface as would greenhouse gases. Combined, these interactions are known as the direct effect of aerosols.

The direct effect changes the regional atmospheric radiative forcing (*Houghton et al.*, 2001), alters regional actinic fluxes (e.g., *Jacobson*, 1999), and dampens the diurnal atmospheric temperature cycle (*Jacobson*, 1998). Direct radiative forcing of sulfate aerosols has been modeled extensively (e.g., *Charlson et al.*, 1992; *Gaffney and Marley*, 1998; *Boucher et al.*, 1998) and is governed by well understood physics. However, inhomogeneities from place-to-place in sulfate concentrations and in the range of aerosol sizes make reducing uncertainty in global mean radiative forcing diffi-

cult. Representing the direct radiative forcing of aerosols on large scales and in the long-term is an ongoing, but apparently tractable, focus of climate research; how these same aerosols affect clouds and, through them, alter the climate has become a focus of research within the past decade and has proven a much more difficult problem.

The Semi-Direct Effect of Aerosols

Elevated concentrations of airborne particulate black carbon absorb solar radiation and as a result both reduce the solar radiation that reaches the Earth's surface and warm the atmosphere at height. This, in turn, decreases the thermal lapse rate and thus increases the static stability of the atmosphere. In so doing, it suppresses convection, cloud formation, and precipitation onto the ground below (*Hansen et al.*, 1997; *Ackerman et al.*, 2000; *Lohmann and Feichter*, 2001; *Ramanathan et al.*, 2001a; *Koren et al.*, 2004). The thermal forcing may also act to evaporate cloud droplets in clouds that do form. This is the semi-direct effect of aerosols. The recent observational study of *Koren et al.* (2004) is very convincing that this effect is real. However, at this point both the theory and modeling under-pinning our understanding of this effect are rather speculative, which makes extrapolations from the available studies to regional and global scale implications difficult and unreliable. The most that can be said is that the effect may lead to a reduction of cloud coverage with increasing levels of pollution, especially over tropical oceans. This would change the overall radiative impact of clouds, with implications for the global climate (*Ackerman et al.*, 2000; *Ramanathan et al.*, 2001a).

The Indirect Effects of Aerosols

Clouds that form in polluted air are thought to be optically thicker and less likely to precipitate than those formed in clean environments (*Twomey*, 1977b; *Albrecht*, 1989; *Feingold and Kreidenweis*, 2000); these are, respectively, the first and second indirect effects of aerosols (also known as the “Twomey” and “Albrecht” effects). It was proposed in the 1970's that the rising aerosol concentrations associated with anthropogenic pollution provide additional aerosols to act as condensation nuclei for atmospheric water vapor, resulting in clouds that have more and smaller droplets (*Matthews*, 1970; *Wilson*, 1970; *Twomey*, 1974). This proposition has been confirmed repeatedly by observations (e.g., *Warner and Twomey*, 1967; *Twomey and Warner*, 1967; *Pueschel et al.*, 1986; *Alkezweeny et al.*, 1993; *Novakov et al.*, 1994; *Twohy et al.*, 1995; *Russell et al.*, 1999; *Seinfeld and Flagan*, 1999).

The first indirect effect is the simple result of the physics of light scattering: increasing the

cloud droplet concentration increases scattering and therefore optical thickness (*Seinfeld and Pandis*, 1998). The second indirect effect results from the fact that coalescence (the collision and combination of two cloud drops) is non-linearly dependent on the mean drop size and that, in ice-free (“warm”) clouds, precipitation is initiated by the coalescent formation of large droplets (*Rogers and Yau*, 1989). Suppression of precipitation shifts rainfall patterns, and increases cloud lifetime which changes global mean fractional cloudiness, albedo, and radiative forcing (*Albrecht*, 1989).

Though each of the indirect effects of aerosols are as yet poorly characterized, observational evidence of the various cloud-altering effects of particulate pollution is mounting. For example, brighter, more stable lines of clouds above shipping corridors (known as “ship tracks”) are clearly distinguishable in satellite images from the unperturbed marine background (*Twomey*, 1991; *King et al.*, 1993; *Russell et al.*, 1999). T-test significant studies reveal that more rain falls during the two days per week of minimum pollution levels ($\sim 16\%$ of the average weekly total per day during the two weekend days) than during other days ($\sim 13\%$ per day) over the heavily urbanized and industrialized American East coast (*Cerveny and Balling*, 1998). Studies that combine satellite observations and global scale models find a strongly significant correlation between aerosol concentrations and both cloud optical depth (*Chameides et al.*, 2002) and the mean cloud drop size (*Han et al.*, 1994; *Breon et al.*, 2002), and that these correlations alter the overall radiative forcing (*Penner et al.*, 2004).

Rotstajn et al. (2000) use the CSIRO general circulation model (GCM) and a modified *Kessler* (1969) cloud bulk microphysics scheme that accounts roughly for the affects of aerosol concentrations on cloud lifetime to investigate both the first and second indirect effects. They approximate that the effects exert equal negative radiative forcings on the climate, which increase from about -0.5 W m^{-2} each in the southern hemisphere to a maximum magnitude of -2 W m^{-2} at 40° north. This inter-hemispheric gradient results from the large pollutant sources in the northern hemisphere, and will be seen in any rendering of the indirect effects. This study is amongst the first that considers the second indirect effect, but is qualitatively representative both of what has been found in studies of the first indirect effect and of what is expected. The background aerosol concentrations in the northern hemisphere are higher both than those in the southern hemisphere and than the pre-industrial equivalents (*Schwartz and Slingo*, 1996), implying that indirect effects occur not only local to point-source pollution (such as near cities, factories, and ship smoke stacks) but also throughout the widely polluted northern hemisphere.

Figure 1-1 shows the Intergovernmental Panel on Climate Change’s (IPCC) estimates of the

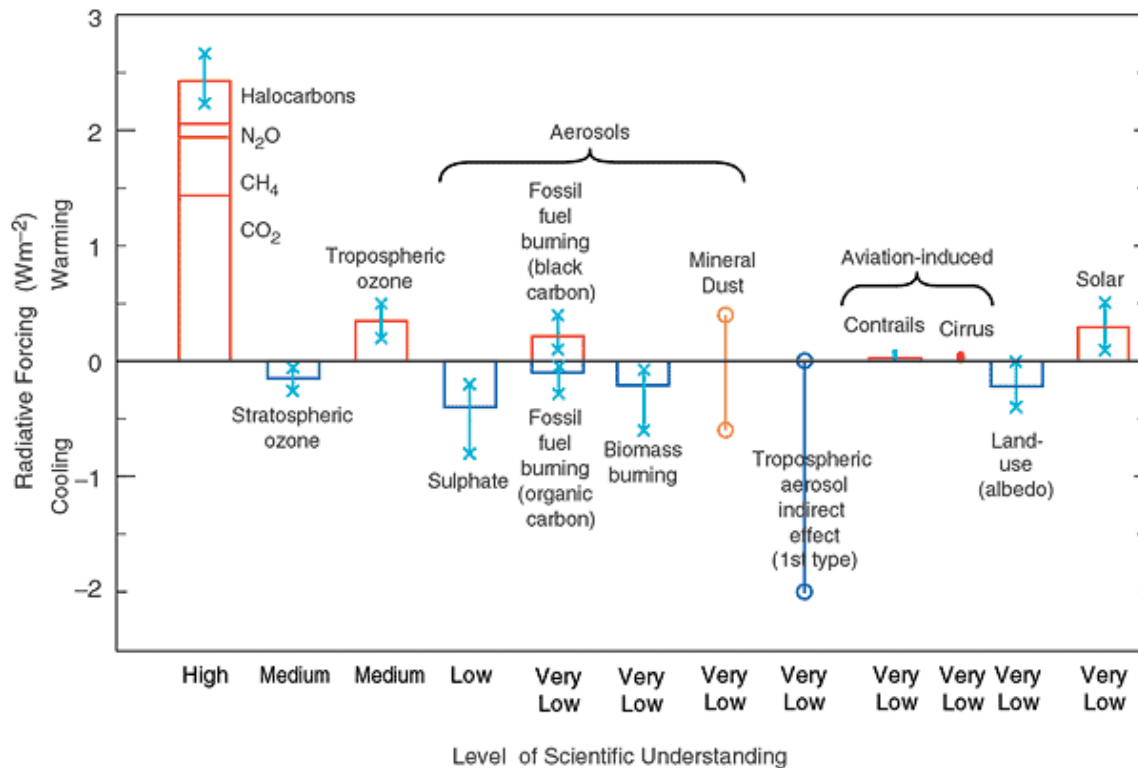


Figure 1-1: Estimates of the radiative forcing of various climate-altering effects, shown as a differential between the radiative forcing in 1750 and 2000; rectangular bars indicate best estimates while lines indicate the range of uncertainty; no rectangular bars are shown for effects for which the uncertainty is so large that no best estimate is possible; the qualitatively evaluated level of scientific understanding is shown beneath the horizontal axis (from *Houghton et al.*, 2001)

change, from 1750 and 2000, in the radiative forcing of various important sources. The rectangular bars indicate the central estimate of the forcing from each effect, and the lines show an estimated range of uncertainty. Forcing by greenhouse gases, the leftmost and strongest warming effect shown in this figure, has a narrow uncertainty range reflective of the well established governing physics and well mixed nature of the gases involved. The direct effect of aerosols, which includes the four categories bracketed under “Aerosols,” are generally cooling effects that primarily affect the regions near aerosol emissions. Direct forcing by sulfate aerosols is the simplest of the various aerosol effects to include in global models, and more effort has been focused on refining the related modeling techniques than those for any other aerosol effect; that this forcing estimate is still relatively uncertain underscores the difficulty of modeling aerosol-related forcings at the global scale. The first indirect effect of aerosols is shown to be a cooling effect that may either completely counteract greenhouse warming (in the global mean) or may have no effect at all, depending on where the true forcing falls within the uncertainty range. The second indirect of aerosols is not shown in this figure but is mentioned in the IPCC’s caption as being potentially important but so

uncertain as to prevent the panel from defining even a qualitative range of uncertainty; this effect is thought to be a cooling effect of comparable magnitude to the first indirect effect (*Rotstayn and Penner*, 2001) but is not included on this figure because it is less well understood even than the first indirect effect. The semi-direct effect is so poorly understood that it is mentioned nowhere in the IPCC’s discussion.

The dependence of the indirect effects of aerosols on environmental parameters, on aerosol size, and on aerosol composition is poorly constrained, and often altogether ignored in global modeling efforts (*Seinfeld and Flagan*, 1999). There have been a proliferation of studies addressing aerosol-cloud interaction from a microphysical, particle-scale perspective (to be discussed in Section 1.2.3), but it is still difficult to link from these studies to quantifications of global-scale climate impacts.

1.2.2 The Scale Problem

The global-scale impacts of the indirect effects of aerosols are exceedingly difficult to quantify since the related calculations depend critically on physics at all scales, including those of microscopic aerosol dynamics, of local convective systems and emissions, and of global radiative and hydrologic balances. Figure 1-2 presents the processes that must be included, either explicitly or through parameterization, in any adequate climate model that includes the indirect effects of aerosols. Beginning our discussion at the bottom of the figure, aerosol particles arrive in the atmosphere either from primary emission from, amongst other sources, smoke-stacks, wind-ablation from the sea surface, incomplete combustion, and nucleation of condensable gas-phase chemicals. Once in the atmosphere, aerosol particles may grow by condensation of water or other volatile chemicals or by colliding and conjoining with other particles. In environments that are super-saturated with respect to liquid water (which we will refer to simply as “super-saturated”), aerosols may “activate” and form cloud condensation nuclei (at which point they are energetically favored to grow rather than shrink), and then continue to grow until they become cloud droplets. The properties of cloud droplets depend on the particulars of the aerosol population in the air in which they formed, and partially determine the character and behavior of the clouds they help compose. In turn, clouds’ aggregate radiative properties and precipitation patterns contribute to the regulation of the global hydrologic cycle, radiative balance, and climate. It is essential to correctly represent the cascading influences of each scale on all of the others when modeling the indirect effects of aerosols at regional or global scales. To accomplish this, the processes and model variables at each scale that are of greatest importance to processes at other scales must be identified and appropriately parameterized.

As yet, most global modeling studies of the indirect effects of aerosols have drawn the link from

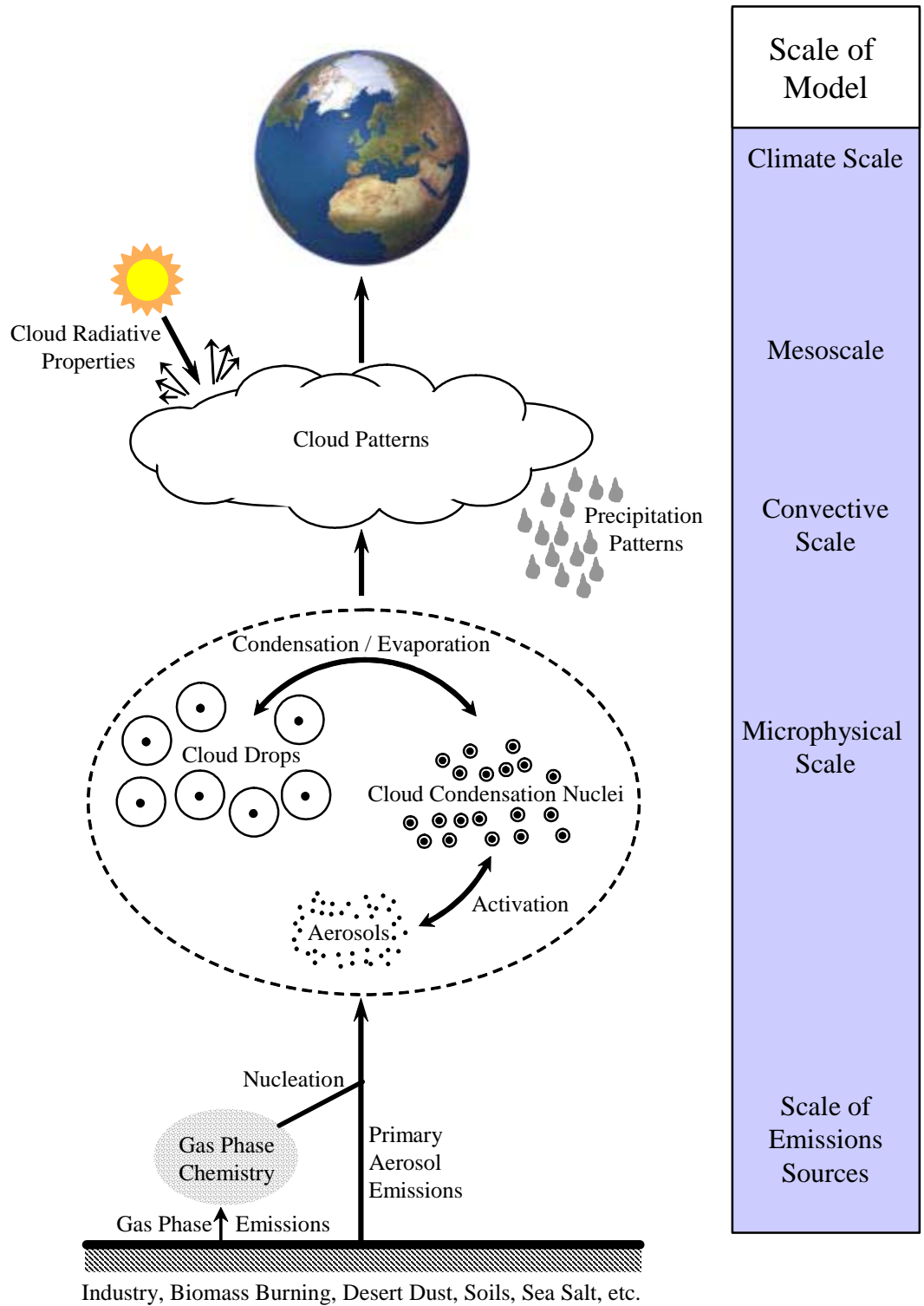


Figure 1-2: Schematic of the necessary components in a model of the role of indirect radiative forcing in the global climate system

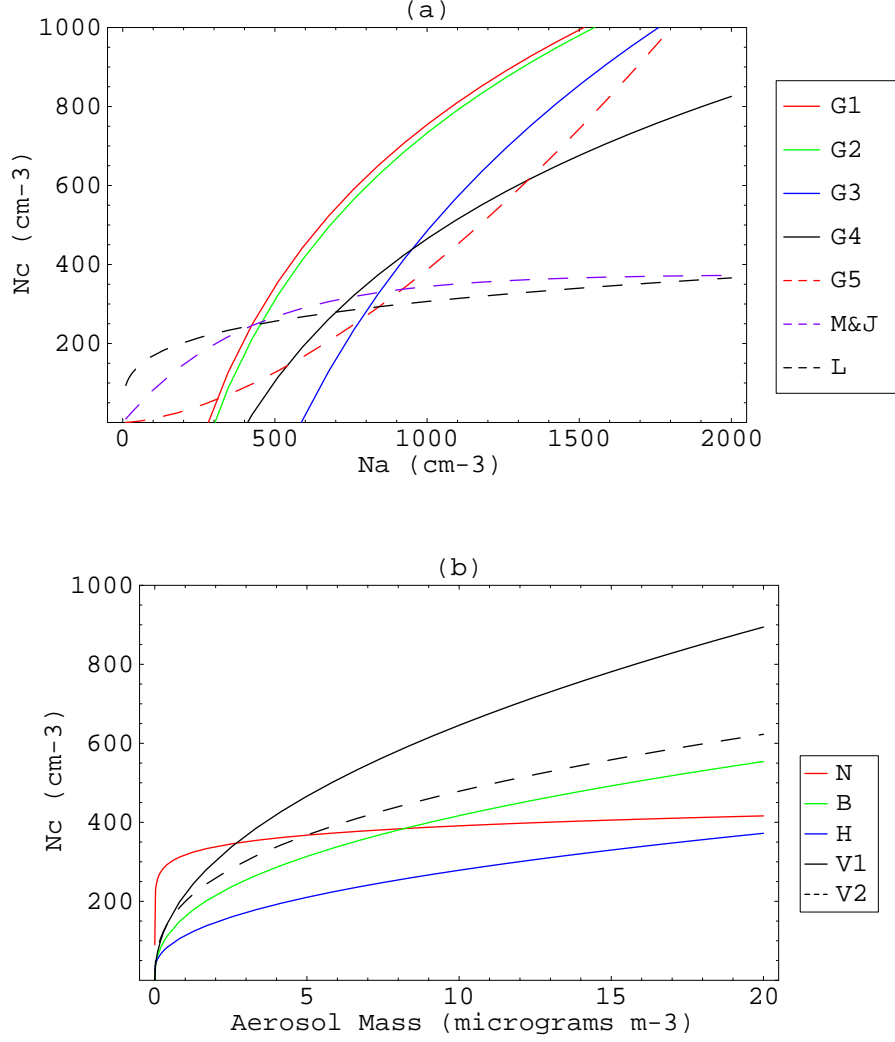


Figure 1-3: (a): Several parameterizations of $N_c(N_a)$ relationships taken from *Gultepe and Isaac* (1999) (G1 uses data collected near Syracuse, NY, G2 uses data from the Eulerian Model Evaluation Field Study (EMEFS) collected in 1988, G3 uses data from EMEFS collected in 1990, G4 uses data from the North Atlantic Regional Experiment, and G5 uses data from the Radiation, Aerosol, and Cloud Experiment), *Martin et al.* (1994) (M&J), and *Leaitch et al.* (1992) (L); (b): Parameterizations of $N_c(m_a)$ taken from *Novakov et al.* (1994) (N), *Boucher and Lohmann* (1995) (B), *Hegg* (1994) (H), and *Van Dingenen et al.* (1995) with all of their collected data points (V1) and excluding one errant point (V2)

aerosol populations to cloud drop distributions by coarsely relating pre-cloud or sub-cloud sulfate aerosol mass concentration (\mathbf{m}_a) or number concentration (N_a) to cloud drop concentration (N_c) by empirical analysis of observations from field campaigns, and developing parameterizations of cloud behavior that depend on this relationship (e.g., *Fitzgerald and Spyers-Duran*, 1973; *Gillani et al.*, 1992; *Boucher and Lohmann*, 1995; *Van Dingenen et al.*, 1995; *Lohmann and Feichter*, 1997; *Gultepe and Isaac*, 1999; *Rotstayn et al.*, 2000; *Rotstayn and Penner*, 2001). Such parameterizations of the relationship between aerosol loading and cloud-drop concentrations are necessarily mediocre as N_c depends to first order on, at least, sub-grid-scale updraft velocities, the maximum supersaturation achieved in cloud updrafts, distributions of aerosol size and composition (which are affected by emission type, age, and environmental parameters), and competition for water vapor between aerosols of various types (*Fitzgerald and Spyers-Duran*, 1973; *Gillani et al.*, 1992; *Hobbs*, 1993; *Kaufman and Tanre*, 1994; *Boucher and Lohmann*, 1995; *Ghan et al.*, 1998; *Facchini et al.*, 1999; *Nenes et al.*, 2001).

Figure 1-3(a) shows seven parameterizations of the functional relationship $N_c \equiv N_c(N_a)$, and 1-3(b) shows five parameterizations of $N_c \equiv N_c(\mathbf{m}_a)$, that are used in global modeling studies of the indirect effects of aerosols. The variation between the several parameterizations is striking. Most of these parameterizations are empirical fittings of the two parameters from a single or small set of field campaigns which necessarily consider only a restricted range of environments and aerosol types. Some studies have gone further and attempted to cobble together parameterizations of the aerosol / cloud droplet relationship from several environments into a more coherent global parameterization (e.g., *Boucher and Lohmann*, 1995) or appealed to a great many historical data sets (e.g., *Van Dingenen et al.*, 1995; *Gultepe and Isaac*, 1999). Not surprisingly given their obvious differences, each of these parameterizations leads to quite different estimates of the climate impacts of the indirect effects of aerosols when embedded in global models (*Lohmann and Feichter*, 1997; *Lohmann et al.*, 1999a); differences between these studies lead to the IPCC's estimate of a huge uncertainty in the radiative forcing associated with the first indirect effect of aerosols (shown in Figure 1-1). These single-factor parameterizations depend critically on the assumption that variations in sulfate aerosol (as represented only by average regional number or mass concentrations) adequately quantify the complicated relationship between sub-cloud aerosols and cloud droplets. Many studies now indicate that this assumption falls short, that the sub-cloud aerosol / cloud droplet relationship depends on convective dynamics and on more properties of the aerosol population than simply total sulfate loading.

Despite the shortcomings of these parameterizations, the studies that employ them are on the

right track: global scale studies of the indirect effects of aerosols must parameterize the relationship between aerosol and cloud drop concentrations, and must also use this parameterization to characterize the dependence of cloud optical properties and of rainfall patterns on specific properties of local aerosol populations. The difficulty is in appropriately formulating these parameterizations. Deconvolving the effects of composition and size distribution from field studies, such as those that under-gird the parameterizations shown in Figure 1-3, would require a huge number of campaigns and large amounts of funding and time, in addition to advances in aerosol and cloud droplet measurement techniques. Microphysical process models, which simulate the physics of the aerosol-cloud transition explicitly, may be used to guide data analysis of field campaign data and of more confined laboratory scenarios, and thus to help determine the aerosol characteristics that most influence the formation of cloud condensation nuclei and cloud droplets. Quite a lot has been learned already from process model studies (and will be reviewed in the next section); their use, when appropriately combined with observations, is very promising.

In order to quantify and predict the climate-scale impacts of the indirect effects of aerosols, additional work is needed at every stage between the tail-pipe and the global climate. In this thesis, we will both take several steps towards resolving outstanding microphysical issues and develop a model appropriate for further microphysical studies. The long term goal of this line of research is to develop an accurate parameterization of the relationship between aerosols populations and cloud behavior, which will certainly depend on many factors related to both local aerosol populations and meteorology.

1.2.3 Microphysical Scale Modeling of Aerosol / Cloud Interaction

In contrast to the empirically informed parameterizations described in the previous section, cloud-aerosol process models seek to explicitly represent the microphysical processes encircled by the dashed line in Figure 1-2, including: gas, aqueous, and heterogeneous chemistry, aerosol thermodynamics, gas-particle partitioning of volatile species, gas-particle and particle-droplet conversion, and coagulation and coalescence. Modeling these microphysical processes requires significant computational resources; all modeling studies necessarily include some simplifications in how aerosol are represented (which we will discuss in Chapter 3) and pare the list of physics to include only those processes required to consider its specific scientific question or capture the essence of the role of aerosols in a particular modeling effort.

When considering the indirect effect of aerosols, process models may be employed to guide development of bulk parameterizations that relate N_c to N_a ; the validity of which depends on

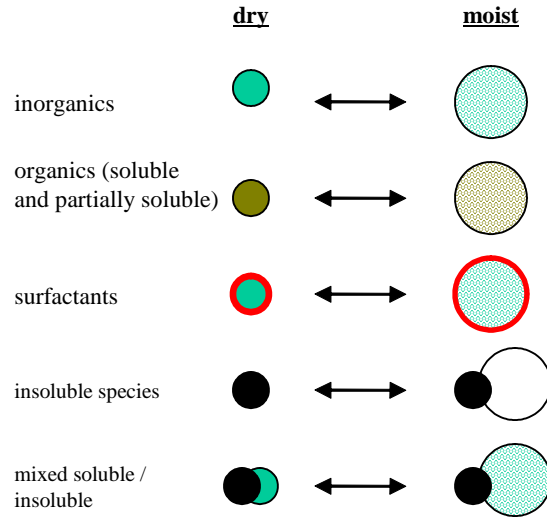


Figure 1-4: Schematic of several aerosol types

the correct formulation of the underlying physics and appropriate input aerosol populations and boundary conditions rather than on explicit field-campaign scale observations. Generally, explicit microphysical process models are embedded in idealized parcel updraft models which provide the boundary conditions that would be expected for an isolated parcel of aerosols and air that is adiabatically lifted. When a parcel is lifted sufficiently far, the air within saturates, water vapor condenses onto the aerosols, and some aerosols activate and grow to become cloud droplets. In this thesis, we will build a microphysical process model tailored towards addressing questions about how the particulars of an aerosol population impact the indirect effects of aerosols; we will then embed the microphysical model in an updraft model. We provide an overview of the combined model in Chapter 2 and discuss it in detail in Chapters 3 through 6.

Although the single-factor empirical models discussed in the previous section generally presume that concentrations of ubiquitous sulfate aerosol are most important for determining cloud drop concentrations, there are many types of aerosols that have been shown to effectively activate and influence cloud development. In fact, there is increasing evidence that aerosol composition and chemical effects may be as important to the formation of cloud droplets on aerosol particles as number concentration and sulfate loading (*Ahr et al.*, 1989; *Svenningsson et al.*, 1992; *Brechtel and Kreidenweis*, 2000; *Nenes et al.*, 2002). Figure 1-4 presents schematic diagrams of some of the many types of aerosols found in the atmosphere that attract water. Inorganic aerosols (of which sulfate aerosols are one type) are extremely hydrophilic and dissolve into solution droplets in humid environments. Organic aerosols may be composed of soluble or partially soluble species and may be either as hydrophilic as inorganic aerosols or essentially hydrophobic, depending on their

composition and oxidation state. Organic aerosols are generally composed of many organic species, most of which are at present unidentifiable (*Seinfeld and Pandis, 1998*), and their concentrations are difficult to measure accurately (*Huebert and Charlson, 2000*). Some organic species are surface-active and form thin films on the surface of solution droplets; these are known as surfactants. These films limit the ability of the host particle to attract water. Water may condense upon insoluble species such as soot and dust, both when that particle contains some inorganic components and when it does not. The presence of any of these various aerosols types may impact condensation onto the overall aerosol population, affect how liquid water is distributed amongst aerosols within the population, and affect cloud formation.

“Conventional wisdom,” *Ghan et al. (1998)* argue, holds that the quantity of CCN that activate in an ascending parcel grows with N_a , and that the only question is: by how much? This is true in the idealized situation of a population of homogeneous aerosols rising in an adiabatic parcel that remains in equilibrium with water vapor as it rises. The introduction of more than one of the many aerosol types listed above and of more realistic cloud dynamics complicates matters significantly (*Phinney et al., 2003*). Studies of aerosol “activation” (the transition of an aerosol to a cloud droplet via condensation) using explicit process models have revealed various physical effects not seen in simpler models. There are now many examples: in marine environments sea salt aerosols compete with sulfate aerosols for water vapor during cloud formation and rising sea salt aerosol concentrations may depress the number of sulfate aerosols that activate (*Ghan et al., 1998; O’Dowd et al., 1999; Phinney et al., 2003*); condensation onto large particles is proportionally slow relative to condensation onto smaller particles, and so large particles that would always activate within an equilibrium framework may not in a more realistic, kinetically-limited situation (*Chuang et al., 1997b*); cloud entrainment, updraft speed, and other dynamical parameters have a large impact on the development of cloud droplets from cloud condensation nuclei (*Yum et al., 1998; Hudson and Xie, 1999; Bower et al., 2000; Hudson and Yum, 2001*); aerosols that form cloud droplets which then evaporate often have substantially different chemical properties, and cloud seeding ability, than those aerosols that are not similarly “processed” by clouds (*Feingold and Kreidenweis, 2000*); and a host of chemical effects – including formation of surfactant layers, dissolution of moderately soluble species during cloud growth, or favorable aerosol mixing states – may be as important as simple number concentration (e.g., *Kulmala et al., 1993; Shulman et al., 1996; Facchini et al., 1999; Feingold and Chuang, 2002a; Nenes et al., 2002*). The implication of these effects, taken to its limit, is that slight variations amongst particle composition may lead to competitive advantages or disadvantages that alter the relationship between an aerosol population and the cloud drop

population that forms upon it.

An accurate parameterization for global models that links characteristics of aerosol populations to cloud drop concentrations and cloud behavior must cope with these many complexities. Parameterizations that appeal only to sulfate loading are but a first attempt, and eventual models will consider more aerosol types, aerosol dynamics, and cloud dynamics (some first examples of these more sophisticated parameterizations include *Abdul-Razzak and Ghan*, 2000, 2002; *Nenes and Seinfeld*, 2003). This thesis focuses on building a model appropriate to considering the microphysical processes encircled by the dashed line in Figure 1-2, linking from the microphysical to convective scales, and answering questions about the role of a particular type of aerosol on cloud formation. It is distinguished from process models available in the literature in that it retains as much information as possible about the aerosol population both in terms of size and of composition and in the simplicity of including new chemical components, aerosol types, or aerosol physics. It is meant to be used to answer questions about aerosol activation, rather than to be used operationally in global scale models. The eventual goal of this modeling effort is to identify the list of important aerosol physics and critical traits of aerosol populations that are important to cloud formation, and then to provide a multi-factor parameterization of cloud drop concentrations for use in regional and global models. In this thesis, we will present the model and address outstanding questions related to the role of cloud dynamics and of mixed soot / sulfate particles in aerosol activation and cloud development.

1.3 Goals and Outline of the Thesis

The subject of this thesis is the microphysics of aerosol activation, with particular emphasis placed on issues related to the indirect effects of aerosols. The specific goal of this thesis is to develop an accurate and flexible computer model of aerosol and cloud microphysics that is capable of answering sophisticated questions regarding the behaviors of complex aerosol populations during cloud development, and then to use it to ask and answer several such questions.

We will introduce a new model – the Mixed Eulerian-Lagrangian Aerosol Model (MELAM) – in Chapter 2 and discuss the details of the constituent physical models in Chapters 3 to 5. MELAM is a microphysical process model specifically tailored to the calculation of the transition of aerosol particles to cloud condensation nuclei in cloud updrafts; its purview includes all of the microphysical processes that lie within the dashed oval in Figure 1-2.

Many of the process models in the literature that have been used to investigate indirect effects of

atmospheric aerosols have adopted approximations that were developed for representing aerosols in air quality models or mature droplets in clouds. In so doing, the published models neglect information that is important to aerosol activation, especially adequate resolution of aerosol composition and aerosol mixing state. MELAM includes a new aerosol representation scheme that tracks a representative sample of individual particles, and thus the model is able to represent many complex aerosol types and aerosol populations with extremely complicated mixing states; MELAM is also capable of using standard representations of aerosol populations or of combining the standard and representative sample techniques.

Many of the studies of aerosol activation in the literature employ adiabatic, constant-updraft-speed parcel models to provide boundary conditions to the rising lagrangian parcel of sub-cloud aerosols. We similarly embed the MELAM model in a parcel updraft model; the combined model is the “MELAM updraft” model. Within the cloud dynamics community, the constant-speed adiabatic updraft model has, for many years, been considered to be a poor analogy to clouds. In Chapter 6 we develop a version of the standard constant-speed adiabatic updraft model and also a new episodically entraining, variable-speed updraft model. We will contrast the behavior of the two models to provide insight into the role and appropriate use of the adiabatic constant-updraft model. We will use the new model to consider the roles of updraft speed and entrainment in aerosol activation, and to discuss how such an updraft model might eventually incorporate information calculated by the convective routine of a global climate model so that it can operate interactively in global modeling studies of the indirect effects of aerosols.

We have made every effort to assure that MELAM is as flexible as possible: we allow the user to specify all of the chemical and dynamical parameters of the model through text input files; and we make no exceptions to generalized physical rules in the model itself. The computer code is quite modular, which will facilitate the inclusion of new aerosol representations, new physical parameterizations, and new experimental configurations as necessary.

In Chapter 7, we will use the MELAM updraft model to consider the role of mixed soot / sulfate particles in cloud formation. New observations suggest that mixed soot / sulfate aerosols are ubiquitous in both clean and polluted marine environments. If these aerosols alter activation and cloud formation in any significant way, the impact on the global radiative balance could be large. The MELAM model includes a model of condensation onto mixed insoluble / soluble particles (a good analogy to soot / sulfate particles) that has been available in the literature for several years but which we constrain with new observations from both laboratory studies and field campaigns. The goal of that chapter is to determine the impact of this important type of mixed particles on

aerosol activation. We will find that these mixed sulfate / soot aerosols influence cloud formation in very polluted environments, but not in clean marine environments where they are observed but in much lower concentrations.

Chapter 2

Overview of the Mixed Eulerian-Lagrangian Aerosol Model

2.1 Introduction

In this thesis, we present a new computer model of aerosol and cloud microphysics that is specifically intended to be used to simulate aerosol activation and cloud formation: the Mixed Eulerian-Lagrangian Aerosol Model (MELAM). A parcel updraft model will be used to provide boundary conditions to MELAM during simulated ascent through a cloud updraft; the combination of the microphysical and parcel models is the “MELAM updraft” model. The dependence of aerosol activation on aerosol composition, the mixing state of the overall aerosol population, and cloud dynamics is very uncertain. We intend to use MELAM to answer related questions both in this thesis and beyond. In this chapter, we discuss the formulation of the various parts of the model in brief. Over the next several chapters we will present detailed discussions of the model’s representation of aerosol particles, the approximations used to calculate the thermodynamic state of aerosols, the governing equations of equilibrium and non-equilibrium condensation and dissolution, and both a standard and a new updraft parcel model.

The MELAM model is distinguished from those available in the literature by its ability to model the activation of extremely complex aerosol populations. It may be used to analyze the sensitivity of aerosol activation and cloud development to aerosol mixing state, multiple aerosol populations, and complexities of aerosol composition. In Chapter 7, we will use the MELAM updraft model to consider the impact of the widespread mixed soot / sulfate aerosols on aerosol activation in marine environments. In studies beyond this thesis, we hope to use the model to investigate the

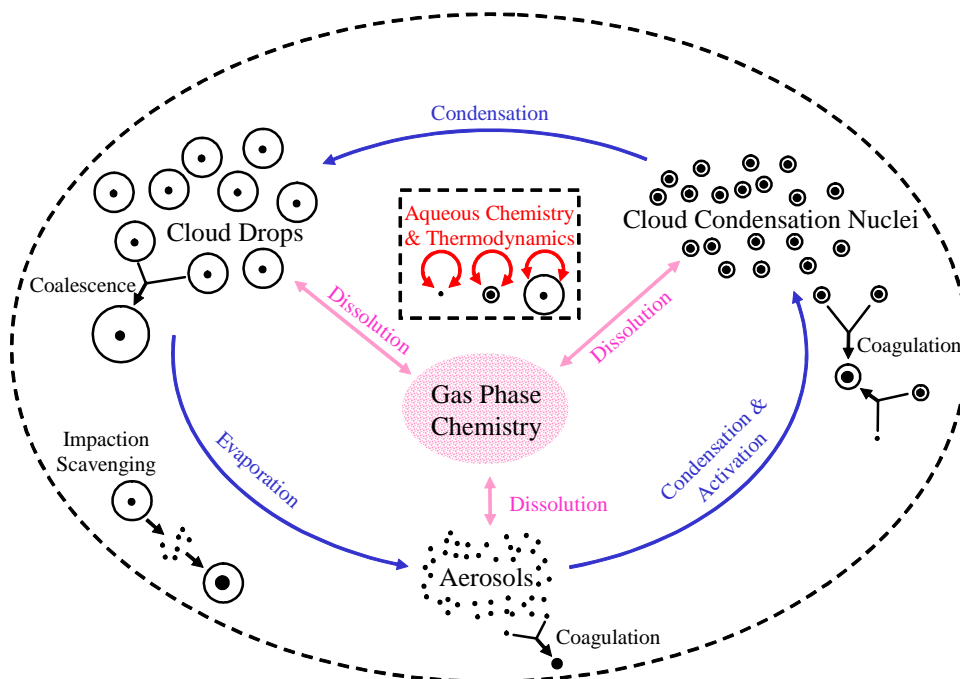


Figure 2-1: Schematic of the microphysical processes included in the MELAM microphysics model

cloud-altering roles of organic aerosols, aerosols with surfactant layers, aerosols in environments with partially soluble organic species, and multi-component populations that are mixed in complex manners. The eventual goal is to use the model to formulate multi-factor parameterizations of aerosol activation based on properties of aerosol distributions and loadings that can be linked to the convective routines in global climate models and used to predict the optical properties of clouds and rainfall patterns. We also hope to use the model to guide future laboratory studies towards refining the measurements that lead to the greatest uncertainty in estimates of the indirect radiative forcing of aerosols, and also to suggest to suites of measurements for field campaigns.

Figure 2-1 is a schematic that indicates the microphysical processes included in the MELAM model. The oval of Figure 2-1 corresponds to the similar dashed oval in Figure 1-2, but includes schematics of the full range of microphysical processes to be considered. Aerosols from a given population may grow by colliding and combining with other aerosols (this is called coagulation) or through the condensation of water vapor or dissolution of other condensable species. If aerosols grow sufficiently large, they activate and become cloud condensation nuclei (CCN). CCN grow rapidly via condensation to become cloud drops and may coagulate with aerosol particles, other CCN, or be scavenged by cloud drops. Cloud drops readily absorb condensable gas phase species via dissolution, collect smaller aerosol particles efficiently via impaction scavenging, may collide with each other and combine to form larger droplets (which is called coalescence), and may eventually

form precipitation after coalescing many times. Cloud droplets may also evaporate completely and re-form aerosols which tend to have quite different composition than freshly emitted particles; this process is known as cloud processing of aerosols and is responsible for the presence of mid-sided “Aitken mode” particles widely observed in marine environments.

All forms of growth or changes in composition via dissolution alter the thermodynamic state of aerosols, CCN, and cloud drops alike. The thermodynamic state of an aerosol encompasses the ionic strength, extent of dissociation of electrolyte, and pH of liquid aerosol and the particle’s surface tension, density, and water activity. The MELAM model approximates all of these processes and is able to evolve the state of a particle distribution forward in time when provided appropriate boundary conditions (which we will predict using a parcel updraft model) and given, as input, an initial aerosol distribution, gas phase concentrations, and environmental parameters.

Figure 1-2 presented the full range of processes and scales that must be considered in order to estimate the impact of the indirect effects of aerosols on the global scale. Estimates of the ambient aerosol population must be provided as input to microphysical models, which in turn provide information on aerosol activation and properties of the distribution of cloud drops to convective parameterizations or to cloud or meso-scale models. Figure 1-2 indicates that both nucleation of gas-phase species and direct emissions contribute to the aerosol population. Global and regional modeling studies must explicitly parameterize both of these processes, while the studies we will perform with the MELAM updraft model will obviate these parameterizations by relying on observations from field campaigns to specify the input aerosol distributions. Figure 1-2 also indicates that microphysical calculations inform large-scale cloud dynamics. The identification of which aerosols from a given aerosol population activate in a given cloud or specified updraft is the simplest proxy of the impact of aerosols on cloud formation; microphysical models present this information to larger scale models, which may be used to interpret the climate scale impacts of these calculations.

The MELAM model uses a combined eulerian and lagrangian framework. The gas phase environment is represented by a series of grid points at which gas phase concentrations and environmental parameters are specified. MELAM calculates the evolution of the thermodynamics and gas phase concentrations at each grid point and transport between them. Aerosols may be specified in either eulerian or lagrangian representations. Standard sectional or functional representations of aerosol size distributions may be specified at each eulerian grid point in the model, or lagrangian aerosol may be scattered through the domain and tracked individually. Each lagrangian aerosol

has a specific location and exchanges gas phase species with the nearest grid point. The specifics of these representations will be discussed in Section 2.2 and Chapter 3. In this thesis, we will embed the MELAM model, using only a single grid point, within a lagrangian parcel updraft model in order to investigate the activation of aerosols during cloud formation. The MELAM model, however, may be run in many configurations – with any boundary conditions and an arbitrarily large or small domain and number of grid points – and used to address many microphysics-related questions.

The MELAM model is flexible and modular. The user may define the set of chemical species, chemical reactions, dissolution and dissociation reactions, and thermodynamic parameters to include using simple text input files. He or she may also select which physical processes to include and whether to use equilibrium or non-equilibrium frameworks for condensation and dissolution.

In this chapter, we will discuss each component of the MELAM microphysics and updraft models in brief. Some of those components will then be discussed in greater length and detail in the chapters that follow. Gas and aerosol phase chemistry and aerosol dynamics are discussed only in the summaries provided in this chapter because they will not be used in the studies presented in this thesis. Chapter 3 addresses the model’s representation of aerosols. Chapter 4 presents the aerosol chemical thermodynamic module. Chapter 5 discusses condensation and dissolution. Chapter 6 presents and contrasts constant-speed adiabatic and variable-speed entraining 1-D updraft models. In Chapter 7, we apply of the model to the activation of mixed soot / sulfate aerosols in marine environments.

2.2 Aerosol Size Representation

Aerosol particles range over a several orders of magnitude in size, from small clusters of a handful of molecules that result from nucleation to large sea salt, dust, and dirt particles swept aloft by wind. The composition of each particle is determined in part by its source, but also by cloud processing, by combination of multiple particles via coagulation, coalescence, or impaction scavenging, by dissolution of condensable species, and by a number of other processes. As a result, the composition of aerosols in polluted populations may be quite inhomogeneous. An individual aerosol particle may include water, inorganic solids, inorganic species in solution, ions, soluble organic species, a surfactant layer, and one or several insoluble soot or dust cores. Microphysical models are able to calculate the dynamics and behaviors of inorganic aerosols with reasonable accuracy; only rudimentary theories and modeling methods exist for other aerosol types.

To formulate an aerosol model, one must decide how to represent the variations within a popu-

lation of aerosols, and in so doing trade between computational expense and resolution of inhomogeneities in size and in composition. There are five standard representations of the size distributions of aerosol particles in models: bulk, moment-based, modal, continuous, and sectional (discussed in Chapter 3 and well reviewed in *Zhang et al., 1999*). The MELAM model is able to use the bulk and sectional distributions. The bulk model represents the total aerosol population as a single mass with no size resolution whatsoever; because it requires few computational resources, it is useful in large models with many grid points for studies in which size resolution is not critically important. Sectional distributions track the total mass and number concentrations for aerosols that lie within particular size ranges; multiple sectional distributions may be used to distinguish between aerosols of different composition, but generally composition is poorly resolved. Insoluble cores, surfactant layers, and other complexities are important when calculating aerosol activation and are difficult to include in sectional distributions and impossible to represent adequately in bulk representations.

In this thesis, we introduce another representation of aerosol populations: the “representative lagrangian” or “representative sample” distribution. This new representation tracks the size and composition of a sample of individual, lagrangian particles. The primary advantage of this representation is that it may represent complicated aerosol structures, variations in mixing state, insoluble cores, and surfactants without approximating a relationship between those properties and aerosol size. The model can also be used to consider whether statistical deviations from the mean evolution of aerosol populations has any impact on aerosol activation, although we leave such a consideration to future studies. The representative sample distribution is especially useful for studies that focus on condensation and activation, as condensation rates are sensitive to composition and structure, and all of the aerosols within a population compete for available water vapor. The representative sample distribution may be used in conjunction with sectional distributions, such that some number of aerosols are tracked in a lagrangian framework and others in an eulerian framework; this is useful, for example, when there are a great number of freshly nucleated aerosols that are relatively homogeneous, well represented by sectional distributions, and too numerous to track individually, and also for particles with very low concentrations that would be poorly sampled in the domain considered. The main drawbacks of the representative sample distribution are that it complicates calculation of coagulation and particle transport (see Section 2.7 for a discussion of this), and that it is computationally expensive compared to bulk formulations and sectional methods that use a small number of bins. The representative sample formulation is most useful for answering scientific questions about how complex mixtures affect aerosol activation or other aerosol behaviors than it is for modeling aerosol behavior in large domains or other more operational applications; sectional

or bulk formulations are more appropriate in such contexts.

MELAM allows the user a choice between bulk, sectional, and representative sample distributions in any appropriate combination, as specified in text input decks. The model is able to represent inorganic electrolytic aerosols and insoluble cores, and at this point is not able to represent organic or surfactant species due to the inability to calculate the related thermodynamics, condensation, and other behaviors. Such species will be easily incorporated into MELAM once appropriate theoretical treatments become available.

2.3 Chemical Continuity

Clouds are of seminal importance in tropospheric chemistry. Most important are their involvement in the removal of soluble trace species in precipitation, venting of gases from the boundary layer to higher altitudes, altering the aerosol populations through cloud processing, and aqueous-phase oxidation of reduced sulfur compounds which transforms S(IV) into S(VI) (*Chameides and Davis*, 1982; *Chameides*, 1984; *Russell et al.*, 1983a,b; *Jacob*, 1986; *Lelieveld and Crutzen*, 1991; *Chameides and Stelson*, 1992; *Wang and Prinn*, 2000; *Lucas*, 2003). Recent studies have also highlighted the role of lightning (*Boldi*, 1993; *Wang and Prinn*, 2000) and that clouds alter actinic fluxes and so change the rates of photo-chemical reactions (*Frederick and Erlick*, 1995; *Liao et al.*, 1999). Gas-phase and aqueous-phase chemistry also impacts the behavior of clouds themselves. As will be discussed in Section 2.5 and Chapter 4, equilibrium aerosol water content and disequilibrium water vapor condensation rates depend critically on aerosol composition. In studies of sufficient extent and duration, including forward chemical reactions is important to determining local gas and aqueous phase concentrations.

We may write an expression of conservation for each chemical species across the gas, aqueous or liquid, and solid phases which states that the total mass of a species i (m_i) present in the model domain changes only via true chemical production and loss:

$$\frac{dm_i}{dt} = \frac{d}{dt} \left(\overbrace{m_i^{(g)}}^{\text{gas-phase}} + \sum_p \overbrace{(m_{i,p}^{(aq)} + m_{i,p}^{(s)})}^{\text{particle-phase}} \right) = \text{Production} - \text{Loss} \quad (2.1)$$

Here, $m_i^{(g)}$ is the total mass of i in the gas phase, $m_{i,p}^{(aq)}$ is the aqueous phase mass of i in particle p , and $m_{i,p}^{(s)}$ is the solid phase mass of i in particle p .

Chemical production and loss results from chemical transformations that may be sub-divided

into two primary types: changes in the equilibrium of rapidly reversible reactions, and forward chemical reactions for which the reverse is not of a comparable rate. Of course, the distinction between these two types is largely semantic as all reactions occur in only the forward direction even if the opposite reaction occurs very soon afterwards; in practice, partitioning across rapid and reversible reactions is best solved in an equilibrium framework. The first type is especially important in the aqueous phase, in which dissociation and re-association of electrolytes and acids is rapid and the equilibrium between the two depends on the overall composition, pH, the strength of the electrolyte, and temperature of the solution (*Jacobson, 1999*).

The MELAM model is able to track gas phase chemistry at each eulerian grid point and the aqueous phase chemistry within each representative particle, within each group of particles in a sectional distribution, and in the bulk aerosol phase. The aqueous chemistry within each particle or section of particles evolves on its own and the particles interact with the gas-phase through condensational and evaporative exchange with the closest eulerian grid point. In this framework, the chemistry of the lagrangian particles generally obeys the following continuity expression:

$$\left(\frac{dc_i}{dt}\right)_{total} = \left(\frac{dc_i}{dt}\right)_{gas/aer\ transfer} + \left(\frac{dc_i}{dt}\right)_{electrolyte\ dissociation} + \left(\frac{dc_i}{dt}\right)_{forward\ chemical\ rxns} \quad (2.2)$$

In which c_i is the concentration of species i in the aerosol phase solution. As indicated in equation (2.2), the total rate of change of a particular aqueous phase species during a time-step is modeled as three separable processes: the transfer of species from the gas to aqueous phase (and the reverse); the dissociation and re-association of electrolytes and acids in solution; and forward chemical reactions. MELAM considers each of these processes to be independent over the duration of a time-step. Such “operator-splitting” approaches are often used for simplifying the integration of systems of ordinary differential equations (ODEs) in microphysical models (*McRae et al., 1982; Jacobson, 1999; Murthy and Nanjundiah, 2000; Müller, 2001*). The error introduced by the adoption of these methods is difficult to quantify and depends on the duration of the time-step over which the equations are decoupled (although these errors are thoughtfully considered in *Müller, 2001*). The time-steps used for calculation of these methods in the MELAM model are very short in this context, on the order of one to fifteen seconds, and should not introduce any significant error (*Müller, 2001*).

The integration of forward chemical reactions is discussed in Section 2.4. The gas-aerosol transfer of trace species is known as dissolution and of water is known as condensation. It may be treated in an equilibrium or non-equilibrium framework, as discussed in Section 2.6 and Chapter

5. MELAM treats the dissociation of electrolytes and acids as an equilibrium process and within the model’s chemical thermodynamics module, as discussed in Section 2.5 and Chapter 4.

2.4 Gas-Phase and Aqueous-Phase Chemistry

The MELAM model calculates forward gas and aqueous phase chemistry for a set of reactions drawn from a user-defined text input deck. Defining a complete chemical mechanism involves selecting the chemical species of interest and assembling a consistent set of gas and aqueous phase forward chemical reactions, thermodynamic parameters, and dissociation and dissolution equilibrium reactions. Appendix A contains one such consistent set of reactions and parameters for a relatively simple inorganic system containing sodium, ammonium, potassium, chlorine, nitrate, sulfate, and bisulfate; many such mechanisms have been defined, each of which are tailored to the needs of particular modeling efforts. Forward chemical reaction sets are not included in Appendix A because none of the studies considered in this thesis make use of MELAM’s ability to integrate forward chemistry. Some recent studies have defined very detailed mechanisms that include the reaction of radical anions with many aqueous chemicals, transition metal chemistry, and updated rate constants (e.g. *Jacob, 2000; Herrmann et al., 2000; Leriche et al., 2000*), and interface with sophisticated gas-phase mechanisms (such as *Madronich and Calvert, 1990; Stockwell et al., 1990*).

Each forward chemical reaction may be represented by an ODE which expresses the rate of change of the reactants and products. For example, consider the gas phase reaction of $O(^1D)$ with O_3 :



A system of three ordinary differential equations describe the evolution, over time, of the concentration of the three chemicals involved in the reaction:

$$\frac{dC_{O(^1D)}}{dt} = -k C_{O(^1D)} C_{O_3} \quad (2.4)$$

$$\frac{dC_{O_3}}{dt} = -k C_{O(^1D)} C_{O_3} \quad (2.5)$$

$$\frac{dC_{O_2}}{dt} = +2k C_{O(^1D)} C_{O_3} \quad (2.6)$$

Here, C_i is the gas phase concentration of species i , and k is a chemical rate constant that is a strong function of temperature according to the Arrhenius equation (*Steinfeld et al., 1999*). There are other

types of reactions as well, including photolytic and pressure dependent reactions; we refer the reader to basic texts for further discussion (e.g., *Jacobson, 1999; Seinfeld et al., 1999*). In a system with many species and reactions, the evolution of the concentration of each species is governed by a single ODE that may depend on several or even all of the other concentrations. The accurate integration of such a system of forward chemical reactions is made difficult by the stiffness of the system of equations (i.e., by the fact that some reactions occur many orders of magnitude more rapidly than others). MELAM uses *Gear (1971)*’s method, as implemented in the *Livermore Solver for Ordinary Differential Equations with Sparse Matrices* (LSODES) of *Hindmarsh and Radhakrishnan (1993)*. Gear’s method uses a Jacobian partial-derivative matrix and adjusts the integration time-step such that errors remain below a specified threshold. LSODES is a modification of *Gear (1971)*’s original code that uses efficiencies of vectorization and sparse-matrix techniques, so-called because they use the fact that many of the terms of Jacobian matrix are zero. MELAM also uses LSODES to calculate coagulation and the condensation or dissolution of a gas phase species onto a population of many aerosol particles or sections. We will discuss LSODES in greater detail in Section 5.10 when we present the numerical solution of the condensation model.

As mentioned briefly in Section 2.3, the studies considered in this thesis will not make use of MELAM’s ability to calculate gas and aqueous phase forward chemistry. Forward chemistry will be important in studies of cloud processing of aerosols, of the oxidation of sulfate within cloud droplets, or a number of other studies that involve the influence of clouds on the nearby tropospheric chemical system. MELAM’s gas phase chemistry model has also been presented separately as a stand-alone urban box model that is able to integrate reactions forward in time and calculate isopleths for the concentrations of any species as a function of initial conditions or emission rates (cf. *Seinfeld and Pandis, 1998*, section 5.11); that model is available from the author by request.

2.5 Aerosol Chemical Thermodynamics

As discussed in Section 2.3, aqueous and solid phase electrolytes and acids may dissociate into their constituent ions in solution within an aerosol or cloud particle. The properties of the resulting solution determine the particle’s equilibrium water content, surface tension, density, and pH and influences the rate of transfer of gases into and from the particle. The MELAM thermodynamic module calculates the equilibrium state of inorganic electrolytic solutions and all of the related properties of the particle. MELAM presumes that the environment is sufficiently humid so that all solid electrolytic species have dissolved (this introduces significant errors only at $\mathcal{RH} \leq 60\%$, which

is considerably drier than the conditions considered in this thesis; *Moya et al.*, 2002). Solids are only explicitly represented insofar as absolutely insoluble cores are attached to otherwise inorganic aerosols; this will be discussed in Section 2.6 and Chapter 5. There is at present no adequate theory to govern the thermodynamics of solutions containing organic species, and as a result organics are not included in the present version of the MELAM thermodynamic module. The specifics of the thermodynamics module are discussed at length in Chapter 4.

We use a reaction-based electrolyte equilibrium scheme in which the extent of dissociation of each electrolytic species is governed by a temperature dependent equilibrium constant (K_{eq}). MELAM forces the ratio of the thermodynamic activity of each electrolyte or acid to the product of the thermodynamic activities of the constituent ions to be equal to K_{eq} at equilibrium. The product of the thermodynamic activities of the constituent ions of a dissociated electrolyte is simply the product of the molality of each ion and a mean activity coefficient raised to the appropriate power. The mean activity coefficient is a function of the overall ionic strength of the solution and of the activities of other ions present in the solution. There are a number of theoretical frameworks for calculating activities in complex solutions (reviewed in *Zemaitis et al.*, 1986; *Jacobson*, 1999; *Zhang et al.*, 2000). MELAM uses the model first presented by *Kusik and Meissner* (1978), which is a two parameter model that relates the mean activity coefficient of an electrolyte in a binary solution with water to the ionic strength of the solution using a function they selected by trial and error. Activities in more complex solutions are calculated by first using the Kusik-Meissner model to calculate a series of single-electrolyte activities and then applying a mixing rule. This model is exceedingly accurate given its simplistic form, may be used to model the thermodynamics of complex solutions of many inorganic components, and is now the preferred method for many aerosol thermodynamic modules available in the literature (*Kim et al.*, 1993a; *Zhang et al.*, 2000). A major limitation is its inability to address electrolytes that partially dissociate, such as sulfate. Since sulfate is a dominant component of most aerosol populations, we work to include partially dissociating species as best we can within the Kusik-Meissner framework, paying particular attention to validation of predicted bisulfate concentrations (following *Kim et al.*, 1993a; *Nenes et al.*, 1998, 1999; *San Martini*, 2004).

Particle surface tension is predicted using a two-parameter parameterization that appeals to a Gibbs dividing surface formulation to calculate the surface tension of single-electrolyte aerosols and uses appropriate mixing rule (*Li and Lu*, 2001). Particle density is predicted using a simple empirically-based parameterization for single-component aerosols and an appropriate mixing rule (*Resch*, 1995). MELAM calculates each particle’s equilibrium water content in sub-saturated environments by directly integrating the Gibbs-Duhem equation for single component aerosols and

using an appropriate mixing rule.

All of the methods introduced in this section are discussed in detail in Chapter 4 with the exception of the calculation of equilibrium water content, which is discussed in Section 5.5. The MELAM model has been extensively tested for systems that include sulfate, nitrate, chloride, ammonium, and sodium; the Kusik-Meissner system has been validated for more complex solutions elsewhere. The dissociation reactions, and parameters of the Kusik-Meissner, surface tension, and density models are read from user-defined input files; Appendix A contains the set of parameters used in this thesis.

The proper calculation of aerosol thermodynamics is limited by a significant lack of data. Much of the experimental data we must use to constrain the various components of the thermodynamic model are very old. There is often inadequate data to calculate reliable temperature dependencies. Updated and more complete data sets are essential to refine and extend aerosol thermodynamic models. Further experiments, however, appear unlikely, as there is little incentive for laboratories capable of making such measurements to do so. Because of its flexibility and modularity, the MELAM model will be easy to extend once more measurements are taken, or when theories become available that govern the thermodynamics organic species or other complexities not considered here.

2.6 Gas-Aerosol Transfer: Condensation and Dissolution

The centerpiece of the MELAM model is its condensation scheme, as studies of aerosol activation, cloud formation, and ultimately the indirect effects of aerosols on climate depend on proper calculation of condensation for complex aerosol distributions. The dependence of the water condensation process on the specifics of aerosol composition encourages the representative sample representation introduced in this thesis. In fact, *Svenningsson et al.* (1992) conclude that exacting measurements of neither bulk aerosol hygroscopic properties nor bulk composition are sufficient in studies of aerosol activation. A full understanding comes only through explicit particle by particle characterization of aerosol composition. *Gillani et al.* (1995) stress the importance of the degree of mixing of aerosol populations on cloud properties. They reason that the competition between various aerosol types for water vapor leads to selective activation of those most hygrophilic particles. Full resolution of an aerosol population’s potential to activate is achieved only through considering the full distribution of size and composition or, in the limit, each particle individually. This section presents an outline of the theoretical considerations that under-pin the MELAM model’s condensation scheme; Chapter 5 will discuss the scheme in full detail.

Often, models assume that droplets grow until they reach equilibrium with a fixed background super-saturation or activate (Köhler, 1936; Abdul-Razzak *et al.*, 1998; Abdul-Razzak and Ghan, 2000; Phinney *et al.*, 2003). However, condensation is one of nature’s methods of ameliorating super-saturations, and aerosol particles must compete for a limited supply of available water vapor. For example, Ghan *et al.* (1998) investigate the competition between sea salt and sulfate particles in the marine environment and conclude that the increase in available aerosol surface area during high winds (which lead to relatively high sea salt concentrations) can draw enough of the condensable water to prevent activation of the sulfate particles. Due to such competition, the relative condensation rates onto aerosols of various sizes and compositions are of paramount importance for correct calculation of N_c (Chuang *et al.*, 1997b). MELAM’s condensation scheme is based on a mass-flux model that calculates kinetic condensation rates and constrains the growth by conserving the total water budget during condensation. MELAM also includes a routine that determines equilibrium water content by direct integration of the Gibbs-Duhem equation, as mentioned in Section 2.5. It is more accurate than the condensation routine when the relative humidity is substantially below saturation, as the condensation routine depends on Raoult’s Law which only strictly applies in the limit of infinitely dilute solutions. The equilibrium model is useful for initial equilibration of the model and for studies of aerosol behavior in sub-saturated environments.

We assume that diffusion limits condensation and use the long standing form of Fick’s Law of Diffusion. In this formulation, gradients of condensable vapor density between the ambient environment and particle surface drive condensation. For water condensation, the difference between the ambient relative humidity (\mathcal{RH}) and the ratio of the modified saturation vapor pressure to the equilibrium saturation vapor pressure over a flat surface of pure water (S') drive condensational flux of water vapor onto or away from the droplet. The most difficult aspect of calculating water condensation rates in cases of mixed-composition aerosol is in determining the value of S' , which may be affected by the specifics of solute concentrations, curvature of the particle’s surface, radiative effects, and the hygroscopicity of insoluble cores when present.

MELAM calculates condensation onto all of the particles at a grid-point in a coupled manner using Gear (1971)’s method as implemented in LSODES; this method was discussed briefly in the context of the integration of forward chemical reactions in Section 2.4 and will be discussed in detail in Chapter 5. The model decouples the gas-aerosol transfer of each species from all others over a given time-step; each condenses or dissolves independently and MELAM forces aqueous-phase thermodynamic equilibrium at the end of each time-step.

MELAM is the first model to incorporate the Gorbunov model of condensation onto mixed

insoluble / soluble aerosols (*Gorbunov and Hamilton, 1997; Gorbunov et al., 1998*). This parameterization will be constrained for the first time by observations from laboratory studies and field campaigns. In Chapter 7, we will use the Gorbunov model to consider the activation of ubiquitous mixed soot / sulfate aerosols in marine environments.

2.7 Aerosol Dynamics

Motions of aerosol particles are induced by random thermal (Brownian) accelerations, by gravity, by motions of the local fluid flow (both small and large scale), and under the influence of other particles. These motions both transport aerosols and cause the particles to collide with each other. Modeling frameworks for both transport and collision are well developed for functional and sectional representations of aerosols and are available in textbooks and in the literature (e.g., *Pruppacher and Klett, 1997; Seinfeld and Pandis, 1998; Jacobson, 1999*). In Section 2.2, we introduced the representative sample approach to modeling aerosol that is especially useful for making detailed calculations of the rapid condensation of water that occurs in cloud updrafts; that representation is fundamentally lagrangian and their dynamics must be treated in that context. In this section, we present stochastic representations that we may apply to representative aerosols in a mixed lagrangian / eulerian model. We will review the methods MELAM uses to calculate collision but not transport. MELAM uses a standard advective / diffusive approximation for aerosol transport of sectional representations of aerosols (e.g., *Jacobson, 1999*) and may calculate transport of lagrangian particles by directly integrating equations of motion, if required, using methods available in the literature (*Pinsky and Khain, 1995, 1996*).

In this thesis, we use the MELAM model to consider aerosol activation in lagrangian rising parcels. We will approximate aerosol transport by assuming the aerosols rise uniformly in the ascending parcel, and we will ignore the collision of particles entirely. In Chapter 6, we will address the implications of the latter assumption. Since we will not calculate aerosol dynamics in the modeling studies considered in this thesis, we will not discuss MELAM's representation of those dynamics beyond the brief discussion in this section.

Aerosols and cloud droplets may grow larger by colliding and accreting with each other. Coagulation is the collision and combination of aerosol particles. Coalescence is the collision and combination of cloud droplets. And impaction scavenging is the collision and combination of an aerosol particle with a cloud or rain droplet. These processes act to reduce the particle number and surface area concentration while conserving total aerosol volume and mass.

Plumes of pollution related aerosols evolve over periods of days by coagulation, in-cloud scavenging, and cloud processing; the size distributions and composition of the aerosol populations are notably different far from their sources than when emitted or nucleated (*Raes et al.*, 2000). Regional and global scale models must track these processes explicitly in order to correctly predict transformations of aerosol populations. For the cloud-formation studies considered here, these calculations are not necessary. We will initialize the MELAM updraft model with detailed aerosol observations from the locations we wish to consider; these observations will account for any coagulation, scavenging, and cloud processing that occurred between the time the aerosols were emitted or formed and when they enter a cloud updraft. The time-scale of aerosol activation during cloud formation is on the order of a half an hour or less. Coagulation is not an important over so short a time period. Coalescence, however, is quite important in cloud dynamics. Development of cloud drop distributions is a two-step process: first aerosols activate within an updraft to become CCN and second CCN grow via condensation and coalescence to form a mature cloud drop distribution. In ice-free “warm” clouds, precipitation is triggered by coalescence once some of the droplets grow to radius of 20 μm or so and becomes the dominant growth process once some droplets reach a radius of 30 μm (*Houze*, 1993). A typical warm-cloud raindrop may be the result of 10^5 collisions (*Rogers and Yau*, 1989). More complicated frameworks than the idealized parcel updraft model we use in this thesis are required to account fully for cloud microphysics.

Particle collisions result from Brownian motion, gravitational overtaking of smaller particles by larger ones, turbulent entrainment of particles into the wakes of falling particles, turbulence-induced relative velocities, electromagnetic forces, and various hydrodynamic forces (*Jacobson*, 1997a; *Pinsky and Khain*, 1997; *Seinfeld and Pandis*, 1998). Brownian coagulation is the dominant mechanism for coagulation of smaller particles and gravitational overtaking of falling particles is the dominant process for larger particles (*Jacobson*, 1999). The rates of coagulation, coalescence, and scavenging are defined in terms of a coagulation kernel ($\beta_{1,2}$ for particles 1 and 2, in units of $\text{cm}^3 \text{ particle}^{-1} \text{ s}^{-1}$), which is usually determined by addition of sub-kernels that each describe a single physical process (*Jacobson*, 1999).

Standard practice in cloud and aerosol models that use sectional or functional representations of aerosols is to use the kinetic coagulation equation, an integro-differential equation that relates changes in aerosol number concentration (N_a) or mass concentration (\mathbf{m}_a) to the coagulation kernel; it is a specialized form of the Boltzmann Transport Equation (*Twomey*, 1977a). It is based upon the recognition that the combination of two particles, of distinct sizes 1 and 2, into a single particle

of size $1 + 2$ may be described by a first-order ordinary differential, kinetic equation:

$$\frac{\partial N_{a,1+2}}{\partial t} = \beta_{1,2} N_{a,1} N_{a,2} \quad (2.7)$$

Here, $N_{a,1}$ and $N_{a,2}$ are the concentrations of particles of type 1 and 2 in the air mass, $N_{a,1+2}$ is the concentration of an aerosol with the properties of the two added aerosol, and $\beta_{1,2}$ is the coagulation kernel of the two colliding particles which depends only on their relative and absolute sizes. Of course, this equation expresses the production rate of the combined particles and so is mechanically related to loss rates of the two smaller ones:

$$\frac{\partial N_{a,1+2}}{\partial t} = -\frac{\partial N_{a,1}}{\partial t} = -\frac{\partial N_{a,2}}{\partial t} \quad (2.8)$$

Using equation (2.7), *Muller* (1928) formulated a continuity equation for the population of particles of a particular volume v :

$$\frac{\partial N_{a,v}}{\partial t} = \frac{1}{2} \int_0^v \beta_{v-v_1,v_1} N_{a,v} N_{a,v-v_1} dv_1 - \int_0^\infty \beta_{v,v_1} N_{a,v} N_{a,v_1} dv_1 \quad (2.9)$$

The first term is a convolution that describes the total production of particles with volume v as the integral over the contribution of all size pairs of aerosol whose volumes add to v (here, an aerosol of volume v_1 and its complement), while the second describes the loss of particles of size v via coagulation with particles of any size v_1 (*Twomey*, 1977a; *Jacobson*, 1999). Equation (2.9) disregards compositional differences. For an aerosol population of heterogeneous composition, one must integrate over each distinct aerosol type as distinguished by both size and composition. This approach is well developed and widely used in models that represent aerosols using sectional or functional formulations. Its accuracy depends on the quality of the coagulation kernels for each physical process, which are well developed except that there is no adequate kernel to represent the influence relative motions induced by small-scale turbulence, which is important in some cases (*Pinsky et al.*, 2000). When using sectional representations, MELAM evolve the concentrations of each bin by integrating equation (2.9) using LSODES, which was also used to solve sets of ODEs related to chemical reactions in Section 2.4 and gas-aerosol transfer in Section 2.6.

Coagulation is a fundamentally a discrete event: two specific particles either collide and accrete within a given time interval or they do not. The coagulative evolution of a large population of particles is determined by a particular combination of a great number of these discrete events (*Twomey*, 1977a). The Weak Law of Large Numbers demands that the distribution of particles

in an increasingly large population converge to the expected result of the distribution's evolution (*Bertsekas and Tsitsiklis*, 2002). The standard predictive theories of coagulation, which generally involve integrating an equation similar to the kinetic coagulation equation (2.9), strive to predict the mean result.

In Section 2.2 and Chapter 3, we argue that the advantage of lagrangian aerosol tracking is that it retains all of the information that is critical to the prediction of aerosol activation, while sectional representations smooth composition and size information in a way that makes such calculations less accurate. Our treatment of coagulation, coalescence, and scavenging for such lagrangian representations does not seek to track the explicit movements and collisions of individual particles, but rather will use a statistical model of the likelihood that particles associated with a given eulerian grid-point collide and combine and the model. We provide a method that stochastically calculates coagulation of lagrangian particles with each other, of lagrangian particles with sections of aerosols, and of sections of aerosols with those in other sections. As *Twomey* (1977a) notes this approach will require repeating experiments a number of times to reasonably sample the range of possible outcomes.

Let us consider a discrete case of a single particle of type 1 and a single particle of type 2 in a domain of unit volume. Equation (2.7) then becomes:

$$\frac{\partial N_{a,1+2}}{\partial t} = \beta_{1,2} \quad (2.10)$$

Note that both sides of equation (2.10) have units of particle concentration per second. Noting that $\beta_{1,2}$ less than or equal to one, equation (2.10) would lead to fractional concentrations, with $\beta_{1,2}$ of the larger particle and $(1 - \beta_{1,2})$ of each of the smaller over a time-step of unity in the appropriate units. Given the discrete nature of the phenomenon, these fractional concentrations should be interpreted as expected values; the standard deviation is $\sqrt{\beta_{1,2}(1 - \beta_{1,2})}$. For a domain D multiples larger than the proposed unit volume, the expected concentration remains the same and the standard deviation scales with $1/\sqrt{D}$, which tends towards zero slowly as D rises. By extension, equations (2.9) and (2.10) strictly hold in the limit where the domain and aerosol concentrations are large enough that $1/\sqrt{DN_{a,1}N_{a,2}}$ is zero.

Given this interpretation, we recognize that equation (2.10) represents a binomial model of coagulation where the probability of two particles coagulating is the appropriate integral of $\beta_{1,2}$

over the time period of interest:

$$P(1 \text{ and } 2 \text{ coagulate sometime in } (t, t + \Delta t]) \approx \Delta t \beta_{1,2} \quad (2.11)$$

We use equation (2.11) to calculate the probability that two lagrangian particles at the same grid-point coagulate. Note that we must assume that the probability that any two particles coagulate is independent of the probability that any other combination of two particles coagulates. The number of coagulation events that occur during a time-step between a lagrangian particles and the aerosols in a particular section, or between the aerosols in one section with those in another, is well approximated by a Poisson random variable. Let us define the Poisson parameter (λ):

$$\lambda \equiv \beta_{1,2} N_{a,1} N_{a,2} \quad (2.12)$$

The probability mass function of the number of collisions (k) in a given time step is then (*Bertsekas and Tsitsiklis*, 2002):

$$P(k \text{ collisions during time - step } \Delta t) = e^{-\lambda} \Delta t \left(\frac{(\lambda \Delta t)^k}{k!} \right) \quad (2.13)$$

This statistical model provides a specific number of coagulative events that occur between two types of aerosols. It is a good approximation when $N_{a,1} N_{a,2}$ is large and Δt is small.

MELAM allows the transport of aerosols between grid-points and coagulation between aerosols at a single grid-point. For sectional representations, coagulation may be treated using this stochastic model or a standard expected-value framework according to equation (2.9). The stochastic representation is advantageous for two reasons: first, because it allows MELAM to use the representative sample distribution; and second, because it allows more careful consideration of particular traits of the combination of two particles that may contain insoluble cores, surfactants, or other not strictly additive structures than does the standard formulation. We will not use coagulation in the studies considered in this thesis, but it will be important to future studies performed using the model.

2.8 Boundary Conditions for Microphysical Studies of Aerosol Activation: Updraft Models

As mentioned in the introduction to this chapter, studies that use microphysical models must provide boundary conditions to simulate the aerosols' interactions with the local environment. Providing boundary conditions generally involves embedding the microphysics module in some other type of model. For studies of aerosol activation and cloud development, the microphysics model must be provided temperature, pressure, relative humidity, and concentrations of gas phase species at each moment. Each of these properties is influenced by the updraft velocity, entrainment, and turbulent mixing between cloud updrafts and downdrafts.

There are two general categories of models that are used to provide appropriate boundary conditions for studies of aerosol activation: lagrangian, single grid-point models that follow a parcel of air as it rises in an updraft; and eulerian models in which there are many grid-points with fixed locations, and in which aerosol particles and cloud drops rising through a cloud updraft move from one grid-point to another during ascent. Lagrangian models are appealing because the calculation of fluid dynamics is very simple and microphysics must be calculated at only a single grid-point, so the model is computationally inexpensive and most of the computing resources may be allocated to very explicit microphysical calculations. Also, there is no artificial numerical diffusion in lagrangian models, whereas the need to pass aerosols from one grid-point to another assures that numerical diffusion occurs in eulerian models. The main drawback of the lagrangian framework is that it allows only a subset of cloud microphysical processes to be calculated. For example, precipitation may form via coalescence and fall from the parcel but it will never fall into the lagrangian parcel from above; there is simply no way to calculate the cloud dynamics outside of the parcel being tracked. Also, entrainment and updraft velocities must be imposed for parcel models using outside sources of information whereas eulerian models may calculate the physical processes that control these dynamics directly. Eulerian meso-scale cloud models (which have been formulated in one, two, and three dimensions) have nearly the opposite set of issues: these models must calculate aerosol and cloud microphysics at many grid points and so, due to computational constraints, may only use greatly simplified microphysical schemes; on the other hand, eulerian models explicitly calculate all of the cloud dynamics and microphysics interactively and, in aerosol activation studies, are able to assess the implications of input aerosol distributions on large scale cloud dynamics.

The ultimate goal of this type of research is to understand the characteristics of sub-cloud aerosol populations that are most important to determining the properties of clouds well enough

to be able to build a parameterization that is useful in large scale models. An understanding of the controlling microphysics, attained using lagrangian parcel models and observations, must eventually be used to design appropriate meso-scale modeling studies; and these meso-scale modeling efforts must be used, in conjunction with data from field campaigns, to provide a link between aerosol populations, convection schemes, and parameterizations of cloud behavior in global models.

In this thesis, we adopt the parcel updraft model approach to providing boundary conditions for MELAM. A long series of studies of the detailed physics of aerosol activation rely on constant-speed adiabatic parcel models. We will adopt such a model for our study of the activation of mixed soot / sulfate aerosols in Chapter 7. However, an adiabatic parcel that rises at a constant speed is a rather imperfect analogy to an actual cloud as it neglects variations in updraft speed, entrainment, and other forms of mixing at the very least. The cloud dynamics community long ago moved away from constant-speed adiabatic updraft models and has developed a series of more sophisticated, more accurate models. In Chapter 6, we will formulate an episodically entraining variable-speed updraft model. We will calculate the updraft speed from a vertical profile of convective available potential energy as provided by a sophisticated and accurate convective scheme. This is a novel approach and relies on a number of assumptions to find the updraft speed; it is only a first step. Advances in understanding of cloud dynamics will allow more refined approaches in the future. We will use this new parcel model as a foil for the constant-speed adiabatic updraft model and as an example of how parcel updraft models might eventually be tied to convective routines in global scale models.

2.9 Summary

In this chapter, we introduced the MELAM model briefly and discussed its various components. The model is specifically designed to simulate the activation of complex aerosol populations and to address open questions to do with aerosols' influence on cloud formation and the indirect effects of aerosols on climate.

Over the next few chapters, we will discuss the implementation of several of MELAM's microphysical schemes in great detail. In Chapter 3, we will discuss how aerosols are represented. In Chapter 4, we will discuss MELAM's aerosol chemical thermodynamics module. In Chapter 5, we will present the formulation of the condensation and dissolution routines. In Chapter 6, we will present a constant-speed adiabatic and a variable-speed entraining updraft parcel model that the MELAM updraft model uses to provide boundary conditions to the microphysical schemes. Fi-

nally, in Chapter 7 we will discuss the application of the MELAM updraft model to the activation of mixed soot / sulfate aerosols in marine environments.

Chapter 3

Representation of Aerosols and Droplets

3.1 Introduction

Typical ambient aerosol populations show a great deal of variety in size, composition, and mixing state. Particles range several orders of magnitude in size (“a size range equivalent to that from baseballs to planets,” notes *Toon*, 2000). Each particle may combine many soluble and insoluble constituents in an inherently disorderly manner, and each particle is distinct in size and composition in potentially important ways. The total population may reach concentrations of up to several thousand per cubic centimeter. Modeling such populations is an inherently many-dimensional problem and doing so at anything beyond the very smallest scales requires making a number of simplifying approximations. Formulating appropriate assumptions requires we pay close attention to the model’s intended use.

The composition of each aerosol particle may be characterized by properties of one or several insoluble cores (which may include dust or soot), water content, inorganic solids, inorganics in solution, soluble organic species, and surfactants. Beyond composition, the state of an aerosol is described by its size, shape, density, temperature, chemical state, surface tension, optical properties, thermodynamic activities, and water activity (all of these will be discussed later in the thesis). The key to developing an aerosol model, which necessarily must abide by constraints of computational expense and computer memory, is to prioritize the aerosol traits that are critical to the scientific question under consideration. Of course, both our ability to observe atmospheric aerosol and our ability to theoretically treat the necessary physics, thermodynamics, and chemistry is extremely

limited at this time and so limits the scientific questions that may be asked.

Many of the available aerosol modeling techniques have their origins in urban air-shed models of regional air pollution (e.g., *Gelbard et al.*, 1980; *Gelbard and Seinfeld*, 1980; *Russell et al.*, 1985; *Jacobson et al.*, 1994), for which aerosol are most important as sinks of gas phase species and scatterers of light. Many simplifications may be made in this case that would be inappropriate in models of aerosol activation, which is highly sensitive to aerosol size and composition. Most global scale models track only total aerosol mass and presume a fixed size distribution, a much more approximate but computationally simple tactic (*Binkowski and Shankar*, 1995; *Zhang et al.*, 2002), although some newer models use air-quality-model-like formulations in an effort to account for aerosol processing (e.g., *Tegen et al.*, 1997; *Wright et al.*, 2001; *Jacobson*, 2001b). Our goal, however, is to better understand the activation of aerosol as clouds form and the implications for the larger climate. And there is reason to believe that aerosol composition is as important to such indirect radiative forcing (IRF) calculations as is the aerosol size distribution (*Svenningsson et al.*, 1992; *Seinfeld and Flagan*, 1999; *Steele and Prinn*, 2002; *Nenes et al.*, 2002)

We attempt to provide both relative completeness and maximum flexibility in the Mixed Eulerian-Lagrangian Aerosol Model's (MELAM's) representation of aerosol. It allows the use of a bulk representation, one or more sectional distributions, and samples of representative individual Lagrangian particles (all of which will be defined later in this chapter). In this chapter, we discuss the various aerosol representations found in the literature and their limitations, and discuss the representations available in the MELAM model. This chapter is divided into three primary sections: Section 3.2 discusses parametric fits to observed aerosol size distributions; Section 3.3 discusses model representations of aerosol size distribution; and Section 3.4 discusses model representations of aerosol composition.

3.2 Functional Representations of Observed Aerosol Size Distributions

In the field, particle sizes are typically measured only coarsely using a stack of meshes with known aperture to separate particles into distinct size ranges. The mass or number loadings in each size range are then typically fit to a functional form which describes a continuous size distribution ranging over many orders of magnitude in size. (Recently introduced advanced systems use calibrated time-of-flight measurements or laser systems to size individual particles, which promises to refine our understanding of aerosol size distributions considerably; *Prather et al.*, 1994; *Noble and*

Prather, 1996, 1998; *Jayne et al.*, 2000). Many forms have been suggested, including the power law distribution, gamma distribution, so-called Woodcock distribution, Marshall-Palmer distribution, and log-normal distribution (*Marshall and Palmer*, 1948; *Squires*, 1958c; *Twomey*, 1959, 1977a; *Seigneur et al.*, 1986; *Jaenicke*, 1993). Each defines a particle distribution function ($\mathcal{P}(r)$) which describes the fraction of particles that exist at a particular radius (r) and integrates over size to unity; it is directly parallel to the standard probability density function (cf., *Bertsekas and Tsi-siklis*, 2002). The n^{th} moment of the distribution is the integral of the product of $\mathcal{P}(r)$, the total aerosol number concentration (N_a), and particle radius to the power of n :

$$\mu_n = N_a \int_0^\infty r^n \mathcal{P}(r) dr \quad (3.1)$$

The 0th moment is particle number concentration, the 2nd is total particle surface area, and the 3rd is total aerosol volume. We may similarly define an aerosol moment within a particular size range (or “bin”) that encompasses all aerosol with radius between some lower and upper limit, r_1 and r_2 :

$$\mu_n(r_1, r_2) = N_a \int_{r_1}^{r_2} r^n \mathcal{P}(r) dr \quad (3.2)$$

Typically microphysical models track the aerosol size distribution either through the coefficients of a functional form of $\mathcal{P}(r)$ or by sub-dividing the possible radii into a number of bins and tracing $\mu_n(r_1, r_2)$ for each, for one or two moments of equation (3.2), although several other approaches have been adopted. The most critical moment may differ according to the scientific question under consideration (*Wu et al.*, 1996; *Zhang et al.*, 1999).

A distribution of the sum of multiple log-normal modes has been found to represent aggregated observed distributions particularly well, across a range of environments. The log-normal distribution is positive definite and Gaussian when plotted on a logarithmic x -axis. Typically there are three modes of increasing size: the nucleation, Aitken, and accumulation modes. Each mode is defined in terms of three parameters: the mean radius (\bar{r}_a), the geometric standard deviation (σ_a), and the total number concentration (N_a):

$$\frac{dn(r)}{d\ln r} \equiv N_a \frac{d\mathcal{P}(r)}{d\ln r} = \frac{N_a}{\sqrt{2\pi} \ln \sigma_a} \exp \left(- \frac{(\ln r - \ln \bar{r}_a)^2}{2 \ln^2 \sigma_a} \right) \quad (3.3)$$

Here, we have defined $n(r)$ to be the total number concentration of the mode multiplied by the

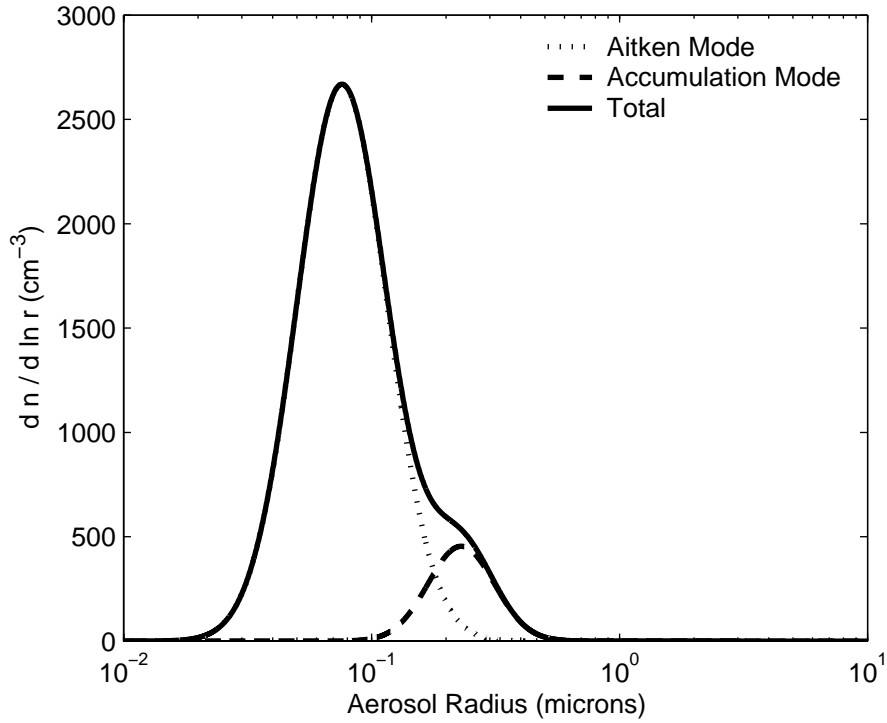


Figure 3-1: Example observed bimodal log-normal aerosol number distribution from ACE-2

particle distribution function. Aerosol number distributions are typically plotted in these units, which is why we have defined equation 3.3 in this way. Figure 3-1 shows an example bimodal log-normal distribution, fitted to the average distribution of aerosol observed during the Second Aerosol Characterization Experiment (ACE-2) in air originating from coastal Portugal (*Quinn et al.*, 2000). This particular example is best fit by two log-normal modes rather than three. The parameters for this distribution will be presented in Table 7.2, and much more about this campaign will be discussed in Chapter 7.

Many models find it useful to presume that aerosol size distributions seldom stray from this idealized form and that composition is a smooth function of radius (e.g., *Ghan et al.*, 1993, 1995; *Abdul-Razzak et al.*, 1998; *Abdul-Razzak and Ghan*, 2000). The accuracy of such models obviously depends on how closely actual distributions track the presumed functional form (*Abdul-Razzak and Ghan*, 2002). The aerosol-cloud transition tends to bifurcate the aerosol distribution and is difficult to track when assuming that the aerosol are log-normally distributed; other types of representation are much more appropriate when considering such dynamics.

3.3 Representing Size Distributions in Models

There are five primary approaches to representing the size distributions of aerosol particles in models: bulk, moment-based, modal, continuous, and sectional (well reviewed in *Zhang et al.*, 1999). In this work, we will add another to the list – representative Lagrangian or representative sample – that is appropriate for aerosol activation studies. In this section, we will review each approach, highlight its limitations, and present the approaches used in the MELAM model.

3.3.1 Bulk

The simplest model of a size distribution is no size-resolution at all, which is known as the bulk formulation. The bulk formulation tracks total aerosol mass, component-by-component, and that is all. For some studies aerosol size resolution is not critical, and ignoring it frees computational resources for studying complex chemical, thermodynamic, or dynamical processes. Such models are often used in sub-saturated environments when aerosols may be considered to be in equilibrium (e.g., *Chaumerliac et al.*, 2000; *San Martini*, 2004) and in cloud models where the only microphysical quantity tracked is liquid water content (e.g., *Kessler*, 1969; *Emanuel*, 1991). Some calculations are strongly dependent on particle size, such as the effect of surfactant properties and kinetics on condensation rates or optical properties, and some simply may not be calculated using the bulk formulation.

MELAM may be run in bulk mode, in which thermodynamics, chemistry, gas-aerosol partitioning, and water content are all predicted using no correction for aerosol size. Time-dependent condensation is not allowed when using this formulation.

3.3.2 Method of Moments

Some large-scale models track one or more moments of aerosol explicitly and nothing else, usually focusing solely on sulfate aerosol and ignoring other types. The advantage of such an approach is that there is only one variable to be tracked per aerosol moment. Aerosol optical, hygroscopic, and other properties are then parameterized in terms of these moments, usually by assuming a scalable size distribution. The traditional approach of global climate models is to track aerosol sulfate mass (the third aerosol moment) and no other aerosol properties (*Zhang et al.*, 2002), although this changing. One recent series of studies explicitly tracks the first six moments of sulfate aerosol (*Wright et al.*, 2000, 2001) and proved successful at calculating large-scale distributions of sulfate aerosol, although its predictions of wet deposition and some other distribution-dependent properties

were less successful (*Yu et al.*, 2003). This one effort at a many-moment aerosol representation is intriguing, but bears further refinement to rectify the limitations highlighted in *Yu et al.* (2003) before it is incorporated in global models.

Although moment-based approaches may ultimately prove adequate for answering some global scale questions, they lose many critical pieces of information that are essential to calculating the details of aerosol-cloud processes. These include aerosol composition, mixing state, and variations in size distribution, amongst others. MELAM does not use the method of moments.

3.3.3 Modal Representations

Modal representations evolve size distributions by tracking the coefficients of functional approximations to one or several modes (*Marshall and Palmer*, 1948; *Twomey*, 1977a; *Whitby*, 1981; *Flossmann et al.*, 1985; *Seigneur et al.*, 1986; *Jaenicke*, 1993). Necessarily, such models must prescribe the number of modes, a functional form (e.g., log-normal or gamma-functional), a relationship between composition and size, and relationships between dynamic processes and the parameters of the distributions. Some log-normal representations (the current preferred functional form for modal models) allow all three parameters of the distribution of equation (3.3) (i.e., \bar{r}_a , σ_a , and N_a) to vary according to the equations governing aerosol evolution, while others fix σ_a to be constant.

The primary advantage of this type of model is that it is capable of representing a broad size spectrum using only a relatively small parameter set and few governing equations. The primary disadvantage of these models, for our purposes, is that they have a very difficult time modeling the transition of the size distribution during activation and cloud formation. Activated size distributions are quite narrow and are not log-normal so modal representations have difficulty replicating the size distribution of the activated particles, although they are able to replicate some of the traits well (*Zhang et al.*, 2002). Models that discretize the modal distributions, according to equation (3.2), have had much more success replicating the aerosol-droplet transition. These are known as sectional models.

3.3.4 Sectional Representations

The most common way to resolve the aerosol size distribution in current microphysical models is with the sectional representation. The basic approach is to sub-divide the aerosol size domain into a series of geometrically distributed bins each containing some fraction of an aerosol moment. That is, one sets a series of radius cut-offs and sets the amount of a particular moment that lies between two boundaries using equation (3.2). We will define each “bin” using an upper and lower edge,

corresponding to $r1$ and $r2$ from equation (3.2):

$$(r1, r2) = \{(0, e_1), (e_1, e_2), (e_2, e_3), \dots, (e_{n-1}, e_n), (e_n, \infty)\} \quad (3.4)$$

So n edges define $(n + 1)$ bins. It is more common in the literature to define $(n - 1)$ bins with the same edges by neglecting aerosol that fall into the intervals $(0, e_1)$ and (e_n, ∞) . Let us call the formulation described by equation (3.4) the “full distribution” and that without the two end bins the “book-ended distribution.” We prefer the full distribution.

We define the bins geometrically, as is usually done, such that $\mathcal{R} \equiv e_i/e_{i-1}$ is constant (where \mathcal{R} is called the radius ratio):

$$\mathcal{R} = \left(\frac{e_n}{e_1}\right)^{1/(N_B-1)} \quad (3.5)$$

Here, N_B is the number of bins defined by the edges including those smaller than e_1 and larger than e_n (*Jacobson, 1999*). Three dimensional air quality models frequently use a book-ended distribution with eight bins between $0.02 \mu\text{m}$ and $10 \mu\text{m}$, although some studies use as few as two or three bins. The common eight-bin formulation is sufficient to adequately calculate both water up-take in sub-saturated environments and simple optical properties (*Zhang et al., 1999*).

In order to construct a sectional model (and, indeed, any model that uses one of the size representations already discussed except the bulk formulation), one must select which moments to track. For each moment considered, the model must track its magnitude for each bin and evolve each of those values using one or more governing differential equations. The standard sectional formulation fixes the location of the edges and writes aerosol dynamics equations by either presuming them to act on particles with the mean properties of particles in each bin, or by presuming them to act on specific size and other quantities to be distributed within the bin in a particular manner (*Gelbard et al., 1980; Seigneur, 1982; Jacobson, 1999*). This “fixed bin” formulation proves problematic in several ways and alternatives now exist which allow either the location of the bin edges or of the bin centers to evolve over time (*Jacobson, 1999; Zhang et al., 2002*); we will discuss these later in this section. The number of values to store and equations to solve can grow very large if multiple moments are tracked and many bins are used; the sectional distribution can therefore require a great deal of computer resources for highly accurate calculations. Most sectional models only explicitly track one moment, often particle mass concentration (*Lurmann et al., 1997; Meng*

et al., 1998); and some more recent models conserve both number and mass (*Tzivion et al.*, 1987; *Jacobson*, 1997a; *Russell and Seinfeld*, 1998; *Steele*, 2000). For detailed calculations of aerosol activation, both particle number and the mass concentration of each component are critical and at least those moments ought be tracked (note that mass concentration is related to the third moment through equation 3.1 and particle density).

At the beginning of the model run, the value of each moment within each bin must be initialized, usually from a parametric form such as a log-normal distribution. (Within the next few years very finely resolved measurements of ambient aerosol may allow more direct initialization; in a few cases it is already.) Towards that end, we introduce the normalized cumulative distribution function of the log-normal (Φ_{ln}) (see *Jacobson*, 1999; *Bertsekas and Tsitsiklis*, 2002), which states the fraction of a particular moment contained in aerosols of a particular radius (r_a) or smaller:

$$\Phi_{ln}(r_a) = \int_0^{r_a} \mathcal{P}(r) \, dr \quad (3.6)$$

$$= 0.5 + 0.5 \operatorname{erf} \left(\frac{\ln(r_a) - \ln(\bar{r}_a)}{\sqrt{2} \ln \sigma_a} \right) \quad (3.7)$$

The content in a given bin of a distribution's zeroth moment is then defined using equations (3.2) and (3.7):

$$\mu_0(e_{i-1}, e_i) = N_a [\Phi_{ln}(e_i) - \Phi_{ln}(e_{i-1})] \quad (3.8)$$

The solution to the integral in equation (3.1) is not an exact function of Φ_{ln} for higher order moments, and so some approximation must be made (see *Jacobson*, 1999).

Figure 3-2(a) shows the same bimodal, log-normal distribution from ACE-2 shown in Figure 3-1 (on different axes). Figure 3-2(b) shows the sectional representation of the same distribution, using twenty bins where $e_1 = 0.01 \, \mu\text{m}$ and $e_{19} = 10 \, \mu\text{m}$. The point-side-up triangles show the number concentrations calculated using equation (3.8), while the point-side-down triangles use the representative sample approach that we will discuss in Section 3.3.5.

Particles change size with time – via condensation of water, coagulative growth, and other processes – and, as a result, some portion of each bin's contents moves from one bin to another during each time step. In the original sectional formulations (see *Gelbard et al.*, 1980; *Seigneur*, 1982), significant numerical diffusion occurs during these events; the represented particle sizes are quantized while particle growth is continuous, and so particles that change size must be apportioned between adjacent bins. During this reapportionment, numerical diffusion artificially broadens the size dis-

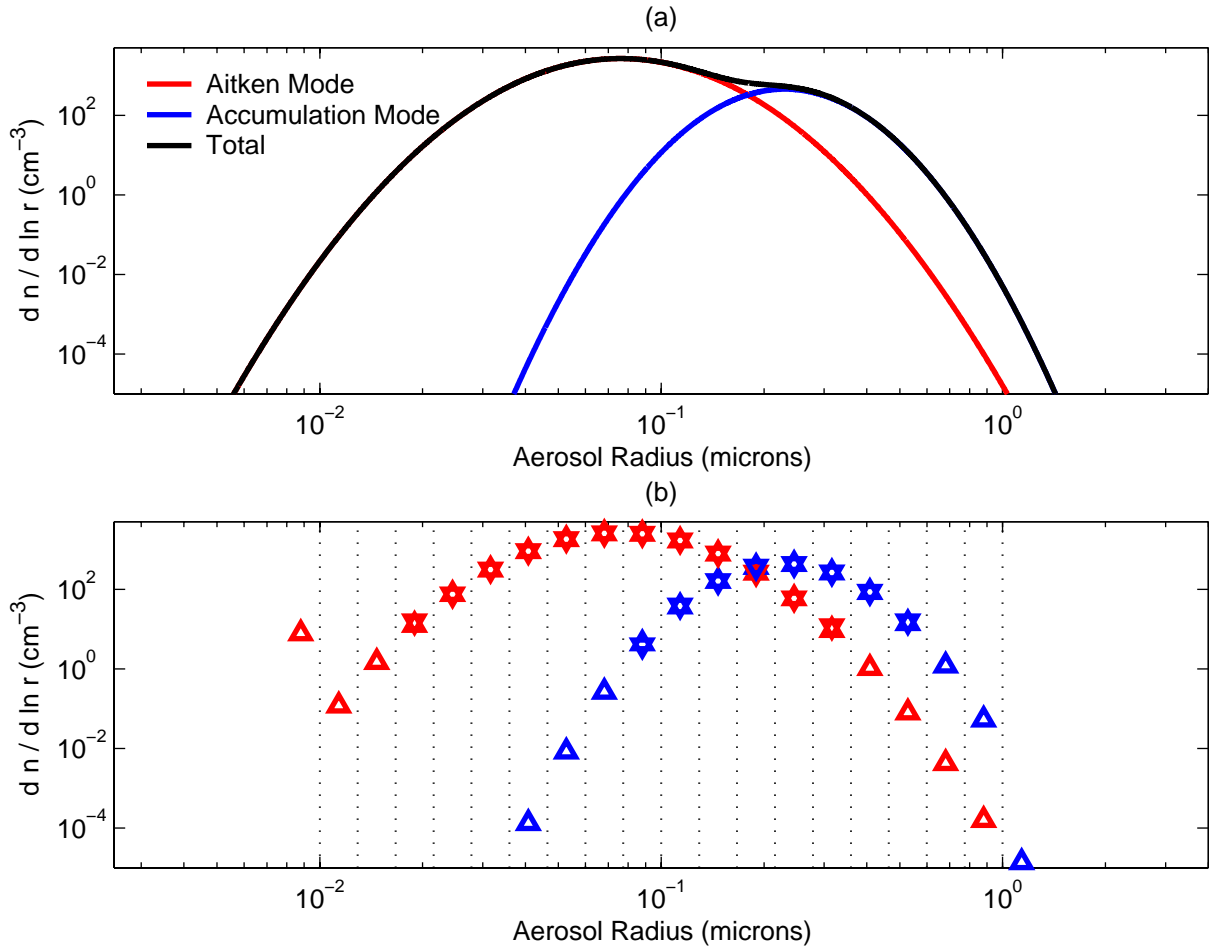


Figure 3-2: (a) the number concentration of the bimodal, log-normal distribution from ACE-2 shown in Figure 3-1; (b) sectional representation of the bimodal representation shown in (a), dotted lines show the bin edges, upward triangles show the bin-by-bin concentration populated using equation (3.8), the downward triangles show that found using the representative sample technique discussed in Section 3.3.5

tribution and those moments not explicitly tracked may not be conserved (*Wexler and Seinfeld, 1990; Dhaniyala and Wexler, 1996; Russell and Seinfeld, 1998*). Both problems are particularly severe when the particles grow or shrink significantly, such as during cloud activation, significantly limiting the effectiveness of such models for that application. These issues also arise during model initialization, as aerosol distributions are often reported for dry aerosol and must be equilibrated at the desired humidity before the model run begins, which for high humidity environments of interest here involves considerable growth.

As mentioned above, a series of alternate formulations now exist that allow bin edges or bin centers to evolve with time, which ameliorates the numerical diffusion and non-conservation issues but introduces other problems. We will call the original sectional formulation introduced above the “all fixed” sectional representation, as the bin edges and bin centers are not allowed to evolve with

time. We will discuss each of the other alternatives in turn.

Moving Center, Fixed Edges

In the “moving center, fixed edges” approach, the bin edges are defined at the beginning and never change but the contents of each bin is represented by a single aerosol which grows or shrinks as it gains or loses mass via condensation, dissolution, coagulation, and other processes (*Jacobson, 1997a,b*). When the moving center of a particular bin crosses the size boundary into an adjacent bin, all of the aerosol from that bin are moved into the adjacent bin. Aerosol are never apportioned between adjacent bins and so numerical diffusion is largely avoided during condensational growth. However, when advection occurs between grid points, there is exchange between the contents of parallel bins, which leads to some amount of diffusion. This formulation does nothing to resolve the issues of numerical diffusion during coagulation.

By allowing the moving center to completely leave a particular bin, the algorithm empties some bins temporarily, which are filled again only when advection, coagulation, nucleation, or growth of aerosol from an adjacent bin introduce more particles. As a result, distributions evolved using this algorithm acquire a jagged structure in which the distribution may not transition smoothly over the series of size bins (cf. *Zhang et al., 2002*). If the distribution is allowed a sufficiently large number of bins, the overall predicted distribution is quite accurate as the algorithm avoids problems of numerical diffusion except during advection.

Moving Edges

The “moving edges” algorithm (more often called “full moving” in the literature) allows the edges between each bin to evolve during condensational growth as a particle of the equivalent size would (*Warren and Seinfeld, 1985; Zhang et al., 2002; Gaydos et al., 2003*). This wholly prevents the numerical diffusion that results from the condensational growth of particles in fixed-edge approaches but does nothing to prevent diffusion during coagulation. The evolution of the edges is not well defined if the composition differs between adjacent bins, as some measure will have to be introduced to govern their growth.

The primary difficulty of the moving edge approach, however, presents itself during advection between grid-points. The evolution of bin edges breaks any symmetry between the sectional representation at adjacent grid points, meaning that some form of interpolation will have to occur when particles move from one grid point to another during advection. This is resolved either by interpolating between the bins during advection or by introducing a so-called hybrid grid structure.

When using a hybrid structure, the bin edges evolve on their own over a series of short time steps used to calculate microphysical evolution but are re-mapped onto the original grid ahead of the much-less-frequent advection events (*Zhang et al.*, 1999).

Combined Fixed-and-Moving Edges

The sectional approach that has been most successfully applied to aerosol activation and cloud processing is the combined fixed-and-moving edge approach (*Jacobson and Turco*, 1995; *Russell and Seinfeld*, 1998). These models track non-water aerosol components separately from liquid water, representing all trace species in a fixed edge sectional distribution and the water components in a moving section. There are two primary advantages to this approach: first, particles that activate to become cloud droplets and then completely dry retain their composition (unlike standard sectional approaches, for which diffusion during bin-shifting would artificially alter composition); and second, advection between grid cells is simpler since one can match the fixed non-water bins and allow numerical errors to be introduced only in the water content, which for many purposes may be considered to be less critical.

Studies using sectional approaches to representing the aerosol size distribution are widespread in the literature, both in large and small scale modeling efforts. As with most models, one must trade between computational expense and accuracy, and the various formulations discussed briefly above afford many options along that continuum. Several papers and books provide more thorough comparisons of the various sectional and modal formulations (*Seigneur et al.*, 1986; *Jacobson*, 1997a, 1999; *Zhang et al.*, 1999, 2002).

The MELAM model introduced in Chapter 2 allows versions of both the moving edges and moving center sectional approaches, in addition to a bulk formulation. The preferred representation for aerosol activation, however, is a representative sample approach we will introduce presently in the next section.

3.3.5 Continuous and Lagrangian Representations

The now rarely used continuous representation of aerosol, tracks the full range of aerosol sizes (*Suck and Brock*, 1979; *Tsang and Brock*, 1983). The method involves solving the aerosol dynamic equations with finite element methods, which is computationally expensive but very accurate (*Varoglu and Finn*, 1980; *Tsang and Brock*, 1986). Continuous models were once used as a point of comparison when validating less well resolved models, but more studies now use sectional representations

with many bins for that purpose (see Section 3.3.4 for a discussion of sectional distributions). Continuous methods do not pay attention to the resolving of aerosol composition, however, and in that way at least are outdated. A truly resolved size-and-composition aerosol model would approach a particle-by-particle treatment, which we would like to do, but choose to approach in another manner.

We propose tracking a representative sample of individual aerosol particles instead of more rigidly defined modal, sectional, continuous, or other distributions. This has the advantages of allowing us to weight the model resolution towards the most populous regions of the range of aerosol size and composition, to avoid most numerical diffusion during aerosol growth, and to resolve aerosol size and composition equally well, thus representing the full range of mixing states. It is especially useful for investigations into cloud activation, for which it: retains all of the advantages of the most sophisticated moving-edges sectional representations; allows much better compositional resolution; and also weights its calculations towards the most populous aerosol types. It also allows investigations of stochastic behavior of aerosol particles, if a sufficiently large aerosol population is tracked (although this will not be done in this thesis). The representation will also be useful in populating sectional distributions, which will allow us to avoid a large source of numerical diffusion.

There are two ways to create a representative distribution from a log-normal or other functional specification of size distribution: structured and unstructured. Both involve inverting the cumulative distribution function given in equation (3.6), which will convert a percentile value between zero and unity into a particle radius. The structured distribution inverts a series of evenly spaced percentile points at $(i - 0.5)/N_a$ for $i \in \{1 \dots N_a\}$ (where N_a is the number of aerosol in the population). Consider how we would do this for the log-normal distribution shown in Figure 3-3(a), for which the three parameters are: $N_a = 40$, $\bar{r}_a = 0.2$, and $\sigma_a = 1.5$. The upper portion of Figure 3-3(b) shows the cumulative distribution function of the log-normal shown in 3-3(a) in a unit volume. The horizontal lines run from each of the specified inversion points along the y -axis to the Φ_{ln} curve and then turn vertically downward; there is a circle (representing a single particle) where each line runs into the size axis. The evenly spaced inversion points lead to a Lagrangian distribution of particles that are crowded near the peak of the log-normal distribution in a deterministic and structured fashion. An equivalent unstructured distribution would involve randomly selecting 40 numbers between zero and unity and inverting each of those to find an aerosol radius; this is a stochastic sampling.

There are several advantages to this approach. First, since the model tracks each aerosol explicitly, each is allowed to activate when it ought to activate rather than being aided or hindered

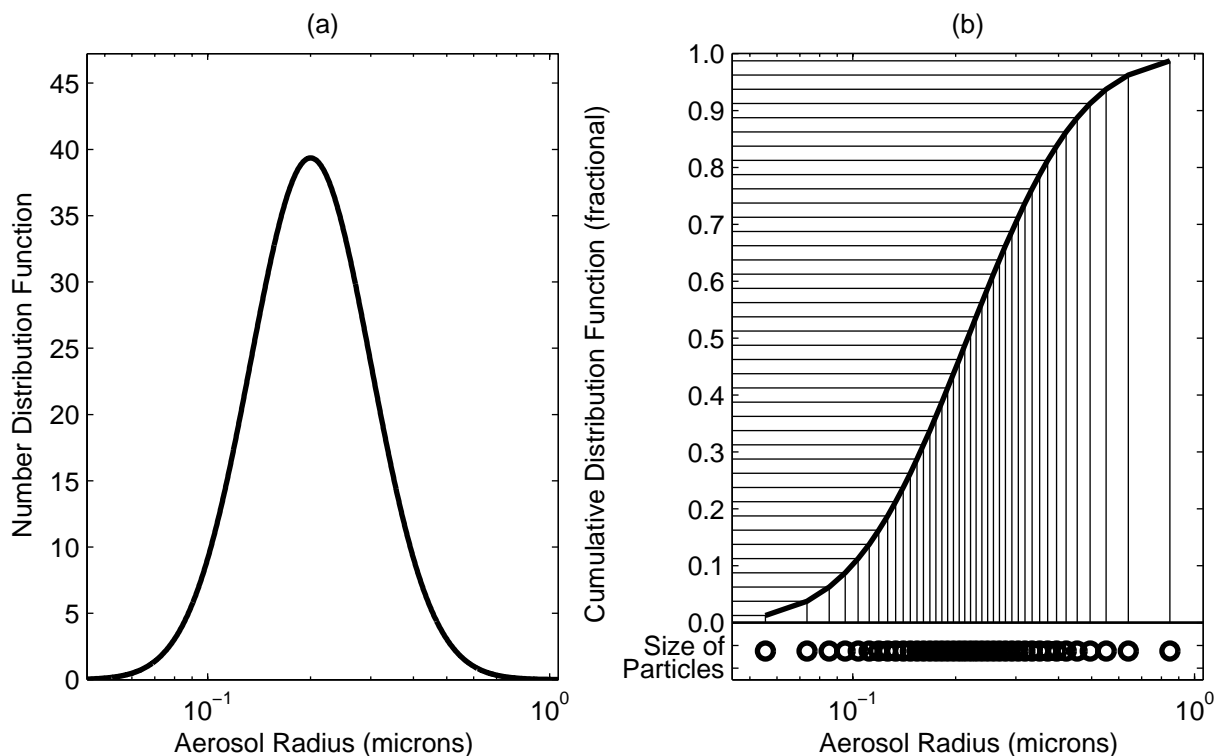


Figure 3-3: (a) Example log-normal aerosol distribution; (b) the cumulative distribution function (Φ_{ln}) of the log-normal distribution shown in (a) (heavy line), mapping from percentiles of distribution to equivalent radii (light lines), and representative sampling of aerosol (circles)

by grouping with other particles in the same section or mode. Second, there is no numerical diffusion during growth and evaporation whatsoever, aiding efforts to model aerosol growth in super-saturated environments and cloud processing. Third, it can track variations in composition as finely as variations in size; this allows serious consideration of the effects of mixed aerosol populations, a fact that will be discussed further in Section 3.4.

The primary limitations of this representation are that coagulation and advection are made more difficult. The usual representations of these processes involve, respectively, calculating the mean number of each aerosol type advected into and out of the grid box, and the mean number of each type of aerosol that coagulate. This representation does not average aerosol quantities, and so is ill-suited to represent those mixing events. There are three solutions to this. The first is to use the model to consider only cases in which neither coagulation nor advection from the grid point are important (advection into the sample are not an issue, as those may simply be added by a sample representation of particles); this will be the case for the updraft parcel model we will consider in Chapter 6. The second is to treat the sample stochastically, such that we relax the mean-number calculations and instead consider the likelihood that each particle collides or

moves from one grid point to the next. This would allow investigations into stochastic behavior of aerosol in situations in which outlying quantities are important, although such studies will have to consider sufficiently representative populations and make numerous runs to be of any use (*Twomey*, 1977a). Methods to make such calculations were introduced in Section 2.7, although we will not consider any such study in this thesis. Studies in the literature have shown that aerosols of different types compete for condensing water vapor in super-saturated environments (*Ghan et al.*, 1998; *O'Dowd et al.*, 1999, also discussed briefly in Section 1.2.3), and surely aerosols of some mixing states are competitively favored over others during competition; we plan to address this competition in a future study using the stochastic version of the model. The third is to use an approach similar to the hybrid sectional approach mentioned briefly in Section 3.3.4: namely allow the aerosol to evolve in a representative-sample framework when convenient and then place them into a sectional representation for the calculations better performed in that framework. In this thesis, we will occasionally use the representative sample distribution to initialize a distribution by drawing a sample of particles in a structured manner, equilibrating them to local conditions, and then placing them into a sectional distribution. Measurements of particle distributions are often cited for dry aerosol, and so the particles must be grown to be in equilibrium with the model's environment. A great deal of numerical diffusion would occur during this calculation for normal sectional models and this system avoids such problems entirely. Consider again Figure 3-2(b), which shows a bi-modal distribution of aerosol represented in a sectional framework. The upward-facing triangles show the number concentration calculated using equation (3.8), and the downward facing triangles show the number concentrations calculated using the routine just described for only a 1 cm^3 volume. Note that the concentrations calculated for bins near the center of each distribution line up exactly while those away from the center of each mode are not sampled at all by the representative distribution. Using a larger initial volume would ameliorate this problem, as would considering a population with higher number concentration, but the same type of truncation error would nonetheless present itself.

3.3.6 Mixed Sectional and Lagrangian Representations

The representative sample distribution works best when each aerosol type is of comparable number concentration. When some types of aerosol are much more populous than others, one may have to choose a large volume in order to adequately sample the less populous distribution and thereby include an unreasonable number of the more populous particles. In order to avoid this issue, the MELAM model provides a mixed sectional / representative sampling framework. In this mixed

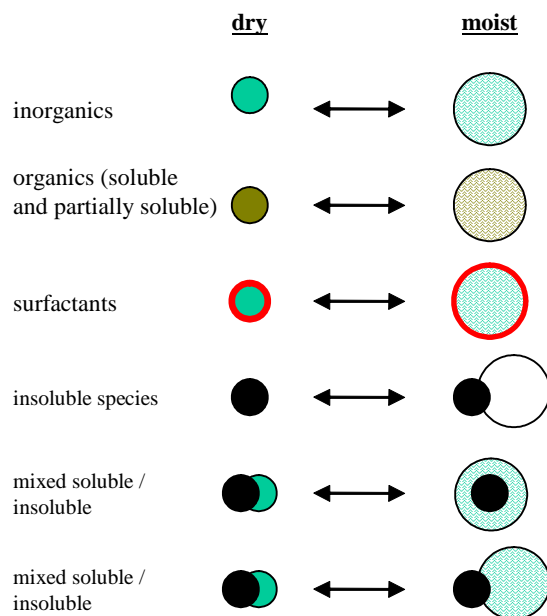


Figure 3-4: Schematic of several aerosol types

framework, all particles below a certain size, or of a particular primary type, may be stored in sectional distributions while the balance of the population are considered in a representative sample framework. The size cutoff provided is useful, for example, when there are a great number of very fine, essentially pure aerosol produced by nucleation events. The separate sectional distribution is useful, for example, when considering polluted marine environments that including both high concentrations of sulfate aerosols (which may reach $1000 \text{ particles cm}^{-3}$) and very low concentrations of sea salt (the most course modes of which may have concentrations of 10^{-5} cm^{-3}) (*O'Dowd et al.*, 1997; *Ghan et al.*, 1998). We will consider such a case in Chapter 7, in which there will be very many sulfate and mixed soot / sulfate aerosol and very few sea salt aerosol.

The MELAM model allows flexibility in aerosol representation, which distinguishes it from many other models in the literature. It easily runs in a bulk formulation, using one or more of the sectional representations, or using the representative sampled distribution. It is simple to introduce mixed representations in which several sectional distributions (of a single or multiple types) are used together or even in combination with the representative sample distribution. This will not be discussed at length in this thesis except where used in specific case studies.

3.4 Representation of Aerosol Composition and Mixing State

Any model of atmospheric particulates must presume some representation of the particles' shape, size, and composition. Generally, models describe aerosol by a radius or volume and the mass of each of a list of constituents. Aerosol populations in which each particle consists of a single component (or that component and water) are called externally mixed; those in which each aerosol contains more than one type are known as internally mixed. In even moderately polluted environments, aerosol tend to mix within their first day in the atmosphere through a variety of processes and so populations are predominantly internally mixed, at least to some degree (*Jacobson, 2002*). The various constituents of a given particle, however many there may be, are often presumed to be either well mixed or to follow a simple geometry when multiple phases are present. Idealized configurations often contrast with what is seen in polluted natural environments, in which aerosol are often irregularly shaped and composed of many species of various phases. Limitations in both observations and theory constrain the aerosol representations available to us, and at present only a sub-group of the known aerosol configurations are well represented in models. In this section, we will highlight how aerosol have been represented in models available in the literature, discuss the various efforts to resolve composition within a sectional framework, and then detail the frameworks used in the MELAM model.

We are primarily interested in aerosol in the moist environments in which cloud form, although we would like to understand aerosol behavior at more moderate relative humidities as well. Many aerosol take on significant amounts of water in very moist environments, and this up-take is dependent on particle composition, shape, mixing state, and surface properties. Figure 3-4 shows schematic representations of some of the many possible aerosol configurations seen in the atmosphere, both as they might exist in relatively dry and very moist environments. Modeling frameworks in the literature are well developed, constrained, and validated for some of the configurations shown, while for others there have only been first attempts. Within the last five years, however, each have been treated in the context of aerosol activation at least cursorily.

Aerosols may be composed of some combination of inorganic electrolytes (modeled, for example, in *Köhler, 1936*; *Gelbard et al., 1980*; *Gelbard and Seinfeld, 1980*; *Wexler and Seinfeld, 1991*; *Kim et al., 1993a*; *Wexler et al., 1994*; *Kim and Seinfeld, 1995*; *Jacobson, 1997b*; *Nenes et al., 1998*; *Russell and Seinfeld, 1998*; *Ansari and Pandis, 1999b*; *Nenes et al., 1999*; *Zhang et al., 2000*; *Wexler and Clegg, 2002*; *Koo et al., 2003*), organic material of low to high solubility (*Shulman et al., 1996*; *Jang et al., 1997*; *Gorbunov et al., 1998*; *Ansari and Pandis, 1999a, 2000*; *Cruz and Pandis, 2000*;

Decesari et al., 2000; *Djikaev and Donaldson*, 2000; *Bessagnet and Rosset*, 2001; *Kerminen*, 2001; *Clegg et al.*, 2001; *Choi and Chan*, 2002; *Ming and Russell*, 2002; *Raymond and Pandis*, 2002; *Hori et al.*, 2003; *Raymond and Pandis*, 2003), and completely insoluble material such as dust or soot spherules or chains (*Jacobson*, 2001a; *Wang*, 2004). Surfactant species may be present, either encasing the entire solution portion of the aerosol or in a broken partial covering (*Cruz and Pandis*, 1998; *Li et al.*, 1998; *Facchini et al.*, 2001; *Rood and Williams*, 2001; *Facchini et al.*, 1999; *Feingold and Chuang*, 2002a; *Abdul-Razzak and Ghan*, 2004; *Broekhuizen et al.*, 2004). Solution droplets may freeze, initiating a very different set of physical behavior than seen in non-frozen aerosols (not shown in Figure 3-4) (*Chen and Lamb*, 1994a,b; *Chen et al.*, 1997; *Pruppacher and Klett*, 1997; *Chen and Lamb*, 1999; *Jacobson*, 2003). Insoluble solid cores may serve as sites of condensation of water (*Fletcher*, 1976; *Zuberi*, 2003). And water may condense onto mixed aerosol containing both insoluble cores and soluble substances either by engulfing the core or by forming an embryo on the core's surface (*Hänel*, 1976; *Gorbunov and Hamilton*, 1996, 1997; *Djikaev and Donaldson*, 2000). Of these various configurations, only that of inorganic electrolytes is well understood; there are significant open questions about the modeling of all of the other aerosol types. In the version presented in this thesis, the MELAM model addresses solution-phase inorganic aerosol and mixed inorganic / insoluble particles. The model is written to be flexible in this representation and should easily extend to new configurations once adequate theory and observations become available.

The simplest particles to describe physically are those consisting only of a well-mixed solution droplet. These are well characterized by volume (or by the radius of the equivalent spherical particle) and by concentrations of each constituent species. Even for these particles, however, the equilibrium relationship between composition, environmental conditions, and aerosol physical properties (including surface tension, density, volume, ionic strength, etc.) is governed by a complex set of thermodynamic relationships. Adequate thermodynamic models of the behavior of inorganic aerosol now exist (e.g. *Zemaitis et al.*, 1986; *Zhang et al.*, 2000). However, serious understanding of the thermodynamics of organic aerosol is currently beyond reach (*Saxena et al.*, 1995; *Raymond and Pandis*, 2002), and understanding of the thermodynamics of mixed inorganic / organic systems is yet further off. The MELAM model uses a complete system of inorganic thermodynamic theories presented in Chapter 4, and considers mixed aerosol that include both some inorganic electrolytic components, and also insoluble cores such as soot or dust as presented in Section 5.8.2.

Whenever a model seeks to represent a heterogeneous population of aerosol efficiently, a number

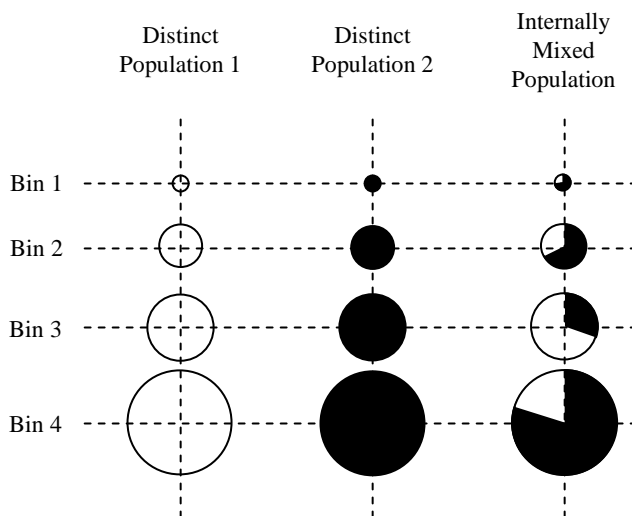


Figure 3-5: Schematic of one way to represent multiple aerosol types in a sectional distribution; there are three aerosol populations, each divided into four separate size bins; populations 1 and 2 include a single type of aerosol (homogeneous in composition, but not necessarily single-component), while the third distribution is “internally mixed” such that each aerosol in each bin is comprised of partially of the components of population 1 and partially of the components of population 2

of simplifying assumptions must be made in the name of computational efficiency. As discussed in Section 3.3 earlier, aerosol size is often represented by assuming either functional forms for the variation of number population with aerosol radius, or by grouping aerosol into a number of sections by size. In general, models resolve aerosol composition much less well than aerosol size, and often aerosol are presumed to be either a single, perfectly internally mixed distribution (*Zhang et al.*, 2002) or have an unchanging relationship between aerosol size and composition (e.g., *Flossmann et al.*, 1985; *Lucas*, 1999). In polluted environments, aerosol rapidly mix and composition no longer adheres to a strict size-dependency or external mixture (*Jacobson*, 2002). Modeling such a population as a single internally mixed distribution, as is often done (*Zhang et al.*, 2002), apparently does not impair correct evolution of a particle spectrum under condensation and evaporation of the various species, which validates the approximation’s use in air quality models (*Fernandez-Diaz et al.*, 1999). However, the internally mixed assumption can significantly distort calculations of hygroscopic (*Fassi-Fihri et al.*, 1997; *Russell and Seinfeld*, 1998) and optical properties (*Haywood and Shine*, 1995; *Fassi-Fihri et al.*, 1997; *Liao and Seinfeld*, 1998).

When composition is to be explicitly tracked and evolved in time, models traditionally represent a population of aerosol as an external mixture of one or more strains of particles that may each contain an internal mixture of several chemical components that may interact with each other. Consider the scenario shown in Figure 3-5: two pure aerosol types that originate from distinct

sources are represented within their own sectional distributions and a third distribution tracks the concentration of the mixture of the two. The relative mass of the two aerosol types within each size bin of the mixed distribution may be different and vary with time. Without additional emission or nucleation, the concentration of two pure aerosol will fall over time and that of the mixed aerosol will rise, due to a variety of aerosol dynamical processes. This is the technique used by Jacobson’s gas, aerosol, transport, and radiation air quality model (GATOR: *Jacobson et al.*, 1994, 1996a; *Jacobson*, 1997a), which includes up to a dozen or more distinct pure aerosol types and a single internally mixed distribution. Each aerosol process model makes slightly different choices about how to represent aerosol distributions as external or internal mixtures, but in general most focus on distinguishing between pure and mixed aerosol, rather than the significant variations amongst the mixed particles. In this way, the representative sample distribution, introduced above in Section 3.3, allows better resolution of aerosol composition. We will come back to this.

Aerosol populations of inhomogeneous inorganic composition have been modeled using a variety of methods, mostly within the sectional framework. The first multi-component sectional scheme represented aerosol as a single, internally mixed distribution that is inhomogeneous in composition (*Gelbard and Seinfeld*, 1980). This formulation has been widely used ever since due to its computational efficiency (*Zhang et al.*, 2002). The GATOR model, as discussed above, focused on representing un-mixed aerosol in addition to average, mixed particles; its techniques represented a significant advance for air quality modeling. *Kleeman et al.* (1997) also represented the distribution of aerosol as a “source-oriented” external mixture, although their model allowed no mixing whatsoever. These techniques are most useful in situations for which mixing is of minor importance. *Chen and Lamb* (1994a) use a single, internally mixed liquid-phase distribution and another for frozen particles. This was the first serious attempt to include the ice phase into an aerosol-cloud sectional model and it was only modestly successful. An adequate microphysical model of ice phase hydro-meteor growth in a changing environment is still unavailable. *Russell and Seinfeld* (1998) presented the first explicit aerosol-cloud model intended to investigate cloud formation and cloud processing of aerosols. Their model is based upon the sectional approaches mentioned above and relegates each internally mixed aerosol to one of the several distributions according to its least volatile component, presuming that this is the most permanent marker of aerosol composition. It thus retains some separation of distinct aerosol compositional types even in mixed particles, prioritizing the less volatile components above the more volatile, while limiting computational expense. *Jacobson* (2002) expands on the earlier formulation of *Jacobson et al.* (1994), and tracks a number of aerosol distributions and also each binary mixture as its own distribution and then an internally

mixed distribution for ternary and higher mixtures. The version of MELAM presented in this thesis allows a choice of three representations: a single internally mixed distribution; multiple distinct distributions plus a single internally mixed distribution (similar to the approach of *Jacobson et al.*, 1994); and the representative sample distribution that defines the aerosol distribution by sampling from one or more input distributions (of the same or of different composition), and then allows the population to evolve without averaging thereby retaining the full variation of compositions.

Mixtures of insoluble aerosols and inorganic electrolytic aerosols prove difficult to represent in the sectional framework. The size and other characteristics of the cores need not correlate with inorganic content. And the properties of the cores are not well conserved during averaging. The representative sampling method works well, however, for such mixed aerosol since the aerosol are never averaged when placed into bins, coagulation, or transport. For considerations of coagulation during cloud formation, this proves extremely valuable. We will discuss an instance of this in Chapter 7.

3.5 Summary

In this chapter, we introduced the various ways models, and the MELAM model in particular, represent aerosol. We introduced the log-normal representation often used to summarize measurements of aerosol size distributions. And we discussed how aerosol size and composition are represented in a variety of modeling frameworks. The intention of the author is to allow the MELAM model to be as flexible as possible, such that a user can select the method most convenient for a particular situation.

Chapter 4

Aerosol Chemical Thermodynamics

4.1 Introduction

In this chapter, we present the thermodynamics modeling approach of the Mixed Eulerian-Lagrangian Aerosol Model (MELAM). The aerosol equilibrium water mass fraction, and the disequilibrium water vapor condensation rates depend critically on aerosol composition. Since we intend to accurately model condensation rates during the aerosol activation process, realistic aerosol chemistry and thermodynamics are central to the successful formulation of this model. MELAM allows the aqueous composition of each lagrangian, representative particle and all bins of particles to evolve on its own through forward chemical reactions and the equilibrating effects of reversible dissociation reactions when they occur. Additionally, concentrations internal to the particles change when molecules enter from or exit to the gas-phase through condensation, evaporation, and surface reaction or by coagulation with another particle.

In the aqueous phase, electrolytes may dissociate into their constituent ions, a process that impacts directly the equilibrium water content, surface tension, density, pH, condensation rates and other particle properties. Predicting these traits for a complex, multi-component aerosol is the purview of MELAM's thermodynamic module, and requires efficient calculation of activity coefficients of electrolytes and other dissociating species, equilibria for electrolyte dissociation reactions, equilibrium water content, density, and surface tension. Solid phase species are only included insofar as there are absolutely insoluble species inside the aerosol, although their impact on activity coefficients is included. The assumption that salts never crystallize introduces considerable errors below 60% \mathcal{RH} (*Moya et al.*, 2002), a humidity range that is not the focus of this model. The theoretical and numerical techniques MELAM uses to describe aerosol thermodynamics are discussed

in this chapter.

The focus of the thermodynamic module is on inorganic species, which require quite different thermodynamic parameterizations than do organics or other classifications of species. The advantage of concentrating on an inorganic formulation is that these systems have been extensively studied and characterized. Fundamental theories and successful parameterizations have long since been collected into research texts, including *Robinson and Stokes* (1959), *Zemaitis et al.* (1986), and *Tester and Modell* (1997). Additionally, the extensive empirical work of Clegg, Wexler, and colleagues characterizes extremely well a subset of inorganic aerosol systems (*Clegg et al.*, 1998a,b, 2001; *Wexler and Seinfeld*, 1991; *Wexler and Clegg*, 2002) and lead to the exquisitely accurate *Aerosol Inorganic Model* (AIM) and a basis for comparison and understanding. *Kim et al.* (1993a) and *Zhang et al.* (2000) recently provided thoughtful inter-comparisons of extant inorganic thermodynamic modules that afford some insight into the trade-offs between accuracy, computational efficiency, and breadth of species modeled.

The partitioning and solubility of organic species is critically important to the resolution of questions surrounding the indirect effect of aerosols on clouds. Organic aerosols and condensable organic species are observed in all environments, and are the dominant share of aerosol-phase species in some. Organic species also no doubt contribute to the composition of many primarily inorganic particles (*Abdul-Razzak and Ghan*, 2000). However, the state of the science is such that the great majority of the organics present in aerosol are unidentified. For those that have been identified, the lack of measurements of solubilities and their dependence on inorganic solute concentration is imposing, not to mention the lack of a suitable unified thermodynamic formulation for mixed inorganic / organic aerosol (*Saxena et al.*, 1995; *Cruz and Pandis*, 1997; *Turpin et al.*, 2000). Hence, our initial thermodynamic model will not include organics. The state of research into organic thermodynamics and the prospects for including them into future versions of this model is discussed further in Section 4.6.4.

Unlike most modules available in the literature, MELAM's thermodynamics module is written to be easily specialized or extended to include new species including non-electrolytes. All of the specifics of the thermodynamic and chemical reactions are read from input files and no exceptions to fundamental rules are made to accommodate exceptional cases. As a result, updates in thermodynamic data, forward, reverse and equilibrium reaction sets, and aerosol composition will be easy incorporated as future research dictates and justifies; the under-girding thermodynamic theories are not as easily modified although the modularity of the computer code will facilitate changes and future inclusions. This flexibility distinguishes MELAM as a research tool from many

of the other available models, which are generally streamlined for speed and operational use in large models and would require rewriting to include an additional component (see ISORROPIA, of *Nenes et al.* (1998) for the most dramatic example of this type of efficient, streamlined model).

4.2 Chemical Continuity

As in standard sectional models, such as those reviewed earlier in Chapter 3, we may write expressions of conservation for each chemical species. The amount of each chemical present in the domain is distributed across the three phases and changes only with true chemical production and loss (which may happen in either the gas or aqueous phases):

$$\frac{dm_i}{dt} = \text{Chemical Production} - \text{Chemical Loss} \quad (4.1)$$

$$\text{where } m_i = \overbrace{m_i^{(\text{vapor})}}^{\text{gas-phase}} + \sum_p \overbrace{\left(m_{i,p}^{(\text{aqueous})} + m_{i,p}^{(\text{solid})} \right)}^{\text{particle-phase}} \quad (4.2)$$

Here, m_i is the total mass of species i and a subscript p indicates the particle-phase.

MELAM tracks each particle of sufficient size individually as it moves through the Eulerian grid of the background environment. Each particle's aqueous composition evolves on its own, and interacts with gas-phase species through dissolutional, condensational and evaporative exchange with the atmospheric volume modeled by the closest Eulerian grid point as described in Chapter 5. In this framework, the chemistry of the Lagrangian particles generally obeys the following continuity expression:

$$\frac{dc_f}{dt} = \text{Chemical Production} - \text{Chemical Loss} + \text{Condensation} - \text{Evaporation} \quad (4.3)$$

Here, c_f is the mole concentration within a particle of a given electrolyte family – the associated and dissociated forms of the species; for example, c_f may include SO_4^{2-} , HSO_4^- , H_2SO_4 , and H^+ (see *Schwartz*, 1986; *Jacobson et al.*, 1996b). Chemical production and loss may involve any of the members of the family while condensation and evaporation usually only pertains to the undissociated electrolytic form, although exceptions to this are discussed in Chapter 5. Equilibrium between the members of the family is determined by reversible aerosol thermodynamic calculations and for the purposes of our model is assumed to be achieved instantaneously. The assumption of instantaneous equilibrium is appropriate for aqueous dissociation of electrolytes and acids but is not appropriate for gas-aerosol equilibrium, especially for larger particles (*Meng and Seinfeld*,

1996), nor is it appropriate for solid-aqueous equilibrium, which may occur over long time scales or be inhibited by hysteresis effects (*Cziczo and Abbatt, 2000*).

We make the simplifying assumption that the solid phase does not interact with either the aqueous or the gas phases, which we justify by noting that this formulation is intended to simulate moist and cloudy environments where the high relative humidity (\mathcal{RH}) values are above the deliquescence points of all but insoluble species. In reality, solids and hydrates of course may form in environments less humid than the deliquescence relative humidities of those species. *Zhang et al. (2000)*’s comparison includes one model, MARS-A (*Binkowski and Shankar, 1995*), that does not allow solid formation. Zhang et al. find that MARS-A’s formulation does not significantly impact composition and other results at high \mathcal{RH} relative to other models, although it leads to greater water contents at mid-range humidities, from approximately 30% to 70% \mathcal{RH} . As the deviations are not substantial and we are not specifically concerned with those humidity ranges, we feel confident in making this assumption.

4.3 Equilibrium Dissociation of Electrolytes and Acids

In the context of atmospheric aerosol, the partitioning of chemicals between the gas and aqueous phases, between associated and dissociated forms in solution, and between aqueous and solid phases are considered as equilibrium processes describable by an equilibrium constant corrected for temperature dependence and non-ideality (*Tester and Modell, 1997*). However, in order to use an equilibrium model to describe inter-phase and associative equilibria, we must be convinced that the equilibration of those processes occurs more rapidly than any of the other dynamics that affect the aerosol composition or, at least, that the approximation that they do does not lead to significant errors. Several studies, reviewed in Section 5.4, draw into question whether observed atmospheric aerosol are predominantly in a state of gas-particle equilibrium. In recognition of that issue, our model uses a flux-based treatment of dissolution and condensation as presented in Chapter 5. However, as noted earlier dissociative equilibrium of electrolytes is reached rapidly with respect to the other processes that govern aerosol dynamics and may be thought of as being in near constant equilibrium.

The equilibrium constant may be related directly to chemical potential, and we can choose either a global minimization of chemical potential or specification of specific equilibrium reactions governed by empirically determined equilibrium constants. This model employs the second approach. Equilibrium constants are discussed generally in Section 4.3.1; the algorithm used to simultaneously

solve for multiple equilibria is discussed in Section 4.3.2; and corrections for ideality are discussed at length in Section 4.4

4.3.1 Equilibrium Coefficients for Dissociating Species

An equilibrium coefficient, K_{eq} , describes the ratio of the amount of an electrolyte that dissociates into the relevant anions and cations to the amount that remains associated in an ideal solutions and it is a function of temperature and the mixture of electrolytes and ions present in the solution. The equilibrium state of dissociation in a generalized, non-ideal solution may be found for an electrolyte by relating K_{eq} to the thermodynamic activity of each of the species involved, such that (*Jacobson*, 1999):

$$K_{eq}(T) = \prod_x a_x^{k_x \nu_x} \quad (4.4)$$

In which a_x is the thermodynamic activity of a species x , $k_x = \pm 1$ according to whether species x is a product (+1) or reactant (−1), and ν_x is a stoichiometric coefficient. The activity of an undissociated electrolyte is simply its molality (\mathbf{m}_x), while the thermodynamic activity of a dissociated electrolyte is its molality corrected for non-ideality:

$$a_{ij} = \mathbf{m}_i^{\nu_i} \mathbf{m}_j^{\nu_j} \gamma_{ij}^{\nu_i + \nu_j} \quad (4.5)$$

Here, ij is an electrolyte comprised of cation i and anion j , γ_{ij} is the mean activity coefficient (the correction for non-ideality), and ν_i and ν_j are stoichiometric coefficients. This definition and the methods used to approximate the mean activity coefficients are addressed at length in Section 4.4.

By relating K_{eq} to the Gibbs free energy of the system and using appropriate thermodynamic identities, we may derive an expression for the temperature dependent form of K_{eq} (*Kim et al.*, 1993a; *Jacobson*, 1999):

$$K_{eq}(T) = K_{eq}(T_0) \exp \left[-\frac{\Delta_f H_0^\circ}{R^* T_0} \left(\frac{T_0}{T} - 1 \right) - \frac{\Delta C_p^\circ}{R} \left(1 + \ln \left(\frac{T_0}{T} \right) - \frac{T_0}{T} \right) \right] \quad (4.6)$$

$$K_{eq}(T_0) = \exp \left(-\frac{\Delta_f G^\circ}{R^* T_0} \right) \quad (4.7)$$

In which $\Delta_f G^\circ$ is the change in standard molal Gibbs free energy of formation, $\Delta_f H_0^\circ$ is the change in standard molal enthalpy of formation, and c_p° is the change in the standard molal heat capacity at constant pressure, each at the reference temperature, T_0 . Equilibrium coefficients are generally

experimentally determinable, which is the preferable means of finding the value at the reference temperature.

4.3.2 Solving for Equilibrium Concentrations

In a complex solution of multiple electrolytes, many equations resembling equation (4.4), one for each equilibrium dissociation reaction, must be satisfied simultaneously for the system to be at equilibrium. Most of the equilibrium thermodynamics models available in the literature employ one of two solution methods: reaction-based bisectional Newton methods (*Pilinis and Seinfeld, 1987; Kim et al., 1993a,b; Jacobson et al., 1996b*); or Gibbs free energy minimization methods (*Wexler and Seinfeld, 1990; Resch, 1995; Wexler and Clegg, 2002*). Numerical formulations of these methods require iteration and often dominate the computation time of an aerosol model (*Jacobson, 1997c*). One notable exception is the *Analytical Predictor of Dissolution* scheme presented in *Jacobson (1997c)* which requires no iteration, is unconditionally stable, and conserves mass and charge. However, this method requires the author to algebraically relate concentrations at equilibrium in a manner that is, at this point, impossible to automate and as a result is not used here. MELAM uses a modified version of the *Mass Flux Iteration* (MFI) method, an iterative solution scheme adapted from *Villars (1959)* by *Jacobson et al. (1996b)*. The procedure is standardized and flexible such that all information related to electrolytes, thermodynamics, and equilibrium reactions are read in from input files and assigned appropriate numerical procedures on the fly. Jacobson adopts the MFI method in his EQUISOLV equilibrium thermodynamics model presented in *Jacobson et al. (1996b)*.

Given a way to find specific values for K_{eq} (described in Section 4.3.1) and activities (outlined in Section 4.4), equation (4.4) may be inverted to find equilibrium ratios between the concentrations of the associated and dissociated forms of an electrolyte. The MFI method guides an iterative re-portioning of the associated and dissociated forms of the electrolyte that leads towards equilibrium, reaching a pre-specified error threshold often within a handful of iterations. In the general case, an electrolyte dissociates into ν_i of cation i and ν_j of anion j pair, incorporating ν_w water molecules along the way. Combining equations (4.4) and (4.5), the equilibrium condition then becomes:

$$\frac{\mathbf{m}_i^{\nu_i} \mathbf{m}_j^{\nu_j}}{\mathbf{m}_{ij} a_w^{\nu_w}} \gamma_{ij}^{\nu_i+\nu_j} = K_{eq}(T) \quad (4.8)$$

For the example of a simple aqueous electrolyte, ij , that dissociates directly to form ν_i of i and ν_j

of j , this becomes:

$$\frac{\mathbf{m}_i^{\nu_i} \mathbf{m}_j^{\nu_j}}{\mathbf{m}_{ij}} = \frac{K_{eq}(T)}{\gamma_{ij}^{\nu_i+\nu_j}} \quad (4.9)$$

Some electrolytes require the incorporation of a water molecule in the dissociation process, and for these electrolytes equation (4.9) must be modified. For example, consider the equilibrium dissociation reaction:



The equivalent formulation to equation (4.9) for this type of reaction must include the water activity (a_w); the method we use to calculate a_w is discussed in later in Section 5.5.2. At equilibrium with the gas phase, a_w is equal to the ambient relative humidity; Section 5.5 discusses the water activity in greater depth. For this reaction, the ratio of the ions to the associated electrolyte is:

$$\frac{\mathbf{m}_{\text{NH}_4^+} \mathbf{m}_{\text{OH}^-}}{\mathbf{m}_{\text{NH}_3}} = \frac{K_{eq}(T) a_w}{\gamma_{(\text{NH}_3+\text{H}_2\text{O})}^2} \quad (4.11)$$

In this case ν_w is unity.

We begin the equilibration algorithm by making a first guess of the size of the correction to the concentrations necessary to reach equilibrium, then update the concentration using these estimations, then check to see if the system is at equilibrium, and then either return those concentrations or refine our correction estimate and go through the process again. Specifically:

1. First, we find the concentrations of the reagents that limit the reaction in each direction, from electrolyte to ions and vice versa, by scaling the concentration of each by appropriate stoichiometric factors and comparing the results. Let $Q_{\text{electrolytes}}$ and Q_{ions} be the scaled limiting concentrations for the electrolyte to ion and ion to electrolyte pathways, respectively. Then:

$$Q_{\text{electrolytes}} = \min\left(\frac{c_A}{\nu_A}, \frac{c_B}{\nu_B}, \dots\right) \quad ; \quad Q_{\text{ions}} = \min\left(\frac{c_C}{\nu_C}, \frac{c_D}{\nu_D}, \dots\right) \quad (4.12)$$

Here, species A and B are electrolytes, water, or, in the more general case, electrolytic solids or water-soluble gases, and C and D are ions. The ellipses are to indicate that there may be more than two reagents in either of these two sets.

2. Next, we initialize a tracking parameter (\mathcal{Z}_1) and mass flux parameter (Δx_1):

$$\mathcal{Z}_1 = \frac{Q_{ions} + Q_{electrolytes}}{2} \quad (4.13)$$

$$\Delta x_1 = \frac{Q_{ions} - Q_{electrolytes}}{2} \quad (4.14)$$

With which we update the concentrations for species involved in the reaction by adding Δx_1 multiplied by the appropriate stoichiometric coefficient to electrolytes and subtracting an equivalent value from the ions. Note that this updating procedure conserves both mass and charge and that Δx_1 may be either positive or negative, correcting towards equilibrium.

3. We then check to see whether equilibrium has been achieved by evaluating whether equation (4.4) is satisfied within a prescribed error.
4. If equilibrium has been acceptably approximated, then we stop the cycle. If it has not been achieved, then we reiterate by setting \mathcal{Z}_{i+1} equal to half of \mathcal{Z}_i and Δx_{i+1} equal to either $+\mathcal{Z}_{i+1}$ or $-\mathcal{Z}_{i+1}$ depending on which side of the equilibrium ratio (4.4) is greater.

Jacobson et al. (1996b) recommend using this procedure to solve for multiple simultaneous equilibria by looping up and down through the list of equilibrium reactions, solving for one equilibrium at a time, until all are within error of equilibrium. During development of our model, however, Jacobson’s method failed too often to converge when specialized reactions that either redistributed very minor constituents or that have very large (or very small) equilibrium constants are included. These specialized reactions are easily knocked out of equilibrium and, if included, dramatically increased computation time in many situations and, in some perverse situations, prevented convergence. We therefore modified the Jacobson MFI algorithm to accommodate these computational difficulties, including a procedure to demote less important reactions and defer their equilibration until the end. Specifically:

1. First, we loop once over the full list of equilibrium reactions using the procedure outlined above to equilibrate each in turn. If any were out of equilibrium initially, we loop again. In simple systems or those already close to equilibrium, all of the reactions may be in equilibrium after this step; in those cases, we simply stop the procedure after the second loop.
2. We then loop through the set of reactions to identify the reaction that is furthest from equilibrium, using the absolute value of fractional distance from equilibrium (ξ) as the appropriate

metric. For a system whose equilibrium is described by equation (4.8), we may write ξ :

$$\xi = \left| 1 - \frac{K_{eq}(T) \mathbf{m}_{ij} a_w^{\nu_w}}{\gamma_{ij}^{\nu_i + \nu_j} \mathbf{m}_i^{\nu_i} \mathbf{m}_j^{\nu_j}} \right| \quad (4.15)$$

If none of the calculated ξ values are greater than some specified minimum value (taken to be 1% in this project), then the system is considered to be in approximate equilibrium and we skip the next step and go directly to step 5. Tests of the model show that the equilibrium is not very sensitive to ξ as long as it is several percent or below, in which range this threshold acts as a true error tolerance term.

3. If the system is still not in equilibrium after some threshold number, we calculate the ionic strength of the system and save it for comparison.
4. Having identified the reaction most out of equilibrium, we equilibrate that reaction using the above procedure. If we are beyond the threshold iteration referenced in step 3, we note the change in the ionic strength across the equilibration. If this change is less than some prescribed portion of the sum calculated in step 3, then the reaction is considered to be of minor importance in the equilibration process and the reaction is removed from consideration of the ranking procedure in step 2 (demoted). We then return to step 2 and repeatedly update the concentrations for the reaction furthest from equilibrium until all of the major reactions are in simultaneous equilibrium.
5. All of the reactions not demoted in step 4 are now in simultaneous equilibrium. We equilibrate each of the minor, demoted reactions once. We then check to make sure that each of the major reactions are still in equilibrium. If they are, then we consider the system to be sufficiently in equilibrium and return. If they are not, which should seldom be the case, then we return to step 2; the system should be quite near equilibrium at this point and few additional calculations ought be necessary.

We find that this procedure efficiently equilibrates an arbitrary number of dissociation reactions. The main difference of this procedure from the MFI method introduced in *Jacobson et al.* (1996b) is its inclusion of demotion of some reactions, which has the effect of speeding the equilibration process and avoiding non-convergence. It is not a fail-safe improvement, however, as it does not guarantee simultaneous equilibrium for the relegated reactions. In a perverse case where the particle's composition is so mixed that several hundred distinct constituents are equally represented

and so nearly every reaction is demoted during the procedure, the solution will look nothing like equilibrium. This perverse case is not a realistic situation, however, and the algorithm works well in the situations considered during validation.

4.4 Thermodynamic Activities

In order to use the equilibration routine outlined in Section 4.3.2 to solve for the concentrations of the various ions and electrolytes at equilibrium, as defined in equation (4.4), MELAM must be able to calculate thermodynamic activities of each of the species. Calculating the activities of non-ionic species is straight forward: the activity of a gas phase species is its partial pressure; the activity of a solid is unity; the activity of liquid water is the ambient relative humidity at equilibrium (this is discussed further in Section 5.5); and the activity of an undissociated electrolyte is its molality. The activity for an ion i in solution is defined to be the activity coefficient (γ_i , unitless) multiplied by the molality (*Jacobson et al.*, 1996b); the activity coefficient is, in effect, a correction for the non-ideality of a concentrated solution in which forces beyond the Coulombic are important (*Jacobson*, 1999).

Several activity coefficient estimation methods, including the Kusik-Meissner method to be implemented here (*Meissner et al.*, 1972; *Kusik and Meissner*, 1978; *Meissner*, 1980), estimate only the mean activity coefficient defined in equation (4.4) and restated here:

$$a_{ij} = \mathbf{m}_i^{\nu_i} \mathbf{m}_j^{\nu_j} \gamma_{ij}^{\nu_i+\nu_j}$$

In which the i and j subscripts correspond to the anion and cation. If $\nu_i = \nu_j$, the electrolyte is referred to as symmetric; if not, it is non-symmetric. If $\nu_i = \nu_j = 1$, the electrolyte is referred to as univalent. All electrolytes, of course, must conform to charge balance such that $z_i \nu_i = -z_j \nu_j$, where z_i is the charge of the ion i ; a loose exception to this rule to account for partial dissociation is included in MELAM, as discussed in Section 4.4.3.

In very dilute solutions, activity coefficients may be calculated using Debye-Hückel theory. In these solutions, ion-ion interactions are limited by solute molecules that shield them from each other and because of simple distance between ion pairs. Given this, Debye-Hückel theory validly approximates the ions to be isolated from each other and that the deviation of molality from thermodynamic activity (the ideal relationship) is predominantly the result of Coulombic attraction (cf., *Seinfeld and Flagan*, 1999, Chapter 4). This theory works well for ionic strengths below 0.01

but becomes progressively worse as ionic strength approaches the heightened values of atmospheric relevance (*Tester and Modell, 1997*).

In more concentrated solutions, including atmospheric aerosol systems, other types of interactions between the ions become important. Several extensions to Debye-Hückel theory have been developed, all of which in some way rely on derived multi-variable relationships tuned to experimental results for binary (a single solute in a single solvent) solutions and require a theory for extension to mixed systems.

Pitzer’s method (*Pitzer, 1973; Pitzer and Mayorga, 1973; Pitzer and Kim, 1974; Pitzer, 1975; Clegg et al., 1992; Clegg and Pitzer, 1992*) predicts the total excess Gibbs free energy of a concentrated electrolytic system using a virial expansion with high order terms for multi-ionic interactions, is the most accurate of the thermodynamics modules (*Zhang et al., 2000*). Its experimental requirements, however, are onerous and for that reason it is difficult to imagine the extension of this method beyond simple inorganic situations into the full complexity of real atmospheric particles. By comparison, the Kusik-Meissner method, which is essentially an extension of Bromley’s scheme (*Bromley, 1973; Zemaitis et al., 1986*), requires a fit of only two parameters per species and sacrifices little in terms of accuracy (*Zemaitis et al., 1986*), except in a few notable cases which unfortunately include the partially dissociating sulfate system so critical to atmospheric aerosol; this deficiency will be addressed in Section 4.4.3. The common multi-component activity coefficient estimation methods include Bromley’s, Pitzer’s, and Kusik and Meissner’s. *Kim et al. (1993b)* compare the performance of the Bromley, Kusik-Meissner, and Pitzer methods in concentrated solutions relevant to atmospheric aerosol, and conclude that Kusik-Meissner is the best balance of accuracy and computational and data efficiency; it is therefore the method we adopt here.

MELAM employs the Kusik-Meissner method for calculating binary activity coefficients, Patwardhan and Kumar’s mixing rule for multi-component systems, and a number of extensions to deal with partially dissociating electrolytes and other special cases. This section discusses each of these techniques in turn.

4.4.1 Calculating Binary Activity Coefficients when Binary Data is Available

The Kusik-Meissner correlation relates the “reduced mean” activity coefficient (discussed below) of a single electrolyte (Γ_{ij}° , where the super-script \circ indicates a pure electrolyte and the i and j refer to the electrolyte’s constituent ions) to the ionic strength of the solution and two empirical parameters. The method arose from Kusik and Meissner’s experimental work, in which they noticed that the activity coefficients of each electrolytic species, when plotted against ionic strength, fell along one

of the set of curves shown in Figure 4-1 (*Zemaitis et al.*, 1986). The history and underpinnings of this model are thoughtfully reviewed in *Tester and Modell* (1997).

Let us define the “mean” activity coefficient, γ_{ij} , for an electrolyte and the related ion pair i and j in a pure solution in terms of the ionic activity coefficients defined in equation (4.5):

$$\gamma_{ij} \equiv (\gamma_i^{\nu_i} \gamma_j^{\nu_j})^{\frac{1}{\nu_i + \nu_j}} \quad (4.16)$$

The equilibrium equations of standard electrolytes use this quantity directly and do not need the activities of the individual ions (γ_i and γ_j). However, a serious limitation of the Kusik-Meissner approach is that the calculated activities are all couched in terms of these mean activities, and a good deal of work is required: to (a) conform partially dissociating electrolytes to this system, (b) include electrolytes composed of more than two ions (such as sodium bisulfate, ammonium bisulfate, and letovicite), and (c) make composite activities for electrolytes for which there is not explicit binary data. Case (a) is discussed in Section 4.4.3, (b) in Section 4.4.4, and (c) in Section 4.4.2. From this mean activity defined in equation (4.16), we may define the “reduced mean” activity coefficient (Γ_{ij}):

$$\Gamma_{ij} \equiv \gamma_{ij}^{\frac{1}{|z_i z_j|}} \quad (4.17)$$

Where the reduction of the activity is in terms of the charge of the constituent ions.

The two parameter Meissner model defines the reduced activity in terms of two empirical parameters and is the foundation of the method of Kusik and Meissner:

$$\log_{10} \Gamma_{ij}^\circ = \log_{10} (1 + [0.75 - 0.065 q] [\{1 + 0.1 I\}^q - 1]) - \frac{\overbrace{0.5107\sqrt{I}}^{\mathcal{D}}}{1 + C\sqrt{I}} \quad (4.18)$$

In which I is the ionic strength of the solution, step \mathcal{D} is discussed below, and:

$$C = 1.0 + 0.055 q \exp[-0.023 I^3] \quad \text{and} \quad q = q_r \left(1 + q_T \frac{T - T_r}{z_i z_j}\right) \quad (4.19)$$

Only the two parameters q_r , the Kusik-Meissner coefficient at a reference temperature, and q_T , the linear dependence of q on temperature, must be determined experimentally. Values of these coefficients for over one hundred electrolytes are tabulated in *Kusik and Meissner* (1978), *Zemaitis*

et al. (1986), *Kim et al.* (1993a), and elsewhere. Those references extensively catalog fit values for q_r , but in general not enough data is available to constrain q_T and they suggest using the default value of -0.0027 proposed in *Meissner* (1980); clearly this lack of extensive temperature dependent activity data is a deficiency, and one that this method shares with all others.

Assuming that q depends linearly on temperature is reasonable to an estimated error of 20%, although in certain unfavorable situations the error may be as large as 45% or behave in a decidedly non-linear fashion (*Meissner et al.*, 1972). This is an improvement upon the temperature dependence suggested in the original formulation, however, and usually the limits of available data overwhelm the errors associated with the assumption of linearity.

The parameter C notation is used in equation (4.18) to emphasize the similarity in the form of term \mathcal{D} to the Debye-Hückel equation, which defines Γ° in an infinitely dilute solution in which only Coulombic interactions are important:

$$\ln \Gamma_{ij}^\circ = \frac{A\sqrt{I}}{1 + A^*\sqrt{I}} \quad (4.20)$$

Here, A is a parameter that varies with solvent and temperature and A^* depends on the ratio of the ionic radius to the Debye length in the solution (*Tester and Modell*, 1997; *Steinfeld et al.*, 1999). At very low ionic strengths, \mathcal{D} dominates the right hand side of equation (4.18) and the Meissner equation converges to equation (4.20). Figure 4-1 shows the values of Γ° for several values of q and over a range of ionic strengths. Note that Γ° asymptotes to unity as I goes to zero for all values of q , and diverges based on q as I grows. The theory is applicable only up to some maximum ionic strength for which data is available (seldom greater than twenty mol kg⁻¹ for any given electrolyte).

Wexler and Seinfeld (1991); *Kim et al.* (1993a,b); *Resch* (1995), and others compare the results of this curve fitting method to reported data over a range of ionic strengths and found good agreement in almost all cases and comparable or better accuracy than other methods (*Kim et al.*, 1993a,b). Tests of MELAM show this as well. The examples of NaCl, HCl, H₂SO₄, and HNO₃ are presented as Figures 4-2, 4-3, 4-4, and 4-5 respectively. In each of the four figures, the estimated activity coefficients using published coefficients are drawn in blue, while those using coefficients fit to this particular data are shown in red. Some of the published data is fit using two successive one-parameter least square minimization fits: the first for q_r at a reference temperature and the second for q_T using the other temperature data. This procedure better fits data at that reference temperature, often 25° C, than away from it and less well overall than a joint estimation. The

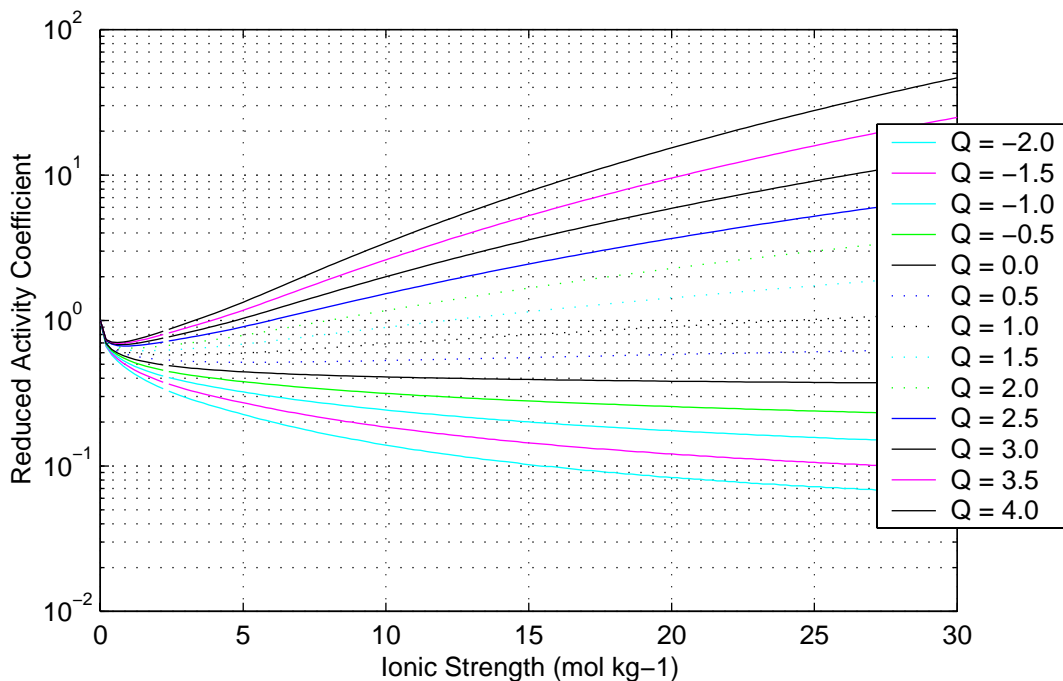


Figure 4-1: Variation of Γ° against I in the Kusik-Meissner formulation

Table 4.1: Kusik-Meissner Parameters for Several Equilibrium Reactions

Figure	Equilibrium Reaction		q_r	Published		Reference	This Work	
				q_T			q_r	q_T
4-2	NaCl	\rightleftharpoons Na + Cl	2.43	0.0035		A	2.290	0.00707
4-3	HCl	\rightleftharpoons H + Cl	6.69	-0.0027		B	6.117	-0.00346
4-4	H ₂ SO ₄	\rightleftharpoons 2 H ⁺ + SO ₄ ²⁻	0.7	-0.0027		C	0.1403	-0.2555
4-5	HNO ₃	\rightleftharpoons H ⁺ + NO ₃ ⁻	2.6	-0.0027		A	2.017	–

References: (A) *Resch* (1995); (B) *Meissner* (1980); (C) *Wexler and Seinfeld* (1991)

fits performed here use a two-parameter jointly estimated least square fit. Table 4.4.1 lists the parameters used in these four plots, both literature values and those fit specifically to these data. The two parameter sets are similar, but using different data sets, fitting techniques, and ranges of ionic strengths causes small differences.

The NaCl and HCl examples exemplify the reasonableness of the Kusik-Meissner approximation, and most electrolytes fall within the few percent error range as these do. There are several exceptions for which the approximation works less well and, taking these into account, *Kusik and Meissner* (1978) loosely estimates errors to fall within 20%.

The temperature dependence of most activities is a minor correction, but for species with low absolute values of q_r the correction may be substantial. Note from Table 4.4.1 that $|q_T|$ is less than

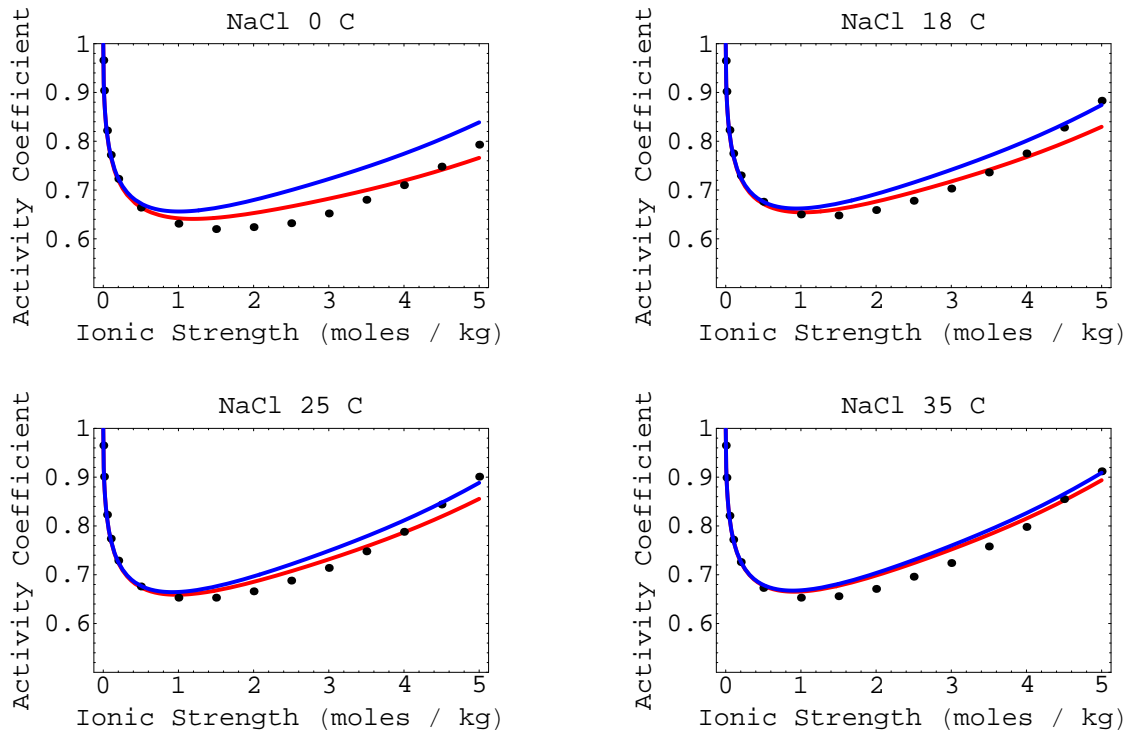


Figure 4-2: γ_{NaCl}° calculated as a function of I at several temperatures using the Kusik-Meissner formulation and compared to data compiled in *Lobo* (1989). The blue curve uses published values of q_r and q_T , while the red curve uses parameters fit specifically to this data for use in MELAM (see Table 4.4.1).

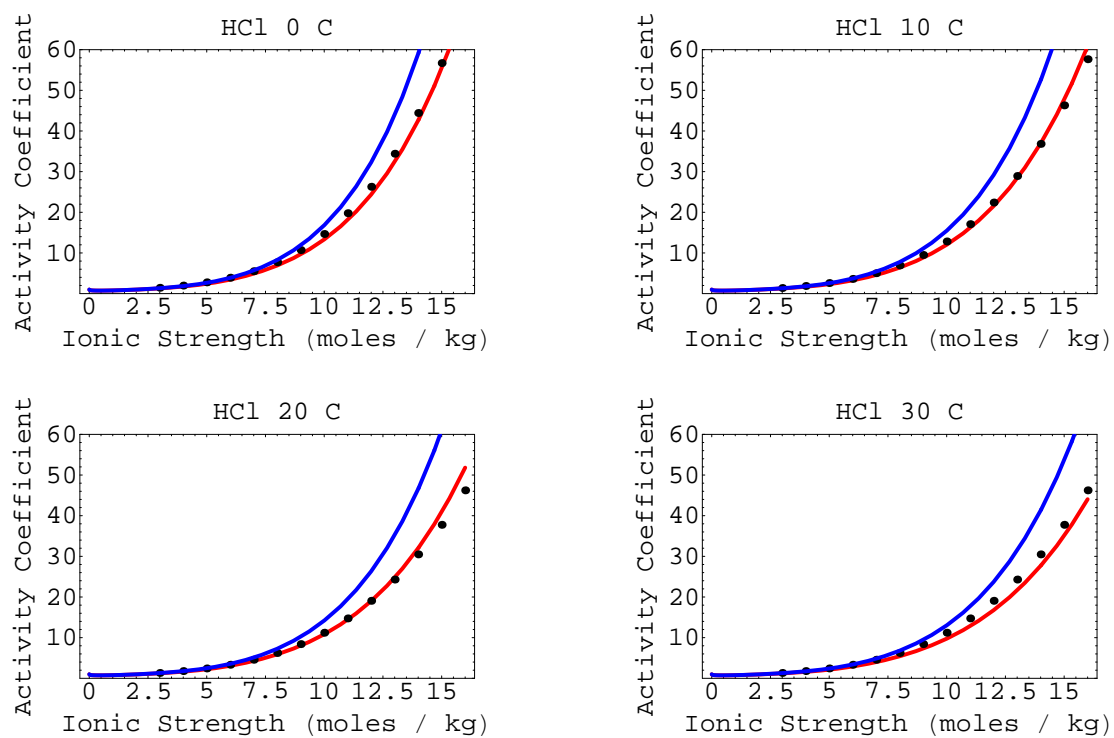


Figure 4-3: γ_{HCl}° calculated as a function of I at several temperatures using the Kusik-Meissner formulation and compared to data compiled in *Lobo* (1989). The blue curve uses published values of q_r and q_T , while the red curve uses parameters fit specifically to this data for use in MELAM (see Table 4.4.1).

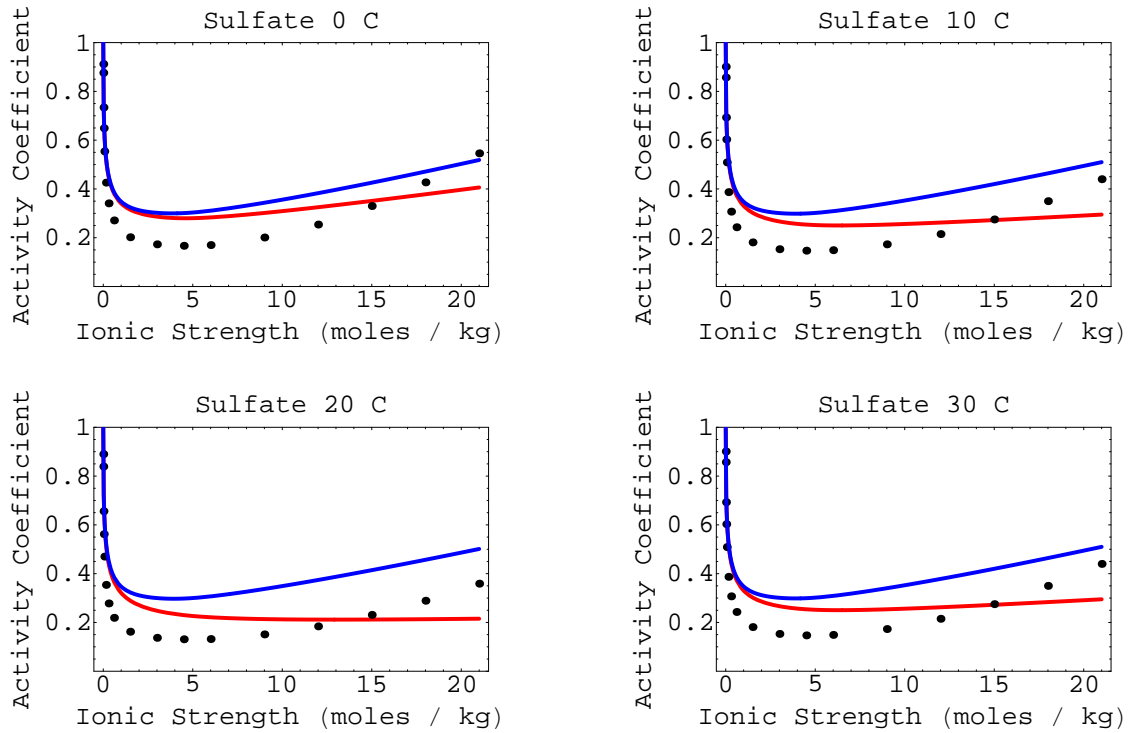


Figure 4-4: $\gamma_{\text{H}_2\text{SO}_4^\circ}$ calculated as a function of I at several temperatures using the Kusik-Meissner formulation and compared to data compiled in *Lobo* (1989). The blue curve uses published values of q_r and q_T , while the red curve uses parameters fit specifically to this data for use in MELAM (see Table 4.4.1).

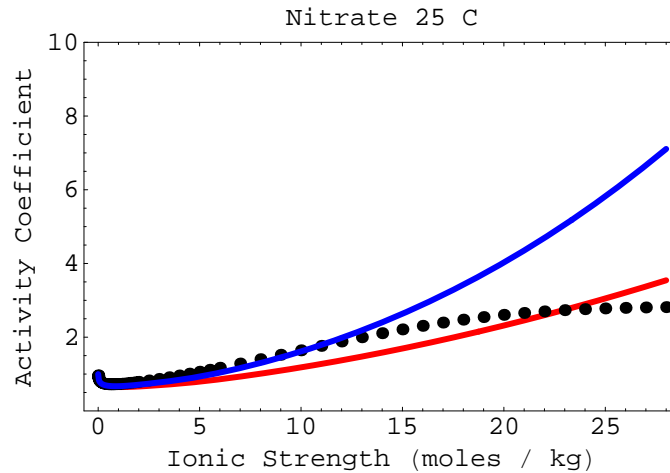


Figure 4-5: $\gamma_{\text{HNO}_3^\circ}$ calculated as a function of I at 25° C using the Kusik-Meissner formulation and compared to data compiled in *Lobo* (1989). The blue curve uses published values of q_r and q_T , while the red curve uses parameters fit specifically to this data for use in MELAM (see Table 4.4.1).

half of a percent of the value of q_r , and mostly ten times less than that, and also that in equation (4.19) q_T is scaled by the deviation of the actual temperature from the reference which at most is order fifty, meaning that the temperature dependence is at most 20% and usually much less than that. We do not calculate a value for q_T for HNO_3 because of a lack of data.

Figure 4-4 reveals that the estimated and realized activity coefficients for H_2SO_4 substantially deviate. The parameterization is unable to capture the steep fall-off with increasing and low ionic strengths and the misfit leads to the Kusik-Meissner parameters' strong dependence on the range of ionic strengths included when fitting to data. Much of the difficulty of this model is a result of the original Kusik-Meissner approach, presented here, which assumed that H_2SO_4 dissociates completely and directly to two protons and SO_4^{2-} . In reality H_2SO_4 dissociates into a multi-component, partially and fully dissociated system containing H^+ , HSO_4^- , and SO_4^{2-} , the relative amounts of which are determined by ionic strength and temperature at equilibrium. The assumption of total dissociation forces a fitting of the convolution of three ionic activities (those of protons, bisulfate, and sulfate) to a single mean activity coefficient, so the fact that the resulting parameterization poorly represents the data should not be a surprise. Alternative treatments of sulfate within the Kusik-Meissner model that can correct some of its deficiencies are discussed in Section 4.4.3.

Figure 4-5 shows the Kusik-Meissner method to activity coefficient data for nitric acid. The form of equation (4.18) is incorrect in this case, as the variation of nitric acid's activity with ionic strength is quite different in reality from what this equation allows. This implies that Kusik-Meissner's assumptions regarding which inter-ionic forces dominate in this case are incorrect. Regardless, the fit is adequate at low and moderate ionic strengths and will not lead to errors significantly greater than the 20% estimated in *Kusik and Meissner* (1978).

Zemaitis et al. (1986) and *Resch* (1995) identify that NaNO_3 is an outlier as well, for which the model works quite exactly up to an ionic strength of fourteen molal and deviates significantly above that value. Sodium nitrate, however, exists only in the solid and ionic phases in atmospheric aerosol and so is beyond the scope of this model (*Jacobson*, 1999).

4.4.2 Calculating Binary Activity Coefficients when Binary Data is Not Available

In certain cases data appropriate for calculating the mean activity of a particular electrolyte is not available in the literature. It is sometimes possible, in these situations, to construct a mean activity coefficient from the appropriate combination of other mean activity coefficients. For example, if we are interested in γ_{ij} for electrolyte with cation i and anion j , we may use mean activity coefficients

for other electrolytes to construct, algebraically, the mean activity coefficient of interest:

$$\gamma_{ij}^{\nu_{ij}} = \frac{\gamma_{Aj}^{\nu_{Aj}} \gamma_{iB}^{\nu_{iB}}}{\gamma_{AB}^{\nu_{AB}}} \quad (4.21)$$

Here, A is an arbitrary cation, B is an arbitrary anion, and there exists appropriate data for electrolytes Aj , iB , and AB to parameterize their values in the Kusik-Meissner framework.

By way of an example, thermodynamic models typically calculate the mean activity for direct dissociation of water into a proton and a hydroxyl ion (OH^-) calculated in this manner. For that case, we could construct a mean activity for this reaction using those for the dissociation of nitric acid, ammonium nitrate, and water and ammonia:

$$\gamma_{\text{H}_2\text{O}}^2 = \gamma_{\text{H}^+} \gamma_{\text{OH}^-} = \frac{(\gamma_{\text{H}^+} \gamma_{\text{NO}_3^-}) (\gamma_{\text{NH}_4^+} \gamma_{\text{OH}^-})}{\gamma_{\text{NH}_4^+} \gamma_{\text{OH}^-}} = \frac{\gamma_{\text{HNO}_3}^2 \gamma_{(\text{NH}_3+\text{H}_2\text{O})}^2}{\gamma_{\text{NH}_4\text{NO}_3}^2} \quad (4.22)$$

Where all of the activity coefficients are corrected for a mixed electrolytic solution, as discussed in Section 4.4.4.

MELAM uses two input files to deal with electrolyte thermodynamics: the first describes all of the equilibrium reactions for which measurements and parameters exist, and the second describes the reactions to be included in the simulation. MELAM automatically searches to find a set of electrolytes appropriate for equation (4.21) when reactions are included in the second input file but not the first.

4.4.3 Calculating Activity Coefficients and Equilibrium for Partially Dissociating Species: Sulfuric Acid

As previously mentioned in Section 4.4.1 and discussed in detail in *Zemaitis et al.* (1986), none of the standard thermodynamic modeling methodologies, including Kusik and Meissner's, adequately represents sulfuric acid's behavior in solution. In this respect, *Kusik and Meissner* (1978) enumerate best fit q_r parameters for some one hundred electrolytes but do not address sulfuric acid. Fortunately, the AIM III model of *Clegg et al.* (1998a,b), which is tailored to a specific system of inorganic electrolytes, is applicable for modeling the sulfuric acid system. However, AIM III is not generalizable to electrolyte mixtures beyond a pre-specified handful of ions without extensive and laborious additional laboratory measurements.

Sulfuric acid is difficult to model because of its high acidity and ability to dissociate partially into bisulfate as well as fully into sulfate. In temperature and concentration ranges of atmospheric

relevance almost no H_2SO_4 is present in solution, all of it having dissociated to some degree (*Clegg and Brimblecombe*, 1995); indeed some atmospheric aerosol models make use of this and disallow aqueous sulfuric acid altogether. The balance between HSO_4^- and SO_4^{2-} is extremely temperature and pH dependent, with bisulfate dominating in more acidic, warmer conditions (*Knopf et al.*, 2003). *Wexler and Seinfeld* (1991) note that under normal atmospheric conditions, sodium and ammonium neutralize sulfate and transform the system so it better conforms to thermodynamic models; as a result, they express hope that the discrepancies observed in the more acidic sulfuric acid systems are fleeting on large scales in the real atmosphere wherever Na^+ and NH_4^+ are abundant.

The Aerosol Inorganics Model (AIM) models of Clegg, Wexler, and Brimblecombe¹ are specific data-derived models that are not expandable beyond specific inorganic systems of up to several components. They often achieve accuracy that is within measurement error (*Clegg et al.*, 1992) except for certain electrolytes, particularly highly concentrated aqueous Na_2SO_4 (*Clegg et al.*, 1998a). *Pitzer and Simonson* (1986) present the theoretical underpinnings of the model, which is a pioneering mole fraction approach to electrolyte thermodynamics for mixed systems containing symmetrically charged ions. They represent the system's excess Gibbs free energy as a sum of a long-range Debye-Hückel term (similar to that discussed in Section 4.4.1) and short-range forces parameterized by a Margules-type virial expansion (to the three suffix level) in mole fraction about a state of infinite dilution. *Clegg et al.* (1992, 1994) then extend the theory beyond symmetric ions and add composition-specific terms into the Debye-Hückel term and additional parameters for interaction between the solvent and ions in concentrated solutions. The virial expansion fails at high concentrations, which we witness later this section when investigating the model's performance in predicting the degree of dissociation of bisulfate. *Clegg and Brimblecombe* (1995) apply Pitzer and Simonson's theoretical model to the concentrated sulfuric acid system. They force the calculations with parameters fit to osmotic coefficients, electromotive force measurements, heats of dilution, heat capacities, freezing points, partial molal enthalpies of water, and even to the degree of dissociation explicitly. The extent of data used stands in stark contrast to the Kusik-Meissner and related, less data hungry, models which are built up from a few parameter fit of the activity coefficients of binary systems. The sulfuric acid work of *Clegg and Brimblecombe* (1995) serves as a basis for expanding the AIM model to a broader, but still quite limited, set of electrolytes including ammonium, sodium, sulfate, nitrate, and chlorine over a range of temperatures. These various AIM I, II, and III models include different sets of the electrolytes and temperature ranges (*Clegg*

¹The AIM models are available online at <http://www.uea.ac.uk/e770/aim.html>

et al., 1998a,b; *Wexler and Clegg*, 2002). Their high accuracy makes the AIM models appropriate for guiding experimental studies (as used in *Knopf et al.*, 2003) and for comparison to other, less accurate models including this one.

In an equilibrium reaction framework, dissociation of sulfuric acid is best conceived as a two step process with sulfuric acid losing one proton in each step:

Sulfuric Acid Dissociation: Model 1				
(a)	H_2SO_4	\Leftrightarrow	H^+	$+$ HSO_4^-
(b)	HSO_4^-	\Leftrightarrow	H^+	$+$ SO_4^{2-}

The thermodynamic properties of this system, including everything necessary to calculate a temperature dependent equilibrium constant for reaction 1(b), were estimated by *Pitzer et al.* (1977) and have been refined several times, most recently in *Knopf et al.* (2003). In this framework, the equilibrium coefficient for the dissociation of bisulfate into sulfate and a hydrogen atom (reaction 1(b) in this model) following equation (4.4), is:

$$K_{1(b)} = \left(\frac{\mathbf{m}_{\text{H}^+} \mathbf{m}_{\text{SO}_4^{2-}}}{\mathbf{m}_{\text{HSO}_4^-}} \right) \left(\frac{\gamma_{\text{H}^+} \gamma_{\text{SO}_4^{2-}}}{\gamma_{\text{HSO}_4^-}} \right) \quad (4.23)$$

Following *San Martini* (2004) and others, we manipulate this expression to find a ratio of bisulfate to sulfate in the solution:

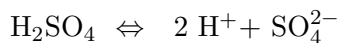
$$\frac{\mathbf{m}_{\text{HSO}_4^-}}{\mathbf{m}_{\text{SO}_4^{2-}}} = \left(\frac{\gamma_{\text{H}^+} \gamma_{\text{SO}_4^{2-}}}{\gamma_{\text{HSO}_4^-}} \right) \frac{\mathbf{m}_{\text{H}^+}}{K_{1(b)}} \quad (4.24)$$

Here, the thermodynamic parameters of the reaction are such that $K_{1(b)}$ increases with temperature. Note the direct dependence of the bisulfate to sulfate ratio on the molality of H^+ , which of course is related to the solution's pH and, in turn, to the relative humidity of the environment, and the concentration of sulfuric acid and of other proton-donor electrolytes. Also note that neither the activity coefficient pair in the numerator of equation (4.24) nor the lone activity coefficient of bisulfate in the denominator take the form of a mean activity as neither have neutral charge and $\gamma_{\text{HSO}_4^-}$ is completely unpaired. All this is to say that Model 1 treats bisulfate as an electrolyte while the Kusik-Meissner theory developed in Section 4.4.1 cannot handle charged electrolytes. As a result, Model 1, despite it being physically realistic, is not useful in the Kusik-Meissner framework and another model must be employed.

As a first attempt at modeling the system in the Kusik-Meissner framework, *Wexler and Seinfeld*

(1991) assumed that sulfuric acid dissociates according to Model 2, in which the equilibrium between sulfuric acid and completely dissociated sulfate is a one step process with a single associated mean activity coefficient:

Sulfuric Acid Dissociation: Model 2
--



This model gained considerable popularity within the Kusik-Meissner framework due to the framework's limitations with respect to charged electrolytes and therefore partial dissociation. The model is obviously lacking, however, in that bisulfate is completely absent and essentially all of the sulfuric acid dissociates all the way to sulfate, making the system too acidic in most cases. Wexler and Seinfeld use the data of *Staples* (1981) to fit the measured activities of the sulfuric acid system to this parameterization, and suggest a value of $q_r = 0.7$. As is evident in Figure 4-4, this formulation for sulfate represents H_2SO_4 behavior in solution extremely poorly. The failure results at least in part because any measured value of $\Gamma_{\text{H}_2\text{SO}_4}$, assuming Model 2, is itself a convolution of activities associated with the H_2SO_4 to HSO_4^- , HSO_4^- to SO_4^{2-} , and possibly direct H_2SO_4 to SO_4^{2-} transitions and should vary over the range of concentrations and ionic strengths as the balance between sulfuric acid, bisulfate, and sulfate shifts. *San Martini* (2004) notes that they use only data for ionic strengths between 1.5 and 16 moles/kg and recalculates $q_r = 0.82$ employing all available data, which span from $I = 0$ to 28 moles/kg. This model, though widely used for several years, is clearly lacking and more recent work attempts to bend the Kusik-Meissner framework to include bisulfate explicitly.

Kim et al. (1993a,b) propose a way to determine the necessary activity coefficient ratio in Model 1. Working from equation (4.24), they cast the activity coefficient ratio in terms of mean activities:

$$\frac{\gamma_{\text{H}^+} \gamma_{\text{SO}_4^{2-}}}{\gamma_{\text{HSO}_4^-}} = \frac{\gamma_{\text{H}^+} \gamma_{\text{H}^+} \gamma_{\text{SO}_4^{2-}}}{\gamma_{\text{H}^+} \gamma_{\text{HSO}_4^-}} = \frac{\gamma_{\text{H}_2\text{SO}_4}^3}{\gamma_{\text{H}-\text{HSO}_4}^2} \quad (4.25)$$

In which the “place-holder” species $\text{H} - \text{HSO}_4$, describing the activity of the sulfuric acid to bisulfate transition, is introduced. *Kim et al.* (1993a) use the data of *Stelson et al.* (1984) to calculate Kusik-Meissner parameters for each of the two steps and find $q_{r,(\text{H}_2\text{SO}_4)} = -0.1$, superseding its value of 0.7 when bisulfate is not explicitly included, and $q_{r,(\text{H}-\text{HSO}_4)} = 8.0$.

There are several complications to *Kim et al.* (1993a)'s approach that limit its effectiveness especially when applied directly to Model 1. First is the potential unsuitability of the empirically derived Kusik-Meissner equation (4.18) in partially dissociating reaction systems. Since there is not a strong theoretical basis to the tendency of activity coefficients to follow the curves of Figure

4-1, we cannot be sure a priori whether the activity ratio $(\gamma_{\text{H}^+} \gamma_{\text{SO}_4^{2-}} / \gamma_{\text{HSO}_4^-})$ traces that curve directly, whether it traces the ratio of powers of two mean activities as per equation (4.25), or if the Kusik-Meissner theory is ultimately useless in this case. The mixing rules detailed in Section 4.4.4 are used to correct activity coefficients in multi-component systems, including this mixture of bisulfate and sulfate, but they are similarly ill-equipped to handle charged electrolytes. So, regardless of equation (4.25)'s ability to describe the bisulfate-to-sulfate ratio, Model 1 cannot be used to determine the values of the necessary mean activities corrected for the mixed system. Ultimately, including bisulfate in the Kusik-Meissner formulation requires that we accept the applicability of the approximation made in equation (4.25), and that we use a hybrid of Model 1 and another model that allows formation of both bisulfate and sulfate but does not require charged electrolytes.

An alternative third model that conforms to the limitations of the Kusik-Meissner theory presumes that sulfuric acid dissociates directly to either bisulfate or sulfate and that the ions do not interchange directly, which is a physically unintuitive process:

Sulfuric Acid Dissociation: Model 3				
(a)	H_2SO_4	\Leftrightarrow	$2 \text{H}^+ + \text{SO}_4^{2-}$	
(b)	H_2SO_4 (or $\text{H} - \text{HSO}_4$)	\Leftrightarrow	$\text{H}^+ + \text{HSO}_4^-$	

In reality, dissociation almost certainly follows a two-step process in which the hydrogen atoms leave each in its turn, as in Model 1. It is possible that the two steps are not independent, such that a direct transition to sulfate such as reaction 3(a) should be included in Model 1, but this is not obvious and the theory for usefully including both the prospective two-step and one-step sulfate pathways is unavailable. It is unlikely that Model 3 is a reasonable representation of reality. It does, however, satisfy the constraints of the Kusik-Meissner model.

Since almost no sulfuric acid remains undissociated in the aqueous phase, the ratio of concentrations of bisulfate to sulfate is the critical prediction of a thermodynamic model of the sulfuric acid system. We begin with Model 3 and work towards an approximation of this ratio for use in MELAM. First, we use equation (4.9) to write equations for Model 3's two equilibria:

$$K_{3(a)} = \frac{\gamma_{\text{H}_2\text{SO}_4}^3 \mathbf{m}_{\text{H}^+}^2 \mathbf{m}_{\text{SO}_4^{2-}}}{\mathbf{m}_{\text{H}_2\text{SO}_4}} \quad ; \quad K_{3(b)} = \frac{\gamma_{\text{H}-\text{HSO}_4}^2 \mathbf{m}_{\text{H}^+} \mathbf{m}_{\text{HSO}_4^-}}{\mathbf{m}_{\text{H}_2\text{SO}_4}} \quad (4.26)$$

Combining these two expressions, we may develop an analog to equation (4.24) describing the ratio of bisulfate to sulfate for Model 3:

$$\frac{\mathbf{m}_{\text{HSO}_4^-}}{\mathbf{m}_{\text{SO}_4^{2-}}} = \left(\frac{\gamma_{\text{H}^+}' \gamma_{\text{SO}_4^{2-}}'}{\gamma_{\text{HSO}_4^-}'} \right) \frac{K_{3(b)}}{K_{3(a)}} \mathbf{m}_{\text{H}^+} \quad (4.27)$$

Here, the primes on the activity coefficients are to remind us that they are not the true values, but rather those calculated using mean activity coefficients and Model 3.

Comparing what we have done in this approximate scheme to equation (4.24), which we must regard as the the true ratio, we note two substitutions: (a) mean activity coefficients calculated assuming a mixed system that follows Model 3 stand in for those calculated with Model 1; and (b) $K_{3(a)}/K_{3(b)}$ replaces $K_{1(b)}$. Model 3 is also impractical to implement using the equilibration routine discussed in Section 4.3.2 since the sole pathway from sulfate to bisulfate and back again is through aqueous sulfuric acid which exists at infinitesimal concentrations, if at all. The number of iterations required to equilibrate the two ionic species would be prohibitively immense. Obviously, this objection does not apply generally to all partially dissociated species.

The ratio of two equilibrium coefficients can exactly equal a single equilibrium coefficient given consistent thermodynamic parameters because of the exponential formulation of equation (4.6). As a result, the equilibrium calculated by Model 3 is equivalent to an equilibrium of the reactions in Model 1 using activity coefficients calculated by Model 3. In that case, the ratio of the ions becomes:

$$\frac{\mathbf{m}_{\text{HSO}_4^-}}{\mathbf{m}_{\text{SO}_4^{2-}}} = \left(\frac{\gamma_{\text{H}^+}' \gamma_{\text{SO}_4^{2-}}'}{\gamma_{\text{HSO}_4^-}'} \right) \frac{\mathbf{m}_{\text{H}^+}}{K_{1(b)}} \quad (4.28)$$

The formulation used by MELAM allows a direct pathway between ionic species but uses activities calculated as though the pathway between them were through the fully associated electrolyte as in Model 3. To facilitate the identification of these pathways and automation of the activity calculations, the user must write the reactions in a partially dissociating system with respect to the most dissociated form such that, in this case (denoted Model 4), each dissociation is written with respect to sulfate.

Sulfuric Acid Dissociation: Model 4				
(a)	H_2SO_4	\Leftrightarrow	$2 \text{H}^+ + \text{SO}_4^{2-}$	
(b)	HSO_4^-	\Leftrightarrow	$\text{H}^+ + \text{SO}_4^{2-}$	

MELAM uses the iterative solution procedure discussed in Section 4.3.2 to equilibrate this model with mean activities calculated according to Model 3, which is roughly equivalent to the procedure presented in *Kim et al.* (1993a) and used in MIT-IAM (*San Martini*, 2004), ISORROPIA (*Nenes et al.*, 1998, 1999), and elsewhere.

As alluded to above, thermodynamic models that include sulfate and bisulfate strive to correctly predict the ratio of sulfate to bisulfate; that ratio is thus the appropriate metric to compare models

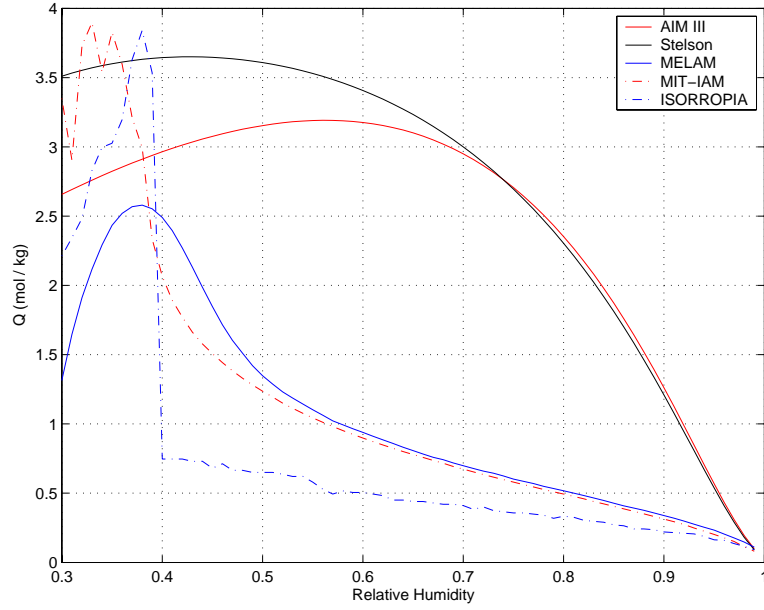


Figure 4-6: Comparison of the dissociation quotients, Q , of several models to a parameterization of data compiled by *Stelson et al.* (1984) (adapted from *San Martini*, 2004)

to each other and to validate against data. *Stelson et al.* (1984) aggregate data from five studies to parameterize a dissociation quotient, Q :

$$Q = \frac{\mathbf{m}_{\text{H}^+} \mathbf{m}_{\text{SO}_4^{2-}}}{\mathbf{m}_{\text{HSO}_4^-}} \approx -4.5740 + 4.0071 \, I^{1/2} - 0.99893 \, I + 0.13250 \, I^{3/2} - 0.010675 \, I^2 \quad (4.29)$$

Figure 4-6 shows a comparison between equation (4.29)’s polynomial fit to data and the results of several models over a range of relative humidities. To include the expression (4.29), in which ionic strength is the independent variable, we used the results of AIM III to relate ionic strength and relative humidity (*San Martini*, 2004). MIT-IAM is the M.I.T. Inorganic Aerosol Model developed first by *Resch* (1995) using sulfate Model 2 and extended by *San Martini* (2004) to include bisulfate. ISORROPIA is an extremely efficient reaction based model popular for large scale models, developed by *Nenes et al.* (1998, 1999). Both MIT-IAM and ISORROPIA use the Kusik-Meissner activity coefficient method and sulfate formulations similar to the one used here. AIM III was discussed above, and uses a sophisticated empirically driven activity coefficient model developed specifically for the sulfate system. AIM III respectfully reproduces the form of the Stelson $Q(\mathcal{RH})$ curve, including great accuracy at moderate and high relative humidities. The reaction based models, including MELAM, all poorly estimate Q , producing too much bisulfate relative to sulfate. Both AIM III and ISORROPIA are unstable below 40% relative humidity, which is related to numerical issues and their schemes governing water content.

Kim et al. (1993a), who proposed the bisulfate scheme employed here, comparatively considered the efficacy of the Pitzer, Bromley, polynomial regression, and Kusik-Meissner methods in modeling mixed atmospheric inorganic aerosol (for a description of these methods, see *Zemaitis et al.*, 1986). They conclude that, despite the obvious limitations in calculating the bisulfate-to-sulfate ratio, the Kusik-Meissner method represents the sulfuric acid system best of the available options because of its computation efficiency and exandability. For models such as MELAM, meant to represent wide arrays of electrolytes, the detailed corrections and empiricism of AIM III are impossible and the Kusik-Meissner approach is, indeed, the most accurate and efficient. This thesis follows *Kim et al.* (1993a)’s recommendation and implements the hybrid of Models 3 and 4, as discussed in this section. Any study requiring careful thermodynamic calculations for laboratory or high accuracy theoretical studies to do with sulfate should seriously consider whether this method is appropriate. Kusik-Meissner models, especially ISORROPIA which is widely used in global modeling studies, are sometimes used inappropriately to guide laboratory studies, create road map phase diagrams, and the like; AIM III is clearly the only appropriate model for such uses.

4.4.4 Calculating Activity Coefficients in Mixtures

In a mixed solution containing more than one electrolyte, inter-ionic interactions change ionic activity coefficients from the values in binary solutions at the same ionic strength. Observations reveal that reduced activity coefficients in a two electrolyte system lie between those of the pure solutions of the constituent electrolytes for all ionic strengths; a similar statement may be made about higher order mixtures (*Kusik and Meissner*, 1978; *Meissner*, 1980). Most computational thermodynamics models use mixing rules to extend the single-salt thermodynamic models to solutions of multiple electrolytes. Mixing rules first calculate ionic activities for equivalent single-salt solutions at the same ionic strength, based on equation (4.18) or a similar approximation, and then set the multi-component ionic activities to the average of these binary reduced activity coefficients weighted by the concentrations of the constituent cations and anions. The alternative to extending single-salt theories using mixing rules involves direct calculation of mixed solution properties, including direct consideration of all two and three body ionic interactions (the AIM model, reviewed in Section 4.4.3, takes this approach); this explicit approach is difficult to extend to complex mixed aerosol because of the number of measurements required. *Zemaitis et al.* (1986) and *Loehe and Donohue* (1997) review the mixing rules available in the literature; that of *Kusik and Meissner* (1978) is used here for activity coefficients and that of *Patwardhan and Kumar* (1993) is used for other thermodynamic properties (discussed in Section 4.5).

In this model, we employ *Kusik and Meissner* (1978)'s and *Meissner* (1980)'s approach to calculate mixed activity coefficients in multi-component strong electrolytic solutions. They define the mixed activity of a single ion using Brønsted's proposal, which posits that activity coefficients are influenced primarily by interactions of ions with opposing charges such that interactions with those with like charges may be ignored (*Zemaitis et al.*, 1986). For cation I and anion J in a solution where the cations are indexed by i and the anions by j , they estimate:

$$\log_{10} \gamma_I = \sum_j F_j \frac{(z_I + z_j)^2}{2 |z_I z_j|} \log_{10} \gamma_{Ij}^\circ \quad ; \quad \log_{10} \gamma_J = \sum_i F_i \frac{(z_i + z_J)^2}{2 |z_i z_J|} \log_{10} \gamma_{iJ}^\circ \quad (4.30)$$

Here, the logarithms of the mean activity coefficients inside the summations are those calculated using equation (4.18) at the ionic strength of the full solution, the fraction containing ionic charges is a particular weighting factor used in Kusik -Meissner's formulation, and F_x for some ion x is its ionic strength fraction:

$$F_x = \frac{\mathbf{m}_x z_x^2}{2 I} \quad (4.31)$$

Other theories assign other weighting factors. We see that the activity coefficients in mixed solutions are equal to a weighted average of those in a pure solution at the same ionic strength, where the weighting is proportional to the portion of the total ionic strength that each ion pairing comprises.

Combining equation (4.16), equation (4.17), the relationship between stoichiometric coefficients and charge, and equation (4.30), we may write the mean activity coefficient of electrolyte IJ in terms of the activity coefficients of the individual ions:

$$\log_{10} \Gamma_{IJ} \equiv \frac{z_I \sum_j F_j \frac{(z_I + z_j)^2}{2 z_I z_j} \log_{10} \Gamma_{Ij}^\circ + z_J \sum_i F_i \frac{(z_i + z_J)^2}{2 z_i z_J} \log_{10} \Gamma_{iJ}^\circ}{z_I + z_J} \quad (4.32)$$

Resch (1995) compared activity coefficients calculated using this rule for a number of simple mixed systems to those derived from the solubility data of *Linke and Atherton* (1965). Errors are in general less than 5%, although occasionally larger.

Equation (4.32), the Kusik-Meissner mixing rule, must be altered slightly to fit MELAM. Notice that the summations in equation (4.30) are over ion pairings, not the set of reactions by which we define ionic interaction. This has two implications. First, a user must define a reaction between some electrolyte and each pair of oppositely charged ions to account for every term in this summation. If any are neglected, which we would assume excludes the relevant term from the summation,

then a sum over the ionic strength fractions of the included terms would not amount to unity, biasing downward the estimation of the mixed activity coefficient. We correct this problem by using a summation of the contributions to l of all allowed pairings instead of the full l in the denominator of equation (4.31), which removes this downward bias. If a reaction is excluded, then this system will still neglect the ionic interaction described by that reaction, but will not implicitly assume that the activity of that interaction is zero. In some cases, left to the user to identify, these may be of marginal importance. The second implication is that the partial dissociation Model 3 given in Section 4.4.3 conforms to equation (4.30)'s summation system, while Model 4 would redundantly count the sulfate ion. Model 3 is not entirely satisfactory, as we understand the bisulfate ion to interact with protons according to two reactions as expressed in Model 1; the inability of this mixing rule to account for that dual interaction is a limitation of the Kusik-Meissner model.

Another limitation of the Kusik-Meissner theory in mixed solutions is that crossed electrolytes, which contain more than two ions, are not appropriately accounted for by either equation (4.18) or equation (4.32). *Wexler and Seinfeld* (1991) posit, without proof or definition, activity definitions of mean activity coefficients for the three crossed-electrolytes sodium bisulfate (NaHSO_4), ammonium bisulfate ($(\text{NH}_4)\text{HSO}_4$), and letovicite ($(\text{NH}_4)_3\text{H}(\text{SO}_4)_2$), each of which are solid-phase electrolytes:

$$\gamma_{\text{NaHSO}_4} = \sqrt{\gamma_{\text{Na}_2\text{SO}_4} \gamma_{\text{H}_2\text{SO}_4}} \quad (4.33)$$

$$\gamma_{(\text{NH}_4)\text{HSO}_4} = \sqrt{\gamma_{(\text{NH}_4)_2\text{SO}_4} \gamma_{\text{H}_2\text{SO}_4}} \quad (4.34)$$

$$\gamma_{(\text{NH}_4)_3\text{H}(\text{SO}_4)_2} = \sqrt[4]{\gamma_{(\text{NH}_4)_2\text{SO}_4}^3 \gamma_{\text{H}_2\text{SO}_4}} \quad (4.35)$$

San Martini (2004) shows mathematically that equation (4.33) is only valid if partial dissociation is disallowed for each of the three electrolytes involved (Na_2SO_4 , H_2SO_4 , and NaHSO_4). We should note that the early work of *Wexler and Seinfeld* (1991) was innovative in that it included sulfuric acid in the Kusik-Meissner model moderately successfully for the first time, and the presumption of full dissociation is consistent with their proposed sulfate Model 2 discussed in Section 4.4.3. *Kim et al.* (1993a), the originators of equation (4.25) and the bisulfate theory used in this model, extend equation (4.33) by calculating a composite mean activity for the partial dissociation of sodium bisulfate into a sodium atom and bisulfate:

$$\gamma_{\text{NaHSO}_4}^2 = \gamma_{\text{Na}^+} \gamma_{\text{HSO}_4^-} = \frac{\gamma_{\text{NaA}} \gamma_{\text{H-HSO}_4}}{\gamma_{\text{HA}}} \quad (4.36)$$

In which A^- is any appropriate anionic species. This type of formulation allows a multi-reaction

system in which partial dissociation of sulfuric acid and the crossed electrolytes is explicitly included. The activity coefficient mixing rule equation (4.32) does not appropriately account for these cases, however, as its summations implicitly assume the inability of crossed electrolytes to form. Our relaxing of equation (4.32) to loop over the set of all defined reactions instead of all pairs of electrolytes allows inclusion of reactions that form crossed electrolytes but there is no basis to believe the mixing rule should be appropriate in those cases. *San Martini* (2004) advances this approach by calculating the appropriate mixed values of the sodium bisulfate in a system containing the electrolytes sulfuric acid, sodium sulfate, and sodium bisulfate (but not a general form mixing rule). He finds the mixed definition of the activity coefficient of sodium bisulfate is circular and uses equation (4.33) internally to calculate a more refined estimate. These limitations of the Kusik-Meissner theory are important obstacles in effective implementation of aerosol thermodynamic models and a more sophisticated mixing rule that could include bisulfate and crossed electrolyte formulations would be a great asset. However, as MELAM avoids dealing explicitly with solids we are able to avoid the brunt of this problem as most crossed electrolytes are solid phase species.

4.5 Mixing Rules for Other Thermodynamic Properties

Kusik-Meissner’s mixing rule, presented in Section 4.4.4, applies only to activity coefficients. *Patwardhan and Kumar* (1986a,b, 1993) developed a set of simple rules that adequately reproduces experimental vapor pressures, solution densities, heat capacities, and other properties of the mixed solution using only the properties of the corresponding single electrolytic systems. We use their rules in conjunction with the Kusik-Meissner theory discussed in this chapter to guide mixing for parameterized thermodynamic properties not solely dependent on the mixed activity coefficients (specifically for water activity, density, and surface tension).

Patwardhan and Kumar (1993) follow a compartmentalization argument to derive a parameter, y_{ij} , that represents the fractional contribution of a single electrolyte toward the total ionic strength:

$$y_{ij} = F_i Z_j + F_j Z_i \quad (4.37)$$

Where the ionic strength fraction (F_x) is defined in equation (4.31) and charge fraction (Z_x) for cation i or anion j is defined to be:

$$Z_x = \frac{\mathbf{m}_x z_x}{\sum_k \mathbf{m}_k z_k} \quad (4.38)$$

The summation over dummy index k is taken over all cations, if x is positively charged, or anions, if x is negatively charged.. We use the factor y_{ij} to weight averages of single solution thermodynamic properties in slightly different formulations for the various properties according to *Patwardhan and Kumar* (1993). We will present the appropriate mixing equation when discussing the calculation of each of the properties.

4.6 Surface Tension

At equilibrium, the partial pressure of water vapor above a flat surface of water is equal to the pressure just below the water's surface, p_{water} , and because the system is in equilibrium that partial pressure of water is the saturation vapor pressure, $e_{s,water}$. A water droplet can support a gradient between the internal pressure and near-surface vapor pressure due to the significant surface tension that results from hydrogen bonding of water molecules along its curved surface, such that:

$$p_{water} - e_{s,water} = \frac{2 \sigma_{w/a}}{r} \quad (4.39)$$

In which we have replaced the surface tension between water and its vapor with the surface tension between water and air, $\sigma_{w/a}$, thereby introducing only a very slight error (*Pruppacher and Klett*, 1997). Here, r is the particle radius. Note from the form of equation (4.39) that a flat surface of water, for which the radius is effectively infinite, cannot support a pressure gradient.

In a non-equilibrium, flux-based model, the condensation of water vapor and dissolution of other species depend on how far the system is from the equilibrium condition (4.39). Both equilibrium particle content and non-equilibrium condensational and dissolutional fluxes depend critically on the accurate estimation of the particle's surface tension.

Surface tension depends on temperature and particle composition. In general, dissolved organic species lower the surface tension of solutions (*Li et al.*, 1999) while dissolved electrolytes tend to raise surface tensions (*Nath*, 1999). This section presents appropriate theory and describes the parameterizations used in this model.

4.6.1 Surface Tension of Flat Surfaces of Pure Water

The surface tension between pure water and air is accurately estimated by a sixth order polynomial fit to temperature (*Pruppacher and Klett, 1997*):

$$\sigma_{w/a} = \sum_{i=0}^6 a_i T^i \quad (4.40)$$

Where a_i are empirical regression coefficients that differ depending on whether or not the droplet is super-cooled and are valid from near the boiling point to the Schaefer point, the temperature at which super-cooled water homogeneously freezes. At 0° C the surface tension of water is 75.93 erg cm⁻².

4.6.2 Surface Tension of Flat Surfaces of Electrolytic Solutions

The presence of dissolved salts may substantially alter the surface tension of a water droplet by as much as 25% in some cases. As surface tension is the result of inter-molecular attractions at the surface of the droplet, the presence of ions can interfere with the strength of the bonding between water molecules. Surface tension in a solution depends directly on the concentration of the solute at the droplet surface. The bulk phase concentration is an imperfect proxy for the surface concentration. Specifically solutes that tend to lower surface tension are drawn to the surface in greater concentration than found in the bulk phase, and are consequently known as surface active, and vice versa (*Pruppacher and Klett, 1997*).

The standard parameterizations of surface tension, which we will not use but will serve as a reference point, linearly relate surface tension to some measure of bulk solute concentration for binary solutions of water and electrolyte IJ :

$$\sigma_{s/a}^{\circ} = \sigma_{w/a} + \beta_{IJ}^{\circ} I \quad (4.41)$$

Here, β_{IJ}° takes a different experimentally determined value for each electrolyte. *Hänel (1970)* suggested equation (4.41), which linearly relates surface tension to the ionic strength of the solution and assumes that the effect of the electrolytes is temperature independent and that $\sigma_{s/a}^{\circ}$ depends on temperature according to equation (4.40). *Abramzon and Gaukhberg (1993a)* similarly propose regressing $\sigma_{s/a}^{\circ}$ against the anion concentration.

For a multi-component solution, a composite β may be used to estimate the surface tension of

the multi-component solution:

$$\sigma_{s/a} = \sigma_{w/a} + \beta \quad (4.42)$$

The coefficient β may be calculated as a composite of the binary solution β_{IJ}° values using some thermodynamic mixing rule, such as that of Patwardhan and Kumar as outlined in Section 4.5:

$$\beta = \sum_{ij} y_{ij} \beta_{ij}^\circ \quad (4.43)$$

Although many thermodynamics models use this approximation, it is limited because it uses the bulk phase concentrations to estimate the surface properties of the droplets. This relationship does not hold in all cases and over all ionic strengths and a series of papers have investigated other parameterizations that distinguish the interface from the gas and liquid phases. The next section details *Li and Lu* (2001)’s interfacial method which is used here.

4.6.3 Surface Tensions Calculated Using the Gibbs Dividing Surface for Electrolytic Solutions

Adamson and Gast (1997), *Nath* (1999), *Li and Lu* (2001), and *Ming and Russell* (2002), among others, have proposed surface tension regressions that acknowledge that the surfactant layer at the interface is distinct from the bulk phase. Such parameterizations are preferable to regressions against bulk concentrations, as reviewed in Section 4.6.2, because they incorporate a more physically realistic treatment of surface physics.

Li and Lu (2001) use a Gibbs dividing surface, the Langmuir adsorption equation (*Langmuir*, 1918b), and Pitzer’s expressions for electrolytic activities to formulate a two-parameter expression for the surface tension of a single-component electrolytic solution. They also present an appropriate mixing rule for multi-component systems and an expression for temperature dependence. Their approximations fit available data better than does the bulk phase regression, given by equation (4.41). We adopt their formulation but use the Kusik-Meissner approximation for electrolyte activities, as detailed in Section 4.4.1, in lieu of Pitzer’s.

This system begins with the recognition that neither the gas nor vapor bulk phases are good representations of the surface layer. Following Gibbs’ work from the 1870’s (thoughtfully restated in *Guggenheim and Adam*, 1933), we assume there are two bulk phase spatial regimes in which chemical potentials, temperature, and pressure of each species are each constant. We divide these

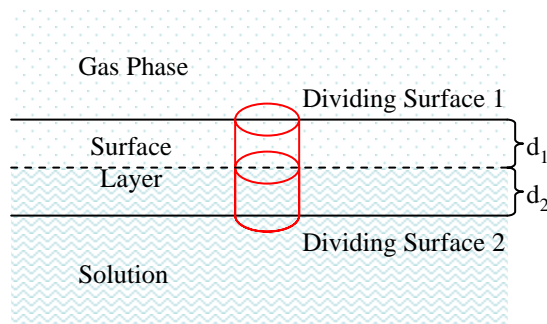


Figure 4-7: Schematic of the Gibbs dividing surface approach to surface tension calculation

two bulk regions with an arbitrarily thick surface layer which we delimit using two arbitrarily placed planes on either side of the complex physical boundary region within which these intensive thermodynamic properties may have strong gradients. This is presented in Figure 4-7, in which the gas and solution phases are homogeneous above dividing surface 1 and below dividing surface 2, respectively.

We then define the surface excess, ζ_i , of species i to be the difference between the amount of i we would expect to find in a column between the two planes if the bulk equilibrium of each phase persisted up to some infinitely abrupt physical boundary and the amount of i observed to be in that column. Restated, it is the difference between the amount of species i found in the red column were it filled with the bulk solution up to height d_2 and the bulk gas from d_2 to d_2+d_1 , and the actual amount found in the red column (*Li and Lu, 2001*). The surface excess ζ_i may be positive or negative and is a measurable quantity which approximates the surface activity of a species. It may also be used in parameterizations of surface tension, but is neglected in the bulk formulation (4.6.2).

Adamson and Gast (1997) define the surface tension in terms of the surface excess and liquid phase chemical potentials in the interface region (μ^s) of water (w) and electrolytic species (ij):

$$-d\sigma_{s/a} = \zeta_w d\mu_w^s + \sum_{ij} \zeta_{ij} d\mu_{ij}^s \quad (4.44)$$

Li and Lu (2001) rewrite the chemical potentials in terms of activities, apply the Gibbs dividing surface (in which they choose ζ_w to be zero), and apply the *Langmuir (1918b)* gas-solid adsorption expression at equilibrium to replace the surface excess with the surface excess at saturation. They also employ a simple mixing rule, based on a compartmentalization logic similar to *Patwardhan and Kumar's*, that links activities to the fraction of the surface covered by each electrolyte. Integrating,

they arrive at an expression of the surface tension at the air-solution interface for a multi-component electrolytic system:

$$\sigma_{s/a} = \sigma_{w/a} + R T \sum_{ij} \zeta_{ij}^{wo} \ln \left(1 - \frac{K_{ij}^a a_{ij}}{1 + \sum_{kl} K_{kl}^a a_{kl}} \right) \quad (4.45)$$

In which K_{ij}^a is the equilibrium adsorption coefficient for electrolyte ij (dimensionless), ζ_{ij}^{wo} is its saturated surface excess (mole m^{-2}), and kl is a dummy electrolyte index (paralleling ij in the earlier summation). We calculate activities from the Kusik-Meissner approximation, whereas *Li and Lu* (2001) use *Pitzer* (1973) formulation. Both ζ_{ij}^{wo} and K_{ij}^a are determined experimentally, one electrolyte at a time, and do not depend on the mixing state of the solution. *Li and Lu* (2001) calculate these two quantities for 45 electrolytes from the data of *Abramzon and Gaukhberg* (1993a,b,c,d,e,f). They find an absolute percentage deviation of 0.47% at a single temperature and 0.91% when extrapolating over a range of temperatures.

4.6.4 Influence of Soluble and Slightly Soluble Organic Species

As far as the issue is understood, the dual roles of soluble organics are to lower particle surface tension and thus increase the likelihood of activation (*Facchini et al.*, 1999, 2001), and to form surfactant film layers that suppress condensation (*Feingold and Chuang*, 2002a,b). The partitioning and solubility of organics is clearly very important, but the deficit of needed measurements of organic solubilities, composition of organics in aerosol, and the dependence of organic solubility on inorganic solute concentration is imposing (*Abdul-Razzak and Ghan*, 2000). Organic species also have the ability to form surfactant films that may suppress activation of particles by preventing condensational growth, thus increasing the likelihood that particles without these films will activate (*Feingold and Chuang*, 2002a). Early modeling of this effect by *Feingold and Chuang* (2002a) is primitive, representing films as a stable and unbroken sheath completely covering the particle which is surely a limiting case in which the films have maximal effect (*Nenes et al.*, 2002).

Many of the thermodynamic routines presented in this chapter become more complicated when non-electrolytes are included. The equations governing equilibrium water content, for example, rely on manipulation of the Gibbs-Duhem equation (which will be introduced in the next chapter as equation (5.10)), which is a statement that the weighted summation of chemical potentials is zero at equilibrium. We will develop an expression for water activity by assuming only electrolytes to be present. Furthermore, mixing rules for activities and other properties that include ion-organic interactions are not available, and significant theoretical work is needed to include their effects.

Some parameterizations for simplified systems are in the literature, including an approximate means to include three representative organic classifications when calculating surface tension and slightly soluble organics (*Shulman et al.*, 1996), surface tension parameterizations (*Demou and Donaldson*, 2002), and a functional dependence of the critical super-saturation (S^* , see Section 5.8) on parameterized surface tension (*Facchini et al.*, 1999).

Dr. Simon Clegg of the University of East Anglia, the scientist who lead the development of the AIM model, will pursue a comprehensive modeling framework for calculating activities and partitioning of organic solutes as part of the forthcoming Tropospheric Organic Chemistry Experiment (TORCH), to begin in late 2003. Some initial modeling work has been completed (*Clegg et al.*, 2001), but much more theoretical work and many more measurements are needed; the results of that enterprise are eagerly awaited.

As noted earlier, the current version of MELAM does not include organic processes. Once appropriate validated parameterizations are developed, they should however be simple to add to the model through the surface tension, density, and activity coefficient routines.

4.7 Solution Density

This model tracks particles by location and composition, but several of the particles processes require knowledge of particle radius or volume and thus requires calculating density as a function of composition and other factors. As for most of the other thermodynamic processes, we calculate densities for equivalent binary solutions of each constituent electrolyte in water and then appropriately combine them using the mixing rule of *Patwardhan and Kumar* (1993). The solution portion of particles that also contain insoluble solids are thought to have the same density as pure solution droplets with equivalent composition (*Pruppacher and Klett*, 1997), so density in these mixed-phase cases is a simple weighted average of the solid and liquid phases by volume.

Resch (1995) proposes a single-solute solution density parameterization that is applicable in both very dilute and quite concentrated solutions (c.f., *Tang*, 1980):

$$\rho_{IJ}^{\circ} = \wp_{IJ}^{(0)} + e^{-\wp_{IJ}^{(1)}} \mathbf{m}_{IJ} \left(\rho_{\text{water}} - \wp_{IJ}^{(0)} \right) \quad (4.46)$$

Here, ρ_{IJ}° is the density of a binary solution of water and electrolyte IJ , \mathbf{m}_{IJ} is the molality of IJ in the solution, ρ_{water} is the density of pure water, taken to be constant with temperature as it varies only a few percent over temperatures of interest (*Bohren and Albrecht*, 1998), $\wp_{IJ}^{(0)}$ and $\wp_{IJ}^{(1)}$

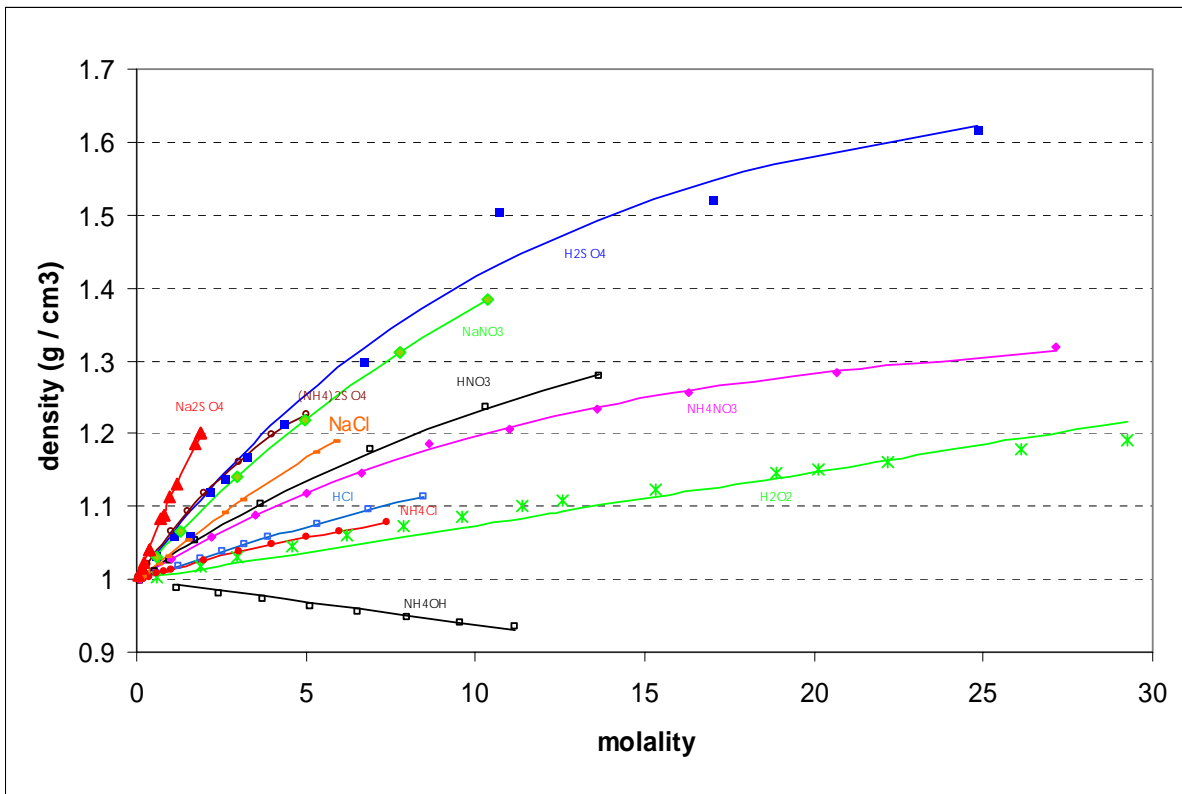


Figure 4-8: Variation of parameterized binary densities of several electrolytes with molality (lines) shown next to data (points) from *Lobo* (1989) at 25° C

are two free, electrolyte-specific parameters that are determined by regressing (4.46) against the solution density tabulations of *Lobo* (1989). Notice that equation (4.46) asymptotes to the density of water as the electrolyte molality approaches zero and to some fixed density $\varphi_{IJ}^{(0)}$ when highly concentrated; $\varphi_{IJ}^{(0)}$ need not be the density of a related crystalline solid, although of course it may be in some cases.

The full, multi-component particle density (ρ) may be calculated in terms of these density parameterizations of single-salt solutions using a mixing rule. Notice that, unlike thermodynamic properties that are functions of ionic strength for which we may calculate the properties of the single-salt solutions at the full ionic strength (e.g. water activity or the linear, bulk approximation of surface tension), equation (4.46) depends on the molality of a particular species and so the mixing rule must be additive rather than averaging, as the earlier examples were. *Patwardhan and Kumar* (1993) provide such a density-specific mixing rule:

$$\rho = \frac{\sum_{ij} \psi_{ij}}{\sum_{ij} (\psi_{ij} / \rho_{ij}^{\circ})} \quad (4.47)$$

Here, ij is an index of all electrolytes for which reactions are specified, which are individually comprised of ions i and j , and ψ_{ij} is a function of molality and the weighting factor, y_{ij} , defined in Section 4.5:

$$\psi_{ij} = (1000 y_{ij} + \mathbf{m}_{ij} M_{ij}) \quad (4.48)$$

Here, M_{ij} is the molecular mass of electrolyte ij . Following the compartmentalization logic used to derive y_{ij} , the numerator of equation (4.47) approximates the mass of the solution, and the denominator approximates the volume it occupies (*Patwardhan and Kumar*, 1993).

Note that \mathbf{m}_{ij} , the molality of the electrolyte of associated ions i and j and not the molality of the individual ions, is used in equations (4.46) and (4.48). The model tracks the concentrations of individual ions, not of ion pairs, and as a result these molalities are hypothetical. *Jacobson* (1999) provides an algorithm for deducing hypothetical electrolyte concentrations, the results of which are non-unique for solutions in which the electrolytes have enough overlapping constituent ions.

Figure 4-8 shows results of the single parameterization for several electrolytes plotted against the data from *Lobo* (1989) to which it was fit. For most electrolytes, the approximation fits the data to within a few percent. The density values are used mostly to convert between composition and radius. Radius, however, is only a weak function of density ($r \propto \rho^{-1/3}$) and so these relatively small errors due to imperfect fits to data, non-uniqueness of the hypothetical electrolyte algorithm, and partially dissociating are inconsequential.

4.8 Summary

This chapter presents the chemical thermodynamic theories and parameterizations that are incorporated into the MELAM model. The MELAM model is flexibly and generally coded such that the data that drives these parameterizations are imported entirely from input files; this facilitates inclusion of updated empirical parameters which are sorely needed.

The chapter focuses on inorganic constituents. However, organic constituents are pervasive in natural aerosol and their presence is thought to play a major role in the aerosol activation process (*Abdul-Razzak and Ghan*, 2000; *Ansari and Pandis*, 2000). As such, the severe lack of theory and data to support appropriate organic thermodynamic parameterizations is a pressing need (*Decesari et al.*, 2000). Hopefully, the flexibility and detail of our inorganic thermodynamic model will prove useful for the future inclusion of thermodynamic parameterizations of organic constituents.

Chapter 5

Mass Transfer to and from Particles: Condensation and Dissolution

5.1 Introduction

Aerosol particles and cloud droplets may grow or shrink by condensation or evaporation of water vapor and may change composition by the dissolving or escaping of condensable species. It is useful to distinguish between vapor diffusing to and attaching onto a nearly homogeneous particle of the same composition, which we call condensation, and a gas diffusing to and dissolving into a heterogeneous particle of a different primary composition, which we call dissolution (Jacobson, 1999). In the context of atmospheric aerosols, water is always the dominant liquid species at the moderate and high relative humidities considered here. In this chapter, we present the water condensation and trace gas dissolution algorithms that are used in the model.

In liquid phase “warm” clouds, droplets form primarily through condensational growth of aerosol particles, while a majority of the trace species found dissolved in the droplets entered via dissolution after the droplets formed. For example, several studies have shown that at most 6% of anthropogenic sulfur emissions form new particles while 44% add mass to existing particles already activated in clouds (*Hegg, 1990; Cruz and Pandis, 1997*). Because condensation rates depend on droplet composition, a generalized microphysical model of aerosol growth and cloud drop formation must be able to accurately account for dissolution.

Often, modelers assume that droplets grow until they reach equilibrium with a fixed background super-saturation of water vapor (e.g., *Abdul-Razzak et al., 1998; Abdul-Razzak and Ghan, 2000*). However, droplet formation is nature’s method of ameliorating super-saturations and aerosol parti-

cles compete for a limited supply of available water vapor. For example, *Ghan et al.* (1998) discuss the competition between sea salt and sulfate particles in the marine environment and conclude that an increase in available aerosol surface area due to high aerosol-phase sea salt levels can draw enough condensable water to prevent activation of the sulfate particles. Due to such competition, reviewed in Section 1.2.3, relative condensation rates are of paramount importance for correct calculation of the cloud drop concentration (N_c) that form on a distribution of aerosols (*Chuang et al.*, 1997b; *Phinney et al.*, 2003). The condensation scheme used here is developed based on a mass-flux model that calculates kinetic condensation rates and constrains the growth by fixing the total available water budget. The model is capable of solving for the equilibrium state as well, which will serve as a baseline and basis for comparison in studies presented later in the thesis. Equilibrium and flux-based formulations for both condensation and dissolution are presented in this chapter.

5.2 Continuity Between Phases

Transfer between the gas and aerosol phases is constrained by a simple continuity law that demands mass conservation:

$$\frac{d}{dt} \left\{ C_i + \sum_{a=1}^{N_a} c_{a,i} \right\} = \text{Chemical Production} - \text{Chemical Loss} \quad (5.1)$$

Here, the sum of the gas (C_i) and aerosol concentrations ($c_{a,i}$) of species i and aerosol a may only change by true chemical production and loss. Within this framework, we may also write a law that governs transfer between the gas and aerosol species:

$$\left(\frac{dC_i}{dt} \right)_{\text{gas/aer transfer}} = \left(- \sum_{a=1}^{N_a} \frac{dc_{a,i}}{dt} \right)_{\text{gas/aer transfer}} \quad (5.2)$$

This states that total mass leaving some set of N_a aerosol particles must end up in the gas phase, and vice versa.

Recall equation (2.2), which expressed the budget for an aqueous phase chemical i within a single particle as:

$$\left(\frac{dc_{a,i}}{dt} \right)_{\text{total}} = \left(\frac{dc_{a,i}}{dt} \right)_{\text{gas/aer transfer}} + \left(\frac{dc_{a,i}}{dt} \right)_{\text{net electrolyte dissociation}} + \left(\frac{dc_{a,i}}{dt} \right)_{\text{net chemical reactions}}$$

The total rate of change for an aqueous chemical i is a composite of several terms, respectively: gas-aerosol transfer, reversible electrolyte dissociation, and forward aqueous chemical reactions.

These terms are not independent as each depends directly on $c_{a,i}$. Full coupling of the calculations is prohibitively expensive in computer time and so some decoupling is necessary; the decoupling method chosen here is discussed in Section 5.3.

The mass flux between phases may be modeled using a diffusion-limited gradient approach which will be discussed at length in Section 5.7. To provide insight into equation (5.2), we may write the so-called quasi-stationary equation which relates the time rate of change of aerosol concentration to the gradient between the gas-phase concentrations far from the particle and at its surface, and a similar expression for the rate of change of the gas-phase concentration in a simplified form:

$$\left(\frac{dc_{a,a}}{dt}\right)_{\text{gas/aer transfer}} = k_{a,i} \{C_i(\infty) - C_{s,a,i}(r_a)\} \quad (5.3)$$

$$\left(\frac{dC_i}{dt}\right)_{\text{gas/aer transfer}} = -\sum_{a=1}^{N_a} k_{a,i} \{C_i(\infty) - C_{s,a,i}(r_a)\} \quad (5.4)$$

The rate constant ($k_{a,i}$) depends on the species (i) and characteristics of the aerosol(a), r_a is the particle radius, $C_i(\infty)$ is the gas phase concentration of i far from the particle, and $C_{s,a,i}(r_a)$ is the effective equilibrium concentration near the surface of the particle (one radius' distance from the center) (*Jacobson et al.*, 1996b). These equations provide a framework for calculating condensational rates and equilibrium conditions.

5.3 Coupling between Condensation and Aqueous Chemistry and Thermodynamics

When solving the budget equation (2.2), we may solve for equilibrium or time-dependent solutions on a term-by-term basis. To model any chemical system as being at equilibrium is equivalent to assuming the time-scale of reaching equilibrium is much shorter than other processes in the system. In previous chapters, we already made the determinations that electrolyte dissociation fits this criterion while forward chemistry does not. Gas-aerosol transfer has historically been treated as an equilibrium process, but of late, especially in cloud studies, it has been treated in a time-dependent manner. We argue in Section 5.4 that gas-aerosol equilibrium is a poor assumption in the systems of interest here. In Section 4.3, we discussed ways to solve for an equilibrium of multiple reversible electrolyte dissociation reactions. In Section 2.4, we briefly discussed time-dependent solutions of multiple aqueous forward chemical reactions, and in this chapter we will present both equilibrium and time-dependent solutions to multiple gas-aerosol transfer equations.

We assume that the aqueous electrolytes remain in equilibrium regardless of the approach taken to gas-aerosol transfer. When the gas and aerosol phases are also assumed to be in equilibrium, the model simply equilibrates each particle at a particular grid-point at some point during the time-step to reinstate equilibrium after other dynamical processes have disturbed it. When we assume a time-dependent mass-flux form of gas-aerosol transfer, such as equations (5.3) and (5.4), an operator-splitting method is used to decouple the equilibrium dissociation reactions. This is discussed briefly in Section 5.10. In this case, we may substitute equation (5.3) into the continuity expression (2.2), neglecting the relatively slow forward chemistry term for the moment to obtain:

$$\left(\frac{dc_{a,i}}{dt}\right)_{total} = k_{a,i} (C_i(\infty) - C_{s,a,i}(r_a)) + \left(\frac{dc_{a,i}}{dt}\right)_{\substack{electrolyte \\ dissociation}} \quad (5.5)$$

A first approach to solving this equation is to solve the time-dependent gas-aerosol transfer term for a condensing gas over a particular time-step and then to allow the aqueous-phase of the gas to attain equilibrium. A second approach, really a variant of the first, is to consider the condensation equations that dissolve a gas-phase electrolytic species into both its undissociated and dissociated forms and to solve those equations in a coupled manner; the electrolyte in this approach should be much closer to equilibrium at the end of the time step than the first procedure at which point full equilibrium is restored (*Jacobson et al.*, 1996b; *Jacobson*, 1997c). A third approach is to define chemical “families” that include the aqueous species that quickly inter-convert and write the gas-aerosol transfer equations with respect to the concentration of the entire family. We take the second approach in this model, the specifics of which are discussed in Section 5.10.

5.4 Equilibrium and Non-Equilibrium Across the Gas and Aerosol Phases

Equation (5.5), which is close to a linear first order differential equation, tells us how an aerosol approaches equilibrium with the gas phase: specifically, while maintaining internal equilibrium among dissolved salts, the concentration of species i approaches equilibrium roughly exponentially with time constant $k_{a,i}$. In practice, we consider equation (5.5) to be in equilibrium when the gradient $(C_i(\infty) - C_{s,a,i}(r_a))$ is zero within some small pre-specified relative error, and the dissociation component of the time-rate-of-change satisfies the equilibration routine discussed in Section 4.3.2. Assuming a volatile species is in constant equilibrium, requires that the equilibration time scale is short as compared to all of the other relevant local processes that affect aerosol and gas-phase

concentrations (*Meng and Seinfeld, 1996*).

Meng and Seinfeld (1996) suggest that coarse particles are not normally in equilibrium with either the smallest aerosols or with the gas phase. They also note that the path to equilibrium may not resemble either the beginning or equilibrium states. For example, a volatile gas-phase species may quickly reach equilibrium with the smallest aerosols, which then slowly lose some of their gas-phase species to larger aerosols as these large particles approach equilibrium on a longer time-scale. This behavior highlights both that gas-aerosol disequilibrium may be widespread in the atmosphere and that aerosols compete with each other during gas-aerosol transfer. As this model is formulated specifically to address cloud activation, we must assure ourselves that we are making the correct choices about equilibrium and flux-based calculations of gas-aerosol transfer. We review the debate in the literature about this topic in this section.

The five thermodynamic modules reviewed in *Zhang et al. (2000)*, and indeed the lion's share of aerosol thermodynamic modules, assume that aqueous species and liquid water equilibrate instantaneously with their gas-phase counterparts. The assumption of instant equilibration has limitations, and some recent studies challenge its appropriateness in detailed studies of cloud activation. It is useful to consider the equilibration of H_2O and of trace species separately, as the two are of differing importance to cloud formation and differ somewhat dynamically.

5.4.1 The Equilibration of Water

In mid-range relative humidities, gas-aerosol equilibrium of water is quickly established. *Resch (1995)* calculates a characteristic equilibration time for water vapor, using standard values for water vapor diffusivity and at 70% \mathcal{RH} and 25° C, of 0.1 seconds for a 10 μm particle and a sharp fall off with radius. This growth process is extremely rapid as compared to other processes in sub-saturated conditions, and Resch asserts that such particles may be assumed to be in equilibrium with surrounding water vapor. Such reasoning under-girds the widespread use of the equilibrium assumption.

Ferron and Soderholm (1990) provide a more comprehensive argument for fast equilibration times through a theoretical discussion of evaporation time for solution droplets and equilibration time for dry salt particles. Using a form of the quasi-stationary equation and appropriate thermodynamic constants, the authors model the required time for aerosols to equilibrate to within 5% after a \mathcal{RH} shock that pushes ambient humidity from below the particles' deliquescence point to above. They report that 10 μm salt particles take no more than a couple of seconds to equilibrate and falls off rapidly for small particles. These results confirm *Resch (1995)*'s assertion that constant

equilibrium may be effectively presumed for mid-sized and small particles, at least in an environment of slowly varying \mathcal{RH} . For larger particles, however, the equilibration time-scale is much longer. They report equilibration times of 17.4 seconds for salt particles of 22.1 μm diameter, 44 seconds for 27.6 μm diameter particles, and 401 seconds for 43.5 μm diameter particles; evaporation times are quite similar for jumps of \mathcal{RH} in the other direction. Salt particles of these larger sizes, however, would only very occasionally be found even at relatively high relative humidities and are more characteristic of cloud droplets (*Pruppacher and Klett, 1997*).

Aerosol models commonly employ Köhler theory, an equilibrium model of the process by which aerosols become cloud droplets. Within that theory, the characteristics of an aerosol particle determine a minimum super-saturation at which the particle will “activate” and become a cloud droplet. The theory is discussed at length in Section 5.8.1. A number of recent studies, however, highlight that the long time-scales required for these larger particles to reach equilibrium inhibits aerosol activation and, as a result, Köhler theory over-predicts activation (*Chuang et al., 1997b; Brechtel and Kreidenweis, 2000; Nenes et al., 2001*).

These results suggest that vapor-liquid water equilibrium may be reasonably assumed at mid-range relative humidities but a kinetic form is more appropriate near and above saturation. This model allows use of a threshold \mathcal{RH} value below which equilibrium is assumed and above which a kinetic formulation is employed. The trade-off between the assumption of equilibrium and the assumptions inherent in using the kinetic growth model for aerosols at various \mathcal{RH} levels is discussed in Section 5.11. That discussion suggests setting the threshold \mathcal{RH} in the high 90% range.

5.4.2 The Equilibration of Trace Species

The time scale required for trace species to reach gas-aerosol equilibrium depends on a number of species-specific parameters and varies with temperature. *Wexler and Seinfeld (1990)* investigated whether aqueous ammonium salts contained in fine aerosols are in thermodynamic equilibrium with the vapor-phase components. (Such salts form by the surface reaction of NH_3 and an acid, such as HCl or HNO_3 .) Their results confirmed a recent observational study that reported lasting gas-aerosol disequilibrium in some atmospheric conditions (*Allen et al., 1989*). In so doing, it challenged the long held belief that such salts remain very close to equilibrium for most background conditions as first postulated by *Stelson et al. (1979)* and upheld through a string of further studies (see, amongst others, *Stelson et al., 1979; Stelson and Seinfeld, 1982a; Pilinis and Seinfeld, 1987; Kim et al., 1993a,b; Kim and Seinfeld, 1995; Meng et al., 1995; Jacobson et al., 1996b; Clegg et al., 1998a,b; Nenes et al., 1998; Ansari and Pandis, 1999a*). Many of these studies considered

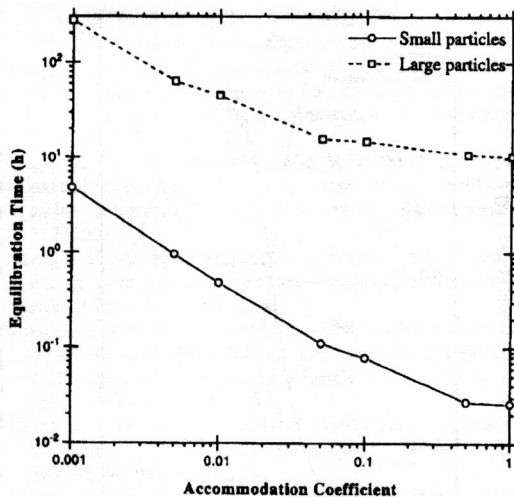


Figure 5-1: Equilibration time-scales for a range of accommodation coefficient values for both small and large mixed aqueous and solid NaCl and $(\text{NH}_4)_2\text{SO}_4$ particles at 80% \mathcal{RH} (Meng and Seinfeld, 1996, their Figure 6)

bulk thermodynamic approximations (which do not account for size distributions or correct for curvature), which lead to partitioning errors (Moya *et al.*, 2002). Some studies partially correct these errors by considering several size bins of aerosols (cf. Pilinis and Seinfeld, 1987; Jacobson *et al.*, 1996b; Jacobson, 1999). Jacobson (1999) quite successfully models inorganic partitioning in Southern Californian using this approach and is a generally promising statement on the equilibrium method.

Meng and collaborators (Meng and Seinfeld, 1996; Meng *et al.*, 1998) note that achieving gas-aerosol thermodynamic equilibrium in coarse mode particles may require several days and that high \mathcal{RH} does not appreciably affect these results. Large particles, they assert, almost always exist in a non-equilibrium transition state. They advocate, as a result, a fully dynamic mass transfer treatment using a diffusion limited model. A number of models have implemented this approach for size-resolved sectional aerosol distributions (including Meng and Seinfeld, 1996; Meng *et al.*, 1998; Jacobson *et al.*, 1996b; Jacobson, 1997a,b,c; Russell and Seinfeld, 1998; Sun and Wexler, 1998a,b). It is considered to be more accurate than the equilibrium approach but computationally very expensive. Moya *et al.* (2002) study the errors introduced by the equilibrium approach and report that it is acceptable for all but the largest particles, similar to what has been found in the context of water condensation as reported in the previous section. Since particle size and \mathcal{RH} correlate strongly, we are again drawn to the threshold \mathcal{RH} approach, using an equilibrium approach below some stated \mathcal{RH} and a kinetic approach above.

The characteristic gas-aerosol equilibration time for trace species is determined largely by the

extent of disequilibrium and the mass accommodation coefficient (α , the fraction of molecules of a given species that are incorporated into an aerosol upon contact). One would expect that lower values of α would lead to longer equilibration times, since more of the molecules that reach the particle in a diffusion-limited process are turned away. *Meng and Seinfeld* (1996) theoretically treat this question with a quasi-stationary modeling approach and vary α between 0.001 and 1.0 for a mixed mass loading of aqueous and solid NaCl and $(\text{NH}_4)_2\text{SO}_4$ distributed in 0.2 μm diameter particles (“small particles” in Figure 5-1) and 3.0 μm diameter particles (“large particles”) at 80% \mathcal{RH} . Their results are presented in Figure 5-1. Note that the time scales vary by two orders of magnitude for small particles and by one for large particles. Despite this strong dependence, there is a paucity of data for accommodation coefficients and many models must assume guessed values for many species. Determining actual, accurate values for α for each important species would greatly assist in determining which must be treated in a kinetic framework.

The debate about the appropriateness of the equilibrium modeling approach when considering gas-aerosol partitioning is still open, with the effect of large particles and environments with strong gas-phase gradients proving the most problematic. Since this model is formulated to study the high \mathcal{RH} environments in which cloud forms, large particles are very frequent and the kinetic approach is apparently most appropriate. We take the approach of setting a threshold \mathcal{RH} value above which we employ the kinetic approach and below which we assume equilibrium.

5.5 Equilibrium Water Content

Aerosol liquid water content in a sub-saturated environment tends towards an equilibrium between the ambient and near-surface water vapor pressures. The equilibrium partial pressure is determined by the relative humidity of the local environment and by the specifics of the solute and tension properties of the liquid interface. Below saturation, equating liquid-phase water activity with gas-phase water activity across the interface (and correcting for curvature) yields the correct equilibrium liquid water content. The model allows this approach to be used for any sub-saturated environment. Typically, the equilibrium approach is used to initialize aerosol distributions below some threshold \mathcal{RH} value, and in other cases a flux-based approach discussed in Section 5.8 is used. Which method is used on a particular modeling run is left to the discretion of the user. However, for all runs the system is initially open and therefore the relative humidity is held fixed during an initial equilibration of the aerosols, but not afterwards.

The activity of bulk phase liquid water at equilibrium with the vapor phase across a flat interface is equal to the ratio of the partial pressure of water vapor in the local environment to the saturation vapor pressure of water over a bulk liquid surface, which is by definition the environmental relative humidity (*Jacobson, 1999*):

$$a_w = \frac{p_v}{p_{v,s}} = \mathcal{RH} \quad (5.6)$$

For pure liquid water in equilibrium with the ambient water vapor, both the liquid phase and gas phase activities, and thus this ratio, are unity. For a solution, some solute molecules bind to water molecules along the interface and in so doing inhibit evaporation and drive water condensation. This in turn lowers the vapor pressure of water over the surface and pushes the relative humidity and water activity below unity.

We discuss a commonly adopted non-iterative aerosol water content approximation (but which is not employed here) in Section 5.5.1. Sections 5.5.2 to 5.5.5 present and discuss the iterative solution MELAM uses to calculate water activity for pure solution, how these values are combined to find the water activity in a mixed system, and then how MELAM equilibrates aerosol water content.

5.5.1 The Zdanovskii-Stokes-Robinson Approximation

The Zdanovskii-Stokes-Robinson (ZSR) equation is a non-iterative approximation to aerosol liquid water content based on electrolyte molalities (*Stokes and Robinson, 1966; Frolov, 1981*). Because of its computational efficiency, it is common in efficient global aerosol equilibrium models including SCAPE-1 of *Kim et al. (1993a)* and *Kim et al. (1993b)*, SCAPE-2 of *Kim and Seinfeld (1995)*, ISORROPIA of *Nenes et al. (1998)*, and others.

The ZSR approximation makes the assumptions that all of the constituent electrolytes are dissociated and that there is no interaction between the solute molecules, neither of which are always valid (*Resch, 1995*). In so doing, it essentially estimates the water content to be the sum of the amounts required to completely dissolve each of the electrolytes in isolation. The system is, however, reasonably accurate above the electrolytes' deliquescence points.

In the ZSR approximation, the equilibrium amount of liquid water is a unique function of electrolyte molality and sub-saturation relative humidity:

$$W = \sum_e \frac{c_e}{m_{e,0}(a_w)} \quad (5.7)$$

In which W is the equilibrium mass of liquid phase water per unit volume of air, e is an identifying index for the associated electrolytes, c_e is in moles of associated electrolyte equivalents per unit volume of air, and $\mathbf{m}_{e,0}(a_w)$ is the molality of a single-component electrolyte solution that has water activity a_w (*Seinfeld and Pandis, 1998*). The molality $\mathbf{m}_{e,0}(a_w)$ is usually parameterized as a polynomial function of a_w , such as:

$$\mathbf{m}_{e,0}(a_w) = \sum_{i=0}^7 Y_i (a_w)^i \quad (5.8)$$

Appropriate data for Y_i parameters are reported in *Robinson and Stokes (1959)*, *Jacobson et al. (1996b)*, *Tang (1997)*, and elsewhere.

The traditional ZSR relationship, here presented as equation (5.7) tends to under-predict equilibrium water content in high \mathcal{RH} environments (see the discussion Section 5.5.5) especially when the mixed solution includes electrolytes of different charge types. *Clegg and Seinfeld (2004)* provide corrections to equation (5.7) that in part account for differing electrolyte charge types.

The next subsection discusses the approximation employed here and later in Figure 5-3 in Section 5.5.5 and the discussion of it reveals the relative quality of the approximations.

5.5.2 Calculating the Water Activity in Single Salt Solutions

The relationship between the water and solute activities may be developed from the Gibbs-Duhem equation following *Meissner (1980)*. The Gibbs-Duhem equation relates changes in the chemical potentials of the various species in a mixed system to changes in temperature, pressure, and bulk thermodynamic state (*Seinfeld and Pandis, 1998*):

$$-S \, dT + V \, dp = \sum_k n_k \, d\mu_k \quad (5.9)$$

In which μ_k is the chemical potential of species k , n_k is the number of moles of that species present in the system, and S , T , V , and p are, respectively: entropy, temperature, volume, and pressure. When the environment is sub-saturated with respect to water vapor (the only case in which the water activity will be used to predict water content) we assume that the system is in thermodynamic equilibrium, in which case the left hand side of equation (5.9) goes to zero. Note that we will assume through this development that non-electrolytes either do not affect water activity or are not present. Moving the water activity term from the summation on the right hand side to the left hand side, we reach a diagnostic expression of the equilibrium chemical potential of water in terms of the

chemical potentials of the other species:

$$-n_w \, d\mu_w = \sum_{k \neq w} n_k \, d\mu_k \quad (5.10)$$

which we then rewrite in terms of activities, noting that $n_i \, d\mu_i = \mathbf{m}_i \, d \ln a_i$ (*Meissner*, 1980; *Resch*, 1995):

$$-55.51 \, d \ln a_w = \sum_{k \neq w} \mathbf{m}_k \, d \ln a_k \quad (5.11)$$

Here, 55.51 is the number of moles of water molecules in 1 kg of water.

For a binary solution of a single electrolyte comprised of ions i and j , for which there will only be one term in the summation on the right hand side of equation (5.11), equation (5.11) may be integrated following *Meissner* (1980):

$$-55.51 \, d \ln a_w^\circ = \frac{2 \, l}{|z_i \, z_j|} + 2 \int_1^{\Gamma_{ij}^\circ} l^\circ \, d \ln \Gamma_{ij}^\circ \quad (5.12)$$

Here, the superscript \circ indicates that the thermodynamic property pertains to a pure, binary solution, z_i is the charge of ion i , and Γ_{ij}° is the reduced mean activity coefficient defined in equation (4.17) and parameterized by the Kusik-Meissner theory as equation (4.18). For our purposes, it is preferable to integrate over ionic strength (l) rather than over the reduced mean activity and so we recast equation (5.12) in the appropriate form:

$$-55.51 \, d \log_{10} a_w^\circ = \frac{2 \, l}{\ln 10 \, |z_i \, z_j|} + 2 \int_0^l \left\{ l' \frac{d \log_{10} \Gamma_{ij}}{dl'} \right\} dl' \quad (5.13)$$

Note that we divided both sides of the equations by $\ln 10$ to introduce the base-ten logarithm in the second term on the right hand side that recalls the Kusik-Meissner definition in equation (4.18). Recall from the discussion of the Kusik-Meissner method in Section 4.4.1 that the reduced activity coefficient (Γ_{ij}°) of an electrolyte ij in a pure binary solution is a function only of ionic strength (or here the dummy variable l') according to equation (4.18).

Using the Kusik-Meissner definition of a reduced activity coefficient for a pure solution, as given in equation (4.18), we may express the integral in equation (5.13) as a function of ionic strength (l) using:

$$l \frac{d \log_{10} \Gamma_{ij}}{dl} = \frac{q \, B \, l \, (1 + 0.1 \, l)^{(q-1)}}{10 \, \ln 10 \, (1 + B \{ (1 + 0.1 \, l)^q - 1 \})} - \frac{0.5107 \, (0.5\sqrt{l} + 0.069(C-1) \, l^4)}{(1 + C\sqrt{l})^2} \quad (5.14)$$

In which $B = (0.75 - 0.065 q)$ and q has the temperature dependent form of equation (4.18). When there is no direct data for the desired binary solution and the activity coefficient must instead be assembled from several others according to equation (4.21), the same expression is a more complicated function of ionic strength (I):

$$I \frac{d \log_{10} \Gamma_{IJ}}{dI} = \frac{I}{z_{IJ}} \left\{ \frac{d(z_{AJ} \log_{10} \Gamma_{AJ})^{\nu_{AJ}}}{dI} + \frac{d(z_{IB} \log_{10} \Gamma_{IB})^{\nu_{IB}}}{dI} - \frac{d(z_{AB} \log_{10} \Gamma_{AB})^{\nu_{AB}}}{dI} \right\} \quad (5.15)$$

Here, $\nu_{ij} = \nu_i + \nu_j$, which is the stoichiometric factor for the cation i and anion j . Similarly, the charge $z_{ij} = |z_i| + |z_j|$, which is the sum of the absolute values of the charges of the two ions. Each of the derivatives on the right hand side of equation (5.15) may be expressed, for an exemplary electrolyte with cation x and anion y :

$$I \frac{d(z_{xy} \log_{10} \Gamma_{xy})^{\nu_{xy}}}{dI} = \nu_{xy} z_{xy}^{\nu_{xy}} \left(I \frac{d \log_{10} \Gamma_{xy}}{dI} \right)^{\mathcal{A}} \left(\log_{10} \Gamma_{xy} \right)^{\mathcal{B}(\nu_{xy}-1)} \quad (5.16)$$

Here, term \mathcal{A} is given by equation (5.14) and term \mathcal{B} is power of the reduced activity coefficient given in equation (4.18).

MELAM evaluates equation (5.13) for each of the electrolytes in the solution, integrating using DGAUS8, which is a public domain adaptive eight step Legendre-Gauss algorithm written by R. E. Jones as part of the SLATEC fortran library. These values of $(a_w^\circ)_{ij}$ are then combined using the mixing rule presented in the next section.

5.5.3 Mixing Single Salt Water Activities to Estimate Water Activity for a Multi-Component System

We are interested, of course, in calculating the water activity in mixed solutions containing multiple electrolytes. It is possible to develop an integro-differential definition of the mixed water activity through direct integration of the Gibbs-Duhem equation (5.11), following the same arguments we used in the previous Section 5.5.2 to define the water activity for a binary solution containing a single electrolyte (5.13) (see *Meissner*, 1980; *Resch*, 1995). However, in that development we must consider the mixed reduced activity coefficient (Γ_{ij}) which is a function of both the ionic strength as stated in equation (4.18) and also each of the other activity coefficients for electrolytes with common ions according to the mixing rule presented in equation (4.32). The form of equation (4.32) means that the mixed solution equivalent of equation (5.13) has many terms and grows increasingly complex as the number of electrolytes in the system increases. Because of the difficulty of evaluating

the complex integral when directly integrating the Gibbs-Duhem equation in a mixed electrolytic system, it is both more accurate and less computationally expensive to develop the water activity for a mixed solution as a function of the theoretical water activities of the corresponding binary solutions using a mixing rule, as we had for many of the thermodynamic properties considered in Chapter 4.

The original presentations of *Kusik and Meissner* (1978) and *Meissner* (1980) propose mixing rules which combine $(a_w^\circ)_{ij}$ calculated for each electrolyte to estimate a_w for the multi-component solution. Neither papers' proposed mixing rule is convenient to use in this context: the one presented in the first paper requires estimation of a residual term in some cases for which no suitable algorithm has been found; while the one presented in the second paper requires use of the Kusik-Meissner activity coefficient equations (it modifies the definition of q from equation (4.18) to approximate the values for the mixed system) which is not generalizable beyond the cases in which the strict Kusik-Meissner theory applies (*Resch*, 1995). We instead prefer the mixing rule of *Patwardhan and Kumar* (1993), discussed in brief in Section 4.5, which is accurate and generalizable.

We approximate the water activity of the solution, a_w , to be an average of the water activities, $(a_w^\circ)_{ij}$, of corresponding pure systems of the same ionic strength weighted by the Patwardhan and Kumar factor y_{ij} :

$$\ln a_w = \sum_{ij} y_{ij} \ln (a_w^\circ)_{ij} \quad (5.17)$$

Patwardhan and Kumar (1993) investigated the effectiveness of this mixing rule in four-ion systems and find an average error of 1.16% with individual errors rarely exceeding 2% as compared to laboratory data. However, thermodynamic data for mixed and highly concentrated electrolytic systems beyond the most simple inorganic mixtures is insufficient and it is risky to speculate on the accuracy of these mixing rules beyond those simple well-characterized systems. *Resch* (1995) compares this mixing rule to several others found in *Zemaitis et al.* (1986) and finds that all four methods considered produce comparable values that are within the error range of available experimental values. He determines that equation (5.17) is the most computationally convenient in systems with multiple electrolytes.

5.5.4 Equilibrating Particle Water Content

With a method to calculate water activity in hand, we may design an algorithm to equilibrate the aerosol particle with the ambient vapor fields. The equilibrium condition for gas-aerosol water

vapor transfer for an aerosol particle is more complicated than that for a bulk liquid that shares a flat interface with the vapor phase. Unlike the bulk phase case, liquid-phase droplets are small and usually near-spherical and so equation (5.6) must be corrected for the curvature of the droplet (*Pruppacher and Klett, 1997*):

$$\mathcal{RH} = a_w \exp\left(\frac{2 M_w \sigma_{s/a}}{T R^* \rho r_a}\right) \quad (5.18)$$

Here, $\sigma_{s/a}$ is the surface tension of the solution discussed in Section 4.6, T is the temperature, R^* is the universal gas constant, ρ is the particle density discussed in Section 4.7, and r is the radius.

We solve for this equilibrium by holding the ambient relative humidity fixed and changing the particle water content, and thus water activity, until equation (5.18) is satisfied within some specified error. The assumption of constant relative humidity during the equilibration process is fair since the particles are equilibrated one at a time and each particle contains very little water in absolute terms.

We guide the search by calculating a water residual, r_w , which we can compare to an error tolerance. Recall that both \mathcal{RH} and a_w are comparably scaled quantities between zero and unity so no normalization is needed:

$$r_w = a_w \exp\left(\frac{2 M_w \sigma_{s/a}}{T R^* \rho r}\right) - \mathcal{RH} \quad (5.19)$$

If r_w is less than zero, the particle is too dry compared to the vapor phase and we add more water to the aerosol; if r_w is greater than zero, the particle is too moist and we take water away. Using this directional guideline, the equilibration is a simple bisectional search:

1. Depending on whether r_w is positive or negative, we halve or double the water content repeatedly and recalculate r_w after each iteration, stopping after r_w changes sign which signals that we overshoot the equilibrium point. We set aside the absolute size of the last halving or doubling step in terms of water molecules.
2. We halve the last step size and retreat that much towards the equilibrium point, using the sign of r_w to determine if that amount is to be added or subtracted.
3. We recalculate r_w . If its absolute value is smaller than some error tolerance, we consider equation (5.18) to be satisfied and end the routine. Otherwise, we return to step 2.
4. Unless this is an initialization equilibration, we change the water vapor content in the local

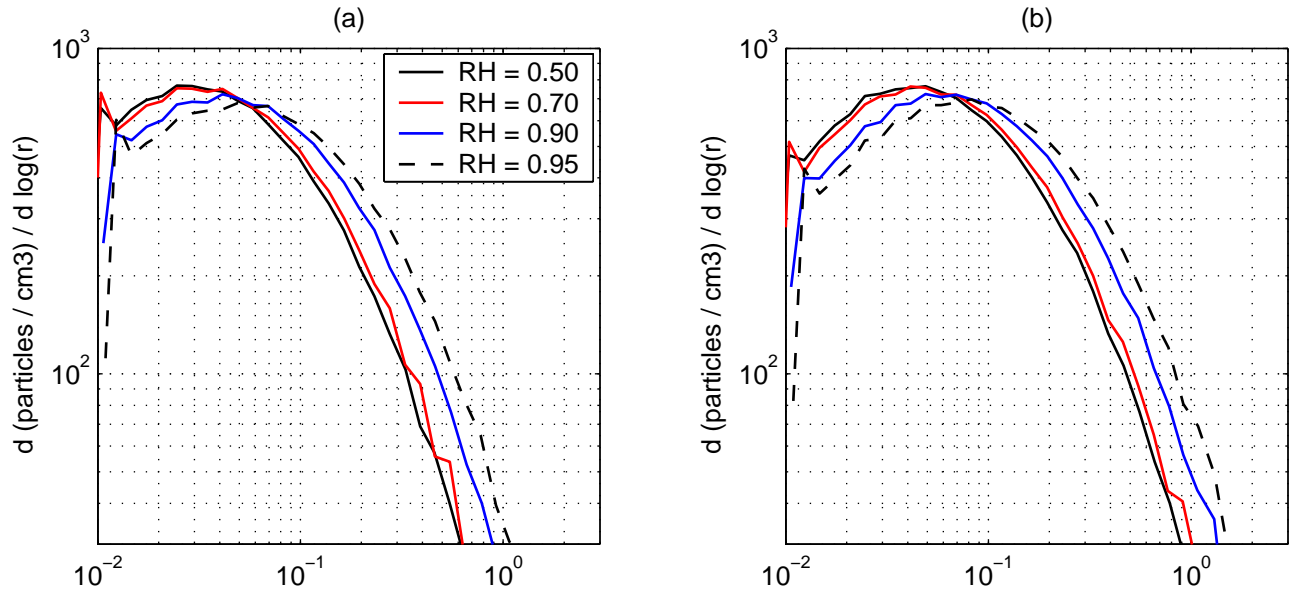


Figure 5-2: (a) $5 \mu\text{g}/\text{m}^3$ and (b) $15 \mu\text{g}/\text{m}^3$ of Na_2SO_4 distributed on 1000 aerosols drawn from a log-normal distribution with a standard deviation of 1.2, equilibrated to four \mathcal{RH} values at 298.15 K and 1000 mbar

grid cell by the appropriate amount to offset the liquid water added or subtracted from the equilibrated particle.

As alluded to above, this equilibration routine is useful primarily for initialization or studies in environments less moist than saturated. Among the assumptions implicit in this equilibrium model are that equilibration is effectively instantaneous with respect to the time scales on which the background environment changes, and that aerosols equilibrate independent of one another. As discussed in Section 5.4, aerosols are not observed to be in constant equilibrium between the vapor and liquid phases and so this assumption is only approximate. In very moist environments in which aerosols are competing for water vapor and seeking to activate, both of these assumptions are violated and a flux based scheme is more appropriate. Such a flux based scheme is the subject of Section 5.8.

Figure 5-2 shows two example particle distributions equilibrated to a range of relative humidities in open environments at 298.15 K and 1000 mbar. Panel 5-2(a) shows $5 \mu\text{g}/\text{m}^3$ of Na_2SO_4 distributed over 1000 particles per cubic centimeter, represented as log-normal distributed lagrangian particles with a standard deviation of 1.2; Panel 5-2(b) shows a similar plot for $15 \mu\text{g}/\text{m}^3$ of Na_2SO_4 . For both, the aerosols are considered on a particle-by-particle basis and collected in an equal-volume-ratio-intervals histogram only at the end; both bisulfate and sulfate are included. Unsurprisingly, the shape of the distribution is basically retained at the four equilibria.

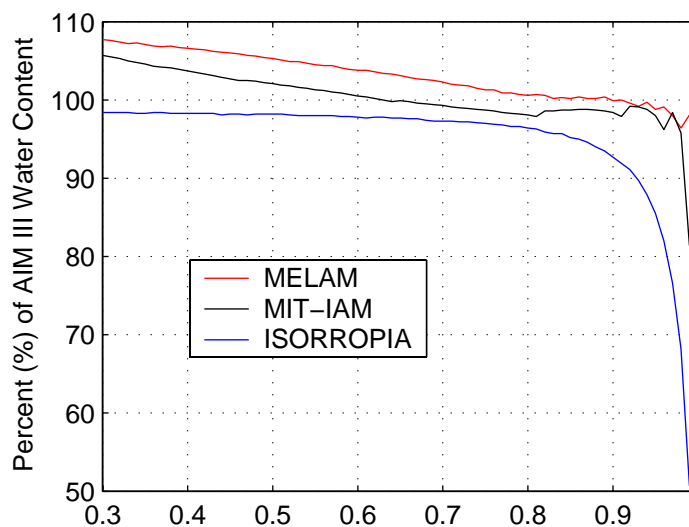


Figure 5-3: Comparison of water content using ISORROPIA, MIT-IAM, and MELAM for $2 \mu\text{mol}/\text{m}^3$ of H_2SO_4 . All values are scaled to percentages by dividing by AIM III’s water content.

Any changes in the distribution’s shape relate to the curvature term in equation (5.18) which tends to concentrate smaller particles and allow larger particles to approach the behavior of a bulk solution.

5.5.5 Comparison of Water Equilibration Methods

By directly integrating the Gibbs-Duhem equation, we avoid the pitfalls of the ZSR approximation and thus our method is considerably more accurate. As discussed in 5.5.1, the ZSR approximation assumes that all of the constituent electrolytes are fully dissociated, while in our method, equation (5.13) is a function of ionic strength and thus of the actual ionic content. The ZSR approximation also assumes that there are no interactions between solute molecules, while in our approach equation (5.17) corrections to activities in mixtures are used to approximate such interactions.

The AIM III model of Clegg, Wexler, and Brimblecombe, discussed in greater length in Section 4.4.3, explicitly accounts for ion-ion interactions in a much more complete, system-specific manner than do either the ZSR or our iterative, Kusik-Meissner based method (*Clegg et al.*, 1998a,b) and thus are considerably more accurate than either the ZSR or our approaches. It is reasonable, therefore, to consider the well tested results from AIM III to be a baseline and compare other models against it. Figure 5-3 shows a comparison of the water content of two models that employ the Gibbs-Duhem integration method – MELAM and the MIT-IAM of *Resch* (1995) – and one that uses the ZSR method – ISORROPIA of *Nenes et al.* (1998) – each scaled by the content of AIM III for a system with $2 \mu\text{mol}/\text{m}^3$ of aerosol phase sulfuric acid. For this exercise, MELAM is

run in bulk mode and no particle distribution or curvature correction has been specified. As can be seen in the figure, ISORROPIA’s implementation of the ZSR method is extremely accurate at mid-range relative humidities but dramatically under-predicts water content as the system approaches saturation with respect to liquid water. The models using the Gibbs-Duhem integration method do much better and closely resemble the results of the AIM III model at high relative humidities.

As noted earlier in Section 5.5.1 and discussed in *Clegg and Seinfeld (2004)*, the traditional ZSR model as implemented in ISORROPIA is inaccurate in dilute solutions (equivalently at high \mathcal{RH}) for mixed solutions with electrolytes with different charge types; the sulfate-bisulfate mixture is such a system and Figure 5-3 shows that ISORROPIA indeed dramatically under-predicts water content at high \mathcal{RH} . It is possible that the corrections to the ZSR theory presented in *Clegg and Seinfeld (2004)*, once it has been studied in systems beyond the NaCl-Na₂SO₄-H₂O system considered in the paper, will remedy these under-prediction problems. Certainly, the non-iterative nature of the ZSR algorithm is very attractive, especially for large scale models in which many equilibrium calculations must be made and wherein its use is already widespread, and its improvement would be welcome.

5.6 Trace Gas - Aerosol Equilibrium

Equations (5.3) and (5.4) described a system that, over time, will reach equilibrium when $C_i(\infty)$ equals $C_{s,a,i}(r_a)$ for each aerosol a (*Jacobson et al., 1996b; Jacobson, 1997c, 1999*). This equilibrium condition, that the actual and effective gas phase concentrations equate, is not directly applicable for trace species because we do not track $C_{s,a,i}(r_a)$ explicitly; we must develop a relationship between this near-surface gas-phase saturation concentration and the characteristics of the particle itself.

Towards that end, we cast gas-solution transfer across a flat boundary as an equilibrium process in which case it is governed by an equilibrium constant similar to that used for dissociation of electrolytes within the aqueous phase in Section 4.3. Recall equation (4.4), which relates the activities of species to an equilibrium constant:

$$K_{eq}(T) = \prod_x a_x^{\pm\nu_x}$$

The product is taken over all of the species involved in the equilibration (indexed by the dummy variable x), both gas and aqueous phase, and the sign in the exponent is positive for products and

negative for reactants. Note that we employed this relationship for water vapor equilibration to write (5.6), in which the only activities involved were those for water vapor (equal to \mathcal{RH}) and liquid phase water. We discussed earlier the calculation of liquid water activity (a_w) for electrolytic solutions; the procedure for equilibrating volatile trace species is very different, and is presented here. In this case, the activities of gas phase species are taken to be their partial pressures while those of aqueous species are their molality multiplied by a correcting activity coefficient. For the case of a single gas phase species equilibrating with a single aqueous species, equation (4.4) (repeated just above) becomes:

$$K_{eq,i}(T) = \frac{\mathbf{m}_i \gamma_i}{\mathbf{p}_{s,i}} \quad \text{or} \quad \mathbf{p}_{s,i} = \frac{\mathbf{m}_i \gamma_i}{K_{eq,i}(T)} \quad (5.20)$$

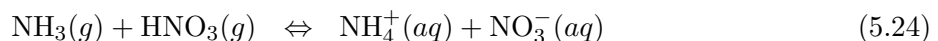
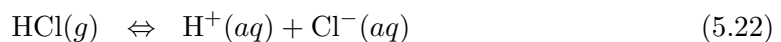
Here, all of the values are for a particular aerosol (a) even though the subscript a is omitted. Note that $\mathbf{p}_{s,i}$ is an environmental variable and so is common for all local aerosols, and so for local equilibrium $\mathbf{m}_i \gamma_i$ must match for all aerosols.

For an increasingly dilute solution, γ_i approaches unity and equation (5.20) is well approximated by Henry's law, for which we rename $K_{eq,i}(T)$ the Henry's Law Coefficient (H_i):

$$\mathbf{p}_{s,i} = \frac{\mathbf{m}_{i,(aq)}}{H_i} \quad (5.21)$$

Henry's law coefficients are determined readily from data and available for a host of species. *Sander* (1999) thoughtfully compiles and reviews the many such experiments available in the literature. In a non-dilute solution, Henry's Law does not hold and we must retain the activity coefficient (cf. Section 4.4) as a correction for non-ideality (*Jacobson, 1997c; Tester and Modell, 1997*).

More complicated situations do exist, of course, than that of a single gas molecule directly dissolving into the solution. Equilibria may also be established by multiple gases equilibrating with a solution via a solid intermediary formed in a surface reaction, by a species immediately dissociating upon dissolving, and by a species that effectively binds with an ion upon entering the solution. By way of examples, consider the following equilibrium reactions that are common to many reaction-based aerosol thermodynamics models (*Zhang et al., 2000*):



Equation (5.22) is exemplary of how many strong acids – including hydrochloric acid, nitric acid, and sulfuric acid – may be reasonably treated as equilibria between the gas phase and the dissolved ions rather than the dissolved gas (*Jacobson*, 1999). Equation (5.23) shows a common treatment for strong bases in which dissolution is written as the net reaction of direct dissolution and incorporation of a proton. Finally, equation (5.24) is a parameterization of a two step process in which two gas phase species react on the surface of the particle to form a solid species, in this case $\text{NH}_4\text{NO}_3 (s)$, which then dissociates into ions as it dissolves into the solution. For surface reactions such as this, the rate of the surface reaction may limit the dissolution rate rather than diffusion time-scales, as the gradient-flux model presented in equations (5.3) and (5.4) assumes. For each of these cases equation (4.4), properly applied, yields the appropriate equilibrium condition and definition of effective near-surface equilibrium partial pressure. The difficulty in many of these cases is adjusting the Kusik-Meissner method to provide the appropriate activities or mean activity ratios; the necessary procedure is discussed next in Section 5.6.1.

5.6.1 Activity Coefficients

The relationships between activities and equilibrium coefficients for gas-aerosol transfer of trace species considered in the previous section are, in some cases, poorly described by the Kusik-Meissner activity coefficient calculation method discussed in Section 4.4, which allows estimation of mean but not individual activities. For example, the equilibrium condition (4.4) properly applied to equation (5.23) is:

$$K_{eq}(T) = \left(\frac{\mathbf{m}_{\text{NH}_4^+}}{\mathbf{p}_{\text{NH}_3} \mathbf{m}_{\text{H}^+}} \right) \left(\frac{\gamma_{\text{NH}_4^+}}{\gamma_{\text{H}^+}} \right) \quad (5.25)$$

The second term on the right hand side is a ratio of un-paired activity coefficients, which is not directly predictable by the Kusik-Meissner method. The model, therefore, searches for mean activity coefficients in which the appropriate terms cancel. For the given example, we may rewrite the activity coefficient ratio:

$$\left(\frac{\gamma_{\text{NH}_4^+}}{\gamma_{\text{H}^+}} \right) = \left(\frac{\gamma_{\text{NH}_4^+} \gamma_{\text{Cl}^-}}{\gamma_{\text{H}^+} \gamma_{\text{Cl}^-}} \right) = \left(\frac{\gamma_{\text{NH}_4\text{Cl}}^2}{\gamma_{\text{HCl}}^2} \right) \quad (5.26)$$

The complication of this is that the model must track the reactions for the dissociation of both HCl and NH_4Cl so the mixed mean activity coefficient may be calculated. The reaction, if appropriate, may be included as “infinitely dissociating,” and therefore the model will not try to form HCl or

NH_4Cl and avoid the related computational expense. The increased cost of calculating the mean activities of all pairings, however, may not always be avoided in this way.

For gas-aerosol equilibria which involve surface reactions, we similarly must track the activity for a species we will not allow to form. By way of example, the equilibrium constant definition in terms of activities, as expressed in equation (4.4), properly applied to equation (5.24) yields:

$$K_{eq} = \left(\frac{\mathbf{m}_{\text{NH}_4^+} \mathbf{m}_{\text{NO}_3^-}}{\mathbf{p}_{\text{NH}_3} \mathbf{p}_{\text{HNO}_3}} \right) (\gamma_{\text{NH}_4^+} \gamma_{\text{NO}_3^-}) \quad (5.27)$$

$$= \left(\frac{\mathbf{m}_{\text{NH}_4^+} \mathbf{m}_{\text{NO}_3^-}}{\mathbf{p}_{\text{NH}_3} \mathbf{p}_{\text{HNO}_3}} \right) \gamma_{\text{NH}_4\text{NO}_3}^2 \quad (5.28)$$

Here, the activity coefficient for NH_4NO_3 , the solid that is formed on the particle's surface as part of the two-step dissolution process, is required even though we assume the quantity of this solid on the surface is negligible (and assume we are above the deliquescence point for the solid otherwise). We must therefore calculate the activity coefficients for all viable pairwise combinations of ions, even including species that are not allowed to form (certainly a counter-intuitive requirement), in order to accurately estimate mixed activity coefficients for the ion pairings that actually form.

5.6.2 Solving for Gas-Particle Equilibrium

As discussed earlier in this chapter, dissolution and water equilibration may be treated as either equilibrium or time-dependent processes. This section details the method our model uses to solve for gas-aerosol equilibrium. We solve for equilibrium of multiple dissolution reactions and multiple aerosols using a two-step procedure: first equilibrate a single aerosol with respect to one gas phase species; and second ensure that all aerosols are in simultaneous equilibrium with each gas phase species as well as in internal equilibrium themselves.

The procedure to equilibrate a single particle with the gas phase environment is identical to the procedure presented for aqueous dissociation reactions presented in Section 4.3.2. Essentially, we identify the limiting product and reactant and then iteratively step towards satisfying the appropriately specialized form of equation (4.4) within a specified error. Please refer directly to Section 4.3.2 for particulars of the approach.

The simultaneous equilibration of multiple aerosols with the gas phase is also performed with an iterative approach:

1. We step through each dissolution reaction in turn (including water content, if it is to be treated as an equilibrium process). For each reaction, we iterate over the set of all local

aerosol particles, equilibrating each one with the gas phase. We continue to iterate over the particles until each is in equilibrium with the gas phase within some pre-specified error.

2. After equilibrating the aerosols with each of the gas phase species, we equilibrate each of the local aerosols with respect to internal electrolyte dissociation reactions using the algorithm presented in Section 4.3.2. If we have iterated over the full algorithm fewer than fifty times (which is almost always the case), the mixed activity coefficients are updated as well. However, this algorithm formally need not converge if the activity coefficients are updated after each iteration. We expect that in almost all cases the system will be very near equilibrium at the fiftieth iteration but the possibility of a small oscillation between activity coefficients and composition prevents us from considering the system to be automatically equilibrated at iteration 50.
3. If any of the aerosols were out of equilibrium, either internally or with the gas phase, we start again at step 1. Otherwise, the system is taken to be at equilibrium.

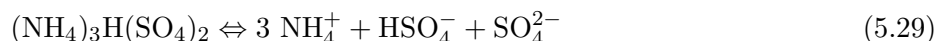
This 3-step scheme is inspired by the iterative solution methods of *Villars (1959)* and *Jacobson et al. (1996b)*.

5.6.3 Model Comparison for Urban Aerosol Case

Nenes et al. (1998) compare the equilibrium composition and partitioning of aerosol thermodynamic models – including their ISORROPIA, as well as SCAPE of *Kim et al. (1993a)* and SEQUILIB of *Pilinis and Seinfeld (1987)* – for a representative urban, marine, remote continental, and non-urban continental mass loadings taken from *Heintzenberg (1989)* and *Fitzgerald (1991)*. The models generally agree within several percent except at high relative humidities, where differences in concentrations of particular ionic species differ by as much as 30%. The discrepancies in ionic content relate to the varying treatments especially of bisulfate, equilibrium constants, thermodynamic data, water content, and deliquescence.

In this section, we compare the equilibrium partitioning and bulk aerosol composition for an urban aerosol example, as predicted by MELAM and ISORROPIA. We use a paradigmatic inorganic urban aerosol that is the basis of the *Nenes et al. (1998)* inter-comparison. Their urban aerosol case includes $3.4 \mu\text{g}/\text{m}^3$ of total ammonia, $9.143 \mu\text{g}/\text{m}^3$ of sulfuric acid, and $1.953 \mu\text{g}/\text{m}^3$ of nitric acid (*Nenes et al., 1998*), and aerosols are considered in bulk. We use a simplified reaction mechanism, presented as Tables A.2 and A.3 in Appendix A that is consistent with those used ISORROPIA and SCAPE. Since our model is formulated for high relative humidities, however, we do not allow

the formation of solid salts. ISORROPIA is run in meta-stable mode, which similarly prevents solid formation, to provide a basis for comparison. A number of reactions in Tables A.2 and A.3 have equilibrium constants listed as ∞ , which means that the reactant is not allowed to form in the solution but that the interaction of those ions is taken into account when calculating mixed activity coefficients. The only difference between the reaction sets used in ISORROPIA and SCAPE and that used in MELAM is the following dissociation of a complex inorganic solid:



MELAM is not able to include a single electrolyte dissociating into three components, nor is the implementation of the mixed activity coefficients method able to consider the system. However, that ISORROPIA and SCAPE include the three-way ionic interaction when considering the mixture of activity coefficients is sufficient to produce slightly different predictions (cf. the discussion of how the activities of electrolytes not allowed to form in a model affect the mixed activities of all other electrolytes at the end of Section 5.6). For all reactions, appropriate thermodynamic data from *Nenes et al.* (1998) are used, which are not always identical to MELAM’s preferred Kusik-Meissner q values which are tabulated in Table A.4 of Appendix A.

A comparison of the equilibrium liquid water contents is presented in Figure 5-4. Panel 5-4(a) shows bulk phase mass concentration as predicted by the two models and Panel 5-4(b) shows the ratio of the mass predicted by MELAM to that predicted by ISORROPIA. Note that MELAM predicts greater water content at most relative humidities except in the 75% to 80% range where they are nearly identical. This is consistent with what we saw in Figure 5-3.

More interesting is the comparison of equilibrium ion concentrations presented in Figure 5-5. That figure includes three panels comparing MELAM’s and ISORROPIA’s predicted gas-aerosol partitioning of: (a) nitric acid, (b) ammonia, and (c) bisulfate-sulfate partitioning. For the purposes of this comparison, MELAM did not solve for equilibrium water content using its own method, but instead rather simply used that predicted by ISORROPIA at each relative humidity, thereby isolating discrepancies in the partitioning, dissociation, and activity prediction portions of the thermodynamic schemes. MELAM predicts slightly more aqueous nitrate and ammonium than ISORROPIA, and a lower bisulfate to sulfate ratio. We know, however, from Section 4.4.3 that the ISORROPIA and MELAM sulfate / bisulfate partitioning methods are nearly identical in binary sulfuric acid / water systems. Hence, we know that the partitioning discrepancies in this case are due to differences in the influence of other species on the predicted mean activities of sulfate and

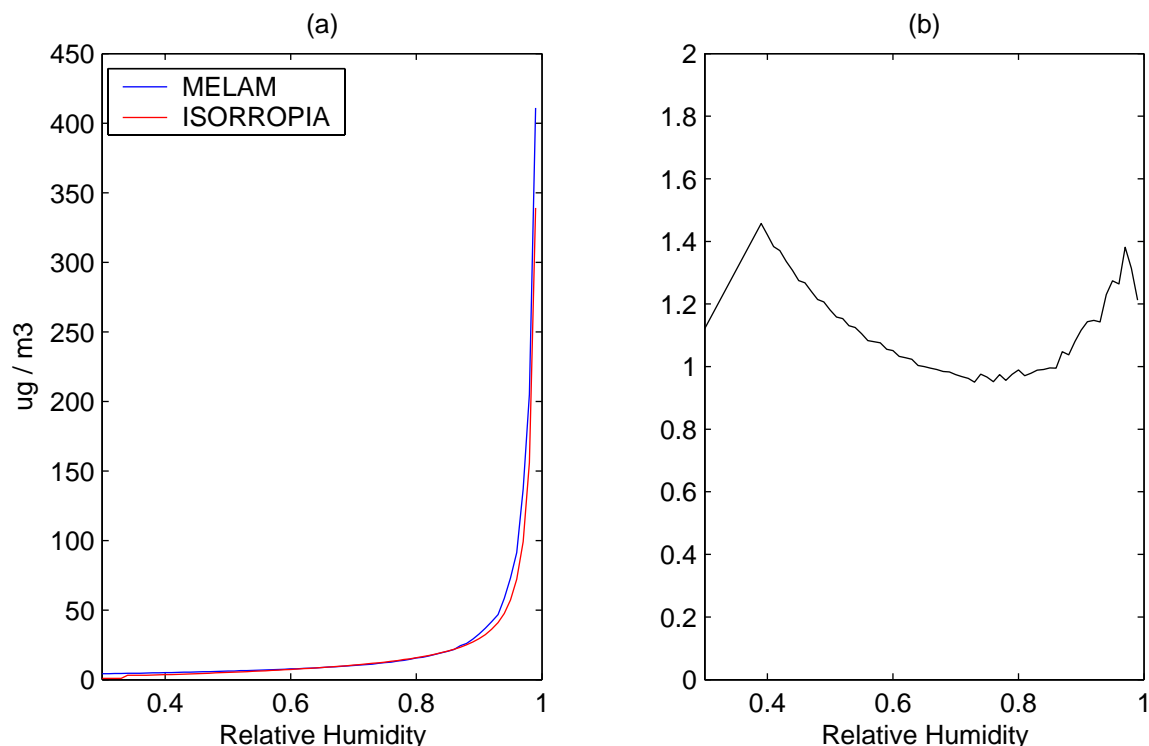


Figure 5-4: Comparison of aerosol liquid water content for the urban aerosol example as predicted by MELAM and ISORROPIA: (a) is bulk mass content in $\mu\text{g}/\text{m}^3$; (b) is ratio of the content predicted by MELAM divided by that predicted by ISORROPIA.

bisulfate dissociation. The differences, however, are small in each case and well within the range seen in the *Nenes et al.* (1998) inter-comparisons.

Note that the interactions between ions are critical to these results. MELAM's results are very different if the ion pairings that lead to solids are not included when calculating mixed activity coefficients. Thermodynamically, this is simply a statement that all ions interact with all other ions (we assume that there are only pairwise interactions, but ternary and higher order interactions of course also occur). Numerically, however, this means that electrolyte dissociation reactions must be included for all pairwise interactions even if the electrolyte never forms. This is why so many "infinitely dissociating" reactions are included in the simplified mechanism in Appendix A.

The linear increase in the predicted water content ratio presented in Panel 5-4(b) at very low relative humidities, and the discontinuity in ammonia and sulfate partitioning seen in Figure 5-5 are related to artificial maximum values MELAM imposes on predicted activity coefficients. The Kusik-Meissner theory is only relevant at ionic strengths that lie within the range explored in the validating experiments, which is typically much lower than those seen at 0.3 to 0.4 \mathcal{RH} for aqueous aerosols, which may be quite concentrated. The artificial limit is imposed to prevent

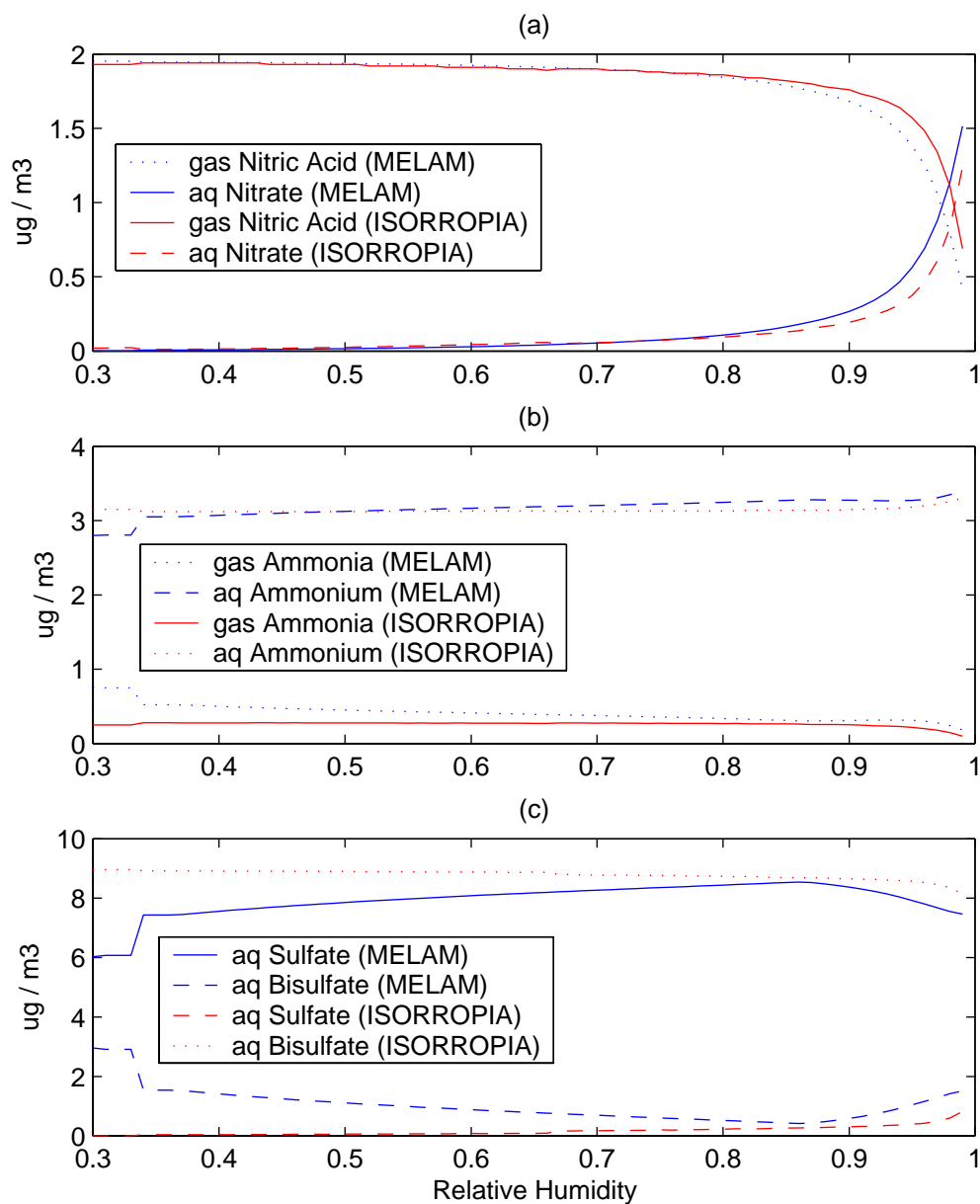


Figure 5-5: Comparison of electrolyte partitioning for urban aerosol by MELAM and ISORROPIA. Panel (a) compares gas-aerosol partitioning of nitric acid; panel (b) compares gas-aerosol partitioning of ammonia; and panel (c) compares sulfate-bisulfate partitioning.

the activity coefficients from growing without bounds at low \mathcal{RH} , which makes equilibration of water and electrolyte concentrations difficult; recall the dependence of water activity on the binary electrolytic activities through equations (5.13) and (5.17). All of the models use some method to prevent the unrecoverable instabilities caused by very high predicted activity coefficients at low relative humidities (i.e., in highly concentrated solutions). In MELAM, this amounts to capping the ionic strength (I) at an artificial maximum of 12 mol kg^{-1} when calculating mean electrolyte activities in equation (4.18). The experimental data used to determine the q values for use in equation (4.18) range from near the dilute to some upper ionic strength that usually lies between 8 and 20 mol kg^{-1} (*Lobo*, 1989) and relies on the data available a case-by-case basis. Of course, the ionic strength is allowed to surpass 12 mol kg^{-1} in MELAM; the limit simply imposes:

$$\gamma_i(I \geq 12 \text{ mol kg}^{-1}) = \gamma_i(I = 12 \text{ mol kg}^{-1}) \quad (5.30)$$

When such a cap is not imposed, the calculated activities grow without bounds in the low \mathcal{RH} environments that lead to such elevated ionic strengths and prevent the water equilibration routine from converging to the correct solution when the \mathcal{RH} rises, effecting an artificial hysteresis related to this mis-application of Kusik-Meissner theory beyond ionic strength ranges over which it has been constrained.

5.7 The Diffusion Limited Aerosol Growth Model

Adsorption or condensation of a gas onto a droplet may be limited either by the flux to the particle surface, the rate of some surface reaction (and thus the surface area), or the rate of some internal chemical reaction (and thus the particle volume). As is common in condensational modeling, we assume that diffusion limits condensation and use the appropriate form of Fick's Law of Diffusion (*Pruppacher and Klett*, 1997). In this formulation, gradients of condensable vapor density (ρ_v) between the ambient environment and particle surface drive condensation. Since we explicitly account for aqueous chemistry and electrolyte behavior, volume limitation is effectively incorporated into the model; surface limitations are not, however. The physical model is one of diffusion limited growth, the nuances of which are discussed in this section.

5.7.1 The Quasi-Stationary Equation

For all species, the gradient between the gas phase concentration at the particle surface and at an appropriate distance from the particle drives a condensational flux onto or away from the droplet, as described by equations (5.3) and (5.4). For water vapor, this driving force is equivalently a scaled gradient between the relative humidity (\mathcal{RH}) and the ratio of the modified saturation vapor pressure to the saturation vapor pressure over a flat surface of pure water (S'). Determining the concentration at the particle surface and equilibrium concentrations is at the heart of the condensation and dissolution routines.

Fick (1855) provided an early theoretical treatment of this process in the form of two diffusion equations. *Maxwell* (1990) and then *Langmuir* (1918a) integrated these under appropriate conditions (assuming, amongst other things, the particle to be isolated from the influence of other particles in the gaseous environment), to reach the quasi-stationary equation. This equation is an expression of condensational mass-flux to a droplet, which we saw earlier in a simplified form as equation (5.3):

$$\frac{dm_{a,i}}{dt} = 4\pi r_a D_i [\rho_{v,i}(\infty) - \rho_{v,a,i}(r)] \quad (5.31)$$

Here, $m_{a,i}$ is the mass of component i in the particle, r_a is the particle radius, and D_i is the molecular diffusion coefficient of vapor i in air. This original theory strongly overestimates growth by water condensation for sub-micron particles. But corrections to D_i for time dependence, non-continuity of the ambient gas, and other non-ideal behavior bring the model into accordance with measurements (*Pruppacher and Klett, 1997*).

5.7.2 Mass-Flux Model for Multi-Component Aerosol Growth

When vapor condenses on an aerosol, latent heat of vaporization (L_e) is released and causes a warming at the surface of the drop, introducing a thermal gradient and concomitant conductive heating rate. Combining this effect with equation (5.31) and standard thermodynamics, one may derive the mass-flux form of the growth equation (*Pruppacher and Klett, 1997; Jacobson, 1999*):

$$\frac{dm_i}{dt} = \{4\pi r_a D_i' (p_i - p_{a,i,s})\} \left\{ \frac{D_i' L_i p_{a,i,s}}{\kappa_d' T} \left(\frac{L_i M_i}{R^* T} - 1 \right) + \frac{R^* T}{M_i} \right\}^{-1} \quad (5.32)$$

In which subscript i implies that the variable depends on the properties of the particular species, κ_d' is the corrected thermal conductivity of dry air, R^* is the universal gas constant, T is Kelvin

temperature, p_i is the ambient partial pressure of the condensing gas, $p_{a,i,s}$ is the saturation vapor pressure of vapor i at the surface of the particle, and M_i is the molecular mass. A prime signals a value corrected for collisional geometry, sticking probability, or thermal ventilation effects (*Jacobson*, 1999; *Pruppacher and Klett*, 1997; *Gorbunov and Hamilton*, 1996; *Gorbunov et al.*, 1998; *Ansari and Pandis*, 2000).

Using the appropriate form of the equation of state ($p = C R^* T$) and defining an effective rate constant (k_i), we may restate the mass transfer rate as a simple ordinary differential equation in which the rate of change of the particle-phase concentration (c_i) of species i is proportional to the gradient between the local ambient (C_i) and effective saturation ($C'_{a,i}$) concentration just above the interface of the particle and gas phases:

$$\frac{dc_i}{dt} = k_i (C_i - C'_{a,i}) \quad (5.33)$$

To facilitate discussion, we define $C'_{a,i}$ to be the product of two quantities: a dimensionless equilibrium saturation ratio of the particle-specific near-surface saturation concentration to the saturation concentration over a flat interface of an equivalent solution ($S'_{a,i}$), and the equilibrium concentration above a flat interface of an equivalent solution ($C_{a,i}$) (*Jacobson*, 1997c). Sections 5.8.1 and 5.8.2, address the determination of $S'_{a,i}$ for various aerosol types and condensing species. The rate constant k_i is defined to be:

$$k_i \equiv 4 \pi r_a D_i' \left\{ \frac{D_i' L_i M_i S'_{a,i} C_{s,i}}{\kappa_d' T} \left(\frac{L_i M_i}{R^* T} - 1 \right) + 1 \right\}^{-1} \quad (5.34)$$

The use of this formulation while integrating condensation and dissolution over time is discussed in Sections 5.8 and 5.9, respectively, and we address the necessary corrections to the terms in equation (5.34) in the next Section 5.7.3.

5.7.3 Corrections to Condensation Rate Constant Terms

The original derivation of the quasi-stationary equation (5.31) scales the vapor density gradient simply by the product of the particle surface area ($4\pi r_a$) and the molecular diffusion coefficient of the vapor in air (D_i) and has been shown to over-predict the mass flux (*Pruppacher and Klett*, 1997; *Seinfeld and Pandis*, 1998). Thermal ventilation and other effects are incorporated into equation (5.34) and we will now further develop corrections to the molecular diffusion coefficient and thermal conductivity of air.

Corrections to the Molecular Diffusion Coefficient

The molecular diffusion coefficient is the constant relating the net kinetic movement of molecules to their average gradient and is in units of length squared divided by time. Its local value is used to scale gradients in gradient-flux-based transport models. The standard definition of D_i for a trace species i depends on both the traits of the trace species as well as those of an average air molecule:

$$D_i = \frac{3}{8 N_A d_{i,a}^2 \rho_a} \sqrt{\frac{R^* T M_a (M_i + M_a)}{2\pi M_i}} \quad (5.35)$$

In which N_A is Avogadro's number, $d_{i,a}$ is the collision diameter of a molecule of species i in a background gas a (approximated here by a characteristic value $\bar{d}_{i,a}$, taken to be the same for all collisions), ρ_a is the air density, and M_a and M_i are the molecular masses of air and of the trace species, respectively (*Davis*, 1983).

For the case at hand, we must further correct D_i to account for collisional geometry and sticking probability (together called $\varsigma_{c,a}^D$) and ventilation ($\varsigma_{V,a}^D$). We then define the corrected diffusion coefficient D_i' :

$$D_i' = D_i \varsigma_{c,a}^D \varsigma_{V,a}^D \quad (5.36)$$

The coefficient $\varsigma_{c,a}^D$ is necessary to account for the disparate relative sizes of the small gas molecules to the much larger aerosols, the fact that either or both may lie out of the continuum regime, and that a molecule will not necessarily stick to the aerosols if they collide. The second coefficient $\varsigma_{V,a}^D$ is necessary because motions of the relatively large aerosol particle cause turbulent wakes that entrain molecules and enhance the likelihood of collision (*Pruppacher and Klett*, 1997; *Jacobson*, 1999).

Following *Pruppacher and Klett* (1997) and *Jacobson* (1999), we write a combined expression for the collisional geometry and sticking probability correction:

$$\varsigma_{c,a}^D = \left(1 + \left\{ \frac{1.33 + 0.71 \text{Kn}_{a,i}^{-1}}{1 + \text{Kn}_{a,i}^{-1}} + \frac{4(1 - \alpha_i)}{3\alpha_i} \right\} \text{Kn}_{a,i} \right)^{-1} \quad (5.37)$$

α_i is the mass accommodation coefficient for i which is the likelihood that a molecule of a particular gas will attach to the particle upon impact (a scalar between zero and one), and Kn_i is the non-dimensional Knudsen number. The primary effect of a low mass accommodation coefficient is to decrease the mass transfer rate by lowering $k_{a,i}$ in equation (5.34). *Meng and Seinfeld* (1996)

studied the relationship between the mass accommodation coefficient and expected equilibration times for volatile species; their key plot is presented here as Figure 5-1 and discussed in Section 1.2.3. Note that α_i is a strong function of temperature (*Vandoren et al.*, 1990; *Shi et al.*, 1999; *Li et al.*, 2001). Current estimates of α_i for volatile aqueous phase species are listed in Table A.1 of Appendix A. Notice in that table that a number of the accommodation coefficients are estimated by a default value of 0.05. The uncertainty in these estimates remain a major limiting factor in many studies in which dissolution times matter.

The Knudsen Number is the ratio of the mean free path of a gas molecule to the radius of an aerosol particle ($\text{Kn}_{a,i} \equiv \lambda_i/r_a$). When $\text{Kn}_{a,i}$ is large, the particle encounters molecules of species i much less frequently than when $\text{Kn}_{a,i}$ is small (these two limits are the slip and continuum regimes, respectively). Notice that $\varsigma_{c,a}^D$ becomes very small when $\text{Kn}_{a,i}$ is large and approaches unity when $\text{Kn}_{a,i}$ approaches zero. Considering these limiting cases in the context of equation (5.34), we see the intuitive behavior that less frequent encounters between molecules of i and an aerosol leads to a slower condensation rate.

The ventilation factor is formulated as a scaling factor that is always greater than or equal to unity, as the entraining wake of the particle acts only to increase the flux to the particle surface relative to the flux when the particle is at rest (*Jacobson*, 1999). $\varsigma_{V,a}^D$ is a non-continuous function, broken into two regimes by the diagnostic parameter $x_{a,i}$:

$$x_{a,i} = \sqrt{Re} \sqrt[3]{Sc_i} \quad (5.38)$$

Here, the Reynolds Number (Re) is defined to be the particle diameter multiplied by the terminal fall velocity divided by the kinetic viscosity of air, and is essentially the ratio of inertial force of the particle to the viscous forces of the air (*Seinfeld and Pandis*, 1998). The Schmidt Number (Sc_i) is the ratio of the kinematic viscosity of air to the uncorrected molecular diffusion coefficient of the gas i , and is essentially the ratio of convective and kinetic diffusion rates at a constant Reynolds number (*Fuchs*, 1964). The kinematic viscosity of air (ν_a), used in the definition of both of these ratios, is itself the ratio of the dynamic viscosity of air to the air density:

$$\nu_a = \frac{\eta_{air}}{\rho_a} \quad (5.39)$$

Where the dynamic viscosity of air is well parameterized by Sutherland's Equation (*List*, 1984):

$$\eta_{air} = 1.8325 \times 10^{-4} \left(\frac{416.16}{T + 120} \right) \left(\frac{T}{296.16} \right)^{1.5} \quad (5.40)$$

We define $\varsigma_{V,a}^D$ in two regimes (*Jacobson*, 1999):

$$\varsigma_{V,a}^D = \begin{cases} 1 + 0.108 x_{a,i}^2 & : x_{a,i} \leq 1.4 \\ 0.78 + 0.308 x_{a,i} & : x_{a,i} > 1.4 \end{cases} \quad (5.41)$$

Note that the intuitive behavior holds: there is no correction (i.e., $\varsigma_{V,a}^D = 1$) when $x_{a,i}$ is very small, which means that Re is very small and the particle is falling extremely slowly (because it is small). In other words, a very small particle causes no wake. In the other extreme, flow towards a very large particle can be enhanced many times as Re grows larger.

Corrections to the Thermal Viscosity of Air

Corrections to the thermal conductivity of air (κ_d) are parallel in structure to those for the molecular diffusion coefficient, requiring a collisional geometry term, a thermal accommodation correction term (these two are grouped as $\varsigma_{c,a}^{\kappa_d}$), and a correction for ventilation ($\varsigma_{V,a}^{\kappa_d}$):

$$\kappa'_d = \kappa_d \varsigma_{c,a}^{\kappa_d} \varsigma_{V,a}^{\kappa_d} \quad (5.42)$$

We conveniently write the definition of $\varsigma_{V,a}^{\kappa_d}$ to closely resemble the form of equation (5.37):

$$\varsigma_{V,a}^{\kappa_d} = \left(1 + \left[\frac{1.33 + 0.71 \text{Kn}_{e,a,i}^{-1}}{1 + \text{Kn}_{e,a,i}^{-1}} + \frac{4(1 - \alpha_h)}{3\alpha_h} \right] \text{Kn}_{e,a,i} \right)^{-1} \quad (5.43)$$

In this instance, $\text{Kn}_{e,a,i}$ is the Knudsen number for the energy of the particle which is defined to be the thermal mean free path of the gas phase species divided by the particle radius, or the expected distance a gas molecule travels without exchanging energy with a particle (*Jacobson*, 1999). Here, α_h is the thermal accommodation coefficient, or the fraction of molecules that interact with (and are not incorporated into) a particle that reach thermal equilibrium with it; here we use a characteristic value of 0.96 (*Jacobson*, 1999).

The thermal ventilation correction ($\varsigma_{V,a}^{\kappa_d}$) is bifurcated as was the expression for the molecular

diffusion case, but in this case we use the diagnostic parameter $y_{a,i}$:

$$y_{a,i} = \sqrt{Re} \sqrt[3]{Pr} \quad (5.44)$$

In which the Prandtl Number (Pr) is proportional to the dynamic viscosity of air (η_{air} , defined in equation (5.40)) and the specific heat of moist air at constant pressure and inversely proportional to the thermal conductivity (κ_d) (*Jacobson*, 1999). Given this definition, we again define the ventilation correction coefficient as a piecewise continuous function:

$$\zeta_{V,a}^{\kappa_d} = \begin{cases} 1 + 0.108 y_{a,i}^2 & : y_{a,i} \leq 1.4 \\ 0.78 + 0.308 y_{a,i} & : y_{a,i} > 1.4 \end{cases} \quad (5.45)$$

These corrections to the condensational rate constant are in widespread use and have proven successful in multiple studies reviewed in *Pruppacher and Klett* (1997).

5.8 Water Condensation

Considering the diffusion-limited condensation equation (5.33) in the context of water vapor condensation, we note that C_i is equal to $(\mathcal{RH} C_w)$ and $C'_{a,i}$ to $(S' C_{s,w})$, in which $C_{s,w}$ is the saturation water vapor concentration with respect to a flat interface with liquid water at the local pressure and S' is the equilibrium super-saturation correction to be defined shortly. This allows us to rewrite equation (5.33) acknowledging S' , calculation of which is the key to the water condensation routine:

$$\frac{dc_w}{dt} = k_w C_{s,w} (\mathcal{RH} - S') \quad (5.46)$$

Note that k_w is positive definite and so the rate of change of the aerosol water content (c_w) is positive only when the ambient relative humidity is greater than S' . As we discuss in sections to follow, S' reaches a maximum, critical value (S^*) when the particle reaches some associated critical radius (r_a^*) during condensational growth. Once the aerosol grows larger than r_a^* , it is considered *activated*. S^* is greater than unity, meaning activation may only occur in an environment super-saturated with respect to liquid water. For a particle to grow past r_a^* , the ambient relative humidity must be larger than S^* for a sufficiently long time. Once activated, growth is energetically favored and S' decreases as the particle grows further.

A number of theories have been developed to deal with calculating S' for idealized circum-

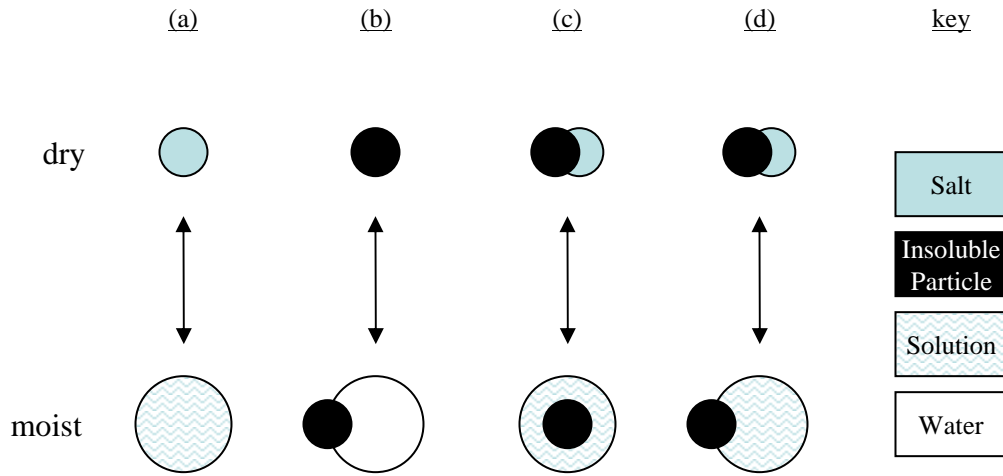


Figure 5-6: Four theoretical targets of water condensation: (a) a completely soluble salt particle; (b) a completely insoluble spherical particle; (c) a mixed salt / insoluble particle; and (d) a mixed salt / partially wettable insoluble particle. Figure adapted from *Gorbunov and Hamilton (1997)*

stances. Most of these theories assume that the particles are spherical and that water is negligibly compressible, and that deviations from these assumptions do not significantly alter vapor pressure effects (*Pruppacher and Klett, 1997*). Figure 5-6 is a schematic showing four situations for which S' has been theoretically considered: Panel 5-6(a) depicts the example of a completely soluble salt aerosol particle considered by *Köhler (1936)*; Panel 5-6(b) shows a completely insoluble particle considered by *Fletcher (1976)*; Panel 5-6(c) shows a salt droplet containing an insoluble core considered by *Hänel (1976)*; and Panel 5-6(d) shows a solution embryo growing on a partially wettable insoluble droplet considered by *Gorbunov and Hamilton (1997)*.

Many studies consider only the case of water condensing on a completely soluble salt shown in Panel 5-6(a) which was addressed by *Köhler (1936)*. This theory is discussed in Section 5.8.1 and fully implemented in the model. However, many aerosols, including those considered here, contain both insoluble substances and soluble electrolytes. *Hänel (1976)* found that the presence of an insoluble core significantly alters S' . *Gorbunov and Hamilton (1997)* note, however, that the simplified situation of an insoluble core completely contained within a solution droplet, as considered in *Hänel (1976)*, is an unusual sub-case of what is seen in nature. Insoluble aerosols are often partially wettable and thus the Hänel model is not appropriate; in those cases growth is better represented as the growth of a droplet embryo that forms a non-zero contact angle as shown in Panel 5-6(d). This situation is discussed later at length in Section 5.8.2.

5.8.1 Condensational Growth of Soluble Aerosol Particles

Köhler (1936) presents the classic theory for determining S' and S^* for salt particles, in which effects related to curvature of a droplet's interface compete with the disruption of surface tension by a dissolved solute. Its formulation, but not its approximations, is still appropriate for completely soluble, inorganic aerosols (*Jacobson*, 1997a). In this section, we discuss the Köhler-inspired formulation we use in this model, and then discuss the behavior and intuition gained from the original formulation.

In solution droplets, some solute molecules replace water at the gas-liquid interface and hydrate, thereby reducing the overall saturation vapor pressure over the drop and increasing the condensational mass flux onto its surface (*Pruppacher and Klett*, 1997). The adjusted vapor pressure over the flat surface of a solution is approximated by Raoult's law:

$$\left(\frac{C'_{s,i}}{C_{s,i}} \right)_{\text{Solute}} \equiv a_w \approx \frac{n_w}{n_w + n_s} \quad (5.47)$$

Here, $C_{s,i}$ is the equilibrium concentration of trace species i over a solution uncorrected for solute interference at the surface, $C'_{s,i}$ is the saturation concentration of water over a flat surface corrected for solute properties, n_w is the number of water molecules in the drop, and n_s the number of all solute molecules (*Pruppacher and Klett*, 1997; *Tester and Modell*, 1997). It is common to consider the growth of an initially dry particle of a given mass assuming that no solute is added to the particle as it grows (as may happen by dissolution or coagulation in reality). For such a particle, equation (5.47) is a monotonically increasing function, which asymptotes to zero for the smallest (driest) particles and unity for the largest. This is the so-called solute effect.

Note that Raoult's Law applies to ideal solutions in which chemical activities approach unity (*McQuarrie and Simon*, 1997), which is a requirement that aerosols at high relative humidities (that are therefore quite dilute) satisfy reasonably well, but that aerosols at low relative humidity do not. Note that the ratios of concentrations in equation (5.47) is equal to the ratio of partial pressures in equation (5.6), and so Raoult's law is truly an approximation of the water activity (a_w) in dilute solutions, as indicated in equation (5.47). It is numerically useful to use this approximation when computing condensation since its derivative is easily calculated, while the formulation for a_w presented in Section 5.5 is much less easily differentiated. (The Jacobian, discussed later in Section 5.10, will require this derivative.) That this approximation is better in dilute solutions (i.e., at high relative humidities), argues for balancing the errors caused by assuming an aerosol is in a constant equilibrium (calculated with better approximations of a_w) with the errors caused by

assuming a flux-based formulation (calculated using Raoult's Law). Consider Figure 5-4(a), which presents the equilibrium water content for a particular characteristic urban aerosol distribution that is to some extent representative. Note that the aerosol liquid water content grows slowly from low \mathcal{RH} to \mathcal{RH} of 85% or 90%, at which point it rises dramatically. In that high growth range, the ionic strengths of the solution are reasonably low, between 0 and 10 mol kg⁻¹ for highly acidic sulfate aerosols, and only drop below 1 mol kg⁻¹ just below 99% \mathcal{RH} . Because activity coefficients may deviate substantially from unity for ionic strengths even less than unity (cf. Figures 4-2, 4-3, 4-4, and 4-5 in Chapter 4), it is reasonably accurate to consider equilibrium water content except for situations quite near to saturation, if not explicitly super-saturated.

Opposing the solute effect is the drive to reduce surface energy which leads molecules to desorb more readily from curved surfaces than from flat. This is the Kelvin effect, which we approximate by:

$$\left(\frac{C'_s}{C_s}\right)_{Kelvin} = \exp\left(\frac{2 \sigma_{s/a} m_p}{r_a R^* T \rho}\right) \quad (5.48)$$

Here, $\sigma_{s/a}$ is the surface tension of the droplet, R^* is the universal gas constant, and m_p is the mass and ρ is the density of the solution particle (*Pruppacher and Klett, 1997*). This function monotonically decreases with increasing particle size, and asymptotes to infinity for the smallest particles and unity for the largest.

In the case of dilute droplets, and ignoring radiative cooling effects, we combine equations (5.47) and (5.48), the derived expressions for the the solute and Kelvin effects, which is an appropriate estimate of S' for dilute droplets:

$$S' \approx \left(\frac{C'_s}{C_s}\right)_{Solute} \left(\frac{C'_s}{C_s}\right)_{Kelvin} = \left(\frac{n_w}{n_w + n_s}\right) \exp\left(\frac{2 \sigma_{s/a} m_p}{r R^* T \rho}\right) \quad (5.49)$$

Note that equation (5.18), the equilibrium condition used for water content in Section 5.5.4, is also the equilibrium condition found by using equation (5.49) to approximate S' in equation (5.46) except that in this case we have assumed Raoult's Law holds. Also note that (5.49) is the product of one function that monotonically decreases and one that monotonically increases with increasing r_a . The curvature of the product of the two curves is very important to understanding cloud activation; we will discuss it in the context of the Köhler example.

The Köhler Example

To illustrate the relationship between the competing curvature and solute effects, we employ a historically important approximation to equation (5.49) that is used in many models that do not explicitly treat aerosol thermodynamics but not including MELAM. Assume first that a particle is comprised entirely of an electrolyte that fully dissociates such that for each single molecule of electrolyte, we have i_v molecules of solute. The scalar i_v is known as the van't Hoff factor and is a crude substitute for the equilibrium thermodynamic state of electrolytes predicted using activity coefficients as detailed in Section 4.3 (*Pruppacher and Klett, 1997*). Next we approximate equation (5.47) as a function of the radius and mass of the particle and molecular attributes of the solute and of water:

$$a_w = \left(\frac{C'_{s,i}}{C_s} \right)_{Solute} = \frac{n_w}{n_w + n_s} \approx \exp \left(-\frac{3 M_w i_v m_S}{4\pi r_a^3 \rho_p M_S} \right) \quad (5.50)$$

Here, m_S is the mass of solute in the particle, M_S is the molecular weight of the solute and M_w of water.

We apply this approximation to equation (5.49) and take the first order Taylor approximation to write what is often known as the Köhler equation:

$$S' \approx 1 - \left(\frac{3 M_w i_v m_S}{4\pi r^3 \rho_p M_S} \right) + \left(\frac{2 \sigma_{s/a} m_p}{r_a R^* T \rho} \right) \quad (5.51)$$

We then cast this as a function of radius and coefficients A and B :

$$S' \equiv 1 - \frac{A}{r_a^3} + \frac{B}{r_a} \quad (5.52)$$

$$\text{where } A \equiv \left(\frac{3 M_w i_v m_S}{4\pi \rho_p M_S} \right) \quad \text{and} \quad B \equiv \left(\frac{2 \sigma_{s/a} m_p}{R^* T \rho} \right) \quad (5.53)$$

We use this expression to derive a maximum equilibrium saturation ratio (S^*) and its corresponding radius (r_a^*):

$$S^* = 1 + \sqrt{\frac{4B^3}{27A}} \quad ; \quad r_a^* = \sqrt{\frac{3A}{B}} \quad (5.54)$$

Which gives the maximum value of S' and the corresponding critical radius for an aerosol particle of a defined solute content that grows by water condensation only.

Figure 5-7 shows $\left(\frac{C'_s}{C_s} \right)_{Kelvin}$ (upper line), $\left(\frac{C'_s}{C_s} \right)_{Solute}$ (bottom line), and S' calculated using

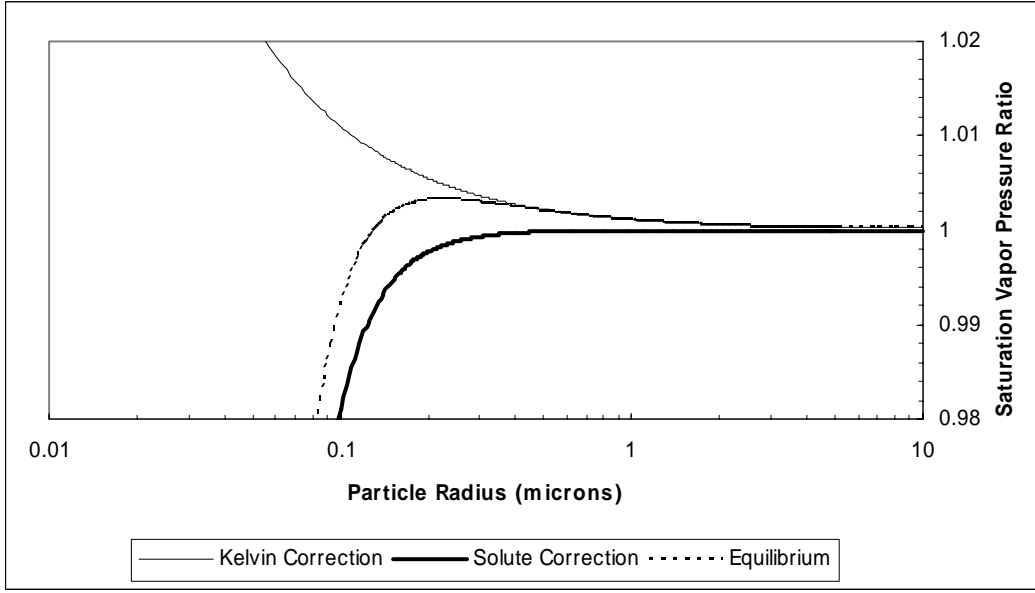


Figure 5-7: Equilibrium saturation vapor pressure curve as a ratio to a flat surface (dotted line), and the contributions from the Kelvin (upper line) and solute (lower line) effects for a sulfate particle aerosol with a $0.01 \mu\text{m}$ dry radius. (*Meng and Seinfeld, 1996*)

equations (5.48), (5.50), and (5.51) for the example of a $0.01 \mu\text{m}$ dry-radius sulfate particle. Note that S' rises, peaks above unity at a critical radius between $0.1 \mu\text{m}$ and $0.2 \mu\text{m}$, and asymptotes towards unity as the radius increases.

We know from equation (5.46) that a particle is only at equilibrium with respect to water vapor when $\mathcal{RH} = S'$. Much below saturation, that equilibrium lies substantially to the left of the critical radius. At saturation, the particle has two equilibria: one at a radius below r_a^* and another at a radius substantially larger than it. However, to grow from the smaller equilibrium size to the larger, \mathcal{RH} must surpass S^* for long enough for the particle to grow to a radius greater than r_a^* . As particles grow, of course, water is transferred from the vapor to liquid phase and thus \mathcal{RH} decreases. As discussed in Section 1.2.3, whether a particle is able to grow larger than r_a^* is a function of how quickly the super-saturation is ameliorated by both that particle and other nearby particles. In an equilibrium framework, models must assume that if \mathcal{RH} is ever greater than unity, the entire aerosol fraction satisfying $S^* \leq \mathcal{RH}$ must activate, meaning they grow until \mathcal{RH} decreases enough so that $S' = \mathcal{RH}$ or they grow heavy and fall out of the atmosphere.

5.8.2 Droplet Formation on Mixed Soluble-Insoluble Aerosol Particles

Activation schemes conventionally rely on Köhler equilibrium theory, discussed in Section 5.8.1 above, for condensation on soluble salt particles, or Fletcher theory for condensation on insoluble

particles (cf. *Pruppacher and Klett*, 1997; *Fletcher*, 1976). Both of these are insufficient models of condensation for our purposes. Although some purely inorganic soluble systems will be considered using the MELAM model in this thesis, MELAM is able to include insoluble substances according to the theory of *Gorbunov and Hamilton* (1996) and *Gorbunov and Hamilton* (1997) which is defined in this section.

There is evidence that aerosol-phase inorganic species, especially sulfates, reside in mixed aerosols that include organics, soots, dust particles, and other less volatile constituents. This is true not only in heavily polluted areas such as the out-flow region from the Indian subcontinent (*Guazzotti et al.*, 2001), where we might expect it, but also in significant amounts in the remote marine troposphere (*Pósfai et al.*, 1999). The widespread presence of such internally mixed particles require more complex theoretical approaches than the simple inorganic equilibrium theories already reviewed. We will use the Gorbunov theory presented here to study the cloud-forming potential of these aerosols in Section 7.3.

When emitted, soot particles generally are quite hydrophobic but aging via oxidation, especially in the presence of nitric acid, can make them more hydrophilic (*Weingartner et al.*, 1995; *Chughtai et al.*, 1996). Also, soot particles, over time, typically acquire a volatile inorganic coating via condensation or accrete onto an inorganic aerosol via coagulation, introducing hydrophilic substances (e.g., *Pósfai et al.*, 2003). The aging process allows aerosols to become wettable and water may condense to form bead on their surface, forming a contact angle with the particle that is characterizable experimentally (e.g., *Zuberi*, 2003). These aged soot particles are a fair analogy to the idealized insoluble particle with defined contact angle considered by the Gorbunov theory. Complexes of soot particles may also act as points of condensation, in which case the area near the point of contact between two spheres may form an effectively negative angle, negative Kelvin effect, and point of condensation (*Crouzet and Marlow*, 1995); such cases are beyond the capabilities of the Gorbunov model and are not considered here. A study of the role of the presence of single insoluble spheres in cloud formation will be discussed in Section 7.3.

Consider the idealized example of a partially wettable insoluble spherical aerosol that is attached to some amount of salt solution, schematically presented in Panels 5-6(d) and 5-8(a). During condensational growth, the insoluble aerosol core maintains interfaces with both the gas phase and the so-called droplet or solution embryo. The embryo interface has a characteristic contact angle (θ) with the insoluble core, the angle the solution embryo's interface with the gas phase forms with the insoluble aerosol's surface as shown in Figure 5-8(b).

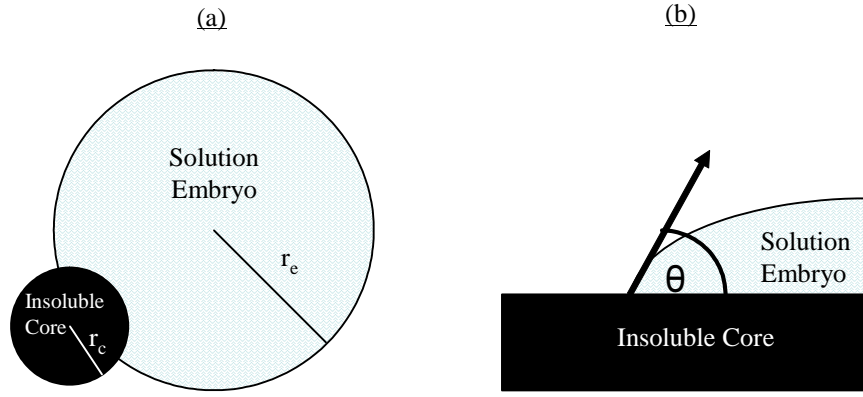


Figure 5-8: Schematic representation of: (a) the moist combined electrolyte / insoluble core aerosol; and (b) the contact angle

The contact angle itself may be defined in terms of the free energies of the air-solid ($\sigma_{a/sd}$), solution-solid ($\sigma_{s/sd}$), and air-solution ($\sigma_{s/a}$) interfaces (*Fletcher, 1976; Gorbunov and Hamilton, 1997*):

$$\cos \theta = \frac{\sigma_{a/sd} - \sigma_{s/sd}}{\sigma_{s/a}} \quad (5.55)$$

The free energy $\sigma_{s/a}$ is, in fact, the surface tension of air-solution interface that we discussed at length and parameterized in Section 4.6. Both $\sigma_{s/a}$ and $\sigma_{s/sd}$ depend directly on the solution properties and composition of the embryo, $\sigma_{s/sd}$ less so than $\sigma_{s/a}$, while $\sigma_{a/sd}$ does not (*Pruppacher and Klett, 1997*). For completely hydrophobic particles, $\theta = 180^\circ$ and $\cos \theta = -1$, implying that the embryo forms a bead on the insoluble core's surface, that the two particles are unattached. For a completely wettable surface, $\theta = 0^\circ$ and $\cos \theta = 1$, implying that the embryo entirely incorporates the insoluble core. These two limiting examples are the Köhler and Fletcher examples pictured in Figures 5-6(a) and 5-6(c), respectively. For cases of atmospheric relevance, the full range of variation of $\cos \theta$ during condensational growth is about 2% and validly approximated to be constant (*Gorbunov and Hamilton, 1997*). *Zuberi (2003)* directly measures θ for representative sooty surfaces (artificially aged in the lab), and we will use such experiments to calculate θ rather than considering the interfacial free energies.

Through a consideration of the free energy dynamics of embryo formation and growth for the mixed electrolyte / insoluble core aerosol, *Gorbunov and Hamilton (1997)* formulate a parameteri-

zation of S' for this case:

$$S' = a_w \exp \left[\frac{\sigma_{s/a}}{R^* T} \frac{M_w}{\rho} \frac{dr_e}{dv_e} \left(\frac{dA_{a/s}}{dr_e} - \cos \theta \frac{dA_{s/sd}}{dr_e} \right) \right] \quad (5.56)$$

Here, M_w is the molecular mass of water, ρ is the density of the solution, $A_{a/s}$ and $A_{s/sd}$ are the areas of the air-solution and solution-solid interfaces, respectively, r_e is the radius and v_e is the volume of the embryo as shown in Figure 5-8, and we have already encountered the other terms. The change of embryo radius with changing volume ($\frac{dr_e}{dv_e}$) depends on the relative sizes r_e and r_c as calculated by *Gorbunov and Hamilton* (1997) (corrected in *Gorbunov et al.*, 1998):

$$\begin{aligned} \frac{dr_e}{dv_e} = & \pi r_c^2 \left(\frac{2}{X^2} - \frac{(1 - \cos^2 \theta)^2 X^2}{Y^5} + \frac{2(1 - X \cos \theta)}{X^2 Y} \right. \\ & \left. + \frac{(1 - \cos^2 \theta)}{Y^3} \left[1 - \frac{(\cos \theta - X)(1 - X \cos \theta)X}{Y^2} \right] \right) \end{aligned} \quad (5.57)$$

Here, r_c is the radius of the insoluble core as shown in Figure 5-8(a), and X and Y are defined to be:

$$X = \frac{r_c}{r_e} \quad ; \quad Y = \sqrt{1 + X^2 - 2X \cos \theta} \quad (5.58)$$

Our condensation routine uses the Raoult's Law approximation for the water activity, so we may rewrite equation (5.56):

$$S' = \left(\frac{c_w}{c_w + c_s} \right) \exp \left[\frac{\sigma_{s/a}}{R^* T} \frac{M_w}{\rho} \frac{dr_e}{dv_e} \left(\frac{dA_{a/s}}{dr_e} - \cos \theta \frac{dA_{s/sd}}{dr_e} \right) \right] \quad (5.59)$$

Gorbunov and Hamilton (1997) derive parameterizations of the derivatives $\frac{dA_{a/s}}{dr_e}$ and $\frac{dA_{s/sd}}{dr_e}$ from their approximations to the interface areas as formulated in *Fletcher* (1976) (corrected in *Gorbunov*, 1999).

$$\frac{dA_{a/s}}{dr_e} = \frac{2\pi r_c X^2}{Y} \left[1 - \left(\frac{X - \cos \theta}{Y} \right)^2 \right] \quad (5.60)$$

$$\frac{dA_{s/sd}}{dr_e} = 2\pi r_c \left[\frac{2}{X} (1 + Y^{-1}) - \frac{\cos \theta}{Y} + \frac{X - \cos \theta}{Y^3} (1 - X \cos \theta) \right] \quad (5.61)$$

The limiting cases of this Gorbunov theory appropriately reduce to the other cases depicted in Figure 5-6. By setting θ equal to π or r_c to zero, approximating the water activity using the van't Hoff formulation found in *Pruppacher and Klett* (1997), and keeping only the first order terms of

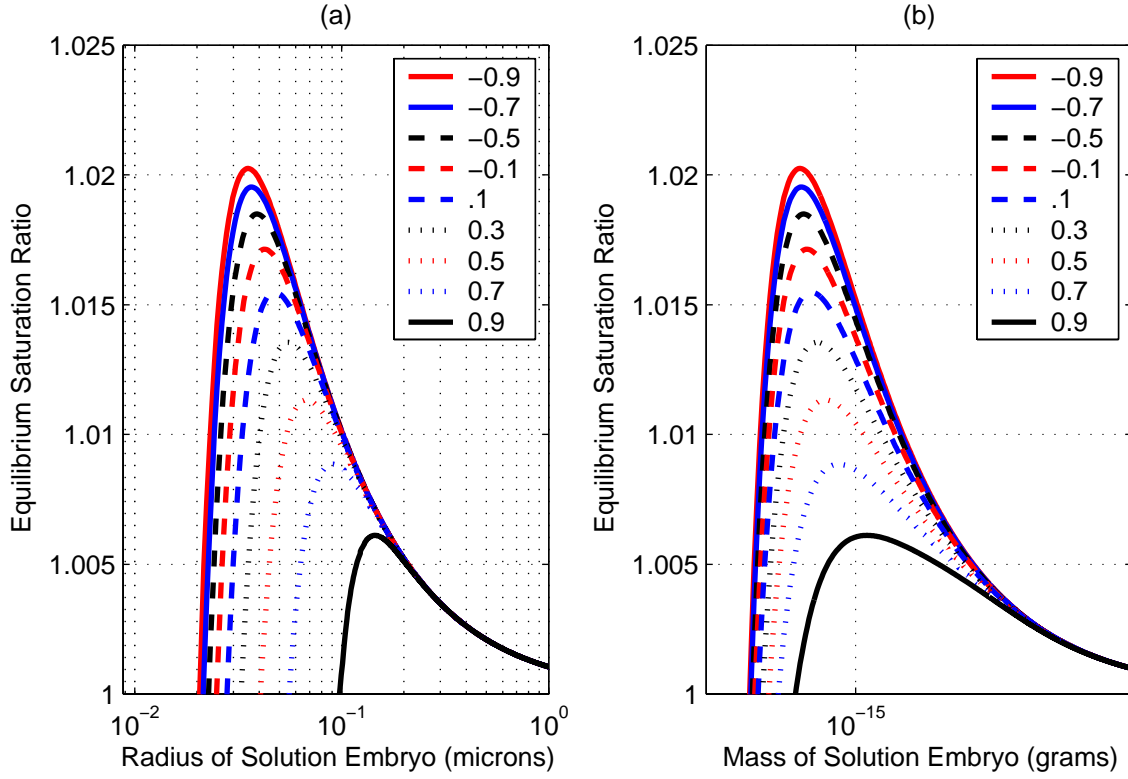


Figure 5-9: Variation of S' with radius of soluble particle and $\cos\theta$ for an insoluble radius of $0.2 \mu\text{m}$ and $4.2 \times 10^{-18} \text{ g}$ of Na_2SO_4 attached; each line is for a particular value of $\cos\theta$ and the legend shows the color coding

the Taylor expansion of the exponential, one can show that equation (5.56) reduces to equation (5.51), the Köhler approximation for hydrophobic aerosol cores. Similarly, equation (5.56) reduces to Hanel's approximation, for which the droplet engulfs the insoluble core, when θ is zero and Fletcher's theory, in which pure water nucleates on the insoluble core, when the number of solute particles vanishes (*Gorbunov and Hamilton, 1997*).

Because of our interest in aerosol activation, we are most interested in the effect of the insoluble core on the evolution of the equilibrium saturation ratio (S') during condensational growth and on the critical super-saturation required for particle activation. Consider Figure 5-9, which presents (S') over a range of contact angles for a particular example. The case considered is for an insoluble core of radius $0.2 \mu\text{m}$ attached to $4.2 \times 10^{-18} \text{ g}$ of Na_2SO_4 at 1000 mb and 298.15 K. Panel 5-9(a) shows S' as a function of r_e for the growth of a solution embryo attached to an insoluble core via water condensation; the several lines are for different values of $\cos\theta$ representing a range from quite hydrophobic to quite hydrophilic. Note first that the shape of the curves resembles those in the simplified Köhler example (shown in Figure 5-7) in several key aspects: they rise from below unity at the smallest radii to a peak corresponding to a small super-saturation, and then fall

asymptotically back towards unity. Once a particle grows sufficiently larger than the critical radius at which it activates, the contact angle no longer influences the equilibrium super-saturation. Note that the more wettable the insoluble core (equivalently, the higher $\cos\theta$), the lower the critical super-saturation required for the particle to activate and the larger the embryo's radius when it does. Panel 5-9(b) shows the same as Panel 5-9(a) except the horizontal axis is the mass of the solution embryo; we include this plot because r_c , the horizontal axis in Panel 5-9(a), is not independent of $\cos\theta$ and so is not proportional to how much solution need be present at activation. We see in Panel 5-9(b) that more hydrophobic particles (with lower values of $\cos\theta$) activate after less water has condensed, while the more wettable cores require a smaller super-saturation but activate only after somewhat more water has condensed. The relationships between critical super-saturation, critical radius at activation, and contact angle depend on the traits of the insoluble core and the amount of electrolyte present according to the equations already presented in this section, but all resemble this example qualitatively.

In their comments on the Gorbunov and Hamilton papers, *Raymond and Pandis* (2002) correctly highlight the difficulty in measuring contact angles of insoluble particles and the lack of related data. Serious experimental validation of the theory is necessary and unavailable at present; the Gorbunov and Hamilton theory is reasonable, at least, in that it asymptotes to better validated theories, as discussed above. It has long been thought that soot particles are hydrophobic when emitted and become more hydrophilic as they age through oxidation and other surface reactions; *Zuberi* (2003) experimentally quantifies this effect by measuring the contact angle of water condensing on a soot surface which aged under controlled conditions. We use his data as inputs to this parameterization in a series of experiments considered in Section 7.3. Clearly, due to the important role soot particles play in polluted environments, much more laboratory and theoretical work will be required in this area, in addition to the expected improvements in field measurement techniques such as aerosol mass spectrometers.

5.8.3 The Role of Soluble Organic Species

There is now considerable evidence that primarily organic aerosols may serve as cloud condensation nuclei (*Shulman et al.*, 1996; *Cruz and Pandis*, 1997; *Corrigan and Novakov*, 1999; *Russell et al.*, 2000; *Ming and Russell*, 2002). *Gorbunov et al.* (1998) distinguish between the effects of surface active soluble organic components, which make it easier for primarily inorganic particles to activate (requiring equivalently less salt or a lower super-saturation). *Ming and Russell* (2002) find that the presence of certain organic acids decreases the condensational growth of ammonium sulfate

substantially and that highly soluble organic species may also substantially lower the deliquescence point. These effects point to strong thermodynamic interaction of the organic and inorganic species, simulation of which is still beyond what is possible within the framework of simple parametric thermodynamic models such as *Kusik and Meissner* (1978)’s which was discussed in Chapter 4 (*Saxena et al.*, 1995).

In the context of condensational growth, highly soluble organics may be adequately described by Köhler, Gorbunov, and other simple growth formulations that dichotomize soluble and insoluble species (*Shulman et al.*, 1996; *Cruz and Pandis*, 1997); this, of course, is not to say that the complete contribution of organic species to aerosol thermodynamics can be modeled. Many organic species are partially soluble, however, and will slowly dissolve as the droplet grows (*Shulman et al.*, 1996; *Laaksonen et al.*, 1998); thermodynamic approximations are necessary to model this but they are currently unavailable. The solubility of pure organic aerosols may also increase over time due to oxidation (*Novakov and Penner*, 1993). Both modern thermodynamic and condensational methods are inadequate for all but the simplest, infinitely soluble or entirely insoluble organic species. However, even for the limiting case of infinite solubility it is unclear what effect the presence of this kind of the aqueous organics would have on the thermodynamic behavior of the inorganic species (i.e., we have neither an adequate solution to the full Gibbs-Duhem equation for that case nor an appropriate mixing rule). Complicating matters, typically only small amounts, between 10% to 30% of the oxidation product mass, of organic aerosols can be identified in the laboratory or in the field (*Ansari and Pandis*, 2000). Organic species are represented in MELAM only insofar as insoluble organic aerosol cores are included via Gorbunov theory.

5.8.4 Activation: A Definition

The Köhler formulation presented in Section 5.8.1 defines activation clearly: if the particle’s radius is larger than r_a^* , it is activated. As discussed earlier, \mathcal{RH} must exceed S^* in order for particles to surpass r_a^* in radius by condensational growth, at which point $\frac{dS'}{dr}$ is negative. The value of r^* depends on solute properties and concentration and varies from 0 μm for pure water to 5 μm or even 15 μm for reasonable atmospheric particle compositions and conditions (*Hobbs*, 1993). If an aerosol is to become a cloud droplet when $\mathcal{RH} < S^*$, it must first grow larger than r_a^* by means other than condensational, such as physical combination with other particles.

In more complex formulations of condensation, such as the diffusion limited model presented in Section 5.7, there are a number of factors that complicate this depiction of activation, which depends on the grossly simplifying assumptions incorporated into equation (5.51). These complications

include the facts that the electrolyte composition of a solution droplet usually changes constantly via dissolution, and the surface tension changes with shifting electrolyte molalities. Here, we use the definition that an aerosol is activated if $\frac{dS'}{dr}$ is negative, meaning that growth is energetically favored over evaporation. When such definitions are necessary, the derivative is calculated using finite differences: specifically the difference between S' calculated with the the actual water content and S' calculated with incrementally more.

5.9 Non-Equilibrium between Trace Gases and Aerosol: Dissolution

We now turn our attention to the gas-to-particle transfer of volatile species besides water vapor. The standard path of an ambient gas-phase molecule into an aerosol particle follows a two step process known as dissolution: first, a molecule must stick to the surface of the droplet and second, it must dissolve into the interior solution. In some cases, the trace species may not dissolve directly, but must instead either bind with an ion on or near the particle's surface or react with another gas molecule on the surface of the particle to form an electrolytic micro-solid, which then may dissociate and dissolve into the interior.

Away from equilibrium, we may define a Fickian diffusion-limited growth model driven by the gradient between the actual and equilibrium surface concentrations of a given species, as expressed by the quasi-stationary equation (5.33). The primary difference between dissolution of volatile non-H₂O species and condensation of water vapor is in the way we define $C'_{a,i}$. For condensation we used a simple scaling of the local saturation water vapor concentration, while for dissolution we will use a generalized form of Henry's law corrected for curvature which depends on particle-specific as well as ambient environmental conditions (*Jacobson, 1999*).

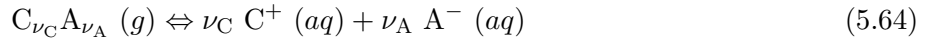
As we did for condensation in Section 5.8, we focus on developing an appropriate formulation for $\left(\frac{dc_i}{dt}\right)_{gas/aer\ transfer}$ in a diffusion limited framework. In this case, a gradient expressing the extent of disequilibrium drives the trace species towards the equilibrium condition discussed in Section 5.6. In order to use the quasi-stationary equation (5.33), we must relate $C'_{a,i}$ to the appropriate form of the expression for dissolutional equilibrium, equation (4.4). We prefer to cast equation (4.4) in a form that resembles equation (5.20) and to express everything in terms of concentrations rather than molalities and partial pressures:

$$C_{a,i} \approx \frac{p_{a,i}}{1000 R^* T} = \frac{m_i \gamma_i}{1000 K_{eq} R^* T} = \frac{c_i \gamma_i}{M_w c_w K_{eq} R^* T} \quad (5.62)$$

$$\equiv \frac{c_i}{H'_i} \quad \text{where} \quad H'_i = \frac{M_w c_w K_{eq} R^* T}{\gamma_i} \quad (5.63)$$

Here, M_w is the molecular mass of water, c_w is the aerosol water concentration, and H'_i is the effective Henry's law coefficient for species i . Equation (5.62) pertains to the case of a single gas-phase species equilibrating between the gas and aqueous aerosol phases. H'_i may also be defined for a dissolving species that dissociates and for a dissolving species that binds with an aqueous ion, which are two of the three special cases described in Section 5.6. The third case discussed in that section, in which two gas phase species form a micro-solid on the particle's surface, is not readily included in this diffusion limited formulation.

We will not discuss the formulation of H'_i in detail for all cases, as they follow directly from equation (4.4). However, we must note briefly that H'_i involves two aqueous species when the dissolving gas species dissociates or incorporates an ion. Consider a generalized example of a dissolving, dissociating species:



In this case, the time rate of change of the concentrations of the two ionic species (c_{C^+} and c_{A^-}) are mechanically related to the rate of change of the concentration of the gas phase species ($C_{\nu_C A_{\nu_A}}$):

$$\left(\frac{dC_{\nu_C A_{\nu_A}}}{dt} \right)_{\text{gas/aer transfer}} = \frac{1}{\nu_C} \left(\frac{dc_{C^+}}{dt} \right)_{\text{gas/aer transfer}} = \frac{1}{\nu_A} \left(\frac{dc_{A^-}}{dt} \right)_{\text{gas/aer transfer}} \quad (5.65)$$

The rate of change of the gas phase species is still expressed by equation (5.33) but H'_i incorporates information about both ionic species. Specifically, noting that the thermodynamic activity of a vapor phase species is its partial pressure, and using the appropriate form of the relationship between activities and equilibrium constant given in equation (4.4), we may write:

$$p_{C_{\nu_C A_{\nu_A}}} = \frac{\mathbf{m}_{C^+}^{\nu_C} \mathbf{m}_{A^-}^{\nu_A} \left(\gamma_{C_{\nu_C A_{\nu_A}}} \right)^{(\nu_C + \nu_A)}}{K_{eq}} \quad (5.66)$$

We may obtain an expression in terms of the concentrations of the gas phase species ($C_{\nu_C A_{\nu_A}}$) and the concentrations of the ionic species (c_{C^+} and c_{A^-}):

$$C_{a, C_{\nu_C A_{\nu_A}}} \equiv \frac{c_{C^+}^{\nu_C} c_{A^-}^{\nu_A}}{H'_{C_{\nu_C A_{\nu_A}}}} \quad (5.67)$$

Here, $H'_{C_{\nu_C}A_{\nu_A}}$ is an appropriate transformation of the equilibrium relationship (5.66) along the lines of equations (5.62) and (5.63). This multiple dependence becomes important when numerically implementing the dissolution routine, as discussed in Section 5.10.2.

We may specialize $\left(\frac{dc_i}{dt}\right)_{gas/aer\ transfer}$ for dissolution by simply substituting equation (5.63) into equation (5.33). Here, we consider only the case of $(C_{s,a,i} = f(c_{a,i}))$ but of course it may be extended to more complicated functional relationships such as equation (5.67).

$$\frac{dc_i}{dt} = k_{a,i} \left(C_i - S'_i \frac{c_{s,i}}{H'_i} \right) \quad (5.68)$$

Here, the saturation ratio correction S'_i accounts only for the Kelvin effect and is appropriately defined by equation (5.48) (*Jacobson, 1997c*). The rate constant $k_{a,i}$ is defined as in (5.34), except that we are able to make use of the fact that the concentrations of non-water trace gases are very small and contribute little to the denominator of the right hand side of equation (5.34) (*Jacobson, 1999*). We thus approximate equation (5.34) to be:

$$k_{a,i} \equiv 4 \pi r D_i' \quad (5.69)$$

All corrections to molecular diffusion discussed in Section 5.7.3 still apply. To maintain continuity, the amount of a particular chemical that enters aerosol particles must leave the ambient gas. Considering the population of N_{gp} particles associated with a particular grid-point gp , we may state the appropriate expression for gas-phase loss (following *Jacobson et al., 1996b*):

$$\frac{dC_i}{dt} = - \sum_{a=1}^{N_{gp}} k_{a,i} \left(C_i - S'_{a,i} \frac{c_{s,a,i}}{H'_i} \right) \quad (5.70)$$

We have thus defined a set of ordinary differential equations that includes equations (5.70) and (5.69) for each aerosol or group of aerosols. We discuss numerical solution methods in the next section.

5.10 Numerical Solution to Time-Dependent Gas-Aerosol Transfer

For numerical simulations of aerosols or bins of aerosols at a particular grid point (numbering N_{gp}), we define a set of at least $N_{gp} + 1$ non-linear, first order ordinary differential equations that govern the transfer to and from each aerosol or bin of each species: N_{gp} with the form of equation (5.3) that

describe the transfers to or from each aerosol or bin, and one with the form of equation (5.4) that tracks net change in the corresponding gas phase concentration. When a gas phase species either dissociates in the aqueous phase or combines with an ionic species, the number of equations grows to $2N_{gp} + 1$, as there are now governing equations for two aqueous species for each N_{gp} aerosols or bins as well as a single gas phase species. The set of reactions may be larger than $2N_{gp} + 1$ when a species dissolves into both dissociated and undissociated forms, NH_3 for example, in which case there are $3N_{gp} + 1$ equations; the particulars of these various cases will be discussed in Section 5.10.2.

Of course, the continuity equation (2.2) shows that the rates of change of different aerosol species are coupled to each other by chemical reactions and electrolyte dissociation. The key to efficient calculation of condensation and dissolution is to decouple the species from each other where possible, and to treat the processes represented by the several rate-of-change terms in equation (2.2) sequentially as discussed briefly in Section 2.3. We make the assumption that condensation of different species can be calculated separately over sufficiently small time-steps, after which each aerosol is then internally equilibrated.

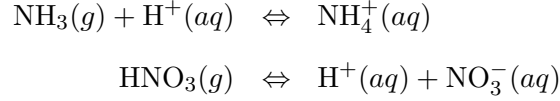
In the remainder of this section, we discuss the numerical techniques used to solve the sets of reactions described by equations (5.3) and (5.4). In Section 5.10.1 we discuss the sparse matrix technique used to solve the equations, and in Section 5.10.2 we discuss the application of this method to the particular sub-cases implemented in the model.

5.10.1 Sparse Matrix Solution Method

For each set of coupled equations, we may define a state vector \vec{x}_t that includes the gas phase and all relevant aqueous concentrations at time t and a state evolution (time derivative) vector \vec{y}_t comprised of the related time rates of change:

$$\vec{x}_t \equiv \begin{pmatrix} C_i(t) \\ \vdots \\ c_{n,j}(t) \\ \vdots \\ c_{m,k}(t) \\ \vdots \end{pmatrix} \quad \text{and} \quad \vec{y}_t \equiv \begin{pmatrix} \frac{dC_i(t)}{dt} \\ \vdots \\ \frac{dc_{n,j}(t)}{dt} \\ \vdots \\ \frac{dc_{m,k}(t)}{dt} \\ \vdots \end{pmatrix} \quad (5.71)$$

Here, $C_i(t)$ is the gas phase concentration of the condensing species i at time t , and $c_{n,j}(t)$ is the liquid or aqueous phase concentration in particle (or bin) n of species j at time t . We indexed the aerosol concentration of species j by dummy index n ($1 \geq n \geq N_{gp}$) and the aerosol concentration of species k by m ($1 \geq m \geq N_{gp}$). The form of equation (5.71) is for the case of a single gas phase species i condensing to become two aqueous species j and k , which is governed by $(2N_{gp} + 1)$ equations. Such a calculation would be made for either of the two dissolution reactions:



In the first reaction between ammonia and ammonium, the single gas phase species is ammonia and the ionic species are protons and ammonium; the concentration of one of the ionic species (NH_4^+) grows as ammonia dissolves and the other (H^+) decreases. In the second reaction, the dissolution of nitric acid, both of the ionic species increase in direct proportion to how much nitric acid dissolves. Depending on the case under consideration, there may be between one and three ionic species involved in the dissolution reaction and equation (5.71) will change to reflect this; this is discussed further in Section 5.10.2.

We also define a Jacobian, or partial-derivative matrix such that $\mathbf{J}_t \equiv \frac{\partial \vec{y}_t}{\partial \vec{x}_t}$, or specifically:

$$\mathbf{J}_t \equiv \begin{pmatrix} \frac{\partial}{\partial C_i} \left(\frac{dC_i(t)}{dt} \right) & \cdots & \frac{\partial}{\partial c_{n,j}} \left(\frac{dC_i(t)}{dt} \right) & \cdots & \frac{\partial}{\partial c_{m,k}} \left(\frac{dC_i(t)}{dt} \right) & \cdots \\ \vdots & \ddots & \vdots & & \vdots & \\ \frac{\partial}{\partial C_{t,i}} \left(\frac{dc_{n,j}(t)}{dt} \right) & \cdots & \frac{\partial}{\partial c_{n,j,t}} \left(\frac{dc_{n,j}(t)}{dt} \right) & \cdots & \frac{\partial}{\partial c_{m,k,t}} \left(\frac{dc_{n,j}(t)}{dt} \right) & \cdots \\ \vdots & & \vdots & \ddots & \vdots & \\ \frac{\partial}{\partial C_{t,i}} \left(\frac{dc_{m,k}(t)}{dt} \right) & \cdots & \frac{\partial}{\partial c_{n,j,t}} \left(\frac{dc_{m,k}(t)}{dt} \right) & \cdots & \frac{\partial}{\partial c_{m,k,t}} \left(\frac{dc_{m,k}(t)}{dt} \right) & \cdots \\ \vdots & & \vdots & & \vdots & \ddots \end{pmatrix} \quad (5.72)$$

The partial-derivative, Jacobian matrix shown in equation (5.72) is again for the example of a single gas phase species i and two ionic species j and k . The ellipses on the rightmost column and bottom row are meant to indicate that more may be necessary.

With these definitions in hand, we follow Gear (1971) to define an equation that calculates the values of \vec{y}_t over a variable time-step (h):

$$(\mathbf{I} - h \beta_0 \mathbf{J}_t) \vec{z} = \vec{y}_t \quad (5.73)$$

Here, \mathbf{I} is an identity matrix of the same dimensions as \mathbf{J} , which consists of unity along the diagonal and zeros elsewhere, β_0 is a scalar that depends on the specifics of the method (see *Gear*, 1971), and \vec{z} is a vector that will be used to correct \vec{x}_t and \vec{y}_t (*Gear*, 1971; *Jacobson and Turco*, 1994). We iteratively solve equation (5.73) until the error in \vec{z} falls below a stated tolerance level, repeating the solution for decreasing h values until the total compounded error over the entire time step is below a pre-specified specific level. (The total compounded error is the error over the full user-defined time step rather than the LSODES-defined variable time step h , which may be much shorter.)

The specifics of the iterative method are left to the particulars of the numerical implementation. Here we employ the *Livermore Solver for Ordinary Differential Equations with Sparse Matrices* (LSODES) of *Hindmarsh and Radhakrishnan* (1993). LSODES is a modification of *Gear* (1971)'s original code that uses efficiencies of vectorization and sparse-matrix techniques, so called because they make use of the fact that many of the terms of \mathbf{J}_t are zero. *Jacobson and Turco* (1994)'s *Sparse-Matrix Vectorized Gear Code* (SMVGEAR) is a competing and also appropriate formulation. SMVGEAR's primary advantage is that it allows flexible inputs specifically implemented for atmospheric chemistry. MELAM provides a similarly flexible interface to use LSODES directly. SMVGEAR also vectorizes the matrices grid-cell-by-grid-cell as opposed to species by species, as LSODE does; this difference is immaterial in this case, however, as MELAM must redefine the matrices at each timestep due to fluctuating numbers of terms in \vec{x}_t and \mathbf{J}_t .

5.10.2 Integration of Operator-Split Condensation and Dissolution Equations

In order to employ the sparse-matrix integration technique discussed above in Section 5.10.1, we must define \vec{x}_t , \vec{y}_t , and \mathbf{J}_t for each of several allowed cases. Key to our method is to fix some variables at their value at the beginning of the time step (*Jacobson*, 1997c). For example, let us consider this approximation for the equation set of (5.68) and (5.70) which describes a simple dissolution scenario with no dissociation or other complications. To facilitate integration, we evaluate the rate constant, the equilibrium saturation ratio, and effective Henry's law coefficient at the beginning of the time step and hold it constant:

$$\frac{dc_{a,i}}{dt} \approx \overline{k_{a,i}} \left(C_i - \overline{\left(\frac{S'_{a,i}}{H'_{a,i}} \right)} c_{a,i} \right) \quad (5.74)$$

$$\frac{dC_i}{dt} \approx - \sum_{a=1}^{N_{gp}} \overline{k_{a,i}} \left(C_i - \overline{\left(\frac{S'_{a,i}}{H'_{a,i}} \right)} c_{a,i} \right) \quad (5.75)$$

Here, the overbar signifies that the variable is held constant at its value at the beginning of the timestep. The set of $N_{gp} + 1$ reactions is thus cast as a simple initial value problem and is integrated directly using LSODES.

This “constant-coefficients” approximation demands short integration time steps, as does our assumption that the condensation and dissolution of each species may be decoupled. As will be shown in Section 5.11, the equilibration time for water in a simple sulfate aerosol system is between 1 and 1000 seconds for the range of \mathcal{RH} over which we expect to use this flux-based condensation scheme. The most damaging miscalculation in this context is to mis-predict the concentrations of aerosols in a long-lived state. We will show in Section 5.11 that the flux-based condensation scheme used in MELAM correctly predicts the equilibrium state when it is used. However, we must also be careful that the “constant-coefficients” approximation does not mis-predict slowly-evolving transitory states. *Jacobson* (1997c, 2002) and *Müller* (2001) consider the error introduced by such assumptions, and show the error in the equilibrium to be small if the time step is one minute or less. MELAM will typically use a much shorter time step on the order of 1 to 15 seconds.

In the remainder of this section, we will discuss the forms of \vec{y}_t and \mathbf{J}_t for each of the gas-aerosol transfer situations allowed in this model, which include:

1. Water condensation.
2. Direct dissolution of a single gas phase species.
3. Dissolution of a single gas phase species that dissociates upon dissolving.
4. Dissolution of a single gas phase species that binds with an ion upon dissolving.
5. Dissolution of a single gas phase species that exhibits several of the behaviors of Types 2, 3, and 4.

We will address each of these cases in turn. We will consider the particular form that equations (5.74) and (5.75) take for each case, and we also develop expressions for the Jacobian matrix elements when it is helpful.

Type 1: Water Condensation

To develop the proper form of equations (5.74) and (5.75) for water condensation, let us first rewrite Raoult’s Law, as expressed in equation (5.47), in an equivalent concentration form for use here by

multiplying by $(1/v_p)/(1/v_p)$ (where v_p is the volume of the particle):

$$a_w \approx \frac{n_w}{n_w + n_s} = \left(\frac{n_w}{n_w + n_s} \right) \left(\frac{\frac{1}{v_p}}{\frac{1}{v_p}} \right) \quad (5.76)$$

$$= \frac{c_{a,w}}{c_{a,w} + c_{a,s}} \approx \frac{c_{a,w}}{c_{a,w} + \overline{c_{a,s}}} \quad (5.77)$$

Here, $c_{a,w}$ is the aerosol water concentration and $c_{a,s}$ is the total solute concentration, and $\overline{c_{a,s}}$ is the total solute concentration at the beginning of the time step which we assume will be constant over the time step. We then fix the rate coefficient, saturation gas phase water concentration, and solute abundance in each aerosol to their values at the beginning of the integration period (expressed by overbars) and rewrite equation (5.46) as:

$$\frac{dc_w}{dt} = \overline{k_{a,i}} \left\{ C_w - \overline{C_{s,w} \left(\frac{C'_s}{C_S} \right)_{Kelvin} \left(\frac{c_{a,w}}{c_{a,w} + \overline{c_{a,s}}} \right)} \right\} \quad (5.78)$$

Here, we have split S' into two components according to equation (5.49) and held the curvature correction constant. We have thus cast the time rate of change as a function only of a changing gas-phase water vapor concentration (C_w), changing aerosol water content ($c_{a,w}$), and various constants. The elements of \mathbf{J}_t then become:

$$\frac{\partial}{\partial C_w} \left(\frac{dC_w}{dt} \right) = - \sum_a \overline{k_{a,i}} \quad (5.79)$$

$$\frac{\partial}{\partial c_{a,w}} \left(\frac{dC_w}{dt} \right) = \overline{k_{a,i} C_{s,w} \left(\frac{C'_s}{C_S} \right)_{Kelvin} \left(\frac{1}{c_{a,w} + \overline{c_{a,s}}} - \frac{c_{a,w}}{(c_{a,w} + \overline{c_{a,s}})^2} \right)} \quad (5.80)$$

$$\frac{\partial}{\partial c_{a,w}} \left(\frac{dc_{a,w}}{dt} \right) = \overline{k_{a,i} C_{s,w} \left(\frac{C'_s}{C_S} \right)_{Kelvin} \left(\frac{1}{c_{a,w} + \overline{c_{a,s}}} - \frac{c_{a,w}}{(c_{a,w} + \overline{c_{a,s}})^2} \right)} \quad (5.81)$$

$$\left[\frac{\partial}{\partial c_{b,w}} \left(\frac{dc_{a,w}}{dt} \right) \right]_{a \neq b} = 0 \quad (5.82)$$

The first column, first row, and diagonal of the Jacobian matrix are populated and every other element is zero. Only a small fraction of the elements take non-zero values, specifically: $(3N_{gp} + 1)/(N_{gp} + 1)^2$. This fraction approaches zero as N_{gp} grows. The Jacobian matrix is thus very sparse, and significant computational savings result from using a sparse-matrix solver such as LSODES.

Type 2: Direct Dissolution

Some dissolved gases neither dissociate nor bind with any aqueous ions; rather they maintain the same structure in the gas phase and in solution. The set of dissolution equations for this case were

given earlier as examples in equations (5.74) and (5.75) for dissolving species i . The elements of \mathbf{J}_t then become:

$$\frac{\partial}{\partial C_i} \left(\frac{dC_i}{dt} \right) = - \sum_a \overline{k_{a,i}} \quad (5.83)$$

$$\frac{\partial}{\partial c_{a,i}} \left(\frac{dC_i}{dt} \right) = \overline{\left(\frac{k_{a,i} S'_{a,i}}{H'_{a,i}} \right)} \quad (5.84)$$

$$\frac{\partial}{\partial c_{a,i}} \left(\frac{dc_{a,i}}{dt} \right) = - \overline{\left(\frac{k_{a,i} S'_{a,i}}{H'_{a,i}} \right)} \quad (5.85)$$

$$\left[\frac{\partial}{\partial c_{b,w}} \left(\frac{dc_{a,w}}{dt} \right) \right]_{a \neq b} = 0 \quad (5.86)$$

This Jacobian has the same sparse structure as did Type 1, with only the first row, first column, and diagonal taking non-zero values. Note also that every in \mathbf{J}_t term is constant in this case.

Types 3 and 4: Dissolution and Dissociation and Dissolution and Binding with an Ion

When a dissolving gas dissociates or binds with an ion, two aqueous species must be accounted for during the integration: the anion and cation in the first case, and the reactant ion and product ion in the second. The case of the dissociating, dissolving species was discussed in Section 5.9. In both of these cases, there are $2N_{gp} + 1$ concentrations to track. Let us consider a gas phase species i that dissociates completely in solution to form ν_j ions of species j and ν_k ions of species k :



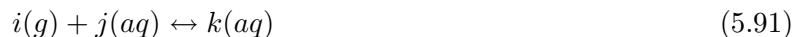
The ODE set is then:

$$\frac{dc_{a,j}}{dt} = \overline{k_{a,i} \nu_j} \left(C_i - \overline{\left(\frac{S'_{a,i}}{H'_{a,i}} \right)} c_{a,j} c_{a,k} \right) \quad (5.88)$$

$$\frac{dc_{a,k}}{dt} = \overline{k_{a,i} \nu_k} \left(C_i - \overline{\left(\frac{S'_{a,i}}{H'_{a,i}} \right)} c_{a,j} c_{a,k} \right) \quad (5.89)$$

$$\frac{dC_i}{dt} = - \sum_{a=1}^{N_{gp}} \overline{k_{a,i}} \left(C_i - \overline{\left(\frac{S'_{a,i}}{H'_{a,i}} \right)} c_{a,j} c_{a,k} \right) \quad (5.90)$$

While the ODE set for the case of a gas (i) dissolving and binding with an ion (j) to form another ion (k) is:



For which the ODE set may be written:

$$\frac{dC_i}{dt} = - \sum_{a=1}^{N_{gp}} \overline{k_{a,i}} \left(C_i - \overline{\left(\frac{S'_{a,i}}{H'_{a,i}} \right)} \frac{c_{a,k}}{c_{a,j}} \right) \quad (5.92)$$

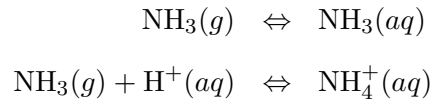
$$\frac{dc_{a,j}}{dt} = - \overline{k_{a,i}} \left(C_i - \overline{\left(\frac{S'_{a,i}}{H'_{a,i}} \right)} \frac{c_{a,k}}{c_{a,j}} \right) \quad (5.93)$$

$$\frac{dc_{a,k}}{dt} = \overline{k_{a,i}} \left(C_i - \overline{\left(\frac{S'_{a,i}}{H'_{a,i}} \right)} \frac{c_{a,k}}{c_{a,j}} \right) \quad (5.94)$$

The Jacobian matrix with respect to C_i , $c_{a,j}$, and $c_{a,k}$, for these two sets of equations – (5.88) to (5.90) and (5.92) to (5.94) – have the same sparse structure and similar expressions, though we will not develop them here. In each case, there are non-zero elements in the first row, first column, diagonal, and one file off-diagonal that corresponds to the other ionic species for the aerosol whose derivative is taken in that column. There are therefore $4N_{gp} + 1$ total non-zero elements.

Type 5: Coupled Dissolution

Often, it is computationally advantageous to include dissolution reactions that lead to both the dissociated and undissociated forms of the aqueous species, or that lead to aqueous forms of the gas phase species that are either bound to an ion or that are not. Consider, for example, gas-phase ammonia dissolving directly to aqueous the ammonia as well as aqueous ammonium, such as is included in aqueous reaction set presented in Table A.2 in Appendix A as reactions (A7) and (A8):



In these cases, we must form an appropriate \vec{x}_t that includes one gas phase concentration and three aqueous phase concentrations for each aerosol or bins of aerosols. \vec{y}_t and \mathbf{J}_t are then appropriate extensions of those presented for Type 2, and either Type 3 or Type 4.

5.11 Comparison of Equilibrium and Non-Equilibrium Prediction of Aerosol Water Content

We have presented two methods for determining particle water content: an equilibrium approach in Section 5.5.4 and a flux-based approach in Section 5.5.5. It is worthwhile to ask how the two

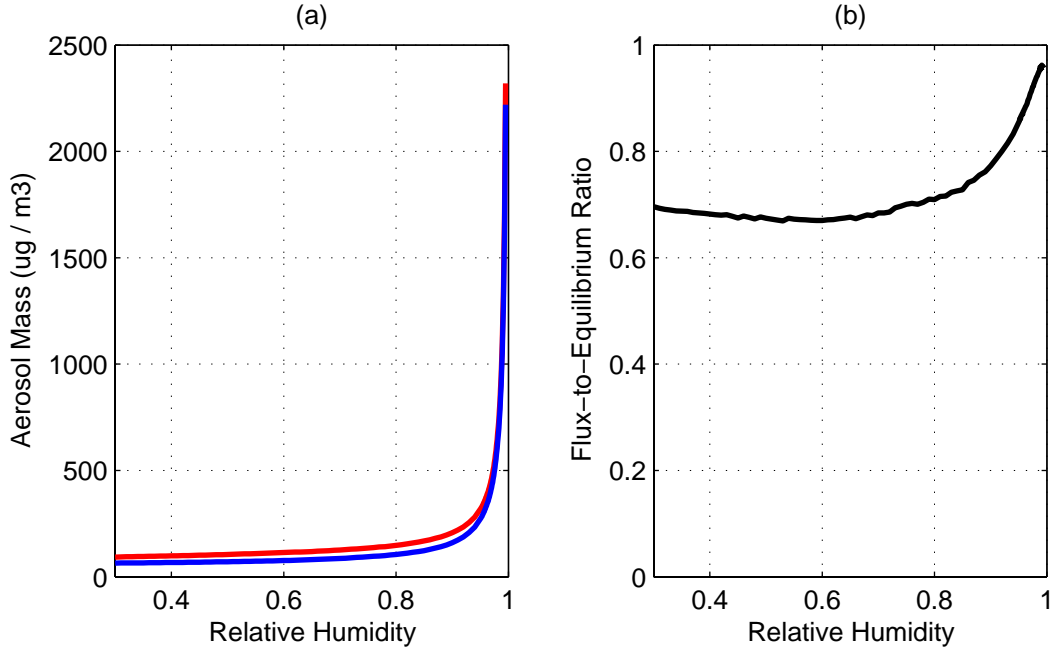


Figure 5-10: (a) Overlay of the water content predicted by the equilibrium approach (red) and the flux-based approach run to equilibrium (blue) for $3 \mu\text{g}/\text{m}^3$ of H_2SO_4 distributed over 100 particles with standard deviation of 1.5. (b) the ratio of the flux-based predicted water content to the equilibrium predicted water content.

agree with each other. Most importantly, we must acknowledge that the two methods calculate water activity (a_w) with very different approaches. The equilibrium method integrates the Gibbs-Duhem equation on a electrolyte-by-electrolyte basis and uses a mixing rule to determine a_w for the full solution, using equations (5.13) and (5.17). The flux-based approach uses Raoult's Law, equation (5.47), which is meant only to approximate the true a_w in dilute solutions (equivalently, for atmospheric aerosols, in high \mathcal{RH} environments).

In Section 5.4.1, we recommended using an equilibrium approach for mid-range \mathcal{RH} values where equilibration times are very fast and a flux-based approach at very high and super-saturated \mathcal{RH} values where equilibration times are longer (or the system is out of equilibrium by definition) and Raoult's Law applies. In this section, we consider how the equilibrium and flux-based approaches compare over the full range of \mathcal{RH} values and then consider equilibration times over this same range of humidities. For our recommended approach to be valid, the flux-based form must drive towards an accurate equilibrium over the range of \mathcal{RH} for which we use it while equilibration times must be short over the range of \mathcal{RH} for which we will assume equilibrium.

Consider a system of $3 \mu\text{g}/\text{m}^3$ of H_2SO_4 distributed over 100 particles with standard deviation of 1.5. For each \mathcal{RH} value between 0.30 and 0.999 (with 0.01 steps from 0.30 to 0.97 and 0.001 steps above that), we equilibrate the water content using both the equilibrium (Gibbs-Duhem) approach

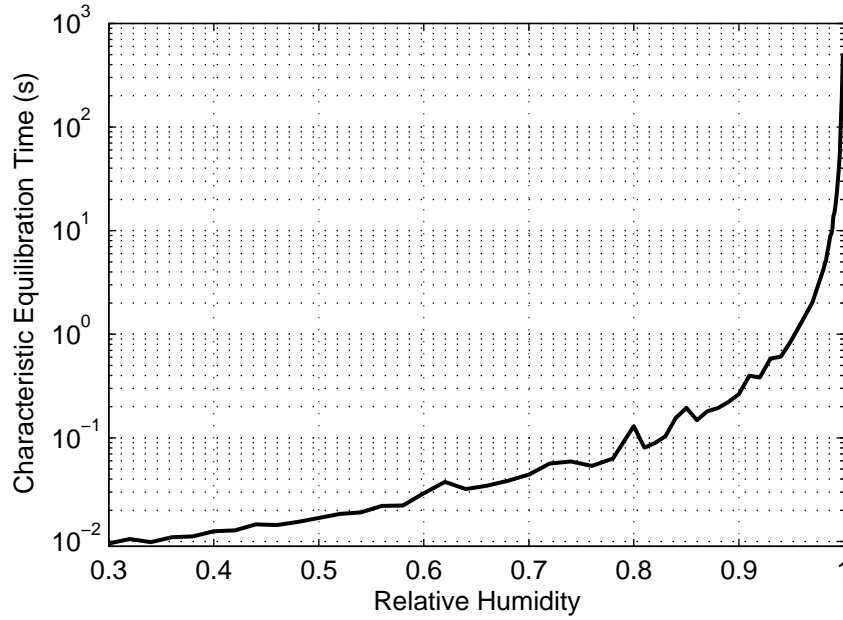


Figure 5-11: Characteristic water equilibration times over a range of \mathcal{RH} for water condensation onto 100 sulfate aerosols totaling $3 \mu\text{g}/\text{m}^3$ of H_2SO_4

and the flux-based (Raoult's Law) approach. The flux-based equilibrium is obtained by integrating for two hours during which we re-equilibrate the aqueous electrolytes once per minute.

Panel (a) of Figure 5-10 shows the total aerosol mass ($3 \mu\text{g}/\text{m}^3$ of dissolved H_2SO_4 plus the liquid water mass) over the range of \mathcal{RH} values as predicted by the equilibrium approach (in red) and the flux-based approach (in blue). Note that the flux-based approach, using Raoult's Law, systematically under-predicts water content over the full range of humidities but approaches parity as the system nears saturation at $\mathcal{RH} = 1$. Note that water content spikes as \mathcal{RH} approaches unity, and so the liquid-phase aerosols are increasingly dilute and the assumptions inherent in Raoult's Law become ever more palatable. Panel (b) shows the ratio of the two predictions. Note that in low and mid-range \mathcal{RH} environments, the flux-based equilibrium is 65% to 80% of the predicted (and more accurate) equilibrium value; recall from Figure 5-3 that MELAM's equilibrium predictions over-predict actual water-content values by approximately 5% over this range of humidities, which may exacerbate the discrepancy between the flux-based equilibrium and predicted equilibrium seen here. However, in very moist environments the flux-based equilibrium water content prediction for this scenario is 96% of the equilibrium prediction and the two methods are essentially in agreement; the two methods are within 5% agreement above 98.6% \mathcal{RH} . This supports the use of the flux-form only in environments very near or above saturation.

To measure characteristic equilibration times for the flux-based model at different \mathcal{RH} , we

follow a three step procedure. Over a range of \mathcal{RH} , we first equilibrate the aerosols, then halve the liquid water abundance on an aerosol-by-aerosol basis, and then integrate forward using the flux-based condensation methods until the system equilibrates. We then measure the equilibration time by assuming the total liquid water mass (m_l)

$$m_l(t) = m_l^{(e)} - e^{(-\tau_e t)} \quad (5.95)$$

Here, $m_l^{(e)}$ is the equilibrium liquid water mass and τ_e is an equilibration constant. The liquid water mass is the sum of the liquid water in each aerosol:

$$m_l = \sum_p m_{i,p}^{(\text{aqueous})} \quad (5.96)$$

Figure 5-10 shows how the characteristic equilibration time ($1/\tau_e$) varies with relative humidity for the same aerosol sulfate system just considered when comparing equilibrium and flux-based water content methods. Note that, in this model, this sulfate aerosol system equilibrates in less than 0.1 second up to 80% \mathcal{RH} , less than 1 second up to 95% \mathcal{RH} , and up to 15 or 20 minutes in the most humid environments. The equilibrium and flux comparison above told us that the flux-based equilibrium is accurate within 5% of the true solution above 98.6% \mathcal{RH} and within 10% of the solution above 96.1% \mathcal{RH} , for which the character equilibration times are approximately 8 seconds and 1.2 seconds, respectively. The goal for setting the transition between the equilibrium assumption and the dilute-solution, flux-based assumption is to maximize the realism of the equilibrium assumption (by applying it only to systems with short equilibration times) and the accuracy of the flux-based approximation (by applying it only for systems where the dilute-solution approximation is accurate). According to this consideration, the appropriate range for that division is between 96% and 98.6% \mathcal{RH} . Which the user chooses should depend on how quickly other aspects of the system evolve.

5.12 Conclusion

In this chapter, we developed the algorithms the MELAM model uses to calculate transfer between the aerosol and gas phases for water and other trace species. The model is able to calculate both the equilibrium gas / aerosol partitioning and the kinetic transfer rates of water vapor and trace volatile species. The calculated equilibria of both water and trace species compare well with other equilibrium models from the literature for several contrived scenarios. Water equilibrium is

calculated via integration of the Gibbs-Duhem equation for single-component solutions and use of an appropriate mixing rule; the kinetic condensation model finds very nearly the same equilibrium state as the more sophisticated Gibbs-Duhem approach at the high relative humidities at which Raoult's Law is most applicable.

As discussed in Section 3.4, there are many types of aerosol particles in the atmosphere and they are found in many mixing states. Traditional aerosol modeling handles only one of these well: inorganic aerosols. We presented the Gorbunov model for calculation of condensation onto mixed inorganic / insoluble aerosol particles. Recent laboratory measurement have provided information necessary to constrain the algorithm, and recent field campaign data has shown that mixed sulfate / soot aerosols, which are appropriately approximated using the Gorbunov model, are found throughout both the clean and polluted marine atmosphere. In Chapter 7, we will consider the activation of realistic populations of these mixed sulfate / soot particles in a rising parcel as a way to investigate their role in the indirect effects of aerosols for the first time. There are a number of aerosol configurations and types of trace species that this condensation and dissolution model is unable to represent. These include condensation onto organic aerosols, the transfer of volatile organic species, condensation onto realistic chains of soot spherules, and condensation or dissolution onto aerosol with surfactant layers. Inclusion of the Gorbunov model is one step forward, and the sophisticated treatment of inorganics is another. The model is intended to easily incorporate future theories that treat these other aerosol types and condensation or dissolution scenarios, and the model is formulated to adopt dissolution reactions and different inorganic species extremely easily through a text input file. It is an appropriate tool for conducting research into various questions of condensation upon and activation of aerosol populations. We will use it to address one such question using the Gorbunov model in Chapter 7 and continue to use it to address others in the future.

Chapter 6

Aerosol Activation within 1-D Updraft Models

6.1 Introduction

We have paid great attention to the specifics of aerosol and cloud microphysics in the preceding Chapters. The goal of the modeling portion of this thesis is to provide a flexible and accurate aerosol model that can represent a wide variety of aerosol types and physical processes and be used to answer questions about aerosol activation. Much of the innovation of this modeling effort is in the representation of the microphysics and the flexibility of the framework of the MELAM model. To be useful, however, the model must be driven within some form of cloud model that provides reasonable boundary conditions. Studies of aerosol activation that consider relatively complex microphysical models within simple dynamical frameworks use an adiabatic constant-updraft model, selecting it for its computational efficiency and the simplicity of its physics. Such adiabatic constant-updraft models, although very popular within the aerosol modeling community, have been largely discredited as an appropriate analogy to real clouds within the cloud physics community since the mid-1900's (see Section 6.2.7). Although the use of constant-updraft adiabatic models in microphysical studies is appropriate, as we will explain, it is worthwhile to consider the limits of their appropriate use.

In this Chapter, we develop a version of the adiabatic constant-updraft model in Section 6.2 and an episodically entraining, variable speed plume model to provide an alternative and a point of comparison in Section 6.3. In those sections, we discuss each model's justifications, uses, and limitations and present examples of their behavior. Adiabatic constant-updraft models are widely

used and our discussion of them will formulate a version that we will use alongside the MELAM model (that will parallel a number of developments available in the literature) and provide a critical review of their uses and limitations. The episodically entraining, variable-speed updraft model is novel in that it seeks to link the output of a parameterization of convection, such as would be used in a regional or global model, to an idealized updraft parcel model. We will present a new and approximate method to extract information about updraft velocities from a convective parameterization. We will also discuss how an eventual parameterization of aerosol activation might be incorporated into a global or regional scale model, and the steps that might be required to do so.

We will argue that the widely-used constant-updraft model is of use, but within a more limited framework than generally assumed. We will also argue that the aerosol activation properties calculated by the constant-updraft model depends too much on the updraft speed through the base of the cloud. This is discussed further in the Chapter’s conclusion, Section 6.4.

6.2 Constant Updraft Parcel Model

The simplest cloud dynamics model we consider is a parcel that rises with constant speed and may or may not entrain air at a constant rate from an idealized environment. This model has its origins in early studies of cloud dynamics (e.g., *Austin and Fleisher*, 1948; *Stommel*, 1947, 1951; *Warner and Squires*, 1958; *Squires and Turner*, 1962), which ultimately culminated in an entraining updraft model based on a closed set of equations and fit to laboratory analogs (*Squires and Turner*, 1962; *Pruppacher and Klett*, 1997). *Warner* (1970b) called the physical realism of these models into question, noting that they are not able to accurately predict both liquid water content and cloud depth simultaneously. Limitations of this modeling method are discussed in Section 6.2.7. Nonetheless, the non-entraining form of the constant updraft parcel model has become a popular means to provide boundary conditions to water condensation models of cloud formation (e.g., *Jensen and Charlson*, 1984; *Ghan et al.*, 1993, 1995; *Chuang et al.*, 1997b; *Abdul-Razzak et al.*, 1998; *Ghan et al.*, 1998; *Liu and Seidl*, 1998; *Abdul-Razzak and Ghan*, 2000; *Nenes et al.*, 2001; *Penner et al.*, 2004), and we will use it to constrain MELAM later in this Chapter for comparison with more comprehensive approaches and then to consider the role of mixed sulfate / soot particles in cloud formation in Chapter 7. We will argue in the discussion at the end of this chapter that non-entraining adiabatic models are useful for studying physical effects such as competition between aerosols for condensing water and kinetic limitations, but not for drawing direct analogies to the

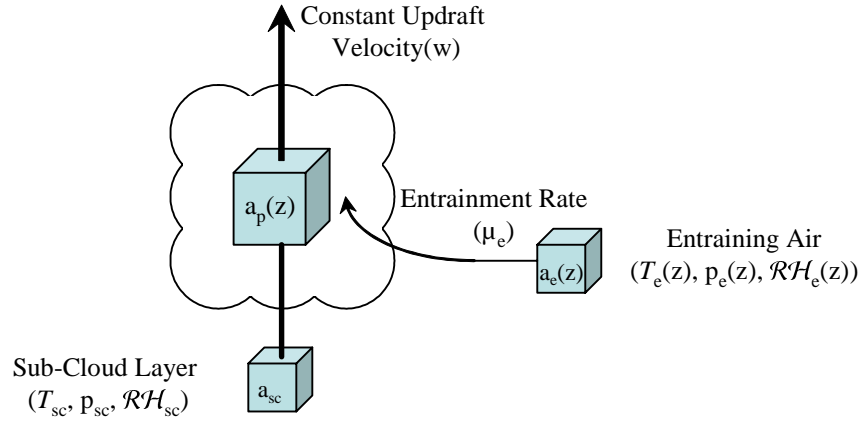


Figure 6-1: Schematic of the constant-velocity updraft parcel model

behavior of a particular group of aerosols within a cloud except in very particular circumstances.

We characterize the rising parcel by a constant updraft velocity, w (the z -component of the air velocity \vec{u}), which we use to calculate changes in the parcel's pressure (p_p), temperature (T_p), and ultimately water content (expressed as a mass mixing ratio, $q_{v,p}$) (following *Pruppacher and Klett*, 1997). The local environment, from which air is entrained, is also characterized by pressure (p_e), temperature (T_e), and water content ($q_{v,e}$), all of which vary with altitude (z). For this model, altitude is continuous as is entrainment, if it occurs.

In the remainder of Section 6.2, we discuss: the framework of the parcel models in Section 6.2.1, the differential equations for each model that govern time evolution of p_p in Section 6.2.2, T_p in Section 6.2.3, water condensation in Section 6.2.4, parcel volume in Section 6.2.5, and problems with these models in Section 6.2.7. Finally, we summarize and discuss an example in Section 6.2.6. Section 6.4 will include further discussion of the uses of these simple parcel models in aerosol activation studies.

6.2.1 Non-Entraining and Continuously Entraining Parcel Models

The continuous updraft models are based on the recognition that a parcel conserves heat and moisture as it rises adiabatically. This process may be modeled by forcing changes in the thermodynamic properties of a single grid-point and calculating condensation and other microphysical processes. Entrainment, if it occurs, is modeled as a constant inflow of air, the properties and thermodynamic state of which may be a function of altitude. Figure 6-1 is a schematic of this model: a parcel of sub-cloud aerosol (a_{sc}), initially at equilibrium with sub-cloud air (at temperature T_{sc} , pressure p_{sc} , and relative humidity \mathcal{RH}_{sc}), rises with a pre-defined constant velocity (w), laterally entraining

air and the aerosol contained therein. The saturation partial pressure of water falls as the parcel rises and cools and so we expect the parcel’s relative humidity to rise until it reaches its lifting condensation level (LCL), which is the altitude at which it becomes saturated and above which water may condense. Above its LCL, the parcel is considered to be cloudy, although in fact the aerosol within the parcel may not activate (this will be discussed in Section 6.2.6). Note that the LCL is defined in terms of a particular parcel: the altitude at which that particular parcel will saturate if lifted adiabatically. The LCL for a parcel of sub-cloud air, such as we will consider, will usually lie near the observed cloud base, but they are not necessarily at the same level.

As a simplifying assumption, neither coagulation nor coalescence are calculated, and so precipitation does not form. This is consistent with parcel models in the literature (cf. *Pruppacher and Klett*, 1997). It would be simple to include coagulation in the MELAM updraft model, as all of the physics discussed throughout this thesis are available, but ignoring it serves to isolate condensational physics, which these models are meant to study. The traditional assumption is that aerosol activation is primarily associated with a peak super-saturation that occurs just above the LCL, and so the focus of the models is restricted to the short distance just above the LCL in which coalescence is not dominant. Modeling coalescence and especially precipitation involves a number of complexities ill suited to a parcel model, for example calculating precipitation that enters the parcel from above. The model we will present in Section 6.3 focuses on much deeper convection in which coalescence and impaction scavenging are certainly important, and yet we will neglect them there as well in order to isolate condensation physics and activation. We will be careful to discuss the implications of this for our results. A number of the conclusions we will draw benefit from isolating a hand-full of physical effects; and the results would be difficult to analyze were all known physics included.

We define the rate at which environmental air is entrained into the rising parcel (μ_e) to be related to the change in the parcel’s mass (m_p) with altitude (z):

$$\mu_e \equiv \frac{1}{m_p} \frac{dm_p}{dz} \quad (6.1)$$

In general, μ_e is estimated by analogy to laboratory experiments or by tuning such that the large scale cloud properties conform to direct measurements of clouds (*Pruppacher and Klett*, 1997). More commonly in aerosol activation studies, however, it is presumed that there is no entrainment whatsoever (i.e., that $\mu_e = 0$). In the following sections, we develop the governing equations for both non-entraining and entraining versions of the constant-updraft model. However, because we will not

provide specific examples of entraining models, we will also not provide specific parameterizations of μ_e . In real clouds, entrainment is not continuous, instead occurring episodically (*Baker et al.*, 1980); the model we will develop in Section 6.3 considers such entrainment.

6.2.2 Pressure Equation

For both the entraining and non-entraining models, a governing equation for a parcel's pressure (p_p) is defined by assuming that the environmental pressure (p_e) is in hydrostatic equilibrium, meaning we assume that the gravitational and buoyancy forces balance:

$$\frac{dp_e}{dz} \approx \frac{dp_p}{dz} = -\frac{g p_p}{R_d T_e} \approx -\frac{g p_p}{R_d T_p} \quad (6.2)$$

Here, g is the gravitational constant, R_d is the gas constant for dry air, and T_e and T_p are the temperatures of the environment and of the parcel, respectively. Noting that the operator $\frac{d}{dz}$ is equal to $w \frac{d}{dz}$, we may write the hydrostatic equation (6.2) as a change with time of the parcel's pressure:

$$\frac{dp_p}{dt} = -\frac{g p_p w}{R_d T_p} \quad (6.3)$$

The presence of p_p in the numerator of the right hand side of (6.3) assures the expected exponential fall off of pressure with height.

6.2.3 Temperature Equation

We will develop the governing temperature equations for the two models by first finding expressions for the appropriate lapse rates, defined to be the fall-off of the ascending parcel's temperature with height ($-\frac{dT_p}{dz}$). The lapse rate takes a different value below and above a parcel's lifting condensation level (LCL) (Γ_d and Γ_s , respectively, where the subscripts indicate “dry” and “saturated”).

Below the LCL, the lapse rate of a sub-saturated, adiabatically lifted air parcel is given by a ratio of thermodynamic constants:

$$\Gamma_d = \frac{g}{c_{pa}} \quad (6.4)$$

Where, c_{pa} is the specific heat of air at constant pressure. The numerical value of Γ_d is approximately $9.8^\circ \text{ C km}^{-1}$ (refer to *Bohren and Albrecht*, 1998, for further discussion).

Above the LCL, lifting the parcel will result in super-saturations of water vapor which will be

ameliorated by water condensation onto aerosol. When this happens, heat is released and the rising parcel cools adiabatically less rapidly than in the dry case. The latent heat of condensing water (L_w) is the amount of heat released during phase-change per unit mass of water. We parameterize the latent heat following laboratory studies to be a linear function of temperature (*Bolton, 1980; List, 1984*):

$$L_w = 2.501 \times 10^6 - 2730 (T_p - 273.15) \quad (6.5)$$

Here, T is expressed in degrees Kelvin and the units of L_w are J kg^{-1} .

To a first approximation condensation balances the super-saturation induced by lifting and the parcel may therefore be assumed to remain exactly saturated. The adiabatic lapse rate in a saturated environment then becomes:

$$\Gamma_s = \frac{g}{c_{pa} + L_w \frac{dq_{v,sat}}{dT_p}} \quad (6.6)$$

Here, $q_{v,sat}$ is the liquid water mass mixing ratio at saturation, which is a function of pressure and temperature according to the Clausius-Clapeyron equation (*Bohren and Albrecht, 1998*). At 0°C and 1000 mb, Γ_s is $5.8^\circ \text{C km}^{-1}$, which is about three-fifths the value of Γ_d .

Of course, the adiabatic saturated lapse rate (Γ_s) applies only when the rising parcel is a closed system that does not exchange mass or heat with the local environment. Entrainment by environmental, drier air into a convectively rising cloud parcel can have the effect of lowering the cloud's liquid water content below that predicted by a closed adiabatic model (*Warner, 1970b*). A somewhat more realistic lapse rate along the track of a rising cloud parcel (Γ_c) accounts for the effects of entrainment. Assuming for now that the parcel remains precisely saturated, entrainment of sub-saturated air requires evaporation of sufficient liquid water to bring the entire parcel back to saturation. Note that this requires that the entrainment is not rapid enough, or the entrained air is not dry enough, to evaporate all liquid water, which may occur in some small regions of the updraft (*Baker et al., 1980; Twohy and Hudson, 1995*). The amount of heat required to be used to keep the parcel exactly saturated through evaporation depends on the relative masses and humidities of the pre-entrainment parcel (m_p) and the entrained air (Δm_p) which we parameterize using the entrainment rate (μ_e) that was discussed in Section 6.2.1. We also must account for the amount of heat required to bring T_e into alignment with T_p . By adding these two terms, we can work from equation (6.6) to write the entraining lapse rate (Γ_e) (*Austin and Fleisher, 1948; Pruppacher and*

Klett, 1997):

$$\Gamma_e = \frac{g + \mu_e [L_w (q_{v,sat} - q_{v,e}) + c_{pa} (T_p - T_e)]}{c_{pa} + L_w \frac{dq_{v,sat}}{dT_p}} \quad (6.7)$$

Here, $q_{v,e}$ is the water vapor mass mixing ratio of the entrained air.

By replacing $\frac{1}{w} \frac{d}{dz}$ and $\frac{d}{dt}$, we may rewrite the above expressions for lapse rates into expressions for the time rate of change of temperature in a parcel. Also, we will replace $q_{v,sat}$ with $q_{v,p}$, thus backing away from the assumption that the parcel is precisely at saturation; although we expect the parcel to be near saturation, it is precisely the small fluctuations about saturation that we wish to model and so this substitution is appropriate. For a non-entraining parcel, we work from equation (6.6):

$$\frac{dT_p}{dt} = -\frac{g}{c_{pa}} - \frac{L_w}{c_{pa}} \frac{dq_{v,p}}{dt} \quad (6.8)$$

While for an entraining parcel, we work from equation (6.7):

$$\frac{dT_p}{dt} = -\frac{g}{c_{pa}} - \frac{L_w}{c_{pa}} \frac{dq_{v,p}}{dt} - \mu_e w \left[\frac{L_w}{c_{pa}} (q_{v,p} - q_{v,e}) + (T_p - T_e) \right] \quad (6.9)$$

We use finite difference forms of each of these two equations in our implementation.

6.2.4 Water Condensation and Aerosol Dynamics Equations

The governing temperature equations (6.8) and (6.9) depend linearly on the parameterization of the rate of condensation onto an aerosol population ($\frac{dq_{v,p}}{dt}$) (see *Jensen and Charlson, 1984; Pruppacher and Klett, 1997; Nenes et al., 2001*). We will use MELAM to represent the aerosol distribution and to calculate condensation rates and other microphysical parameters within the parcel model. We will call this combined model – the MELAM microphysical model driven by the constant speed, adiabatic updraft model – the “MELAM updraft model.” Recall that MELAM employs the diffusion limited aerosol growth model to drive the condensation routine, as discussed in Section 5.7. Condensation also depends on detailed information about aerosol composition and sizes and on the thermodynamic calculation methods outlined in Chapter 4. By contrast, most similar updraft models do not include detailed composition data and thermodynamic calculations. They instead rely on condensation routines that depend on the gradient between the Köhler-type equilibrium discussed in Section 5.8.1 and the predicted super-saturation (see *Jensen and Charlson, 1984; Ghan et al., 1993, 1995; Abdul-Razzak et al., 1998; Abdul-Razzak and Ghan, 2000; Nenes et al., 2001*);

and their approach ignores the potentially important effects of composition on partial dissociation, surface tension, and other composition-related properties. Note that not all of the studies in the literature make these simplifications.

Equations (6.8) and (6.9) do not depend explicitly on coagulation, coalescence or any microphysical calculations beyond condensation as these processes have no direct thermal implications. These processes do impact (6.8) and (6.9) indirectly by changing the condensation rate $dq_{v,p}/dt$ slightly, but only at the one percent level or lower (and they will affect which aerosols attract the water vapor more intensely). Most aerosol activation studies in the literature calculate only condensation and no other microphysical dynamics. By embedding the full MELAM model in the rising parcel model, we have the option to calculate the effects of coalescence, dissolution, aqueous, or chemistry although in the studies considered in this Section and then next Chapter we will not. The decision of which physics to include in the model for a given study must relate to the scientific question being considered. The model must include all of the physics related to the specific effect under consideration, but including additional processes may make analyzing the results of the modeling run more difficult. In the introduction to each study, we will discuss which physics are to be included and justify the list.

6.2.5 Volume Equation

Parcels expand as they rise due to the falling pressure, changing temperature, and, in some cases, the entrainment of outside air. We relate a non-entraining parcel's volume at some arbitrary position 2 to its volume at another position 1 via the ideal gas law:

$$V_{p,2} = \left(\frac{p_{p,1}}{p_{p,2}} \right) \left(\frac{T_{p,2}}{T_{p,1}} \right) V_{p,1} \quad (6.10)$$

The numerical subscripts (1,2) indicate the parcel position to which the temperature ($T_{p,1}$ and $T_{p,2}$), pressure ($p_{p,1}$ and $p_{p,2}$), or volume ($V_{p,1}$ and $V_{p,2}$) relates.

We may also express equation (6.10) as a rate of change of volume with time by differentiating it:

$$\frac{d \ln V_p}{dt} = -\frac{d \ln \rho_a}{dt} = \frac{1}{\rho_a} \left(\frac{p_p}{R_d T_p^2} \frac{dT_p}{dt} - \frac{1}{R_d T_p} \frac{dp_p}{dt} \right) \quad (6.11)$$

Accounting for entrainment is then straightforward as it dilutes the parcel at a rate given by the

product of the entrainment rate and the vertical velocity:

$$\frac{d \ln V_p}{dt} = \mu_e w - \frac{d \ln \rho_a}{dt} = \mu_e w + \frac{1}{\rho_a} \left(\frac{p_p}{R_d T_p^2} \frac{dT_p}{dt} - \frac{1}{R_d T_p} \frac{dp_p}{dt} \right) \quad (6.12)$$

6.2.6 Summary and Example

Earlier in Section 6.2, we developed a set of differential equations that together define entraining and non-entraining constant updraft velocity parcel models. The non-entraining model is defined by the appropriate pressure equation (6.3), temperature equation (6.8), volume equation (6.11), and, once again, aerosol calculations from MELAM. The entraining model is similarly defined by an appropriate entrainment rate (6.1), pressure equation (6.3), temperature equation (6.9), volume equation (6.12), and aerosol calculations from MELAM. To integrate the adiabatic model forward in time, each of these processes are split from each other and stepped forward with a constant time-step (usually defined here to be the time period required to rise five meters, which is short enough so calculations are insensitive to its exact value).

By way of example, let us consider a population of 300 ammonium sulfate aerosol particle cm^{-3} which are initially log-normally distributed with a geometric standard deviation of 1.5 and a mean radius of $0.1 \mu\text{m}$, modeled with the representative sample distribution discussed in Section 3.3.5. The population is initially equilibrated at 98% \mathcal{RH} near the surface at 1000 mb and then lifted with a constant updraft velocity and no entrainment. MELAM is used to calculate time-dependent condensation and thermodynamics, but neither coagulation nor coalescence are included and so no precipitation is formed. This is comparable to the method used in *Jensen and Charlson* (1984), *Chuang et al.* (1997b), *Ghan et al.* (1998), and *Nenes et al.* (2001).

Figure 6-2(a) shows the evolution of \mathcal{RH} with altitude. Figure 6-2(b) shows the fraction of particles activated as a function of altitude. Finally, Figure 6-2(c) shows the liquid water content of the parcel. As defined in Section 5.8.4, an aerosol is considered activated when the derivative of the equilibrium saturation ratio with radius ($\frac{dS'}{dr}$) is negative, as evaluated by perturbation of its water content. Several important features of this type of parcel model are apparent in Figure 6-2.

First, as seen in Figure 6-2(a), \mathcal{RH} increases with altitude to a super-saturated peak just above the LCL that depends on the updraft speed; stronger updrafts lead to more dramatic super-saturations than do weaker ones. This, of course, relates to the amount of time required for water to condense upon the aerosol beginning once the lifted parcel reaches saturation at its LCL, and so relates to the properties of the aerosols themselves (refer to Section 5.8 for further discussion). Were Köhler theory strictly obeyed, all droplets with a critical super-saturation below the max-

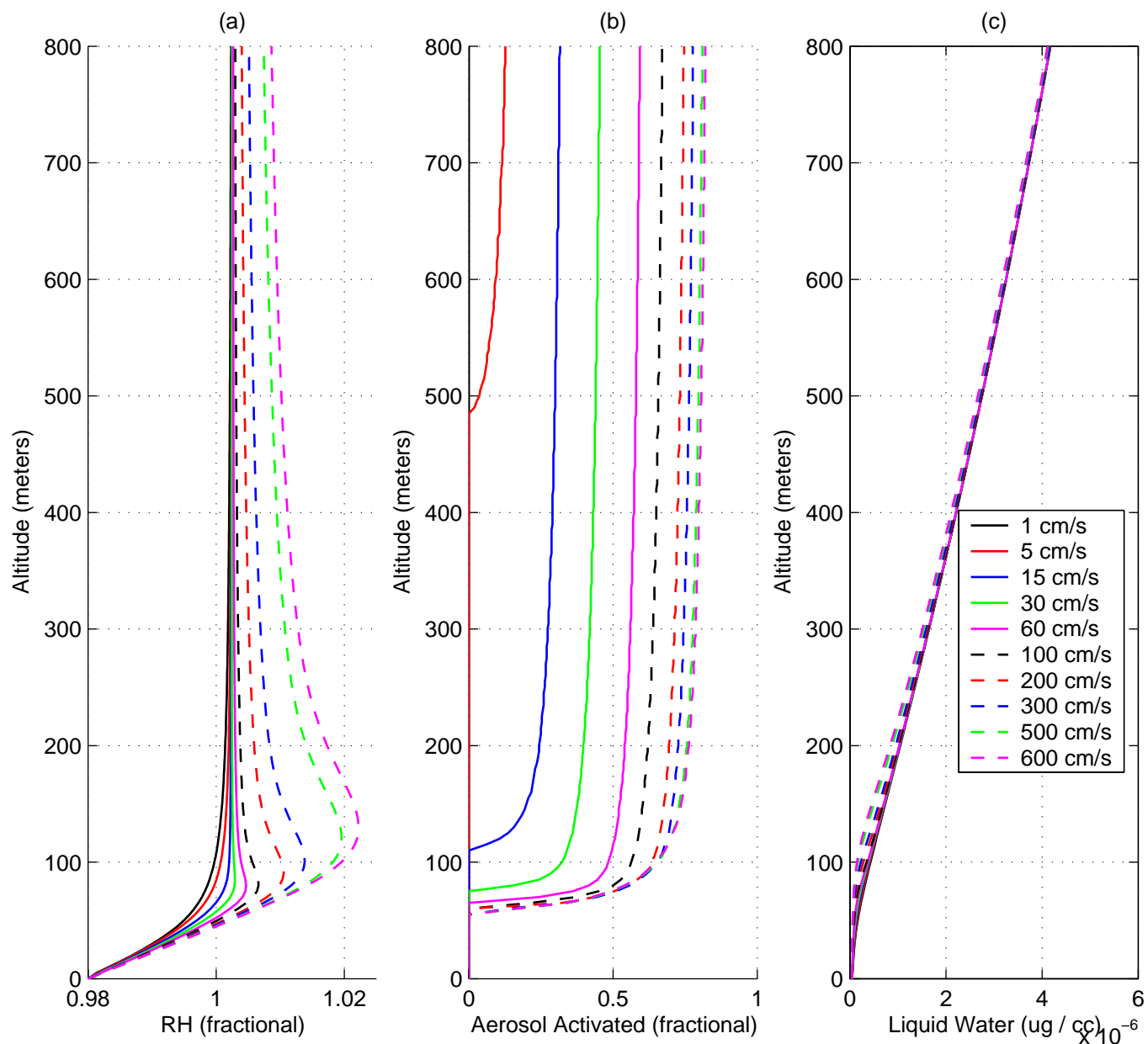


Figure 6-2: Non-entraining parcel model used to calculate the activation of a 300 particle cm^{-3} $(\text{NH}_4)_2\text{SO}_4$ aerosol population (mean radius of $0.1 \mu\text{m}$ and geometric standard deviation of 1.5) adiabatically lifted the indicated distance

imum super-saturation achieved in the updraft would activate. This is not what is seen. Large particles, which require significant amounts of time to grow to their equilibrium size (see Section 5.4), may take a sustained super-saturation above their critical level to activate, rather than activation according to the peak super-saturation as suggested by equilibrium theories (*Chuang et al.*, 1997b). In none of the updrafts do the largest aerosol activate within the 800 m ascent considered.

Second, increasing the updraft velocity above a certain level yields a very small marginal increase in activated particles. Figure 6-2(b) shows that once updrafts of more than 2 m/s have been achieved, increasing the updraft velocity further has little effect. Of course, there is a critical updraft velocity above which all aerosol will activate (it will sustain a super-saturation above the critical super-saturation of all particles for a sufficient amount of time that they activate), but for this particular distribution that velocity is above the range considered. It is very unlikely that reasonable updraft velocities activate the entire aerosol distributions seen in nature except in the most remote, aerosol-poor environments.

Third, the liquid water content of the parcel, shown in Figure 6-2(c), is approximately the same regardless of the updraft velocity and increases approximately linearly with altitude (although we will see in Section 6.3.6 that this is simply the linear region of more complex profile that balances condensation with parcel expansion). As shown in Figure 6-2(a), a parcel maintains a \mathcal{RH} value near (but slightly above) unity during ascent even though the parcel saturates at decreasing specific humidities (due to decreasing pressure and temperature), implying a similar amount of condensation for each parcel. Interestingly, the strongest updrafts activate dramatically more aerosol than the weakest, as shown in Figure 6-2(b), and yet yield slightly less liquid water overall, as shown in Figure 6-2(c). This occurs because the strong updrafts are able to maintain higher super-saturations thus keeping slightly more water in the vapor phase. That is, parcels in which no aerosols activate (e.g., those in a 1 cm/s updraft) contain more liquid water at comparable altitudes than those in which most of the aerosols do activate (e.g., that in a 6 m/s updraft); note that the slow parcels will take considerably longer to reach a particular altitude.

Consider Figure 6-3, which presents a binned-representation of the initial aerosol distribution (in black) and final distributions for updraft speeds of 1 cm/s (blue), 15 cm/s (green), and 6 m/s (red). Note that all of the final distributions have absorbed almost the same amount of liquid water. All activated particles cluster into concentration peaks near a 10 μm radius, while the unactivated particles (typically all the particles below a certain critical radius) maintain their relative size distribution and grow rather uniformly. The blue distribution, which contains no activated particles, has some fraction of particles that have grown to the size of the activated

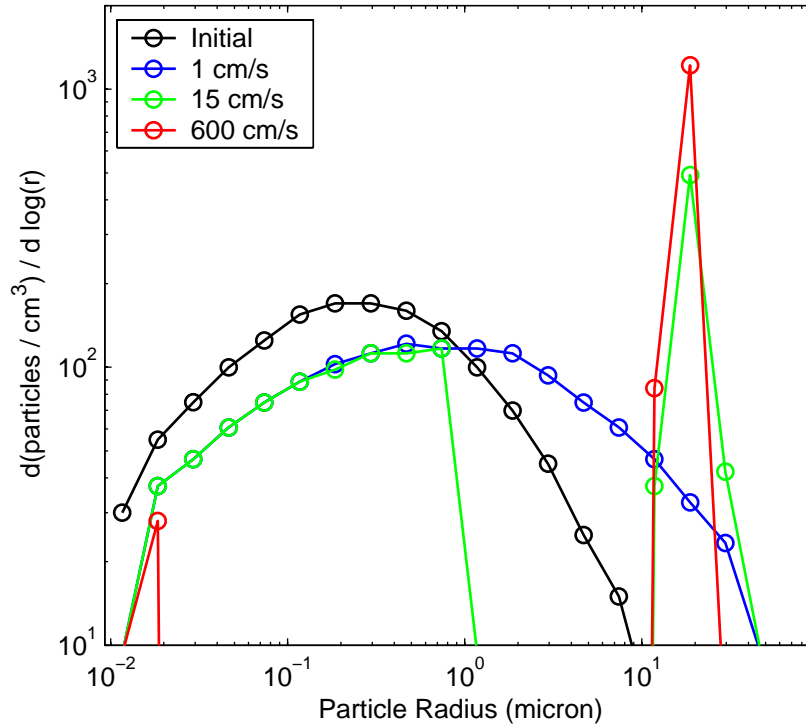


Figure 6-3: Initial (black) and final distributions for $300 \text{ cm}^{-3} (\text{NH}_4)_2 \text{SO}_4$ aerosol with mean radius of $0.1 \mu\text{m}$ and geometric standard deviation of 1.5, adiabatically lifted for 800 m at 1 cm/s (blue), 15 cm/s (green), and 6 m/s (red)

droplets from other distributions. The radiative properties of these three final distributions will be quite different despite the fact that they contain nearly the same amount of liquid water. Traditional coalescence models neglect turbulence and so will grow these distributions quite differently as well, as the droplets in the the narrow peak will have comparable terminal fall velocities (cf. *Khain and Pinsky*, 1995; *Pinsky and Khain*, 1997). Hopefully the current difficulties in traditional aerosol models of in representing turbulent effects in a coagulation kernel will soon be resolved.

As mentioned earlier, this type of adiabatic constant-updraft parcel model has been used in a long series of studies seeking to model aerosol activation. It allows a highly idealized means to study some of the physics of activation since it isolates purely condensational (or, generally, microphysical) effects from the many other dynamics that exist within a cloud, such as precipitation, turbulence, and entrainment (*Yum et al.*, 1998; *Hudson and Yum*, 2001). In Section 6.3, we will present an updraft model that incorporates entrainment and other cloud processes into the simple framework of a parcel updraft model. Before we do, we will discuss in Section 6.2.7 the limitations of the constant speed, adiabatic updraft parcel model and its appropriate use.

6.2.7 Problems with the Constant Updraft Model

Although the adiabatic constant-updraft parcel model of cumulus convection was once dominant within the cloud physics community, critiques based both on theory and observation surfaced as early as the late 1940's. Many subsequent improvements in the adiabatic model have been proposed over the intervening half century, all of which incorporate entrainment. There is still some debate on how to define the origin of the entrained air and the mixing procedure. Despite its shortcomings, the adiabatic constant-updraft parcel model remains the dominant dynamical framework for microphysical aerosol activation modeling studies within the aerosol microphysics community. As we alluded to before, assuming a parcel rises adiabatically and at a constant speed isolates condensational physics from the competing influences of cloud dynamics, and is useful when one wants to calculate the distribution of cloud condensation nuclei (CCN) from which a cloud develops rather than the cloud droplet distribution at a particular point within a cloud (*Hudson and Yum, 2001*). Parcel models are simply not sophisticated enough to replicate the large-scale behavior of clouds and direct analogies between CCN and cloud droplet distributions should be carefully considered.

In this Section, we discuss and critique both the adiabatic constant-updraft models in the literature from the perspectives of both the cloud dynamics and the aerosol microphysics communities, discuss in brief to the so-called buoyancy-sorting model which has set the current standard for accuracy in simplified convection routines, and allude to the modeling frameworks upon which we will base a new updraft model in Section 6.3, and then argue that adiabatic constant-updraft models have a role to play in studies of aerosol activation although not as direct analogies to full clouds.

The first thoughtful critiques of the adiabatic constant-updraft model from within the cloud physics community noted (from observations) that the properties most favorable to an adiabatic cloud's persistence are breadth, high liquid water content, and a steep lapse rate. Adiabatic models are unable to predict all three, since in the framework of the model they are mutually exclusive (*Austin, 1948; Austin and Fleisher, 1948*). *Warner (1970b)* addresses the water content issue by comparing mean liquid water content data from several field campaigns (q_{obs}) to the values expected were cloud base air adiabatically lifted ($q_{\text{adiabatic}}$). Figure 6-4 reproduces a figure from *Warner (1970b)* in which he specifically compares observations of in-cloud liquid water content by *Ackerman (1959, 1963)*, *Squires (1958b)*, *Warner (1955)*, and *Skatskii (1965)*, presenting each observation as a ratio to the water contents he calculated using a simple adiabatic parcel model. *Warner (1955)*'s and *Squires (1958b)*'s observations were specifically for non-precipitating cumulus,

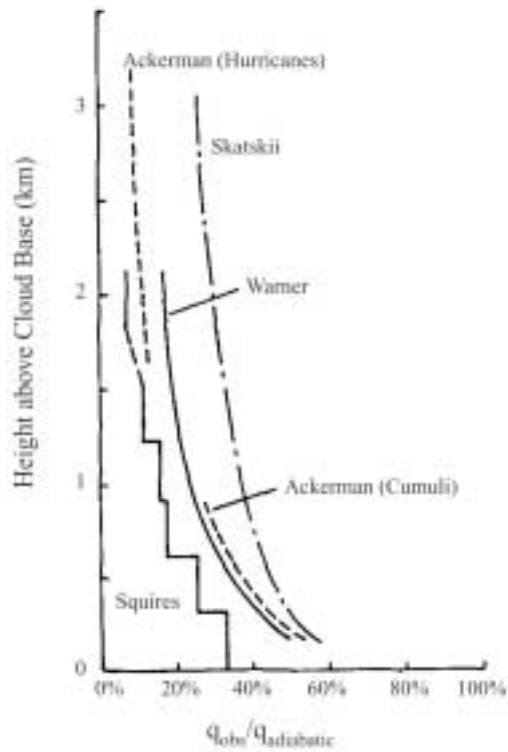


Figure 6-4: Ratio of observed mean liquid water content to the value expected were cloud base air, adiabatically lifted, is given as a function of altitude (adapted from *Warner*, 1970b)

while the others may be skewed by the drying effects of precipitation. Note that all observed liquid water content values are well below those calculated by the adiabatic model, with the maximum values (relative to the adiabatic calculations) occurring near cloud base and decaying with height. *Warner* (1970b) and others attribute this decay to the entrainment of air into a rising parcel.

Initial mixing theories suggested that an appropriate analogy to non-precipitating cumulus convection is a rising plume (*Stommel*, 1947; *Squires and Turner*, 1962) or thermal (*Scorer*, 1957) that entrains laterally at a constant rate. (In these models the entrainment parameter μ_e , or its equivalent, is drawn from an analogy to tank experiments and tuned so that the calculated cloud properties match observations.) However, *Warner* (1970a,b) showed that the models could not accurately predict mean liquid water content and cloud top height of even non-precipitating cumulus clouds; tuning μ_e could successfully match one of the quantities but not both. Also, *Warner* (1955)'s observations showed that clouds may be as wet near their edges as towards their centers, at odds with what would be expected in a constantly entraining updraft. These models did provide the insight that entrainment could explain the disparity between the observed liquid water content and that calculated using a constant-speed adiabatic updraft model.

Other authors counter-proposed that mixing occurs primarily due to unsaturated downdrafts originating at the cloud top which are given negative buoyancy from the evaporation of precipitation, and then exit at the appropriate level of neutral buoyancy (LNB) (*Squires, 1958a; Emanuel, 1981*). Such models successfully replicated water contents given a specified cloud top, but do not provide a physical mechanism for the determination of the cloud top height or overall development of the cloud.

The most successful theories yet proposed appeal to a stochastic mixing hypothesis in which mixing of air from outside the cloud occurs episodically with a cloud parcel that otherwise rises (or falls) without mixing (*Baker et al., 1984; Raymond and Blyth, 1986*). In this model, the cloud top level is set at the LNB of the portion of sub-cloud air lifted through the cloud base that never mixes. These theories were made operational as the “buoyancy sorting” hypothesis (*Raymond and Blyth, 1986, 1992*) and resulting parameterizations (e.g., *Emanuel, 1991*). We will discuss this hypothesis further in Section 6.3.1, and discuss how it contrasts with the episodically entraining updraft model we will propose in Section 6.3.

The buoyancy sorting appears to yield an accurate picture of the large-scale effects of cumulus convection such as water vapor distribution and cloud extent (*Emanuel and Zivkovic-Rothman, 1999; Bony and Emanuel, 2001; Hogan et al., 2001*); note that this is not the same as saying that the physical model is entirely correct, rather it is a statement that the parameterization represents the effects of convection on the large scale well in regional models (again, see Section 6.3.1). In the buoyancy-sorting model, parcels rise and fall without entrainment between mixing events and the simplified context of an adiabatic model is useful when considering physical effects, such as competition or kinetic limitation, that occur during the relatively short periods of adiabatic ascent. Also, some parcels will rise from cloud base to cloud top and encounter no mixing events along the way (indeed, this is one notion of how the level of the cloud top is defined), which ought to be described well by an adiabatic updraft model in the absence of precipitation. Any physical effect seen in an adiabatic updraft model will also be seen within a cloud. Results of these studies should not be interpreted, however, as providing analogies to any complete clouds we observe in nature (as some studies in the literature have done). In particular, the formulations of the adiabatic ascent models gloss over how critical and how un-representative the exact updraft speed at the LCL actually is: this updraft speed is not constrained by convective dynamics, nor is it easy to constrain with observations. We will return to this discussion when considering a new parcel model in Section 6.3.

The aerosol measurement and modeling communities has been dependent on the constant-

speed adiabatic updraft model, and a number of research groups have thoughtfully considered the appropriate use of these models. *Baker et al.* (1980) discusses the evolution of the droplet size distribution in adiabatic, constantly entraining, and episodically entraining updraft models. They note that adiabatic models estimate a droplet spectrum which is too narrow, while the episodically entraining model leads to a broader distribution in much better in accord with observations. This does not imply that entrainment changes the number of aerosols that activate to form CCN, as that is determined largely by the updraft speed through the cloud base and the characteristics of the aerosols themselves (*Twomey, 1977a*). Rather, non-adiabatic cloud dynamics play a large role in the development of the cloud droplet distribution from the CCN formed near cloud base.

In observational studies that relate measurements of sub-cloud aerosols to the droplet distributions in the clouds above, aerosols are commonly characterized by their critical super-saturation (the super-saturation that would cause them to activate within an equilibrium framework, per Section 5.8.1). In an adiabatic updraft model, all of the aerosol with critical super-saturations below the maximum achieved super-saturation would activate if equilibrium were assumed (we discussed earlier that large aerosols may not activate despite their low critical super-saturations, in violation of the equilibrium assumption). In the observational studies, an effective achieved super-saturation is calculated by considering the observed cloud droplet size distribution and reasoning towards how many and which of the sub-cloud aerosols activated and what the maximum super-saturation must have been (e.g., *Yum et al., 1998*). *Yum et al.* (1998) note that there are often significant deviations between the effective super-saturation calculated from observations and the expected maximum super-saturation calculated using observed updraft speeds for stratus clouds and an adiabatic constant-speed updraft model. These disparities are related to cloud dynamics that are not included in the idealized constant-updraft adiabatic parcel models – notably precipitation, variability of updraft speeds, and entrainment – the last two of which tend to de-activate the activated aerosols with the highest critical super-saturations. This de-activation has the effect of making the resulting droplet distribution resemble those formed in an updraft with a lower maximum super-saturation than actually occurred (*Yum et al., 1998; Hudson and Yum, 2001*). This is one example of how the constant-updraft adiabatic updraft model misrepresents the microphysical development, as well as the large-scale dynamical development, of clouds.

Aerosol observations have the potential to shed light onto open questions of cloud dynamics, notably entrainment. *Twohy and Hudson* (1995) compare measurements of the critical super-saturation of cloud droplets and interstitial aerosol (refer to Section 5.8 for relevant discussion). They show that clouds contain aerosols with various super-saturation histories, also implying that

entrainment of air occurs above cloud base. Measurements similar to those taken by *Twohy and Hudson* (1995) could reveal a great deal about the mixing history and dynamics of clouds if taken on a finer spatial scale.

Both the cloud dynamics and aerosol microphysics communities have found serious limitations in the analogy between constant-speed adiabatic updraft models and actual clouds. Entrainment and a prescription of an appropriate variability in updraft velocity, at the very least, must be incorporated to make such a relationship credible. These models do, however, provide important insights into aerosol physics, especially the activation of aerosols to CCN near cloud base and the behavior of aerosols and cloud droplets during adiabatic parcel movement between entrainment events. The behaviors observed in these models are easily attributable to condensation and are uncluttered by other dynamics. They therefore provide useful insight into the microphysical development of clouds.

The ultimate goal of this type of simple updraft modeling, however, is to link aerosol populations to the properties of clouds formed on them (notably, cloud optical properties and precipitation patterns) for use in large scale models. The goal is to link changes in large-scale aerosol patterns to changes in climate. That link cannot be made complete without consideration of the implications of all cloud dynamical processes on aerosol activation, and vice versa. And it cannot be made without some method to predict updraft velocities. In the next Section, we will present an episodically entraining, variable-speed updraft model that highlights some of these relationships.

6.3 A New Entraining, Variable-Updraft-Speed Parcel Model

As discussed above, many aerosol activation studies available in the literature use adiabatic constant-updraft parcel models to provide boundary conditions to complex aerosol-cloud microphysical models. Observations and theoretical work by the cloud physics community, however, has proved the adiabatic constant updraft model to be a poor analogy to cloud formation (see Section 6.2.7). Alternatives to the adiabatic constant-updraft model have, until recently, used entraining plumes or thermals as analogies to convective clouds. More recent theoretical work lead to the “buoyancy sorting” hypothesis which more accurately predicts the effects of convection on large-scale distribution of water vapor and other regional-scale environmental variables.

In this Section, we present a new episodically entraining, variable-updraft-speed parcel model which will rely upon calculations by the *Emanuel* (1991) cloud parameterization. This model differs

significantly from the constant updraft parcel model presented in Section 6.2 in that it assumes more realistic lateral mixing and vertical velocities and is linked to information that is available from the convective cloud parameterizations of regional and global models. We will use the *Emanuel* (1991) model, which is based upon the sophisticated buoyancy sorting framework, to determine cloud entrainment and the large-scale thermodynamic state of the atmosphere, which we will then use to define a vertically-varying mean updraft velocity. We do not, however, pattern the updraft model after the buoyancy sorting models available in the literature; doing so would involve calculating the development of many separate sub-parcels and providing appropriate vertical velocities for each. Our model is an entraining parcel model that is driven by a buoyancy-sorting convective routine.

We will use the new parcel model to consider what happens in convection that is deeper than boundary-layer topping clouds. The example application of this model that we will consider at the end of this chapter will not incorporate the effects of coagulation and coalescence to limit the already significant complexity. However, since the full MELAM model is embedded these effects will be simple to incorporate in future studies.

In the the remainder of this section, we outline and discuss the justifications of the episodically entraining plume model and the buoyancy sorting hypothesis in Section 6.3.1, present a framework for a new parcel model in Section 6.3.2, formulate an approach to calculating vertical velocities in Section 6.3.3, parameterize lateral entrainment in Section 6.3.4, present a parameterization of the vertical distribution of aerosol in Section 6.3.5, and summarize and discuss a simple example application in Section 6.3.6.

6.3.1 The Episodically Entraining Plume and the Buoyancy Sorting Hypothesis

Observations of non-precipitating warm cumulus clouds from the Cooperative Convective Precipitation Experiment (CCOPE) revealed such clouds to be a patchwork of small, apparently well-mixed regions on the order of hundreds of meters across. The data revealed no clear trend in bulk microphysics with height (including cloud drop concentration and liquid water content), but rather showed variability on the same scales in the horizontal and vertical. The CCOPE data also apparently support none of the prevailing cloud evolution theories, which generally are based on the notion of homogeneous microphysical parameters at a given altitude and some combination of horizontal mixing, mixing from the cloud top, fluctuating vertical velocities, and other proposals (*Austin et al.*, 1985). The CCOPE data does, however, appear to support *Telford* (1975)’s “buoyancy sorting” hypothesis (*Blyth and Raymond*, 1988). In a model based on the buoyancy sorting hypothesis, a parcel rises adiabatically for some distance, episodically mixes, and then proceeds

either upwards or downwards according to the buoyancy of the new mixture. The parcel first rises adiabatically from cloud base as either a thermal (e.g., *Blyth and Raymond*, 1988) or a plume (e.g., *Jensen et al.*, 1985) towards its level of neutral buoyancy.

In the buoyancy sorting model, a parcel that rises through the cloud base ascends until it mixes laterally and irreversibly with environmental air (one must assume that the environmental air is representative of the free atmosphere and that it does not contain traces of detrained cloud air or other influences of the local cloud), after which it proceeds to its new level of neutral buoyancy and exits the cloud (*Raymond and Blyth*, 1986). Of course, multiple mixing events occur in nature but are not required in the parameterizations to correctly approximate the effects of convection on larger scales (*Taylor and Baker*, 1991). Operational models must assume some likelihood that a mixing event occurs at a particular altitude. *Raymond and Blyth* (1986), as a first proposal, assume that a rising parcel is equally likely to have a mixing event at each model level between cloud base and the level of neutral buoyancy for the sub-cloud air (an acknowledgement that they had no information to justify using anything but a “white noise” distribution).

The microphysics of an episodically entraining parcel are determined in part by how much environmental air is entrained, and thus how much each mixing event dilutes the parcel and adds new aerosols (*Baker et al.*, 1980). Models based on the buoyancy sorting hypothesis have assumed several forms for the PDF that describes the mixing ratio as a function of altitude: dependent on vertical velocities (*Bretherton and Smolarkiewicz*, 1989; *Emanuel and Zivkovic-Rothman*, 1999), uniform (*Emanuel*, 1991), centered Gaussian (*Kain and Fritsch*, 1990), “U-shaped” negative-Gaussian (*Cohen*, 2000), and bi-modal (*Grandpeix et al.*, 2004). There is not much data or theory to constrain either the PDF that describes the altitude of mixing or the PDF that describes the proportion of mixing at each level, but these two PDFs play a large role in the control of environmental relative humidity and are the subject of active research (*Grandpeix et al.*, 2004). Their eventual refinement will improve the performance of buoyancy sorting models, and shed light on the proper formulation of entraining parcel updraft models.

In the buoyancy sorting model, a newly mixed parcel rises or falls according to its buoyancy (mixing can produce both positive and negative buoyancies although sub-saturated mixtures are always negatively buoyant) and exits the cloud at its level of neutral buoyancy (*Raymond and Blyth*, 1986). This buoyancy sorting model, in which small parcels rise and fall after discrete mixing events, produces vertical profiles of temperature and dew point that match the CCOPE data reasonably well (*Blyth and Raymond*, 1988).

Emanuel (1991) (henceforth E91) presents a convective parameterization for use in larger mod-

els that follows on *Raymond and Blyth* (1986)’s buoyancy sorting hypothesis. It successfully replicates many of the observed properties of clouds, including: the appropriate levels and origins of dilution, the presence of saturated downdrafts that are comparably strong to the updrafts in non-precipitating cumulus clouds, and unsaturated downdrafts driven by the evaporation of precipitation (*Emanuel*, 1991; *Taylor and Baker*, 1991). E91’s model, after tuning, reproduces large-scale environmental humidity and temperature data from the Tropical Ocean Global Atmosphere Coupled Ocean–Atmosphere Response Experiment (TOGA COARE) (*Emanuel and Zivkovic-Rothman*, 1999; *Bony and Emanuel*, 2001). Without further tuning, it has also proved dramatically more successful than a relaxed Arakawa and Schubert type scheme (essentially an entraining plume that relaxes towards equilibrium *Arakawa and Schubert*, 1974; *Moorthi and Suarez*, 1992) in the Navy Operational Global Atmospheric Prediction System (*Hogan et al.*, 2001). Despite its accuracy, most large-scale operational forecasting models and global climate models have not adopted parameterizations based on the buoyancy sorting hypothesis, in part due to its large computational expense relative to other convection schemes (cf. *Mahowald et al.*, 1995). The model’s success, we should note, is in representing the behavior of all the clouds in a given region, and in all phases of the life cycle of a cloud, rather than modeling the behavior and development of a particular cloud. The parcel model we will develop from it should be understood in this context: as representative of the overall behavior of the entire ensemble of clouds in a region rather than of a particular cloud or type of cloud.

The buoyancy sorting hypothesis and E91 model have successfully replicated small-scale traits of clouds and large scale environmental properties, which lends some confidence in the model’s correctness. At this point, however, it is not clear how one would make the link between this hypothesis and a parcel model. The primary complication is in calculating appropriate updraft speeds. The buoyancy sorting model produces a large number of parcels at each level that have different buoyancies and move in different directions, presumably at different speeds. Unfortunately, an unresolved difficulty in developing parameterizations of cloud dynamics is the calculation of vertical velocities, even on average (e.f., *Emanuel and Bister*, 1996; *Pauluis and Held*, 2002b). A more complete model, one which would approximate the microphysics at each vertical layer within a convective cloud, might track and aggregate individual updrafts and individual downdrafts; however, the E91 model is not formulated to necessarily yield realistic vertical cloud profiles (rather, it approximates the behavior of clouds relative to a regional environment). An explicit finely-resolved dynamical-physical cloud model such as *Wang and Chang* (1993a)’s would be more appropriate for such a study. At this point, such large scale, complex, cloud-resolving models are appropriate for

detailed studies of aerosol venting processes and assessing approximations of the indirect effects of aerosols (e.g. *Ekman et al.*, 2004), but due to our computational limitations they are not appropriate for including the complex small-scale microphysics we wish to consider. Our intent is simply to introduce reasonable vertical profiles of updraft speed and mixing into a parcel model, and for this purpose our treatment and adoption of the E91 model is sufficient.

In Section 6.3.3, we will develop a simple method to approximate mean vertical velocities within clouds using a thermodynamic sounding. We will use the *Emanuel* (1991) model to calculate this sounding, as this model has proven very successful at calculating the large scale thermodynamic state of the atmosphere near convection. However, we will use the velocities and entrainment rates derived from the *Emanuel* (1991) model to drive a rather simpler entraining plume model. We will use the entraining plume to consider the two limiting examples of a parcel that never entrains and a parcel that entrains air at every possible level. What we will learn by doing this will provide some understanding of the impact of the dynamics of the buoyancy sorting model on the microphysical development of the droplet distribution, and will shed light on the inadequacies of the the analogy between constant speed updraft models and actual clouds. Our investigation will shed light on the effects of a variable updraft speed and of episodic entrainment, but is not to be interpreted as a direct application of the buoyancy sorting hypothesis to a parcel model. The appropriate representation of aerosol activation and other microphysics alongside realistic cloud dynamics is an important subject that will take more time, and faster computers, to resolve.

6.3.2 Framework for an Episodically Entraining, Variable-Updraft-Speed Parcel Model

We can imagine two methods to turn the buoyancy sorting hypothesis into a lagrangian parcel updraft model. The first is to track the mixing and fate of each parcel that detaches from the sub-cloud parcel as it rises and sub-divides according to the algorithm detailed in *Raymond and Blyth* (1986). The second is to force an entraining model with the entrainment and mass fluxes calculated from a convective parameterization either run transiently or to radiative-convective equilibrium. Near the end of the last section, we discussed the inherent difficulty of adopting the first approach: the difficulty of approximating updraft speeds even in mean, much less for each of numerous parcels; the lack of understanding of the PDFs that govern the likelihood a parcel will mix at a given level and the amount of environmental air entrained during a mixing event; and the general inability to measure microphysical properties at the scale of the updraft. Due to these limitations, we choose the second approach for this study.

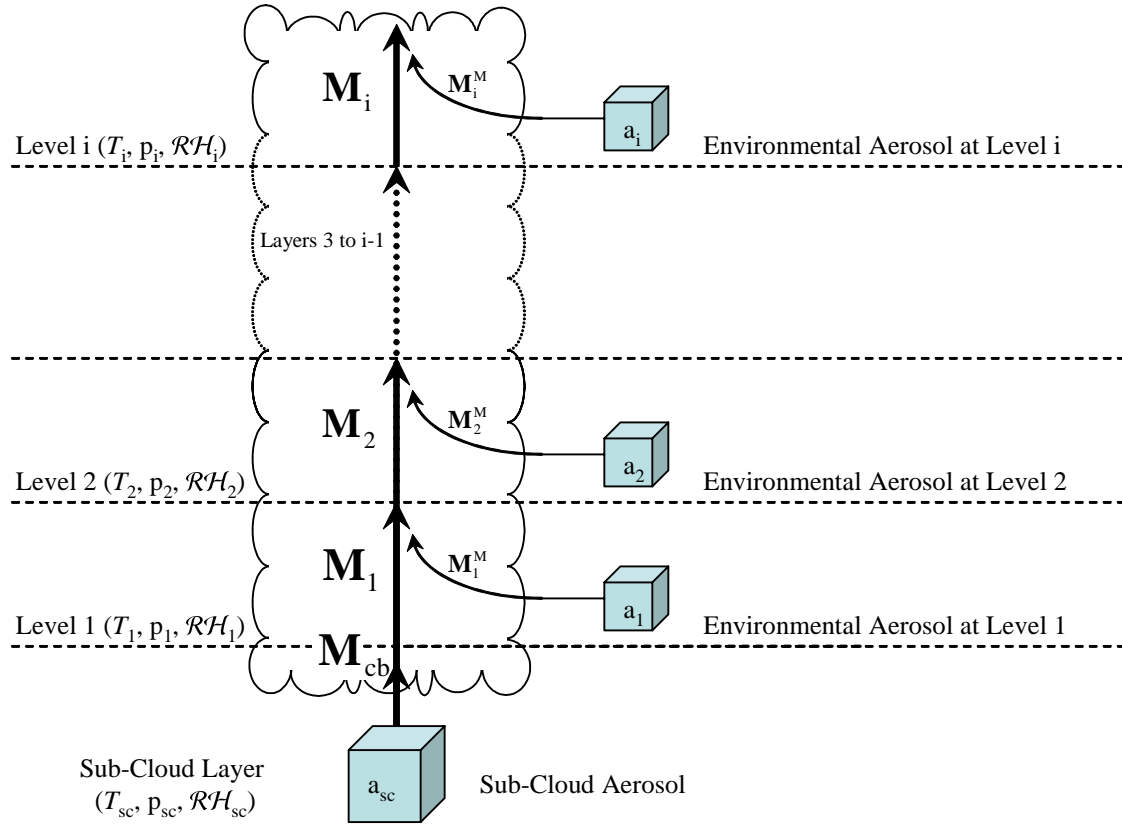


Figure 6-5: Diagram of the lagrangian episodically entraining, variable-speed parcel updraft model proposed in Section 6.3

For the study, we will use the E91 convective parameterization to calculate vertical distributions of thermodynamic environmental variables and entrainment rates into clouds at all levels. We discussed the E91 parameterization in Section 6.3.1 (see *Emanuel, 1991; Emanuel and Zivkovic-Rothman, 1999*), along with enhancements for diagnosing cloud cover (*Bony and Emanuel, 2001*). The radiation scheme uses a two-stream method to solve the radiative transfer equation, with two spectral intervals in the short-wave parts of the spectrum (*Fouquart and Bonnel, 1980*) and six in the long-wave (*Morcrette, 1990, 1991*).

The E91 model is based on the theories of *Telford (1975)* and *Raymond and Blyth (1986)*, as discussed in the preceding Section 6.3.1, and uses a uniform PDF to determine the relative amount of environmental air entrained during each mixing event (with respect to the amount of air pulled from the original sub-cloud parcel).

Figure 6-5 is a schematic of our parcel model. Since we will use this model to consider aerosol activation, we concern ourselves with only the updrafts and do not track air that exits the cloud or enters the downdraft.

The E91 model is 1.5 dimensional with simple categories in the horizontal and a finely resolved vertical domain with 25 mb steps (accurate calculation of vertical environmental \mathcal{RH} requires less than 50 mb steps; *Emanuel and Zivkovic-Rothman, 1999*). At each pressure level, a set fraction of the horizontal domain is within the unsaturated downdraft and the rest is either in a saturated updraft within the cloud, an saturated downdraft within the cloud, or outside of the cloud; the distribution between these regions is not well understood, and we discuss it further in Section 6.3.3 when we consider the parcel’s vertical velocity. At each model level i , the non-cloudy environment is described by a temperature (T_i), a pressure (p_i), a relative humidity (\mathcal{RH}_i), and an aerosol distribution that is in equilibrium with the environmental properties of the air outside of the cloud at that altitude.

Referring to Figure 6-5, a parcel of air begins in the sub-cloud layer and contains a distribution of aerosol (a_{sc}). It ascends with an upward mass flux through the cloud base (\mathbf{M}_{CB}) that is determined in E91 according to the sub-cloud layer quasi-equilibrium hypothesis (*Raymond, 1995; Emanuel and Zivkovic-Rothman, 1999*). At each level i above the cloud base, a certain amount of environmental air entrains or detrains (in net), as described by the mixing mass flux (\mathbf{M}_i^M). Entraining air brings with it some amount of aerosols (a_i) that, as noted above, are in equilibrium with the environment at that altitude and mixes irreversibly with the updraft parcel. Between mixing events, the parcel rises adiabatically.

For the purposes of developing our parcel model, we run the E91 model to radiative-convective equilibrium (using constant, daily average radiation), and use the mass fluxes and other quantities averaged over one full day at equilibrium. The simplifying assumption of radiative-convective equilibrium is meant to provide a generalized first example; a study that used this method to compare with specific field campaign data would want to embed this convective parameterization within a regional scale mode and calculate variations in convection and the environmental thermodynamic profile with time. We consider the cloud base to be located at the model level that presents the first non-zero upward mass flux and the convective cloud top to be at the level of the first significant detrainment (which is usually one third to one half of the total upward mass flux).

6.3.3 Vertical Velocities

In order to compute activation in the model presented in Section 6.3.2, we must externally impose vertical updraft velocities. Unfortunately, although theory allows us to determine net vertical mass flux in a convective system, current theories are unable to separate the vertical velocity from the cross-section of the aggregated updrafts. In this section, we present a simple model of updraft

velocities that depends on a relationship between vertical velocity and the convective available potential energy (CAPE) and several other simplifying assumptions. Given that microphysical models of cloud activation predominantly use constant updraft assumptions, this is nevertheless a step forward. It should not, however, be considered as anything more than a first step, since here we come up against the limits of our basic understanding of convection. Our updraft velocity model, while appropriate for our purposes, will give us very little insight into updraft speeds at cloud base, which we will show is a critical parameter in aerosol activation.

In radiative-convective equilibrium, heating at the surface balances radiative cooling at height and moist convection transports heat upwards from the surface (e.g., *Pauluis et al.*, 2000). Convective upward mass flux in clouds is constrained thermodynamically by the subsidence of radiatively-cooled clear air between clouds (*Emanuel and Bister*, 1996). This thermodynamic constraint is placed on the total saturated convective mass flux rather than on the finer scale properties:

$$\mathbf{M}_i^{(\text{subsidence})} = f(\text{radiative cooling}) \quad (6.13)$$

$$= \sum_j \mathbf{M}_{i,j}^{(\text{updraft})} \quad (6.14)$$

$$= \rho_i w_i \mathcal{A}_i \quad (6.15)$$

Equation (6.13) states that total downdraft mass flux is a function of radiative cooling. Equation 6.14 states that the subsiding mass flux is balanced by the total updraft mass flux, and that the average upward mass flux at level i (\mathbf{M}_i) is the sum of the mass fluxes of many smaller updrafts at that altitude, here indexed by j ($\mathbf{M}_{i,j}$). Equation (6.15) states that the average upward mass flux at level i may be expressed as the product of an average upward velocity across all updrafts (w_i), the total fractional updraft cross-section (\mathcal{A}_i), and the average air density (ρ_i). Various convective theories, including buoyancy sorting which was outlined in Section 6.3.1, provide some basis for understanding the relative distribution of mass fluxes between separate updrafts, if only in the simplest case to presume that there is a single updraft element (see, for example, the review of *Mahowald et al.*, 1995).

It is appealing to attempt to determine w_i by separating w_i and \mathcal{A}_i in equation (6.15), but this is beyond the present state of relevant theory. Furthermore, direct observations of the variation of \mathcal{A}_i with altitude are inconsistent, suggesting that there is no useful way to impose a direct constraint on a cloud's vertical cross-sectional profile in conjunction with equation (6.15). Some studies have suggested that \mathcal{A}_i does not vary much with altitude in cumulus and cumulonimbus convective systems, either in mean or in the cases of the strongest updrafts, except for perhaps at

very low levels (*Byers and Braham, 1949; LeMone and Zipser, 1980; Jorgensen and LeMone, 1989*). However, other studies have shown the opposite, namely that \mathcal{A}_i varies significantly with height within individual clouds, including within hurricane rain-bands (*Jorgensen et al., 1985*) and, in one instance, within the strongest convecting 10% of a moderately convective region (*Lucas et al., 1994*). Even if we understood how the cross-section of individual clouds varied with altitude, calculating \mathcal{A}_i for the aggregation of all the clouds in a region is even further beyond our understanding. And even understanding the tendencies of cross-sections with altitude is not enough, since the E91 model, and others like it, predict aggregate properties of cloud ensembles which are still more complicated. So, even though we may calculate vertical mass fluxes using E91 or other convective models, there is as yet no theory governing how this flux is apportioned between vertical velocity and the updraft's horizontal cross section and we must look for other guidance to address this.

Another approach to calculating w_i is to appeal to the convective available potential energy (CAPE). CAPE is the amount of potential energy available to a parcel lifted adiabatically from cloud base (CB) to the parcel's level of neutral buoyancy (LNB), or equivalently the integral of the adiabatically-lifted parcel's buoyancy between those pressure levels (*Emanuel, 1994*):

$$\text{CAPE} = \int_{\text{CB}}^{\text{LNB}} B \, d \ln p \quad (6.16)$$

Presuming that all of this potential energy is converted to kinetic energy during ascent, and there is no drag or other decelerating force, we may write a maximum achievable vertical velocity for the parcel:

$$w^{\text{max}} = \sqrt{2 \text{CAPE}} + w_{\text{CB}} \quad (6.17)$$

Here, w_{CB} is the vertical velocity at cloud base, which is a poorly understood property. Note that w^{max} is a true upper limit updraft velocity attainable by the parcel during ascent, as it does not consider any kinetic energy-dissipating friction, irreversible mixing, or the details of any instabilities. So this maximum vertical velocity is out of reach in all realistic situations except perhaps in the most severe thunderstorms (*Emanuel, 1994*). It does appear to have some relationship to observed maximum updraft velocities (*Jorgensen and LeMone, 1989*), although admittedly there are very few studies of this relationship. Insight into how much CAPE is actually converted into kinetic energy would lead to some knowledge of vertical velocities and an effective means of partitioning \mathcal{A}_i from w_i . Even if the maximum velocity were achieved, the updraft speed would not be constant.

Instead, it would increase through vertical layers that contribute positively to CAPE (and decrease through those that contribute negatively to CAPE) until it eventually reaches w^{\max} .

Both *Rennó and Ingersoll* (1996a) (see also *Rennó and Ingersoll*, 1996b) and *Emanuel and Bister* (1996) present velocity scaling arguments based on an analogy of radiative convective statistical equilibrium to a heat engine, and consider how w_i relates to CAPE. Conservation of energy requires that the work done by convection be balanced by frictional dissipation (e.g., *Pauluis and Held*, 2002a). In order to determine a velocity scale for convection one must consider both the accelerating forces and the magnitude of loss to various forms of friction. *Rennó and Ingersoll* (1996a) and *Emanuel and Bister* (1996) assume that the only irreversible process of any importance is frictional dissipation due to turbulence associated with the convection itself (dry, in the boundary layer, and moist aloft). They thereby ignore the gains in entropy due to the diffusion of water vapor and of heat, frictional dissipation of falling precipitation, and numerous other processes. *Pauluis et al.* (2000) argue that the drag associated with falling precipitation accounts for one third of the work in the reversible heat engine, and that some two thirds of the rest is associated with diffusion of water vapor and to the phase change of water. Each of these processes then contributes more work than does the frictional dissipation through a turbulent energy cascade acting against convective drafts that was considered to be dominant by *Rennó and Ingersoll* (1996a) and *Emanuel and Bister* (1996). *Pauluis and Held* (2002a) consider the mechanical energy budget of a convective system and find, for their particular example of a simulated deep convective system, that only 21% of the dissipation occurs via turbulent cascading to small scales while the balance is dissipated via falling precipitation. To a first approximation, this implies that only 21% of the available CAPE is converted into upward velocities, which, in the absence of any other constraints, is the assumption we will use here. This is a somewhat arbitrary assumption as it is based on a single modeling study, and this problem clearly demands more work by the cloud physics and dynamics community. Fortunately, the model we propose is not very sensitive to the specific value of this fraction; our assumptions of radiative-convective equilibrium and that clouds are well represented by an episodically entraining plume introduce more error than does this particular value of the energy-conversion fraction. The updraft speeds we calculate will provide qualitatively accurate vertical profiles of updraft velocity that are only qualitatively verifiable by observation; more quantitatively accurate calculations will only be possible after our understanding of updraft speeds in clouds advances.

Loosely justified by the arguments of *Pauluis and Held* (2002a), we assume that some fraction of CAPE is converted to kinetic energy in the form of updraft velocity and that this fraction (here

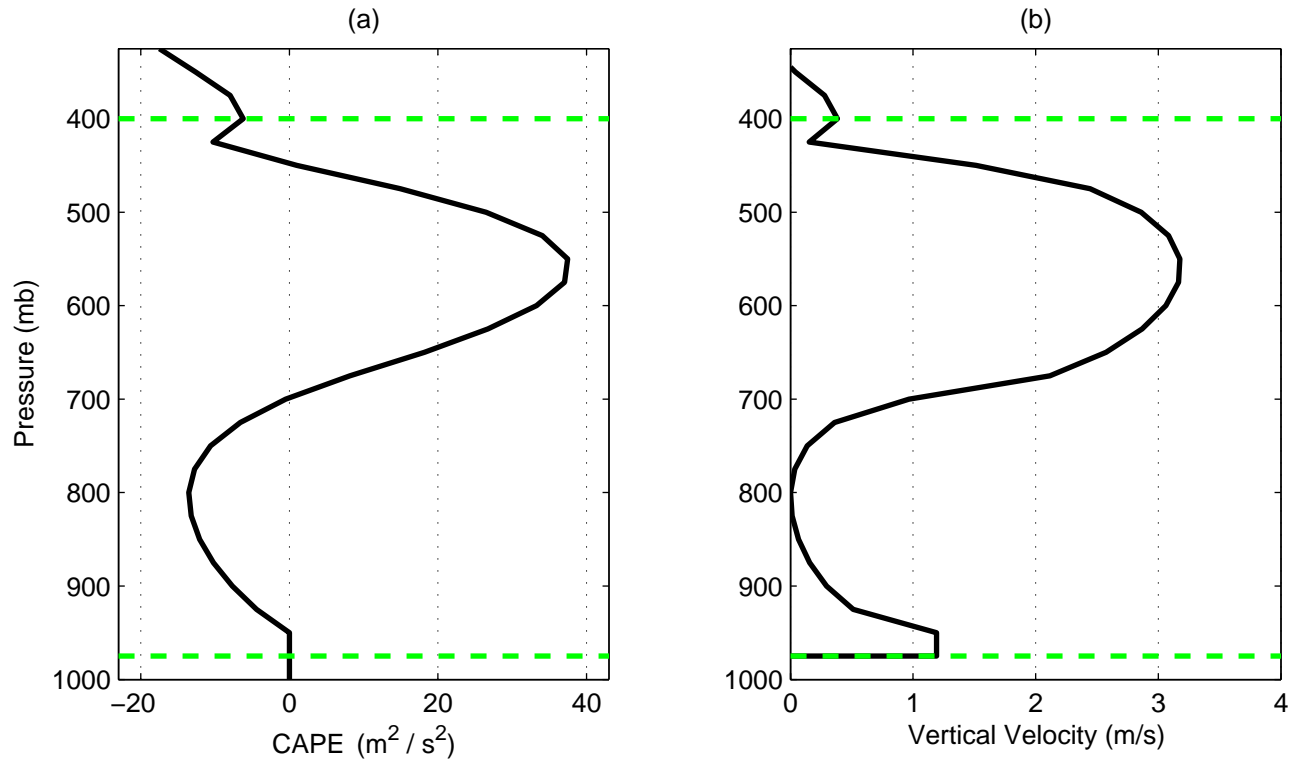


Figure 6-6: (a) CAPE_i through the depth of a cloud; (b) calculated minimum updraft vertical velocity through the cloud. In both panels, the green dashed lines indicate the cloud base and cloud top.

called \mathcal{C}) is independent of altitude and all other parameters (surely, this is not precisely true). At each level i above the cloud base, we define CAPE_i to be the amount of potential energy the parcel might have accessed had it been lifted from the cloud base to level i :

$$\text{CAPE}_i = \int_{\text{CB}}^i B \, d \ln p \quad (6.18)$$

The vertical velocity of the updraft at level i (w_i) is then a function of \mathcal{C} , CAPE_i , and the vertical velocity at cloud base (w_{CB}):

$$w_i = w_{\text{CB}} + \left(\frac{\text{CAPE}_i}{|\text{CAPE}_i|} \right) \sqrt{2 \mathcal{C} |\text{CAPE}_i|} \quad (6.19)$$

The absolute values and the parenthetical term are included because CAPE_i may be positive or negative and the sign must be preserved.

By way of example, let us consider the aforementioned E91 model run to radiative convective equilibrium with constant (daily and annual average) insolation, interactive radiation, and 46 vertical layers (roughly one every 25 mb up to the 100 mb level and with finer pressure resolution

above that). The model location is set at 40° latitude over a 22.22° C ocean surface with an albedo of 0.4.

Figure 6-6(a) shows CAPE_i through the depth of a cloud. Note that CAPE_i declines over a region beginning just above the cloud base, indicating that a rising parcel will decelerate in this region. Also note that the parcel will accelerate once it reaches the convectively unstable region, over which CAPE_i is increasing, which lies above the decreasing CAPE_i region. Since we know that the air in the updraft is always rising by definition, equation (6.19) indicates that w_{CB} must be at least large enough to prevent w_i from becoming negative at any altitude within the cloud. Imposing only that constraint, we present the calculated minimum vertical velocity through the depth of the cloud (using $\mathcal{C} = 0.21$) as Panel 6-6(b). Here, we present the profile yielded by assuming the minimum value of w_{CB} ; we may legitimately increase the velocity by any amount above this by raising our estimate of w_{CB} above its minimum value, which is the equivalent of holding the shape of the profile constant and shifting it to the right.

There are few appropriate observations of vertical velocity profiles with height in cumulus convection, and those that do exist exhibit heterogeneity across the diameter of a cloud consistent with the multiple updraft and downdraft character of the buoyancy sorting hypothesis (e.g., *Warner, 1970a; Barnes et al., 1996*). *Barnes et al. (1996)* review the Convection and Precipitation/Electrification Experiment, in which two aircraft made multiple simultaneous passes through convective clouds at two set vertical levels, and reported larger measured updraft velocities at the higher level than at the lower one. This is broadly consistent with *Warner (1970a)* who noticed an increase of average measured RMS vertical velocity with height over many cloud passes during many phases of cloud development. Such increasing updraft speed with altitude is consistent with the model presented here and implies that the updraft speed at cloud base is likely lower than the mean updraft speed. A series of other observational studies of average updraft velocities were made involving many passes through many clouds by a single aircraft (*LeMone and Zipser, 1980; Zipser and LeMone, 1980; Jorgensen et al., 1985; Jorgensen and LeMone, 1989; Lucas et al., 1994*). These studies generally noted an updraft acceleration with height over the lowest few (two or three) kilometers of the atmosphere and no variation in speed above that. Some of the studies, notably *Jorgensen and LeMone (1989)* and *Lucas et al. (1994)*, show on average a two-peak profile similar to that seen in Figure 6-6(b), although neither paper remarks on this behavior and instead suggests a simple increase with height. Large eddy simulations of convection in a computer model yield profiles of vertical velocity that are markedly similar to that calculated here (and shown in Figure 6-6), exhibiting both the low and high peaks and similar magnitudes, although the nadir

velocity between the two peaks does not appear to fall below $O(0.5 \text{ m/s})$ (*de Roode and Bretherton, 2003*). The weight of the evidence suggests our modeled vertical velocities are reasonable, although we admittedly have no way to determine the velocity through the cloud base beyond noting its minimum possible value. We will consider a range of reasonable values for the updraft speed at cloud base in the examples presented in Section 6.3.6 and 6.3.7.

6.3.4 Lateral Mixing of Environmental Air

As discussed in brief in Section 6.3.2, our model will consider two scenarios: one in which the rising parcel entrains no environmental air; and another in which some amount of environmental air is laterally entrained at each vertical level. In this section, we focus on the latter and discuss the method we use to incorporate the entrainment rates of the E91 model into our entraining parcel model. During episodic mixing events, both environmental air and aerosols equilibrated with water vapor in that air, irreversibly mix into the rising parcel, spawning sub-parcels that then move towards their new level of neutral buoyancy. As a simplifying assumption, we consider the cloud to be comprised of a single updraft that dilutes with entrained air as it rises rather than tracking each of the many sub-parcels explicitly. We are using the calculated entrainment rates of the E91 buoyancy sorting model to provide inputs to a much simpler entraining parcel model. Preserving the separate smaller updrafts would require that we relate vertical velocity to buoyancy throughout the cloudy region, which surely we are not capable of doing. Our model also maintains the feature of updrafts rising adiabatically between mixing events. In these way it is similar to the innovative model of *Baker et al. (1980)*, although their model presumes evaporation is localized in a way that ours does not (there is more recent evidence that observed evaporation patterns are more consistent with non-localized evaporation; *Yum et al., 1998*). The E91 model calculates the amount of air that is entrained and detrained at each level, and we use its results to drive entrainment in our updraft model.

The E91 model’s mixing calculations are based on the modeling work by *Bretherton and Smolarkiewicz (1989)* who related entrainment and detrainment to the vertical buoyancy gradient. In *Bretherton and Smolarkiewicz (1989)*’s scheme, all of the updraft mixes laterally with the environment somewhere within the depth of the cloud, either via entrainment or detrainment. The relative volume of the air entrained at model level i to the original updraft ($\mathbf{M}_i^M/\mathbf{M}_{CB}$) is determined by a combination of the buoyancy gradient over the model level (ΔB_i), the pressure gradient over the

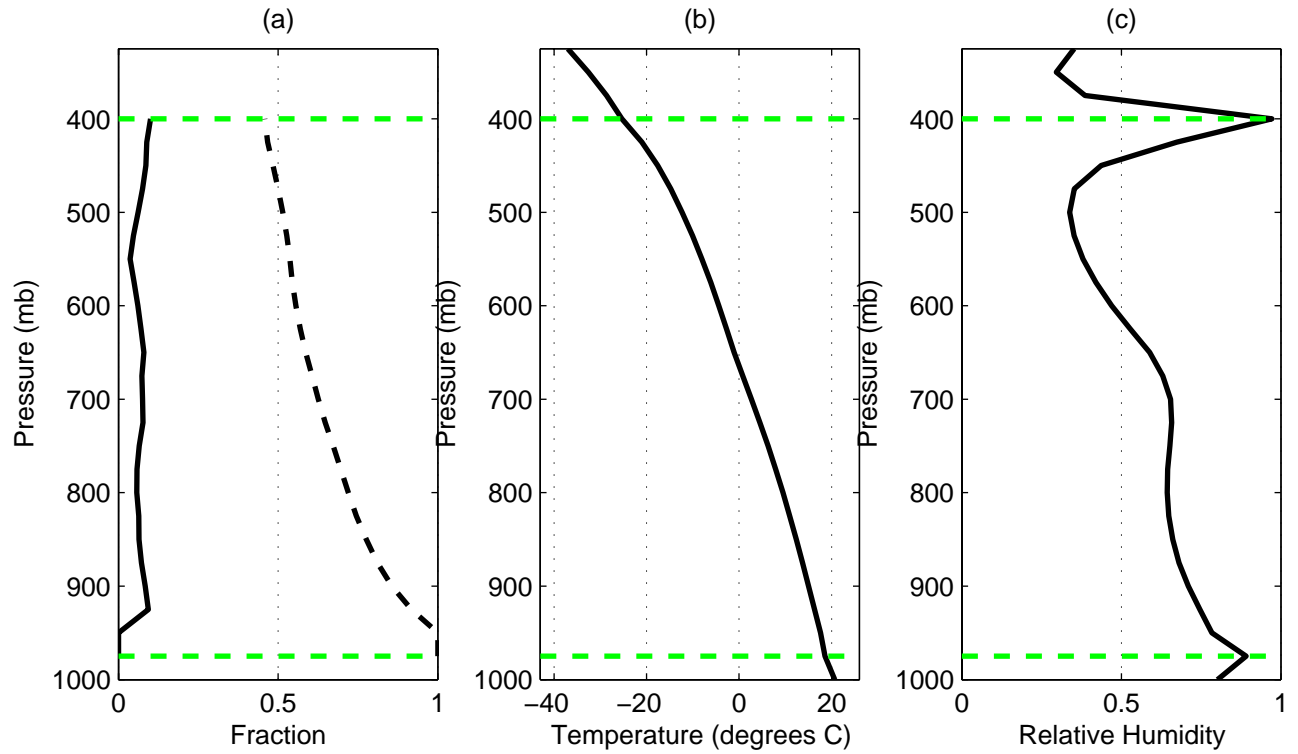


Figure 6-7: (a) The amount of dilution that occurs at each model level, shown as the entraining mass flux divided by the total updraft mass flux (solid line) and the fraction of cloud air at each model level that entered the cloud at its base (dashed line); (b) Environmental temperature; (c) Environmental relative humidity; the green dashed lines indicate the level of the cloud base and the cloud top respectively

model level (Δp_i), and an empirical parameter (Λ).

$$\frac{M_i^M}{M_{CB}} = \frac{|\Delta B_i| + \Lambda \Delta p_i}{\sum_{j=CB}^{CT} (|\Delta B_j| + \Lambda \Delta p_j)} \quad (6.20)$$

The indices CB and CT correspond to the model levels of the cloud base and cloud top, respectively. *Bony and Emanuel* (2001)’s optimized value, based on observations from TOGA COARE, for Λ is 1.5 mb^{-1} (it is their version of the E91 model that we use here). Note that equation (6.20) does not specify whether the mixing event is an entraining or detraining event. Mixed parcels that are created via entrainment then find their level of neutral buoyancy and exit the cloud. We do not account for detraining in the model, as removing a portion of the mixed parcel, after mixing has occurred, does not change its composition. The E91 model’s calculations account for the mass balance of entrainment and detraining, and this ensures that we dilute the updraft by the correct portion at each level even though we do not explicitly track the mass balance ourselves.

Figure 6-7 presents E91’s predictions of several quantities key to our mixing parameterization. Panel (a) shows two quantities related to the dilution of the parcel by entrainment. The solid line

indicates the ratio of the entrainment mass flux (\mathbf{M}_i^M) to the upward mass flux (\mathbf{M}_i) at each model level i (refer to Figure 6-5), which is a somewhat different quantity than that defined in equation (6.20). The dashed line shows the amount of sub-cloud air in the parcel divided by its total volume, which is a measure of the parcel’s dilution. The dashed horizontal green lines indicate our estimation of the cloud base and cloud top levels. Panels (b) and (c) show the vertical profile of the environmental temperature and relative humidity, respectively. The entrained air carries aerosols equilibrated to the environmental \mathcal{RH} , temperature, and pressure at the appropriate altitude.

6.3.5 Vertical Distribution of Aerosol

Entraining air introduces aerosols from the altitude of entrainment at equilibrium with the \mathcal{RH} , temperature, and pressure of the local environment. In order to include aerosol entrainment in our model, we must assume a vertical distribution of aerosols. Studies have shown a roughly exponential fall-off of aerosol concentration with altitude over the first five or so kilometers and roughly constant concentrations in the troposphere above that. The scale height of the exponential decay depends on aerosol size, composition, and environmental factors (*Pruppacher and Klett, 1997*). Some studies have presumed that concentrations scale with air density (e.g., *Ekman et al., 2004*), while others assign independent scale heights. Clouds affect the local aerosol concentrations by redistribution through venting, impaction scavenging, and depletion through wet deposition. Parcel models, however, are ill suited to calculating such a redistribution. Such calculations instead require two or three dimensional cloud dynamics models.

In our example model run, we follow *Jaenicke (1992)*, who calculated a remote continental aerosol mass scale height of 730 meters from a collection of observations. In the example we consider, much of the entrainment occurs above the altitudes at which there is a significant aerosol population and so our choice of this parameterization, and of this particular scale height, impacts the results very little.

6.3.6 Example

Let us now consider the results of a specific run of the new parcel model. We will use the same example that we have considered throughout this section: an episodically entraining, variable speed updraft model driven with entrainment rates and a thermodynamic sounding as calculated by the E91 model run to radiative convective equilibrium at 40° latitude with constant (daily and annual average) radiation and 46 vertical layers (roughly one every 25 mb up to the 100 mb level and with finer pressure resolution above that). We presented the resulting minimum vertical velocities in

Figure 6-6(b), environmental parameters in Figure 6-7(b) and 6-7(c), and mixing parameters in Figure 6-7(a).

We consider a sub-cloud aerosol population of $300 \text{ (NH}_4\text{)}_2\text{SO}_4$ particles cm^{-3} , log-normally distributed with a mean radius of $0.1 \text{ }\mu\text{m}$ and a geometric standard deviation of 1.5, represented using the representative sample distribution discussed in Section 3.3.5. The population falls off exponentially with height with a scale height of 730 m, as discussed in Section 6.3.5. We consider three cases in which the minimum vertical velocity (i.e., the minimum w_i) in the cloud updraft is 1 cm/s, 50 cm/s, and 100 m/s. As discussed in Section 6.3.3, observations suggest that the minimum speeds in cloud updrafts are usually around 50 cm/s, so these three cases represent low, expected, and high estimates. We will discuss the 50 cm/s minimum updraft speed case in this section to show the features of the model, and then compare the results of all three cases to show the impact of cloud base velocity in Section 6.3.7.

We consider four versions of the model: 1) the full entraining variable-updraft-speed parcel model that was developed in the preceding sections; 2) an adiabatic parcel model driven with the variable vertical velocities developed in Section 6.3.3 (i.e., version 2 is the same as version 1 with no entrainment); 3) a constant-speed updraft model driven by the mean of the variable vertical velocity distribution; and 4) a constant-speed updraft model driven by the maximum vertical velocity seen in the variable distribution. The first version is included to exemplify the behavior of the limiting case in which a cloud parcel entrains repeatedly but continues to rise. We will refer to this version as the “entraining variable-speed updraft model.” In fact, a parcel that entrains so often is very likely to detrain, or even sink, before reaching the top of the cloud; we will use this case to discuss the effect of entrainment on a parcels at different altitudes and which are rising at different speeds. The second version is included to exemplify the behavior of a cloud parcel that rises to the top of the cloud without mixing (the buoyancy sorting hypothesis holds that at least one such parcel exists), and as a point of contrast to the entraining variable-speed updraft model. We refer to this version as the “adiabatic variable-speed updraft model.” Note that a cloud parcel may effectively be considered adiabatic if it neither entrains nor precipitates (this is a loose definition); in this case “adiabatic” and “non-entraining” are almost synonymous. The third and fourth versions are included to show the behavior of the constant-updraft models, the updraft velocities in which are presumably meant to represent the mean, median, or maximum velocities achieved in nature. For the 50 cm/s minimum updraft speed case considered here, the calculated mean updraft speed is 198.6 cm/s and the maximum updraft speed is 367.6 cm/s. It is unclear how one would pick a single updraft velocity for a constant-speed model if one knew the vertical velocity profile, and this

represents two possible methods.

Figure 6-8(a) shows the relative humidity profile in each of the four model versions. Note that Figure 6-2(a) is the parallel plot for the non-entraining constant updraft example presented in Section 6.2.

As in the earlier example, the super-saturation in the lifted parcel peaks just above the LCL (the level at which \mathcal{RH} exceeds unity for the first time) at which point a large fraction of the aerosol activate, as shown in Figure 6-8(b). We showed in Section 6.2 that the peak super-saturation just above the LCL depends on the vertical velocity at that level, and the same relationship exists here. The peaks of the two variable-updraft-speed cases lie directly on top of each other while those for the two constant-updraft cases are considerably higher. We will come back to this point shortly.

The super-saturations in both versions of the variable-updraft-speed model first decay with height above the super-saturation peak above the LCL and then rise again as the updraft accelerates above that. The acceleration allows the parcels to maintain prolonged super-saturations at height that are as great or greater than the peak near the LCL. The constant updraft parcel models do not accelerate with height and super-saturations simply peak near the LCL and decay above. (Their eventual gradual rise with height is related to the dilution of aerosol concentrations by adiabatic expansion, which allows a parcel to maintain a greater super-saturation.) These super-saturations are often, in reality, ameliorated by condensation onto the super-large particles that form via coalescence and will precipitate. Coalescence is not calculated in our model, in an effort to isolate convective physics, and it would be impossible to accurately include precipitation falling from and through the rising parcel; these dynamical complications are beyond the scope of parcel modeling. Raised super-saturations aloft are observed, however, in strong updrafts, and so we expect this effect to be real but perhaps less dramatic than calculated here (Chien Wang, personal communication 2004).

In each of the four versions of the model, the updraft speed at the LCL is critical for the low-level activation of droplets. However, for the constant-updraft model, the velocity at the LCL is the most critical parameter for determining the super-saturation achieved for a given lifted aerosol population, while for the variable-speed updraft model it is not. This is not obvious from the 50 cm/s minimum updraft speed case presented here, but will be made considerably more apparent when we consider the 1 cm/s minimum updraft speed case in Section 6.3.7; we will return to this discussion then.

As we have already discussed, our understanding of vertical velocities is poor; but we do know some things, including a little about how we expect velocities to change with height in deep convec-

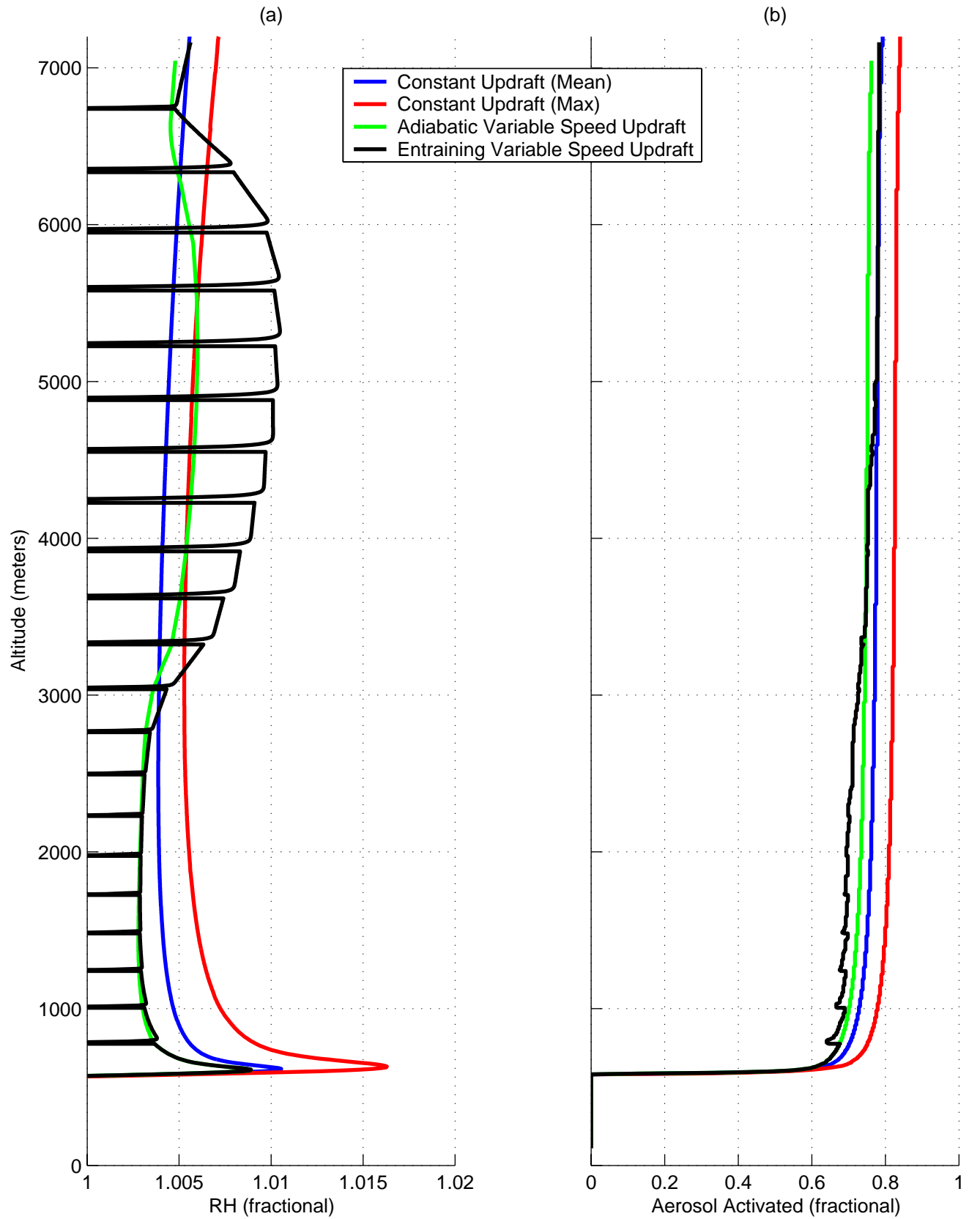


Figure 6-8: Panel (a) shows the relative humidity profile with altitude and Panel (b) shows the fraction of aerosol that have activated at each altitude, for a $300 \text{ particle cm}^{-3}$ $(\text{NH}_4)_2\text{SO}_4$ aerosol population ($\bar{r}_a = 0.1 \mu\text{m}$ and $\sigma_a = 1.5$) lifted using four updraft models: constant updraft models at two different speeds (the blue and red lines), an entraining variable-speed updraft model (black line), and an adiabatic variable-speed updraft model (green line)

tion. But the velocity and mass-flux at low levels is not well understood, and in nature is driven by a number of mechanisms that do not relate to the potential energy profile including, in the case of convection over oceans, shedding of boundary layer eddies (*Raymond, 1995*). The E91 model uses the sub-cloud layer quasi-equilibrium hypothesis (*Raymond, 1995; Emanuel and Zivkovic-Rothman, 1999*), which constrains the updraft's mass flux but not its velocity. Of the parcel model aerosol activation studies available in the literature, only *Kuba et al. (2003)* pay significant attention to updraft velocity profiles, and their focus is on very shallow, boundary layer topping clouds which are only about 300 m thick. *Yum et al. (1998)* take numerous observations of updraft speed in thin stratus clouds and find that the mean updraft speeds are quite low (in the range of 20 to 30 cm/s) but highly variable (having standard deviations of 35 to 105 cm/s).

During each mixing event, the entraining variable-speed-updraft model becomes momentarily sub-saturated only to exhibit another local peak super-saturation as it is re-saturated by a combination of droplet evaporation and adiabatic lifting (see Figure 6-8). Entrainment impacts aerosol activation in two ways. First, aerosols may deactivate due to evaporation while the parcel is sub-saturated following a mixing event. Not surprisingly, mixing events most efficiently deactivate aerosols when they occur near the level of minimum upward velocity where saturation is replenished predominantly by evaporation rather than adiabatic expansion and cooling, and when they occur low in the cloud before the aerosol have grown much larger than their critical radius so that less evaporation is necessary for deactivation. Second, the air parcel is able to support a greater super-saturation in the accelerating updraft, positive CAPE region far above the cloud base because the aerosol concentration is diluted so that the time-scale of condensation is lengthened. A greater fraction of the aerosols activate in this region if mixing is allowed than if it is not. The activation at higher altitudes more than makes up for the evaporative de-activation below, and overall more aerosol activate if entrainment is allowed; again, this will be more obvious for the 1 cm/s minimum updraft speed case we will consider in Section 6.3.7. We will see in Section 6.3.7 that large scale deactivation at low cloud levels (such as occurs in the 1 cm/s minimum updraft speed case) does not impact the ability for aerosols to reactivate at a higher altitude.

Recall that the entraining example presented here is a limiting case in which many entrainment events occur to the same parcel. In reality, we expect a given parcel to entrain a more limited number of times before detraining. This example shows the impact of entrainment at different level, however. When a parcel entrains near the level of its minimum upward velocity, aerosols may deactivate in sometimes significant numbers. Dilution of the parcel increases the sustained super-saturation by reducing the concentration of aerosol that may serve as points of condensation.

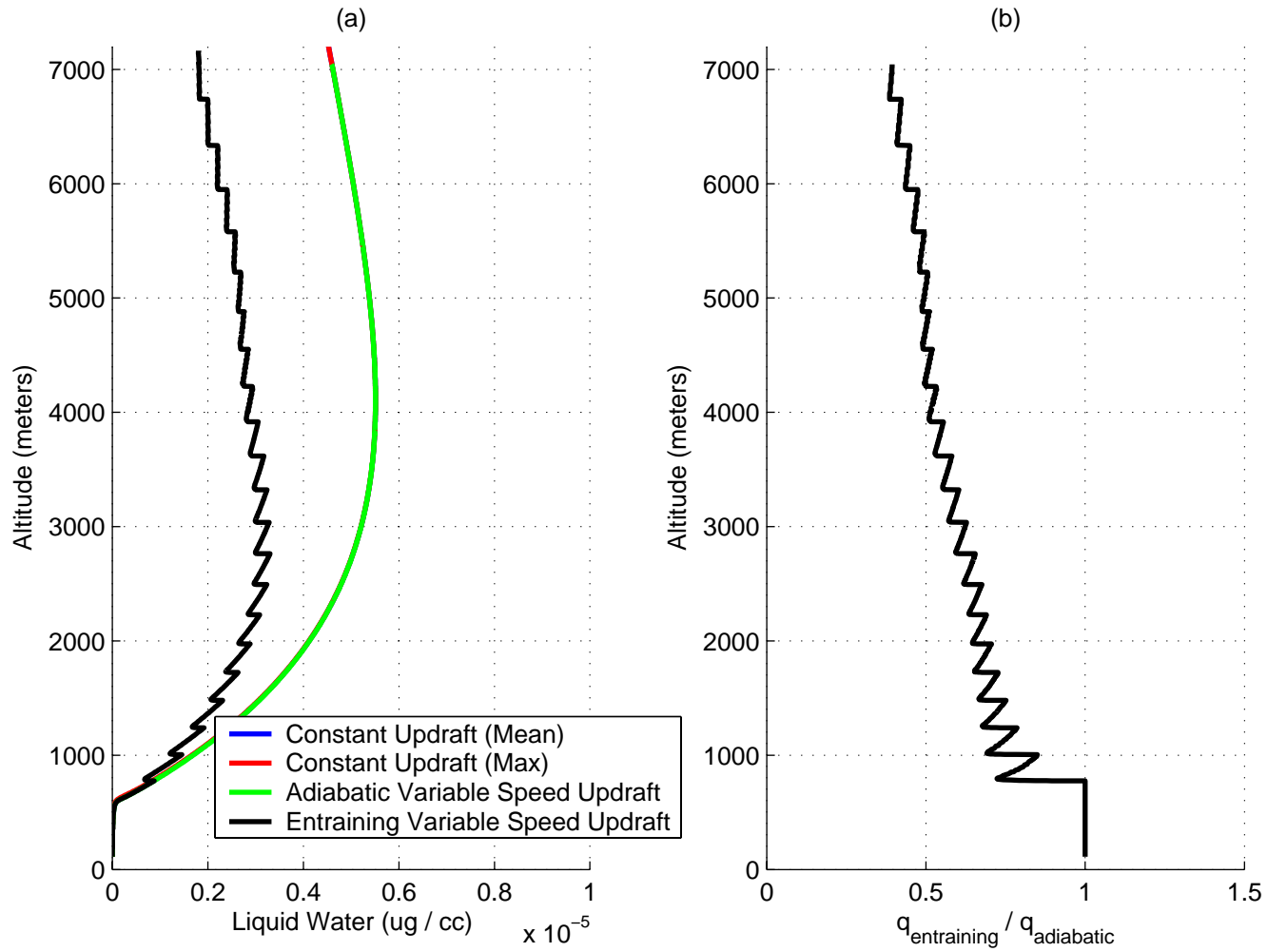


Figure 6-9: Comparison of parcel liquid water content for the four updraft models associated with the 50 cm/s minimum updraft speed case: (a) liquid water content as a function of altitude (note that the profiles of all three adiabatic models lie very nearly on top of one another); and (b) the ratio of liquid water content in the entraining model to that in the non-entraining, adiabatic models

These effects would occur in any parcel that entrains.

We discussed observations of the vertical profile of liquid water content in Section 6.2.7. Many studies, summarized by *Warner* (1970b), have shown that in real clouds the ratio of the observed liquid water content to that predicted by adiabatic updraft models decreases with altitude. This is true for both precipitating and non-precipitating clouds, although the fall-off with height is more dramatic for precipitating clouds. Figure 6-9(a) presents the vertical profiles of liquid water content calculated by the four updraft models we are considering. Note that the three non-entraining model versions lie almost exactly on top of each other while that for the entraining variable updraft speed model is considerably lower. The saw-tooth nature of the entraining variable-updraft-speed model is

the result of evaporation that follows each episodic mixing event; note that evaporation occurs very rapidly and condensation takes considerably longer. Water content in the adiabatic updraft model considered earlier, presented as Figure 6-2(c), appeared to increase almost linearly with altitude, but this is an artifact of the small vertical domain considered in that case. The curvature seen in Figure 6-9(a) results from the competition between condensation on one hand, and dilution and adiabatic expansion on the other; liquid water content in parcels in these non-entraining models increase monotonically with height, but the parcels' volume may increase more rapidly.

Figure 6-9(b) presents the ratio of the liquid water content in the entraining variable-updraft-speed and the adiabatic value. This profile compares favorably with the qualitative form of the observed from *Warner* (1970b) profiles presented in Figure 6-4, although it reaches only approximately 0.4 at its minimum whereas the observed profiles sometimes reach as low as 0.2. Recall, however, that some of the studies summarized in *Warner* (1970b) include clouds dried by precipitation, and a lower ratio is expected in such cases. Also, the fact that *Warner* (1970b)'s calculated ratios do not equal unity at the cloud base draws into question how he calculated the updraft parcel ratios, as in our formulation this ratio is forced to unity at cloud base. Nonetheless, the shape and rough magnitude of *Warner* (1970b)'s and our curves suggest that similar dynamics control both, as has been observed in other studies.

Baker et al. (1980) showed that the aerosol distribution in an episodically entraining plume model is broad and flat, as is generally observed in cumulus clouds. In contrast, distributions in modeled adiabatic clouds are characterized by a bimodal distribution consisting of a narrow peak of droplets and a somewhat broader mode of interstitial unactivated aerosol, as was seen in the two strongest updrafts considered in Figure 6-3. Figure 6-10 shows the size distribution of the aerosol in the entraining (red lines) and adiabatic (black lines) variable-updraft-speed models at several model levels.

At all model levels, the bimodal aerosol distribution of the entraining parcel model is broader than that of the adiabatic model. This behavior is consistent with the findings of *Baker et al.* (1980)'s modeling study and *Warner* (1969)'s observations. *Baker et al.* (1980) note that the extent of the bimodality depends on the frequency of the episodic entrainment, which is a quantity that is not well understood and not varied in this model. The entraining variable-updraft-speed parcel model developed here does not allow the mixed portions of the updraft to segment from the primary updraft, and so mixing events effectively occur at each model level. Our presumption has been that the episodically entraining version of the model presented here encounters more

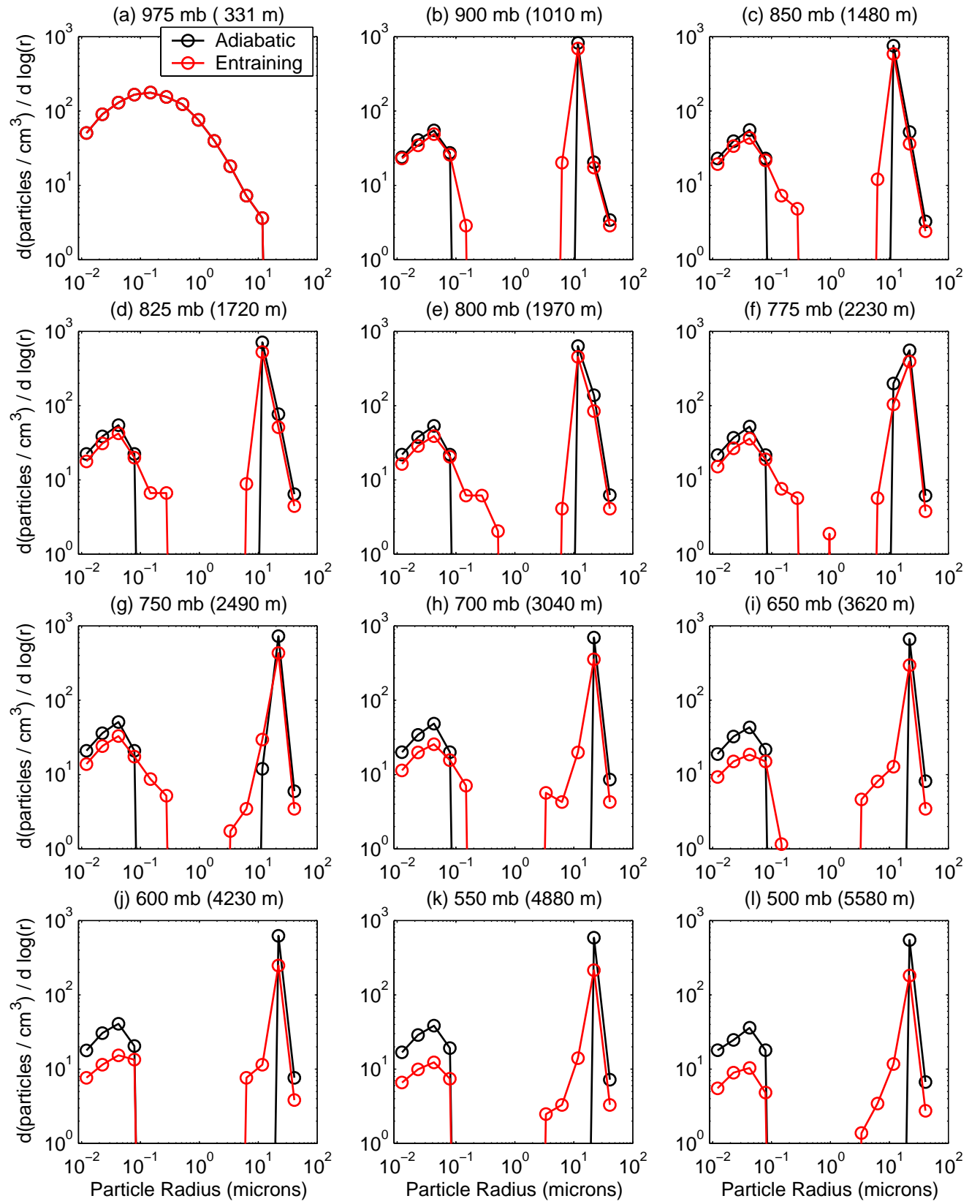


Figure 6-10: Aerosol size spectra at various altitudes in the entraining (red lines) and adiabatic (black lines) variable-updraft-speed parcel models for an initial distribution of $300 (\text{NH}_4)_2\text{SO}_4$ particles cm^{-3} , with mean radius of $0.1 \mu\text{m}$ and geometric standard deviation of 1.5

entrainment events that are generally encountered by a parcel. In the E91 model, each parcel is presumed to mix only once on its way through the cloud, and each mixing even might dilute a parcel significantly more than in our model. Observations of cloud droplet distributions appear to be inconsistent with the notion that evaporation after a mixing event occurs only is a sub-portion of the updraft (in shallow clouds, at least) (*Yum et al.*, 1998, although more observational studies would help resolve this point) and so it is unclear whether strict adherence to the subdividing-updraft formulation of the buoyancy sorting model would accurately reflect observed microphysical development. More work from both the cloud dynamics and cloud microphysics communities is required to resolve how entrainment and in-cloud mixing occurs, and what implications this has for the microphysical development of the cloud drop distribution.

In the positive-CAPE zone, however, the distribution in the entraining model becomes bimodal, which is the result of the strengthened updraft activating a greater fraction of the unactivated mid-sized aerosols. Furthermore, concentrations decrease across the full size range because of entrainment continues to dilute the parcel and relatively few aerosols enter with the entraining environmental air.

In this section, we considered the impact of including a realistic vertical velocity profile and episodic entrainment in a parcel updraft model. We saw that the model produces realistic vertical profiles of liquid water content and aerosol size distributions. This is true despite the fact that we did not consider coalescence or other cloud dynamics. We learned two important points about the behavior of aerosols in updrafts. First, we learned that although the super-saturation peak near the LCL entirely controls the fraction of aerosol that activate in constant-updraft models, aerosol activation in variable-speed updraft models is controlled both by the size of that peak and by the magnitude of the sustained super-saturation above that. Second, we learned that entrainment increases the magnitude of the sustained super-saturation by diluting the aerosol and cloud droplet concentrations, thereby activating interstitial aerosols that did not activated below (or activated and then deactivated again). These points are consistent with the assertions of *Yum et al.* (1998), *Hudson and Yum* (2001), and *Hudson and Yum* (2002) that cloud dynamics assert considerable influence upon the aerosol and cloud droplet size distributions in clouds, and that predictions of CCN concentration near cloud base are not necessarily strongly correlated to the droplet distributions aloft.

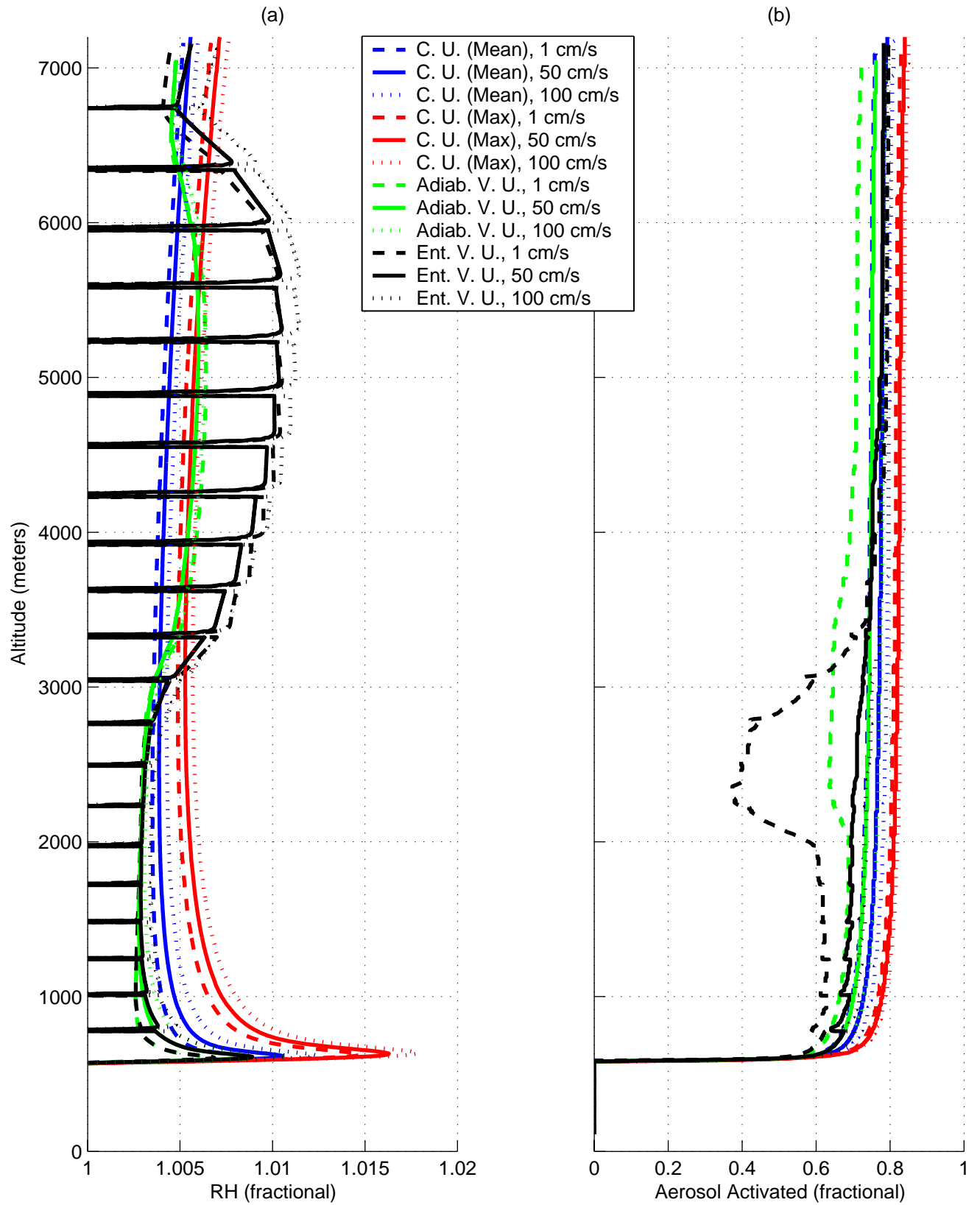


Figure 6-11: Sensitivity of the vertical distribution of: (a) super-saturation, and (b) activation fraction to the minimum updraft speed in the entraining variable-updraft-speed parcel model (black), adiabatic variable-updraft-speed parcel model (green), and constant updraft adiabatic parcel models at the mean (blue) and maximum (red) updraft speeds; dashed lines are for the 1 cm/s minimum updraft speed, solid lines for the 50 cm/s minimum updraft speed, and dotted lines for the 100 cm/s minimum updraft speed; the solid lines are the same as shown in Figure 6-8

6.3.7 Sensitivities of the Updraft Parcel Models to Minimum Updraft Speed

We will now consider the differences in results between the three different minimum updraft speeds: 1 cm/s, 50 cm/s, and 100 cm/s. To review, each vertical profile of updraft speed is calculated by adding the velocity that results from conversion of CAPE into kinetic energy (which may be positive or negative at a particular altitude) to the vertical velocity at cloud base according to equation (6.19); the vertical profile of the first, CAPE-related term for the example we have been considering was presented as Figure 6-6(b). Figure 6-11 shows the variation of \mathcal{RH} and aerosol activation fraction with altitude for the entraining and adiabatic versions of the variable-updraft-speed parcel model as well as constant updraft adiabatic parcel models traveling at both the mean and maximum updraft speeds seen in the variable-updraft-speed parcel model. Figure 6-11 directly parallels Figure 6-8 and presents the results for all three minimum updraft speed cases.

First note in Figure 6-11(a) that the basic features of the \mathcal{RH} profile are insensitive to the minimum updraft speed, although the results of the three cases differ quantitatively. In each of the three minimum updraft speed cases, the super-saturation peak at cloud base is significantly greater in the constant updraft models than for the variable-updraft-speed models. And in each of the three minimum updraft speed cases, the super-saturation grows in the accelerating, positive-CAPE region for the variable-updraft-speed models and sustains a comparably high super-saturation to that which was achieved at the peak just above the LCL. Variation of minimum updraft speed does not alter the vertical-scale of re-saturation after a drying entrainment event.

The fraction of aerosol activated at each altitude, shown in Figure 6-11(b), is quite sensitive to minimum updraft speeds for the entraining variable-updraft-speed model. The fraction of aerosols that activate just above the LCL shows little sensitivity to minimum updraft speed. This is also true higher in the cloud within the accelerating region, where the activation fractions of the three minimum-updraft-speed cases of each version of the model are within approximately five percent (or less) of each other. Stronger updrafts activate a greater fraction of the aerosol in both of these regions, but the behavior is as expected from the earlier discussion Section 6.2.6 of the impact of updraft speed in the adiabatic updraft model. The activation fraction calculated by the entraining variable-updraft-speed model shows considerable sensitivity to the minimum updraft speed in the mid-levels near the altitude of the minimum updraft. Specifically, a significant fraction of the aerosol deactivate for the 1 cm/s minimum updraft speed model for both the entraining and adiabatic versions of the variable-updraft-speed model. Presumably, in the entraining version of the model, evaporation plays a comparatively greater role, relative to adiabatic expansion and cooling, in

replenishing the super-saturation commensurate with the parcel's updraft speed for this case than for the other minimum updraft speed cases. Interestingly, similar although less dramatic behavior is seen in the adiabatic case, which suggests that some fraction of the activated aerosols shrink at the expense of other aerosols at these meager super-saturations. This large-scale deactivation does not significantly affect the activation fraction calculated in the positive-CAPE, accelerating updraft region of the cloud above. This suggests that the kinetic limitations seen in *Chuang et al.* (1997b) and *Nenes et al.* (2001) are less important in deep convection than in very shallow clouds because the high super-saturations at higher altitudes are sustained long enough to allow all of the aerosols with critical super-saturations below the level of the sustained super-saturation to activation. Remember that we have not calculated coalescence in this example, and that the development of rain-sized droplets may reduce the magnitude of the sustained super-saturation. Rain droplets, however, do not always form and do not necessarily negate this point even if they do. All of this suggests that there are two parameters that control aerosol activation in cumulus convection: the magnitude of the peak super-saturation that occurs just above the LCL; and the magnitude and extent of the sustained super-saturation at higher altitudes.

Next we consider the impact of the minimum updraft speed on the aerosol size distribution in the entraining and adiabatic variable-updraft-speed parcel models. Figure 6-12 shows specifically the aerosol size distribution for each of the three minimum updraft speeds for the adiabatic and entraining models (in the left column and right column, respectively) at three altitudes. The three altitudes roughly correspond to: (a) the altitude of the minimum updraft speed (850 mb); (b) the base of the positive-CAPE region (750 mb); and (c) a level deep inside the positive-CAPE, heightened super-saturation region (650 mb) where most of the aerosol that will activate have already done so.

As we discussed in Section 6.3.6, *Baker et al.* (1980) showed that episodic entrainment broadens the aerosol spectrum. This behavior is observed in our model as well: at all three levels the calculated spectrum is markedly broader when entrainment is included than when it is not. For the 50 cm/s and 100 cm/s minimum updraft speed cases in particular, the droplet mode (i.e., aerosol with radii of 5 to 100 μm) is considerably broader at each of the three levels.

The behavior of the 1 cm/s minimum updraft speed case is somewhat different. We saw in Figure 6-11(b) that, for the 1 cm/s case, a portion of the aerosol activated at the parcel's LCL later deactivate near the level of minimum updraft. This appears to force a broader distribution in the droplet mode in both the adiabatic and entraining cases at higher altitudes relative to the stronger updraft cases, as shown in Panels 6-12(c1) and 6-12(c2). Even though deactivated aerosols

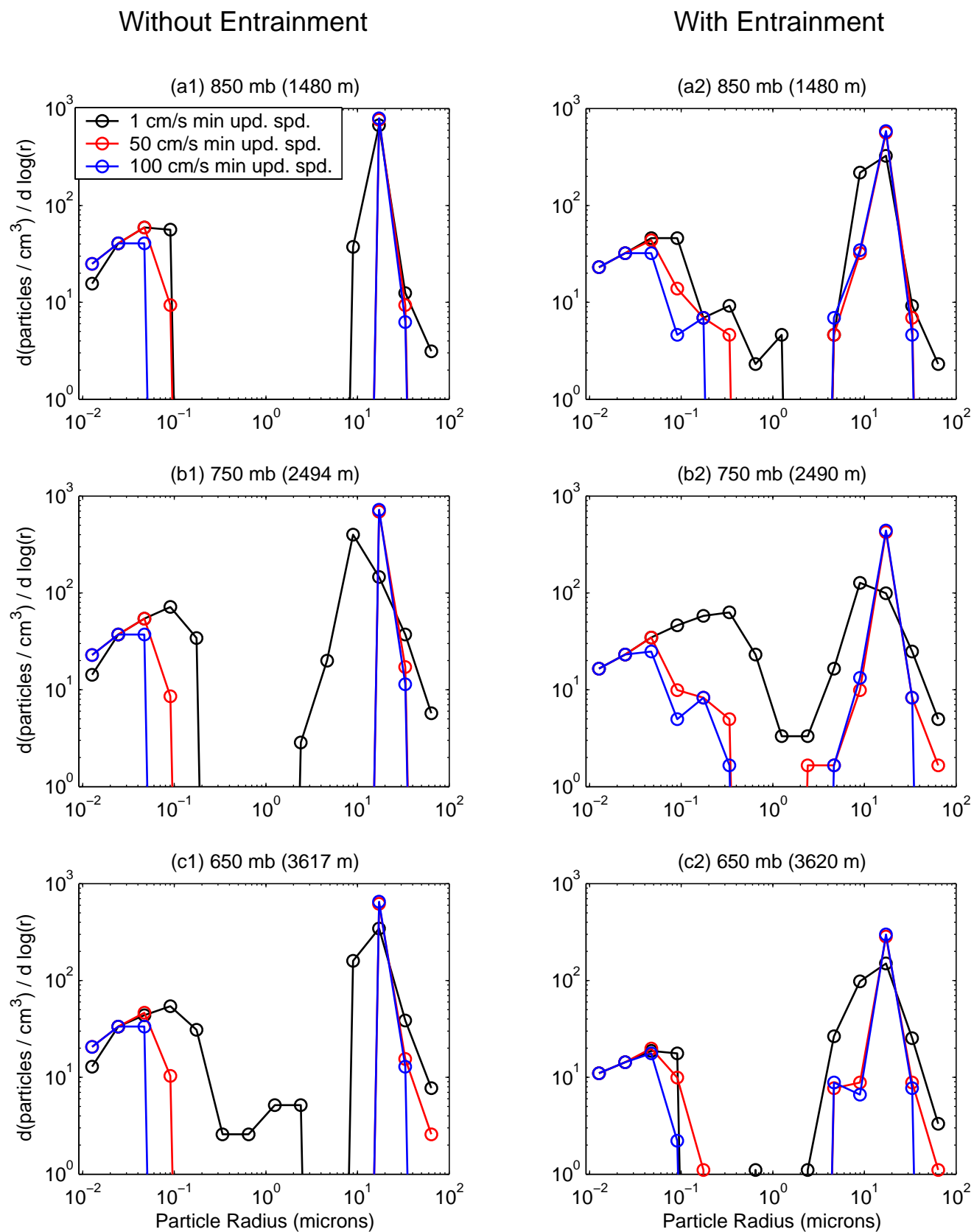


Figure 6-12: Aerosol size distributions at three vertical levels for the variable-updraft-speed parcel models with minimum updraft speeds of 1 cm/s (black lines), 50 cm/s (red lines), and 100 cm/s (blue lines); the left column of figures is for the adiabatic variable-updraft-speed updraft model and the right column is for the entraining model

reactivate in these cases once the parcel reaches the positive-CAPE region, they will never grow to the size of the aerosols that never deactivated. The relative broadness of the droplet mode will have obvious implications for both radiative transfer and the formation of precipitation.

6.3.8 Summary and Discussion

Our simple studies using the variable-updraft-speed parcel model developed in this Section 6.3 shed light on aerosol activation in deep convection. It represents a first attempt to link the very idealized updraft parcel models to information available from a convective parameterization.

We showed that the fraction of aerosol that activates depends on the sustained super-saturation at higher altitudes as well as on the peak super-saturation at the LCL. This suggests that a parameterization of aerosol activation based on CAPE for cumulus clouds is feasible and that the behavior at cloud base is less important. This second point is contrary to the notion that the updraft speed at the LCL is the only critical parameter, which is what the traditional constant updraft assumption suggests.

We also showed that the aerosol size distribution at higher altitudes depends both on the level of the sustained super-saturation at these altitudes and on the minimum updraft speed below; the weaker the minimum updraft speed, the broader the droplet spectrum at greater heights.

We were not able to present a theory to constrain the minimum updraft speed, which limits our ability to use that variable in future parameterizations of cloud activation. We were, however, able to provide a framework for calculating a vertical profile of updraft speed from CAPE, and for using that to determine the sustained super-saturation at higher altitudes; this suggests that we should be able to parameterize aerosol activation in large-scale models that employ the Emanuel or similar convective schemes. We leave that work to future studies.

There have been several attempts to include updraft-speed-dependent parcel type models in global models to address indirect aerosol effects, although none have approached the calculation using CAPE. *Ghan et al.* (1997) and *Lohmann et al.* (1999a) (corrected in *Lohmann et al.*, 1999b) utilize a Köhler type activation schemes. These schemes assume a log-normal aerosol distribution (*Abdul-Razzak et al.*, 1998; *Chuang and Penner*, 1995, respectively) with a probability distribution of vertical velocities parameterized using adiabatic cooling and a proxy of either turbulent kinetic energy or of eddy diffusivity. *Chuang et al.* (1997a) adopt a similar scheme but use only a mean updraft speed rather than a probability distribution. Models that explicitly resolve clouds on a regional scale (e.g., *Wang and Chang*, 1993a) determine vertical velocities by direct integration of the momentum, heat, and other equations but must proscribe an initial perturbation to incite convec-

tion. There is a question, of course, about whether the results of these models are representative of what happens on a larger scale, because they lack the thermodynamic and fluid constraints imposed by that scale (which tend to be imposed rather than calculated). These models are appropriate first steps but a more complete and accurate parameterization is necessary to reduce uncertainties in the global impact of the indirect effects of aerosols.

An appropriate ultimate goal of this line of work would be to extend a parameterization that links a convection routine to cloudiness at various levels, such as that of *Bony and Emanuel* (2001), to include a dependence of the optical properties and precipitation likelihood of each type of cloud to the local aerosol distributions through information available in the convective parameterization and dynamical state variables. A parameterization of aerosol activation and cloud properties that relied entirely on CAPE to calculate updraft speeds would only be applicable to cumulus convection and high clouds and would need to be combined with turbulence parameterizations or other proxies of updraft velocities in low-level thin clouds. Such a parameterization would allow representation of the indirect effects of aerosols in regional and climate scale models. A path to developing such a parameterization might be to extend the work done here to include consideration of coalescence and other cloud dynamics, embed either the full MELAM model or a parameterization of it into a 2-D or 3-D mesoscale cloud model, and then work towards a parameterization of cloud properties that would work alongside a convective parameterization. The study here provides an initial effort in this direction, but is by no means represents an ultimate solution. Considerably more work must be done, in a number of areas, for such a parameterization to be possible.

6.4 Conclusions

In this Chapter, we developed two types of parcel updraft models and used them to provide boundary conditions to the MELAM microphysics model.

The first modeling framework is a constant speed adiabatic updraft model similar to many used over the past two decades to investigate the microphysics of cloud formation. We showed that this model is overly dependent on the updraft speed through the LCL, which is poorly understood and is unconstrained in most larger scale models. Despite this limitation, we argued that the model is useful for isolating the specific processes of condensation and activation from the complexities of cloud dynamics, and thus it is quite useful for investigating the physics of the indirect effect. In the next Chapter, we will use the constant-updraft adiabatic parcel model to constrain the MELAM aerosol microphysics model (which together we will call the “MELAM updraft” model) in a series

of investigations into the impact of soot aerosol on aerosol activation in marine environments.

The second modeling framework is a new variable speed, episodically entraining parcel model driven by entrainment rates and thermodynamic soundings calculated by the E91 convective model. We used this model to investigate the parameters of the updraft that are critical for determining the fraction of the aerosol population that activates in deep convection and the properties of the droplet distribution. We found that these parameters include the minimum updraft speed and the sustained super-saturation level at higher altitudes.

A critical assumption of the proposed new variable-updraft-speed updraft model is that we take the updraft to be primarily a single flue rather which episodically entrains air at multiple levels, rather than the collection of isolated smaller updrafts and downdrafts suggested by the buoyancy sorting hypothesis. Current measurement techniques cannot sample rapidly enough to know how much in-cloud mixing of parcels occurs (*Twohy and Hudson, 1995*), and a combination of future measurements and theory will hopefully allow better insight into how correct our model actually is.

A further critical assumption of the proposed new variable-updraft-speed updraft model is that we know the fraction of convective potential energy converted to updraft velocity instead of lost to friction or other sinks. We based this parameter on the compelling recent work of *Pauluis and Held (2002b)* and *Pauluis and Held (2002a)* but this science is far from settled in the cloud physics community. In time, a better understanding of the updraft velocities in clouds will allow greater insight into aerosol activation processes.

There are two primary goals of this line of research. The first is to understand the physics of aerosol activation: to represent aerosol in all of their known complexities and determine the impact of composition, mixing state, size, and characteristics of the entire population. We use the MELAM updraft model to consider such a study in the next Chapter. The second is to provide a link in larger scale models between properties of the aerosol distribution and characteristics of clouds formed in the region, specifically optical properties and likeliness to precipitate. This second goal must be considered the ultimate goal of all aerosol activation studies, as reducing the huge uncertainties in the climate impacts of indirect effects of aerosols is critical to modeling the climate successfully (*Houghton et al., 2001*).

Chapter 7

Aerosol Activation in Sooty Environments

7.1 Introduction

Atmospheric aerosols may be classified into several broad categories, including insoluble (dust and soot), water soluble (inorganic salts and some organic species), surface active (some organic acids), and partially soluble (other organic acids). We know that these aerosols scatter and absorb radiation both directly and indirectly by altering cloud behavior, may change the absorbing properties of individual cloud droplets, and may suppress boundary layer convection by absorbing solar radiation at greater heights (see Section 1.2). Yet we are only coming to understand how each aerosol type becomes involved in each of the climate-altering effects.

In this chapter, we address the activation of internally mixed soot and sulfate aerosols which have been observed throughout both clean and polluted marine environments. We will consider their role in a number of representative environments, and suggest how such aerosols might be important in the climate system. In so doing, we advance understanding of this particular aerosol type. But we will only have a full picture of their behavior and role in the environment once we understand the role of the many aerosol types in the several different aerosol effects mentioned above.

Studies of the direct effect are most advanced. We understand the global impact of scattering by sulfate aerosols fairly well (*Charlson et al.*, 1990; *Schwartz*, 1996; *Boucher et al.*, 1998; *Penner et al.*, 1998; *Haywood and Boucher*, 2000; *Houghton et al.*, 2001). And recent modeling studies have made great strides towards quantifying the impact of scattering and absorption by the full range of

aerosol types (*Haywood and Shine, 1995; Myhre et al., 1998; Jacobson, 2001b; Miller et al., 2004*). These global modeling studies are based on detailed radiation schemes that represent the radiative impact of the aerosols well (*Houghton et al., 2001*).

By contrast, our understanding of the global-scale impact of the first and second indirect effects and the semi-direct effect is meager and most studies are therefore necessarily based on relatively poorly constrained parameterizations (*Jones et al., 1994; Jones and Slingo, 1996; Haywood and Boucher, 2000; Lohmann et al., 2000; Rotstayn et al., 2000; Houghton et al., 2001; Lohmann and Feichter, 2001; Rotstayn and Penner, 2001; Adams and Seinfeld, 2003; Nenes and Seinfeld, 2003*). There is still much cloud-scale work to be done on the role of aerosols in cloud formation, from both the chemist's and from the cloud physicist's perspectives. A series of studies have sought to understand the role that inorganic aerosols play in forming droplets in cloud updrafts (see Section 6.2). These studies have deepened our understanding of the governing physics (e.g., *Chuang et al., 1997b; Ghan et al., 1998; Nenes et al., 2001*) and of the specific relationship between aerosol loading and cloud droplet concentration (e.g., *Ghan et al., 1993, 1995; Chuang et al., 1997a; Liu and Seidl, 1998; Abdul-Razzak et al., 1998; Abdul-Razzak and Ghan, 2000, 2002*). These efforts provide a foundation of physical understanding, modeling procedures, and basic parameterizations upon which the climate community simultaneously is extrapolating first guesses of global impacts (*Houghton et al., 2001*) and building towards a deeper understanding of the role of aerosols beyond simple inorganic particles.

A host of chemical effects that complicate this idealized picture of aerosol activation, related to the dissolution of low-solubility organics, surface tension depression by organic species, surfactant effects, and insoluble cores together may have as much radiative impact as the first indirect effect (*Nenes et al., 2002*). Satellite observations show strong correlations between the optical thickness of smoke plumes and size of the average cloud droplet, revealing an indirect effect of smoke aerosols (*Kaufman and Fraser, 1997*). Laboratory studies confirm that organic particles act as effective CCN (*Novakov and Penner, 1993; Rivera-Carpio et al., 1996; Cruz and Pandis, 1997, 1998; Corrigan and Novakov, 1999*), and that trace amounts of soluble inorganics or organics dramatically increase the ability of less soluble aerosols to activate (*Hori et al., 2003; Bilde and Svenningsson, 2004; Broekhuizen et al., 2004*). Although the standard condensational Köhler model for inorganic aerosols (see Section 5.8.1) may work well for extremely soluble organics, it does not appear to be a reasonable model for those with lower solubility (*Raymond and Pandis, 2002*). Further, theoretical approaches to representing organic surfactants are limited (*Li et al., 1998; Facchini et al., 2001; Rood and Williams, 2001; Abdul-Razzak and Ghan, 2004*) and more work is needed to incorporate

these dynamics in a theoretical framework.

Other studies have used these yet-immature theoretical models of organic thermodynamics, solubility, and surface behavior in theoretical aerosol activation studies such as those considered in Chapter 6. *Facchini et al.* (1999) investigated the global implications of the surface-tension-depressing effects of representative soluble organic aerosols, estimating that inclusion of this effect increases cloud droplet number concentrations by 20% with a concomitant cooling effect. *Shantz et al.* (2003) and *Lohmann et al.* (2004) found that the low-solubility, surface active organics are slow to partition into the aerosol phase and inclusion of these dynamics reduces cloud droplet concentrations, which acts as a warming influence on the climate. *Raymond and Pandis* (2003) consider mixed aerosols in updraft models, treating inorganic, organic, and insoluble particles in various mixtures; their representation of insoluble dust particles is relatively simple, however, and we present a more thorough consideration of such mixed particles here.

Clearly, indirect effects depend on all of the many types of aerosols, not simply soluble inorganics. In this chapter, given the global ubiquity of soot, we concern ourselves specifically with the role of insoluble soot in aerosol activation within constant-speed cloud updrafts.

Recently, the direct and semi-direct effects of soot, or black carbon (BC), have garnered rather a lot of attention in the modeling community. According to only a few global modeling studies, soot aerosols assert a strong radiative warming influence on the globe which depends on the mixing state of the soot aerosols (*Jacobson*, 2001a), and alter the thermodynamic structure of the lower atmosphere enough to shift the hydrological cycle through the semi-direct effect (*Penner et al.*, 2003; *Wang*, 2004).

Soot aerosols are widespread, generated in large quantities through combustion as un-mixed, fine aerosols (*Shah and Rau*, 1990; *Seinfeld and Pandis*, 1998). Soot particles are a combination of organic and elemental carbon and are formed by the combustion of fuels. Chemically, they consist mainly of carbon, small amounts of hydrogen (perhaps 10% molar mixing ratio), and traces of other substances arranged in a more complex array than that of pure graphite (*Seinfeld and Pandis*, 1998). Often, studies distinguish between black carbon (graphite), which is produced only during combustion, and organic carbon (OC), which may be produced during combustion and by condensation of gas-phase species. Soot, however, is a combination of what should be considered BC and OC; often taking the form of a not-quite-graphite core with an organic coating. An accurate accounting of its mass loading would include the full BC loading and a fraction of the OC loading.

Soot aerosol mass concentrations range from 20 to 40 ng/m³ over the remote ocean and in

the Arctic, and up to 800 ng/m³ in continental rural regions (*Penner et al.*, 1993; *Pósfai et al.*, 1999). Soot is present in everywhere in the troposphere and appears in even the cleanest remote environments (*Lioussé et al.*, 1993; *Pósfai et al.*, 1999; *Hara et al.*, 2003). Fresh soot is largely un-mixed and hydrophobic, and so is not efficiently removed via wet deposition until several days after emission, when it becomes more hydrophilic after mixing with other aerosol types through coagulation and oxidation and by which point it has traveled great distances (*Ramanathan et al.*, 2001b). Volatilization during oxidation may be another efficient removal process (*Molina et al.*, 2004). We will discuss this further in Section 7.2.1. Total carbonaceous (TC) aerosols account for a significant portion of aerosol loading in urban environments, up to 10% to 30% of the total particulate mass, of which 50% to 70% is organic (OC) and the balance is black (BC) carbon, or soot (*Shah and Rau*, 1990). Carbonate, occasionally included in aerosol chemistry models because of its relative chemical simplicity (e.g., *Jacobson*, 1997a), accounts for only approximately 2% of TC and is not globally important (*Shah and Rau*, 1990). The full composition and chemistry of actual organic aerosols are complex and not currently understood.

Transmission electron microscopy (TEM) imagery reveals that soot particles exist as aggregations of spherules 10 to 50 nm in diameter, both in chain-like strands and more compact agglomerations often connected by an organic film (*Pósfai et al.*, 1999, 2003; *Li et al.*, 2003a; *Zuberi*, 2003). In extremely polluted environments, soot may appear both as pure soot aerosols (which we will call “free soot”) and as internal mixtures, while in more remote environments soot is almost entirely found in mixtures with sulfate or other species. Recent studies have shed some light on the mixing state of BC, but more work is certainly required. We will discuss the soot aerosol mixing state further in Section 7.2.4.

Three processes allow soot to act as CCN: the direct condensation of water onto aged, wettable soot; the vapor-pressure altering effects of condensation along junction-points in aged soot chains; and condensation onto internally mixed soot / inorganic particles. These are shown schematically in Figure 7-1. As soot particles age, oxidation and other reactions allow the particles to become more hydrophilic and to act directly as CCN (see Section 7.2.1). There is also some suggestion that, for soot with a contact angle less than 90°, the particles’ complex structure allows a so-called inverse Kelvin effect, wherein changed equilibrium water vapor pressure over a concave surface near the seam between two or several spherules allows activation at much lower super-saturations than for isolated spherical particles (*Crouzet and Marlow*, 1995); this phenomenon is shown schematically in Figure 7-1(b). Mixed aerosols containing insoluble soot cores and soluble organics and inorganics may also activate, although models of this behavior have thus far been very approximate (e.g.,

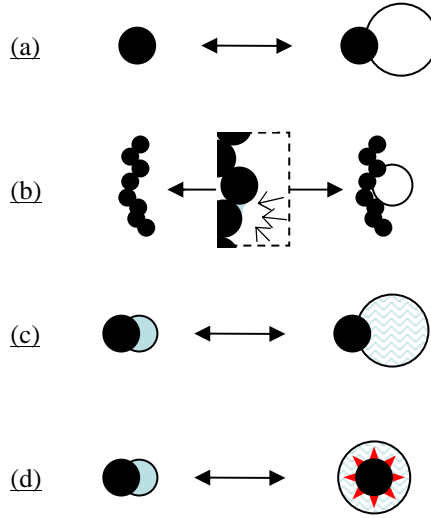


Figure 7-1: Schematics of the known mechanisms by which soot aerosols may become involved in aerosol activation and cloud formation: (a) condensation of water onto a soot spherule; (b) condensation of water onto a concave surface of water spanning the crevice between two attached spherules in a complex soot agglomerate (the “reverse Kelvin effect”); (c) condensation of water onto an internally mixed soot / inorganic particle; (d) radiative heating of soot aerosols during condensation, which warms the growing droplet

Hallett et al., 1989; *Rogers et al.*, 1991; *Lammel and Novakov*, 1995; *Kaufman and Fraser*, 1997; *Weingartner et al.*, 1997; *Jacobson*, 2001a; *Lohmann et al.*, 2004); this process is shown in Figure 7-1(c). Radiatively-heated soot particles may influence condensation in these mixed particles by warming the growing droplet and thus shifting the particle equilibrium water content (*Conant et al.*, 2002); this case is shown in Figure 7-1(d). There is still a great deal of uncertainty about each of these processes: how to observe them, how to model them, and even how to characterize the important aerosol physical properties appropriately. In Section 5.8.2, we discussed the Gorbunov parameterization for the activation of such mixed soluble-insoluble particles (as shown schematically in Figure 7-1(c)) and in this section we will use it within the constant updraft activation model as a way to shed light on the role of mixed soot / inorganic particles in cloud formation. We will not address the other three mechanisms in Figure 7-1 in this work, leaving that to future studies.

The Gorbunov model requires a knowledge of both the mixing state of soot with inorganics and the contact angle that soot forms with condensed liquid. Until quite recently, no laboratories had considered either of these traits and so the Gorbunov theory was considered to be beyond practical use (*Raymond and Pandis*, 2002). However, *Zuberi* (2003) recently measured contact angles in fresh and aged soot and a series of papers using both TEM and aerosol mass spectrometers have provided initial insights into the mixing state of soot in various representative situations. Each of these measurements is made accessible by new instrumental techniques, and for each there is

either a single or a very few papers supporting the results, so their conclusions should be considered preliminary. Although further studies will be necessary to refine our understanding of both contact angle and typical mixing states, we trust that the results are at least qualitatively correct and somewhat representative. Using these data, for the first time we have enough data and insight to use the Gorbunov theory appropriately, as we will in this chapter to consider the activation of mixed soot / inorganic particles. We will use the MELAM model presented in this thesis, the Gorbunov theory, new laboratory results, and data from the Indian Ocean Experiment (INDOEX) and the first and second Aerosol Characterization Experiments (ACE-1 and ACE-2) in the context of a constant updraft model to try to answer several key questions for the first time:

1. Do mixed soot / inorganic particles activate more or less efficiently than comparable inorganic particles?
2. What role does contact angle play in the activation of mixed soot / inorganic particles?
3. Does the ubiquitous soot found in clean marine environments affect cloud formation?

In the remainder of this chapter, we will pose these questions in more detail and attempt to answer them. In Section 7.2, we will discuss the laboratory measurements and field campaigns that will under-gird our use of the Gorbunov model in two modeling studies. In Section 7.3, we will consider the activation of mixed soot / sulfate aerosols in polluted marine environments and consider questions 1 and 2. Lastly, in Section 7.4, we will consider the role of mixed soot / sulfate aerosols in moderately polluted and clean marine environments and consider question 3.

7.2 Soot Data

In this section, we discuss the literature that will support our use of the Gorbunov model in studies of cloud formation in marine environments.

We need to define input aerosol distributions for the MELAM updraft model, and so will need information about aerosol composition and mixing state, and the contact angle of soot. Despite recognition that the burning of bio-mass and fossil fuels produce both sooty and inorganic aerosols (*Crutzen and Andreae, 1990; Hobbs et al., 1997*), very few studies have considered the mixing state of the resulting aerosols (*Pósfai et al., 1999*). In large part, this is due to the lack of appropriate instrumentation; such instruments are now available and we will introduce results from them, and discuss some of what has been learned using them, in Section 7.2.4. The contact angle of soot surfaces has been even less frequently observed, and we will depend on a single experimental study

that we will introduce in Section 7.2.1. We will also discuss the three field campaigns that will constrain our use of the MELAM updraft model: ACE-1, ACE-2, and INDOEX.

7.2.1 Chemical Aging, Hygroscopic Properties, and Contact Angle of Soot Aerosols

As discussed in brief above, soot aerosols are hydrophobic when emitted but may become more hydrophilic over time via mixing with soluble species (*Dentener et al.*, 1996; *DeMott et al.*, 1999) and chemical aging (*Chughtai et al.*, 1996; *Zuberi*, 2003). These are different effects, and we will appeal to both of them in the studies presented in this chapter. The Gorbunov parameterization depends on both of them: water condenses onto the surface of a soot sphere by forming a solution with electrolytic inorganic material and then grows as an embryo attached to the surface of the sphere with a characteristic contact angle (θ); refer to Section 5.8.2 for a discussion of this process and the Gorbunov theory we use to describe it.

Both the organic surface-layer film on liquid phase aerosols (*Eliason et al.*, 2004) and the insoluble core of aerosols (including insoluble soot, diesel, and other carbonaceous cores; *Weingartner et al.*, 1997; *Lary et al.*, 1999) may oxidize over time, creating polar surface groups that are more attractive to water.

Pure *n*-hexane soot has widely been considered an appropriate laboratory analog to the particulate soot found in nature. A series of recent studies have revealed the specific kinetics and resulting surface properties of the surface reaction of *n*-hexane with OH, and O₃ (*Chughtai et al.*, 1996; *Smith and Chughtai*, 1996; *Kotzick et al.*, 1997; *Kotzick and Niessner*, 1999; *Chughtai et al.*, 1999b; *Decesari et al.*, 2002), NO_x and HNO₃ (*Chughtai et al.*, 1996; *Lary et al.*, 1999; *Disselkamp et al.*, 2000; *Kirchner et al.*, 2000), and sulfur species (*Smith and Chughtai*, 1995). Such reactions have the effect of chemically aging the aerosols, increasing their affinity for water through the addition of polar surface groups and increasing their acidity. Other experiments have established the reasonableness of the *n*-hexane representation of soot aerosols by comparison to those formed during the combustion of JP-8 jet fuel, diesel, kerosene, pinewood needles, and synthetic fuels (*Weingartner et al.*, 1997; *Chughtai et al.*, 1999a,b).

Together, the experiments establish an ordering of the hygroscopicity of aerosols chemically aged with the various radical species: fresh soot < soot reacted with SO₂ < soot oxidized with ozone < soot reacted with nitrate species (*Chughtai et al.*, 1996; *Kirchner et al.*, 2000; *Chughtai et al.*, 2002). The particulars of the reactivity and hygroscopicity apparently depend on the air-to-fuel ratio during combustion as well as on the fuel source, although this ordering applies more generally

(*Chughtai et al.*, 2002). Incorporation of trace metals increases particle hydration considerably (*Chughtai et al.*, 1996). A chemical kinetic model of soot aging is currently not available, and we will therefore appeal to direct observations of the contact angle of soot surfaces rather than attempt to track these properties in a modeling framework. We expect that chemical aging occurs over one or several days, much longer than the cloud formation time-scale of an hour or less, and so are willing to take contact angle as an input to the aerosol-cloud model. *Zuberi* (2003) provides apparently the first experiments in this line of research that directly consider the contact angle chemically aged methane-derived and *n*-hexane soots with beads of condensed water (θ , see Section 5.8.2). He finds: for fresh soot, $\theta \geq 135^\circ$; for soot oxidized with OH, O₃, and UV light, $\theta = 101^\circ$; and for soot aged using HNO₃ for three hours, $\theta = 90^\circ$. To our knowledge no other studies of the contact angle of aged soot are available. We must make several caveats about our use of this data. First, the chemical aging process used in the laboratory was an imperfect analog to atmospheric oxidation. *Zuberi* (2003) contends that reactive uptake of O₃ and HNO₃ is rapid and likely plateaus quickly (citing *Tabor et al.*, 1994; *Choi and Leu*, 1998; *Disselkamp et al.*, 2000; *Grassian*, 2002; *Kirchner et al.*, 2000; *Prince et al.*, 2002); this may be true, but direct measurements of contact angle are few and the applicability of *Zuberi* (2003)'s or other oxidation techniques to real aerosols is not clear. Second, we will apply his measurements of the contact angle of actual atmospheric water with a flat soot surface to atmospheric particulates. It is not clear that the contact angle will be the same for a flat soot surface and a spherical soot particle, identically aged. At this point, no direct observations of the contact angle of soot particulates are available. So, while the availability of these laboratory measurements allow us a measure of comfort while using the Gorbunov model, we should consider the observed contact angles to be broadly representative, defining a range of probable contact angles for atmospheric particulates, rather than quantitatively exact. When answering the question of whether contact angle affects particle activation, we will therefore consider the full range of possible contact angles and note those observed by (*Zuberi*, 2003).

7.2.2 Measurements in the Ambient Environment

In order to provide aerosol distributions as input to the aerosol updraft model, we must know total aerosol composition and size distribution and understand the particles' mixing state. There are four primary measurement techniques we will appeal to for these data: cascade impactors for bulk composition and coarse sizing; thermal carbon mass retrieval; transmission electron microscopy (TEM) for mixing state analysis; and aerosol mass spectrometers (with time-of-flight sizing devices)

for analyzing the size and composition of individual particles. The first two instrumental techniques have been available for at least three decades while the latter two have become available in only the last several years and have allowed much greater insight into how various constituents are distributed within the aerosol population.

A cascade impactor is a layering of screens with known perforation diameters that decrease with each successive layer (e.g., *Berner et al.*, 1979). Aerosols settle into the impactor over time and are caught by the first screen through which they cannot pass, thus subdividing the population into several size ranges. A variety of techniques are then used to characterize the mass abundance and chemical characteristics of the aerosols on each screen. These instruments are widely used because they are inexpensive and easy to deploy and analyze. They provide an ample aerosol sample for most analysis techniques to yield accurate portraits of the aerosol size distribution and chemical composition. Their main disadvantage is that they allow low resolution in time and in aerosol size, and that they allow no insight into how the chemical constituents are distributed among the many different particles in each size range using standard techniques.

A number of measurement techniques, including thermal, solvent extraction, and acid digestion, provide an accurate understanding of the total carbonaceous aerosol mass in a cascade impactor sample (*Shah and Rau*, 1990; *Novakov et al.*, 2000). The errors of each technique's determination of TC are well understood and largely correctable. It is much more difficult, however, to subdivide the TC value into BC and OC, and results are inconsistent between each laboratory and technique. Of the various BC measurement techniques, thermal methods that burn OC from the TC sample are most effective, although it is difficult to assign errors to the technique due to lack of standards and difference between laboratories (*Shah and Rau*, 1990). Thermal methods are employed for BC measurement in the various field studies we will consider, although there are many more TC than BC measurements.

TEM can resolve the images of aerosol samples down to a fraction of nm using a radiation beam, essentially yielding a photographic portrait of individual particles collected using cascade impactors (*Li et al.*, 2003a). The microscopes are evacuated and thus all volatile species and water are lost from the particles. The remaining portion crystallizes, sometimes rearranging its soluble and insoluble components while drying, and the radiation beam causes some species (such as ammonium sulfate) to form bubbles. There is no transfer between particles, however, and so the mixing state of each is accurately retained. These images have yielded the best observations of how soot is distributed among inorganic ammonium sulfate particles in marine environments (e.g., *Pósfai et al.*, 1999; *Li et al.*, 2003a). The main drawback of the technique is its labor intensity,

as particles must be observed and counted one-by-one; the great abundance of aerosols mean that collecting an appropriately representative sample takes a very long time.

During the past decade, several new aerosol mass spectrometers (AMS) developed in parallel have introduced an automated system that simultaneously analyzes the size and composition of individual particles sampled directly from the ambient environment (*Prather et al.*, 1994; *Noble and Prather*, 1996; *Jayne et al.*, 2000). The systems collimate the aerosols through an inlet into a single beam at much lower than atmospheric pressure, measure the size of each particle by tracking its time of flight between two lasers (or some other time-of-flight technique), and then flash heat the particle either on a heated surface or with a laser and send the ionized components into a mass spectrometer. The system used in the studies we consider here is the Aerosol Time of Flight Mass Spectrometer (ATOFMS) developed at the University of California, Riverside and is able to simultaneously present both negative and positive mass spectra (*Prather et al.*, 1994; *Noble and Prather*, 1996; *Guazzotti et al.*, 2001). Most electrolyte species, when ionized cleanly, are extremely well characterized, but organics are much more difficult to identify. Hydrocarbons tend to disintegrate into ionized fragments containing one to three carbons. The degree of fragmentation depends on the power of the laser or temperature of the heating surface used to fragment the aerosols, although there is a balance to be struck between adequate power to ionize the inorganics without causing undue destruction of the organic species (*Noble and Prather*, 1998). A great deal of information is lost when the organics are reduced to such small fragments, and it is very difficult to reconstruct the aerosol-phase organic species from the mass spectra. Typically, much less than half of the aerosol-phase organic matter by mass is identifiable (*Seinfeld and Pandis*, 1998). The great benefit of the AMS technology is that it allows an explicit understanding of the mixing state of aerosols, of the correlation between composition and size, and of compositional variation among particles of a particular size.

The introduction of the TEM and AMS technologies over the last ten years has fostered a new level of understanding of ambient aerosols that supports a new generation of theoretical and modeling efforts. The coordinated field campaigns discussed in Section 7.2.3 make use of each of these four measurement techniques and allow us to construct the input aerosol distributions appropriate to the constant updraft model.

7.2.3 Field Campaigns

Our study of the activation of mixed soot / inorganic aerosols requires that we understand the composition, distribution, and mixing state of sub-cloud aerosols appropriately. We would like to

use the most representative data, and must decide between using the direct results from the many field campaigns aimed at aerosol characterization over the past fifteen years, or using those from a reanalyzed global distribution data set based on these many campaigns. We are interested in considering both polluted and clean marine environments.

Heintzenberg et al. (2000) assembled the results of the many previous field campaigns to that date into a global parameterization of background aerosols but the effort was hampered by inadequate global measurement coverage. Their model is unresolved in longitude but shows strong variations with latitude. Mean Aitken mode particle concentrations range from 150 to 600 cm^{-3} while the accumulation mode concentrations range from 60 to 250 cm^{-3} . Their work also reveals how little is known about global aerosol coverage, as there are no data to constrain broad latitude bands and many questions about the representativeness where data does exist. Also, because of the short and species-dependent atmospheric lifetime of aerosol particles, we expect the global distribution to be characterized as much by environment as by coordinate. To wit, the series of Aerosol Characterization Experiment campaigns selected a variety of times and locations intended to be broadly representative of various marine environments: polluted and clean, remote marine and near-shore. Their data, though local, are more broadly representative than the reconstructions of *Heintzenberg et al.* (2000) and others, which are likely more appropriate for driving global models than answering detailed process questions.

We will consider cloud activation in a variety of clean and polluted marine environments using representations of the aerosol distributions obtained during three coordinated field campaigns: ACE-1, ACE-2, and INDOEX. The locations and timing of the ACE campaigns were meant to be as representative as possible of marine environments, and their focus was on careful aerosol characterization; INDOEX was staged because of the critical public health and environmental concerns of South Asia, and also as a representative extremely polluted environment.

ACE-1 targeted a natural marine aerosol system thought to be remote from anthropogenic and industrial influence. The campaign convened a number of groups in the Southern Ocean south of Australia and west of Tasmania for November and December of 1995 to track aerosol size and composition, meteorology, and microphysics (*Bates et al.*, 1998).

ACE-2 set up in the northeast Atlantic Ocean off the coast of Portugal, Tenerife, and the Azores during June and July of 1997 (*Raes et al.*, 2000; *Verver et al.*, 2000). Data were collected from both land-based sites and from the deck of the moored *R.V. Vodyanitskiy*. During the two months of the experiment, air masses with several distinct histories passed over the sight, including clean air masses with Atlantic and polar origins, and polluted air masses from the Iberian peninsula, the

Mediterranean, and from Western Europe.

INDOEX took place down-wind of the Indian sub-continent during the winter monsoon in February and March of 1999, during which the winds were generally northerly or northeasterly (*Ramanathan et al.*, 2001b). Advected particulate pollution from industry, bio-mass burning, and desert regions formed a thick haze layer over the North Indian Ocean (*Twohy et al.*, 2001). The experiment extensively sampled ambient aerosols and cloud microphysics and chemistry. Black carbon aerosols were especially featured in measurement and analysis because of the growing understanding of their role in direct radiative forcing in the region (*Podgorny et al.*, 2000; *Ramanathan et al.*, 2001b).

The data from three field campaigns provide descriptions of a wide range of aerosol populations that are presumably representative of clean, polluted, and extremely polluted marine environments. Our modeling effort considers how the aerosols seen in each of these cases activate in cloud updrafts.

7.2.4 Overview of Observed Aerosol Mixing State

As we discussed earlier, soot particles activate by three mechanisms, two of which involve direct activation of pure soot particles and a third which depends on the particle being mixed with soluble species. Our current model is able to explicitly represent the third mechanism but not the first two. In order to understand soot's role in cloud formation through this third mechanism, it is critical that we understand the degree to which soot is mixed with other species in the atmosphere.

Several studies observed a combination of externally mixed and aggregated sulfate and soot in urban and polluted marine environments (*Okada*, 1985; *Meszaros and Meszaros*, 1989; *Katrinak et al.*, 1992; *Parungo et al.*, 1994). Until recently, however, the degree of mixing of soot and sulfate particles in remote environments had not yet been studied (*Pósfai et al.*, 1999), although correlations between BC and sulfate loading were observed (*O'Dowd et al.*, 1993; *Van Dingenen et al.*, 1995). In part because of the lack of observations of mixing state and of other species, and in part to ease calculation, most modeling of the marine boundary layer to date presumed distributions of pure sulfate and pure sea salt, often segregating the two types by size (*Fitzgerald et al.*, 1998; *O'Dowd et al.*, 1999; *Guazzotti et al.*, 2001). For many applications, the explicit representation of BC is not important to the resulting aerosol properties and behavior; however, we will show later in this chapter that it is important to consider when calculating activation. The introduction of TEM and AMS measurement systems facilitated the observation of mixing state, and of late several studies have included AMS sampling (e.g., *Guazzotti et al.*, 2001) and analyzed impactor samples using a TEM (e.g., *Pósfai et al.*, 1999; *Hara et al.*, 2003). Other recent studies have appealed to

radiative arguments, calculating the scattering by the bracketing internally-mixed and externally-mixed examples and comparing those to observations (e.g., *Mallet et al.*, 2004). The combination of these three new techniques promises an increased understanding of mean mixing state, which will be useful for both aerosol activation studies and for global direct effect estimates (*Jacobson*, 2001a).

Observations reveal that, away from sources, sulfate and soot present as heterogeneous internal mixtures, are generally classifiable into two categories: populations with “free soot” and those with “free sulfate.” In a population with free soot, all of the sulfate is mixed with aerosols that are primarily composed of other species and there are soot particles that contain no sulfate whatsoever. In a population with free sulfate, all of the soot is aggregated with sulfate aerosols and there are sulfate aerosols that contain no soot whatsoever. The aerosols observed in INDOEX fall into the first category (*Guazzotti et al.*, 2001), while those observed in both the remote and continentally-influenced marine environments of ACE-1, ACE-2, and the Arctic Study of Tropospheric Aerosol and Radiation (ASTAR) fall into the second (*Pósfai et al.*, 1999; *Hara et al.*, 2003).

During INDOEX, observations using the ATOFMS revealed that all detectable sulfate was internally mixed with other particle types such that no pure sulfate particles were detected (*Guazzotti et al.*, 2001). Unfortunately, this instrument is ill suited to detect pure sulfuric acid particles, due to difficulties in ionization of such particles, although those wholly or partially neutralized with ammonium (which is the probably state of sulfate particles in these environments) should be detectable (*Guazzotti et al.*, 2001). Previous observations show cases both of the presence of fine sulfuric acid particles (*Murphy et al.*, 1998) and of the presence in the MBL of only sulfuric acid particles polluted with organic components (*Middlebrook et al.*, 1997, 1998). The presence of organics would allow the ATOFMS to ionize and thus observe the particles. Nonetheless, this uncertainty is a limitation of the observation technique. Despite this limitation, the ATOFMS measurements during INDOEX convincingly suggest that all environmental sulfate resides in internal mixtures with other particle types. The INDOEX case study is a free soot marine environment.

A number of studies have shown that BC aerosols are ubiquitous in the marine environment, even air that is far from combustion sources and apparently clean (*Parungo et al.*, 1993; *Pósfai et al.*, 1999); ships, aircraft, and bio-mass burning are the likely source of soot (*Gardner et al.*, 1997; *Capaldo et al.*, 1999; *Pósfai et al.*, 1999; *Yamasoe et al.*, 2000; *Ito and Penner*, 2004). In an innovative study, (*Pósfai et al.*, 1999) used a TEM to characterize the soot / sulfate mixing state during the ACE-1, ACE-2, and Atlantic Stratocumulus Transition Experiment / Marine Aerosol and Gas Exchange (ASTEX/MAGE) campaigns. By tallying the sooty and non-sooty

sulfate particles in sub-micron and super-micron size ranges (divided using a cascade impactor), they characterized the mean mixing state in the polluted MBL, the free troposphere above the Atlantic and Southern Oceans, and the clean remote MBL in the Southern Ocean. Each of their samples showed a trend of increasing soot inclusion ratio with particle size and a lack of free soot. Similar mixing states and relationship with size are observed in the clean environments considered by *Hara et al.* (2003).

Soot was more broadly distributed in the ASTEX/MAGE aerosol samples than in those from the ACE campaigns. In the ASTEX/MAGE samples, roughly half of the 0.1 μm to 0.2 μm diameter sulfate particles and 90% of the super-micron sulfate particles included soot. By contrast, samples from both ACE campaigns showed that 11% to 46% of the sulfate particles were aggregated with soot and that the ratio increased with particle size; interestingly, this ratio did not appear to change between the clean and polluted samples.

That soot is only found in internal mixtures is something of a surprising result. *Hara et al.* (2003) suggest three mechanisms that internally mix soot in marine environments: cloud processing (impaction scavenging of soot particles into cloud droplets formed on inorganic particles, which then evaporate to form internally mixed aerosols); coagulation of externally mixed soot and sulfate aerosols; and surface reaction of sulfuric acid or sulfur dioxide on the soot surfaces. *Hara et al.* (2003) note both that coagulation in dry environments is too slow of a process to lead to the extent of mixing seen in the observations, and that back trajectory analysis was not always consistent with the cloud processing hypothesis. Regardless, cloud processing appears to be a likely source of the internally mixed particles; how likely remains an open question.

We will use these mixing state data from the INDOEX and ACE campaigns to constrain inputs to the aerosol updraft model in Sections 7.3 and 7.4. These few studies just discussed are sufficient guidance for our modeling effort and should be broadly representative of the various marine environments worldwide. We should mention in passing, however, that closer to large emission sources, we expect soot and sulfate to be externally mixed (*Jacobson, 2001a; Hasegawa and Ohta, 2002*) and for the soot to be hydrophobic (refer to the discussion of Section 7.2.1 for more on the second point). The global modeling study of *Jacobson* (2001a) suggests that emitted soot takes roughly 5 days to transform from externally to internally mixed, although these results should be considered preliminary.

The modeling studies we will present in the next two sections in this chapter focus on two types of environments: polluted marine environments as represented by the INDOEX observations;

and clean to moderately polluted environments as represented by the ACE campaigns. They will combine the information briefly reviewed in this section with field campaign data to initialize the MELAM updraft model, and will seek to answer the three questions posed in the introduction to this chapter.

7.3 Effect of Contact Angle on Aerosol Activation for Internally Mixed Soot / Sulfate Particles in Heavily Polluted Regions

We will first consider cloud formation in the polluted marine environment. We will use INDOEX data to formulate seven exemplary distributions that span a range of the observations of internally mixed sulfate / soot aerosols during INDOEX. We will then use these distributions to consider the effect of contact angle on aerosol activation.

The procedure of the study is straight-forward: first we define a set of input aerosol distributions; second we use an adiabatic updraft parcel model in combination with the MELAM model to calculate aerosol growth and activation during a 1000 m lift using a range updraft speeds and contact angles; and third, we consider which aerosols activate and whether contact angle matters. We are interested in determining whether internal mixtures of sulfate and soot activate in greater or lesser proportion than pure sulfate particles. If there is a difference, we would like to learn which properties of the soot particles (e.g., contact angle, radius) determine the size of the effect.

In Section 7.3.1 we will define the seven exemplary distributions, in Section 7.3.2 we will describe the modeling results, and finally in Section 7.3.3 we will draw conclusions about the role of mixed soot / inorganic aerosols in updrafts.

7.3.1 Aerosol Distributions

As part of the INDOEX campaign, a series of measurements of aerosol composition, mass loading, size distribution, and mixing state were taken at the Kaashidhoo Climate Observatory in the Republic of Maldives in mid-February, 1999, during the winter monsoon. When averaged over 48 hour time periods (the collection time used for cascade impactor sampling), mass loading of sub-micron particles averaged $17.7 \pm 0.22 \mu\text{g}/\text{m}^3$ and ranged from $8.3 \pm 0.33 \mu\text{g}/\text{m}^3$ to $24.7 \pm 0.21 \mu\text{g}/\text{m}^3$ (Chowdhury *et al.*, 2001). The mass loading related to the average back trajectory of the observed air and extent of continental influence for that trajectory. Note that, in their study, sub-micron is defined by the particulars of their cascade impactor to include all aerosols with radius of $0.9 \mu\text{m}$ or less. Of the total non-water aerosol mass, sulfate ion accounted for roughly

Table 7.1: Observed Aerosol Size Distributions from INDOEX Campaigns

	N_a (particles cm^{-3})	Sulfate			Soot	
		\bar{r}_a (μm)	σ_a (-)	Mass ($\mu\text{g}/\text{m}^3$) ($r \leq 0.9 \mu\text{m}$)	Core Radius (μm)	Mass ($\mu\text{g}/\text{m}^3$) ($r \leq 0.9 \mu\text{m}$)
Polluted Marine	300	0.1	1.5	39.1	0.1	2.3
	300	0.1	1.5	36.0	0.2	18.7
	300	0.1	1.5	36.0	0.3	63.1
Maldives	70	0.2	1.1	14.4	0.1	0.6
	70	0.2	1.1	14.4	0.15	2.0
	70	0.2	1.1	14.4	0.2	4.7
	70	0.2	1.1	14.4	0.25	9.2

33-37%, ammonium for 7-9%, carbonaceous species for 26-27%, and 28-30% was not identifiable (Chowdhury *et al.*, 2001). It is thought that acids near the sub-continent are approximately 64-69% neutralized by ammonium, and either entirely or very nearly (95%+) neutralized by a combination of ammonium and potassium (Ball *et al.*, 2003), and as a simplifying assumption we will presume that all of the sulfate is present as ammonium sulfate.

Aerosol Mass Spectrometer measurements from the INDOEX campaign revealed that all of the sulfate was internally mixed with other aerosol types, including dust, sea salt, and carbonaceous particles. The total number concentration (N_a) of sulfate-associated particles at the Maldives location, during the same dates was approximately 70 cm^{-3} for sub-micron particles, and 0.5 cm^{-3} for super-micron (Guazzotti *et al.*, 2001).

We propose four example distributions that approximate those seen in these Maldives observations. In each case, the particle distribution consists of a single log-normal mode of ammonium sulfate aerosols, onto each of which a soot spherule attached. In this model, the soot spherules are all the same size, whereas in reality we expect them only to be narrowly distributed between 0.1 and $0.4 \mu\text{m}$ in radius (e.g., Zuberi, 2003). The four Maldives sample distributions in Table 7.1 all have identical sulfate content, total number concentration of 70 cm^{-3} and a total sub-micron mass of $14.4 \mu\text{g}/\text{m}^3$. The soot spherule core radius, however, differs between the four cases. The spheres range in radius from $0.1 \mu\text{m}$ to $0.25 \mu\text{m}$, implying the the portion of the soot loading associated with sulfate is between $0.6 \mu\text{g}/\text{m}^3$ and $9.2 \mu\text{g}/\text{m}^3$. Although we know there are other aerosol types externally mixed with the aggregated soot / sulfate particles (Guazzotti *et al.*, 2001), we do not include them in this study. These cases approximate the distributions of the more polluted air masses observed at the Maldives location.

We will also introduce three ‘‘Polluted Marine’’ cases which have higher mass loading of both

sulfate and soot than do the Maldives cases in order to consider a case study of the more polluted air characteristic of marine environments closer to the sub-continental sources. Those cases are inspired by more polluted observations taken above the northern Indian Ocean during INDOEX, which exhibit substantially higher number and mass loadings than those observed near the Maldives (*de Reus et al.*, 2001), although the composition and mixing state are less well quantified. Table 7.1 includes those distributions as well. Each is characterized by an ammonium sulfate distribution with number loading of 300 cm^{-3} , mean radius (\bar{r}_a) of $0.1 \text{ }\mu\text{m}$, and geometric standard deviation (σ_a) of 1.5, attached to soot radii of between $0.1 \text{ }\mu\text{m}$ and $0.3 \text{ }\mu\text{m}$ in radius. The size and number distribution represent approximately one quarter of the boundary layer loading (and is comparable the 1-3.5 km loading) with slightly larger mean size and identical distribution to the distributions observed over the northern Indian Ocean by *de Reus et al.* (2001). We do not use the full value of their observed number distribution because we believe the particles in that region to be 80% or more carbonaceous particles with no sulfate and roughly the balance to be carbonaceous particles mixed with sulfates (*Guazzotti et al.*, 2001). We are unable to model condensation upon pure carbonaceous particles, although such condensation likely occurs (refer to the discussion of Figure 7-1 in the introduction to this chapter) and may compete with the mixed soot / sulfate particles for available water. In this study, we would simply like to consider the activation of the mixed particles, and as a simplifying assumption presume the pure carbonaceous particles do not uptake water directly.

7.3.2 Results

We will consider the role of contact angle in the activation of each of the seven sample distributions defined in Section 7.3.1. We use the constant updraft model defined in Section 6.2 to adiabatically lift each of the seven example distributions 1000 m. During the ascent, water condenses upon the particles and a number of them activate. We will report the number of aerosols that activate during ascent and the peak relative humidity (\mathcal{RH}) achieved during the ascent. (Recall from the discussion of Section 6.2.6 that, in adiabatic lifting models, \mathcal{RH} peaks above the lifting condensation level.) For each of the seven aerosol distributions described in Section 7.3.1 above, we consider a range of updraft velocities and contact angles (in this case, the cosine of contact angle). All of the initial distributions are equilibrated with the environment at 1000 mb pressure, 298.15 K temperature, and 98% \mathcal{RH} , and are represented in the model using the structured representative sample method over 1 cm^3 (refer to Section 3.3.5 for discussion of this representation).

Let us first consider the Polluted Marine cases. Figure 7-2 shows a contour plot of the fraction

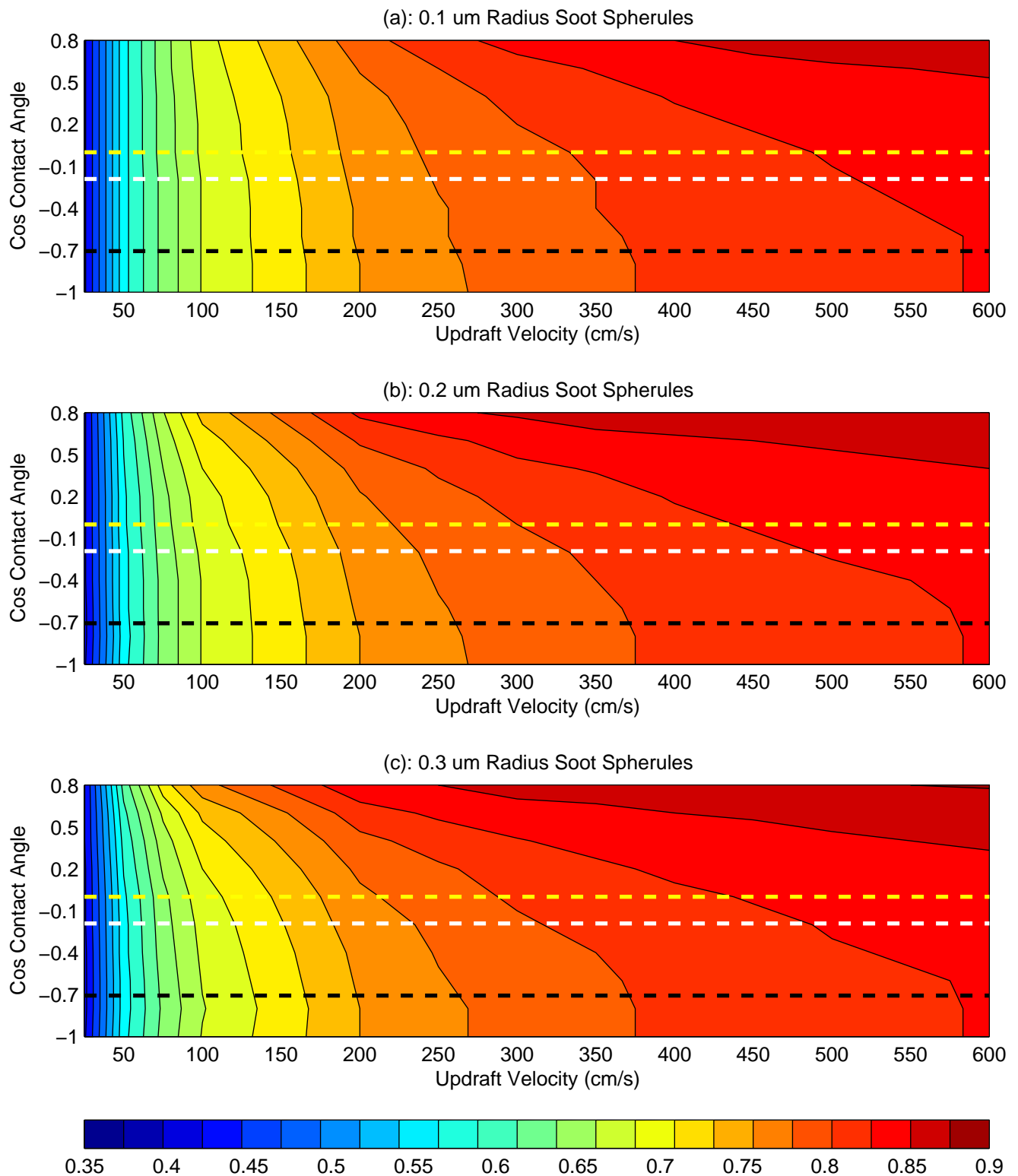


Figure 7-2: Activation fraction as a function of updraft velocity and the cosine of the contact angle for the three Polluted Marine distributions; the contours are isolines of the fraction of the aerosol population activated (color coding is shown in the color bar below the plots); the three dashed lines show the three contact angles observed by *Zuberi* (2003) for fresh soot (black), oxidized soot (white), and nitrated soot (yellow)

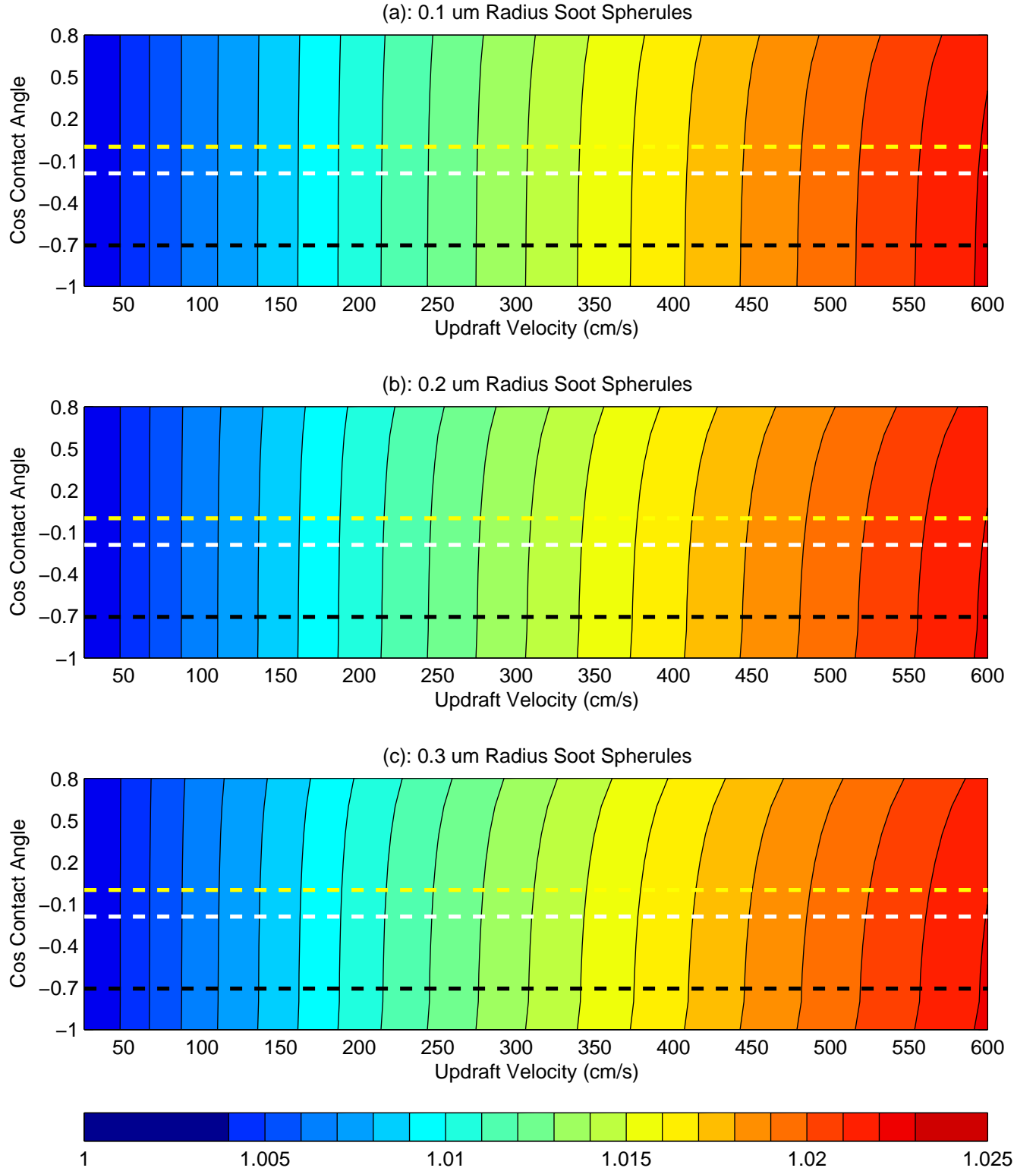


Figure 7-3: Maximum \mathcal{RH} reached during adiabatic lifting as a function of updraft velocity and the cosine of the contact angle for the three Polluted Marine distributions; the contours are \mathcal{RH} isolines (color coding is shown in the color bar below the plots); the three dashed lines show the three contact angles observed by Zuberi (2003) for fresh soot (black), oxidized soot (white), and nitrated soot (yellow)

of mixed soot / sulfate particles that activate as a function of both updraft velocity and of the cosine of contact angle ($\cos\theta$). The three dashed lines are drawn at the contact angles observed by *Zuberi* (2003) for water beading on flat surfaces of fresh soot (black line), soot aged with OH, O₃, and UV light (white line), and soot aged with HNO₃ (yellow line) (see Section 7.2.1 for a discussion of these experiments). The three panels (a), (b), and (c) show the results for the cases that include 0.1 μm , 0.2 μm , and 0.3 μm radius soot spherules, respectively. The bottom axis of each contour plot, at $\cos\theta = -1$, is the hydrophobic limit at which soot particles repel water completely; here the calculations are for “clean” cases with no soot whatsoever and are the same in each of the three panels.

For all cases, the isolines bend to the left as they move from the bottom of the plot towards the top. That is, increasing $\cos\theta$ (or, equivalently, making the particles more wettable) allows a greater fraction of the distribution to activate. If soot had no impact, the isolines would be vertical; they clearly are not. The effect increases with the size of the soot spherule and with increasing updraft velocity. The case with the largest soot spherules, the results of which are shown as Figure 7-2(c), show a 6% - 8% difference between the hydrophobic and hydrophilic limits in the fraction of available aerosols that activate in mid-range updrafts (200 - 400 cm s^{-1}). In this same updraft range, there is a 2% - 3% difference in activation fraction between the fresh and aged soot cases.

Figure 7-3 shows the maximum relative humidity (\mathcal{RH}) achieved in each of the updrafts. The isolines make a slight S-curve as they trace from the bottom of the plot towards the top. Rightward curvature, wherever it occurs in the plots, indicates that an increase in $\cos\theta$ increases the condensation rate onto the particles sufficiently to reduce the build-up of a super-saturation near the lifting condensation level (LCL, see Chapter 6 for further discussion of this phenomenon). Curvature of the isolines near the bottom of the plots indicates that including even slightly wettable soot (with θ near 180°) reduces the maximum \mathcal{RH} even though there is no impact on the overall fraction activated (note that the isolines are vertical in the equivalent regions of Figure 7-2).

Activation fractions for the Maldives examples are shown in Figure 7-4. The plots have the same format as those in Figure 7-2, except note that the colors are not to the same scale. There are two obvious differences between these cases and the Polluted Marine cases just considered: first, the fraction of aerosols that activate saturates near 90% at a relatively modest updraft of one meter per second, such that increases above that speed activate no more aerosols; and second, the curvature of the activation fraction isolines occurs only for aerosols with higher values of $\cos\theta$ than we expect to generally exist for atmospheric aerosols. Similar to the Polluted Marine cases, the effects of the soot inclusion (curvature in Figure 7-4) increase for increasing particle size.

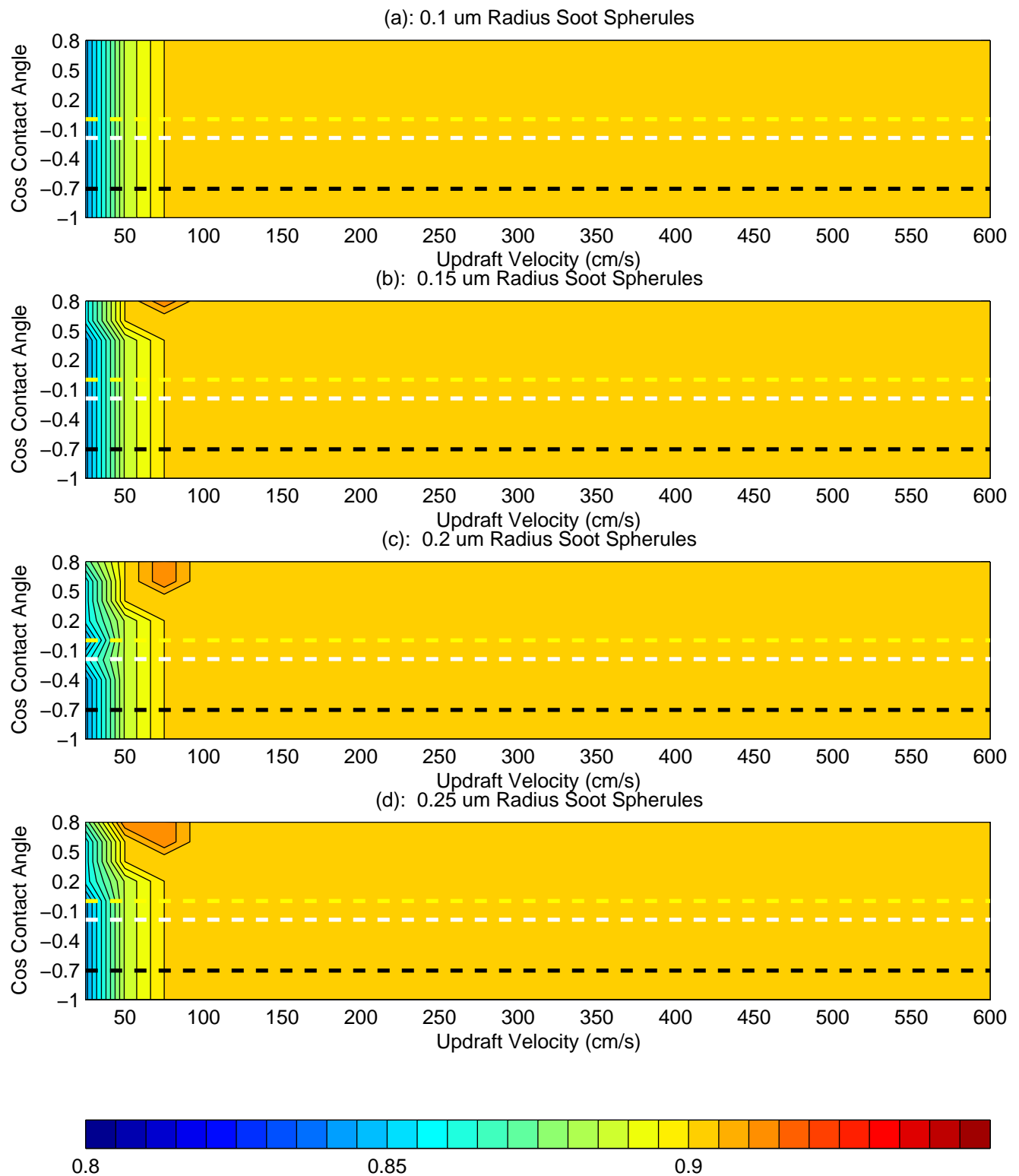


Figure 7-4: Activation fraction as a function of updraft velocity and the cosine of the contact angle for the four Maldives aerosol distributions; the contours are isolines of the fraction of the aerosol population activated (color coding is shown in the color bar below the plots); the three dashed lines show the three contact angles observed by *Zuberi* (2003) for fresh soot (black), oxidized soot (white), and nitrated soot (yellow)

7.3.3 Summary

In the introduction to this chapter, we asked three questions about the role of internally mixed soot / sulfate particles in cloud formation in marine environments. In this section, we address two of those questions: Do mixed soot / inorganic particles activate more or less efficiently than comparable inorganic particles? And what role does contact angle play in the activation of mixed soot / inorganic particles?

In answer to the first question, these results show that a sulfate aerosol is at least as likely to activate if it is attached to a insoluble soot core than if it is not. When we discussed the Gorbunov parameterization in Section 5.8.2, we learned that the addition of a soot core reduces the critical super-saturation required for a given amount of ammonium sulfate to activate, and that the higher the cosine of the contact angle, the more dramatic the effect. The implications of this are borne out in the numerical experiments considered in this section. We will return to a discussion of the potential magnitude of the effect in a moment. In answer to the second question, we saw in the Polluted Marine results that increasing $\cos \theta$ increases the fraction of the aerosols that activate and reduces the maximum super-saturation achieved in the updraft. Some particles that would not have activated when attached to hydrophobic soot spheres (i.e., those with low values of $\cos \theta$) have their critical super-saturations sufficiently reduced by a change in the contact angle to activate in an equivalent updraft. Once a particle activates, it becomes a condensation focal point at even very slight super-saturations; hence increasing the number of particles that activate near the LCL reduces the maximum super-saturation achieved in an updraft.

For polluted cases with high number concentration, as represented by the Polluted Marine cases, the enhancement in activation fraction between the no-soot and completely hydrophilic cases may be a relatively large effect at the order of 5-10%. Several studies considering the role of insoluble species in cloud activation have used only the hydrophilic limit in which the insoluble core is completely engulfed by the growing solution embryo (e.g., *Conant et al.*, 2002; *Raymond and Pandis*, 2002; *Lohmann et al.*, 2004), similarly finding that this is a potentially large effect (*Raymond and Pandis*, 2002). Including realistic contact angles, however, as represented by the *Zuberi* (2003) measurements, reduces the potential effect to 1-5% in the Polluted Marine cases. *Facchini et al.* (1999) estimated that a potential 20% increase in cloud drop concentrations related to surface tension reductions by soluble organics would translate to an upper limit global mean radiative forcing of -1 W m^{-2} were all stratus clouds affected by the noted enhancements. The effective 5-10% enhancement estimated here would similarly scale to -0.25 to -0.5 W m^{-2} forcing at

the surface, and the more realistic 1-5% enhancement would relate to -0.05 to -0.25 W m⁻². This is overall a small effect but potentially large in specific types of polluted marine environments.

The Maldives example raised the issue of saturation. In that case, more than 90% of the available aerosols activate at wind speeds above 75 cm s⁻¹ and the addition of soot does not increase this ratio further. The maximum super-saturations observed in the Maldives case (not shown) were higher than those in the Polluted Marine examples – which we expect due to the presence of fewer condensation nuclei – and so all of the aerosols but the very smallest activate. These smallest aerosols are not aided by being internally mixed with soot particulates. More generally, this implies that in CCN-poor environments in which most of the available aerosols activate into cloud droplets, the addition of soot particulates to sulfate particles has a negligible effect.

We also found, in both the Maldives and in the Polluted Marine examples, that the size of the attached soot particle matters, or really that the relative size of the soot and sulfate particles matters. The larger the soot particle relative to the attached sulfate mass, the more impact the particle will have on the ability of the droplet to activate. This relates directly to how much the inclusion of a soot particle increases the effective radius of the growing solution embryo (how r_c affects r_e , in the parlance of Chapter 5). This raises a host of issues about the appropriateness of our model. First, the design of the parameterization forces us to represent soot particles as spheres when we know they have much more complex, chain-like structures that may crumple into sphere-like forms but will never be solid spheres. When relating the soot mass loading to size of the soot spheres, we assume a soot density (2 g cm⁻³; *Seinfeld and Pandis*, 1998) that does not take the effectively less-dense structure of the crumpled chains into account. We also presume that the appropriate effective soot radius is that calculated using the solid-sphere relationship to mass loading. In these ways, our study follows on a number of other studies that have considered solid soot spheres, which generally also made the significant simplification that the spheres are completely wettable. Our study is an advance in that it includes particle contact angle, even though it makes no advance on how to relate observations of soot to parameterizations that require soot be represented as solid spherical particles. Furthermore, we assumed a mono-dispersion of soot spherules when we expect actual particles to be distributed over a narrow range (0.1 and 0.4 μm in radius by one estimate *Zuberi*, 2003). Just as the activation fraction and maximum super-saturation results changed as the size of the soot spherule increased, so would the results if we introduced a broader dispersion of soot spherules. Observations are insufficient to constrain the relationship between the relative sizes of soot and sulfate components in internally mixed distributions; such observations would help to constrain our results.

7.4 The Role of Soot in Cloud Formation in the Clean Marine Atmosphere

As discussed earlier in the chapter, recent studies found soot in even clean marine environments (*Pósfai et al.*, 1999; *Hara et al.*, 2003; *Li et al.*, 2003b). In these environments, soot is generally found to be mixed with ambient sulfate aerosols such that up to half of the sulfate particles have some soot inclusion. Stratus and stratocumulus clouds over the ocean are widespread and radiatively important (*Seinfeld and Pandis*, 1998), and it is worthwhile to consider whether the presence of pollutant soot affects their formation or optical properties. The internally mixed state of the sulfate / soot aerosols mean that condensation upon these aerosols may be modeled using the Gorbunov parameterization used in our model. In this section, we use published information about aerosols observed during ACE-1 and ACE-2 to initialize a constant updraft model. We will use the model to consider whether the soot inclusions have any impact on cloud formation.

The presence of internally mixed sulfate / soot aerosols in these environments is surprising. *Pósfai et al.* (1999) postulate that source of the soot found in remote regions (such at the Southern Ocean) is airplane contrails. And *Hara et al.* (2003) suggest that one possible mechanism of internal mixing is through cloud processing – where droplets form on sulfate particles, scavenge interstitial soot particles, and then evaporate and leave an internally mixed particle behind. The well defined Aitken and accumulation mode particles in the ACE-1 and ACE-2 samples (*Bates et al.*, 2000, we will discuss these observations in Section 7.4.1) result from cloud processing as well (*Hoppel et al.*, 1986, 1990). It is likely that the sulfate and soot formed internal mixtures in non-precipitating clouds.

In this section we will consider whether the presence of internally mixed soot in these remote marine environments has any impact on aerosol activation and cloud formation. Similar to the study of aerosol activation in polluted marine environments presented in the previous section, we will define a series of representative aerosol populations and use the MELAM updraft model to calculate the fraction that activate at a range of updraft speeds and soot contact angles. We will define the various components of the aerosol distribution in Sections 7.4.1, 7.4.2, and 7.4.3, discuss the results of the model runs in Section 7.4.4, and summarize the results in Section 7.4.5.

7.4.1 Aerosol Populations

We will consider air from six marine regions: the clean environment observed over the Southern Ocean South of Australia during ACE-1 and air observed over the North-East Atlantic during

Table 7.2: Observed aerosol size distributions from the ACE field campaigns

	Nucleation Mode		
	$N_a(\text{cm}^{-3})$	$\bar{r}_a (\mu\text{m})$	σ_a
ACE-1 Clean	190 ± 180	0.008 ± 0.000275	1.45 ± 0.55
ACE-2 Clean (Atlantic)	60 ± 70	0.007 ± 0.00165	1.19 ± 0.16
ACE-2 Clean (Arctic)	120 ± 150	0.007 ± 0.0017	1.22 ± 0.13
ACE-2 Coastal Portugal		n/a	
ACE-2 Mediterranean		n/a	
ACE-2 W. Europe		n/a	
	Aitken Mode		
	$N_a(\text{cm}^{-3})$	$\bar{r}_a (\mu\text{m})$	σ_a
ACE-1 Clean	210 ± 160	0.0165 ± 0.0034	1.4 ± 0.16
ACE-2 Clean (Atlantic)	235 ± 125	0.0185 ± 0.00465	1.43 ± 0.13
ACE-2 Clean (Arctic)	420 ± 220	0.018 ± 0.003	1.38 ± 0.14
ACE-2 Coastal Portugal	2800 ± 1900	0.038 ± 0.0075	1.52 ± 0.13
ACE-2 Mediterranean	4600 ± 1300	0.0525 ± 0.0075	1.51 ± 0.06
ACE-2 W. Europe	650 ± 310	0.0465 ± 0.0105	1.6 ± 0.11
	Accumulation Mode		
	$N_a(\text{cm}^{-3})$	$\bar{r}_a (\mu\text{m})$	σ_a
ACE-1 Clean	74 ± 35	0.055 ± 0.0125	1.41 ± 0.09
ACE-2 Clean (Atlantic)	110 ± 70	0.085 ± 0.012	1.44 ± 0.06
ACE-2 Clean (Arctic)	110 ± 36	0.085 ± 0.0085	1.42 ± 0.05
ACE-2 Coastal Portugal	350 ± 160	0.115 ± 0.0205	1.36 ± 0.14
ACE-2 Mediterranean		n/a	
ACE-2 W. Europe	420 ± 190	0.110 ± 0.0195	1.37 ± 0.08

ACE-2. The observations from ACE-2 are grouped into five types based on their points of origin as determined using their calculated back trajectories: clean air originating from the Atlantic; clean air originating from the Arctic; polluted air originating from over coastal Portugal; polluted air originating from the Mediterranean; and polluted air originating from Western Europe.

Aerosol populations observed in the three clean environments exhibited tri-modal size distributions, while the polluted environments are better characterized on average by one or two modes. Table 7.2 lists the three parameters for each of up to three log-normal modes, with the associated uncertainties, of the number concentration distribution with size observed in the six environments (data from *Bates et al.*, 2000). (Refer to Section 3.2 for discussion of log-normal modes and how such data are obtained.) The reported aerosols were measured by ship-board instruments, drawn through a heated mast that dries the aerosols at $55 \pm 5\%$ RH. The reported results are dry distributions, adjusted using growth factors that depend on aerosol type, and are corrected to account for known systematic measurement errors (*Bates et al.*, 2000). Note that the total number concentrations of the aerosols are dramatically higher for the polluted cases, in which concentrations of thousands of particles per cubic centimeter occur, rather than hundreds for the clean environments.

Table 7.3: Aerosol SO_4^{2-} mass implied by observed size distributions compared to observed values

	Sub-Micron Mass ($\mu\text{g}/\text{m}^3$)		Super-Micron Mass ($\mu\text{g}/\text{m}^3$)	
	Calculated	Observed	Calculated	Observed
ACE-1 Clean	0.13	0.19 ± 0.06	8.43×10^{-10}	0.07 ± 0.09
ACE-2 Clean (Atlantic)	0.71	0.74 ± 0.2	1.97×10^{-05}	0.15 ± 0.03
ACE-2 Clean (Arctic)	0.69	0.67 ± 0.12	6.41×10^{-06}	0.06 ± 0.01
ACE-2 Coastal Portugal	6.53	7.9 ± 2.4	7.14×10^{-05}	0.66 ± 0.45
ACE-2 Mediterranean	8.09	6.6 ± 1.8	3.26×10^{-05}	0.22 ± 0.01
ACE-2 W. Europe	5.95	7.7 ± 1.9	1.36×10^{-04}	0.37 ± 0.23

Sulfate aerosols effectively comprise the entirety of the aerosol number concentration: soot particles are internally mixed with sulfate and sea salt is not an important contributor to number concentration (*Bates et al.*, 2000), although because the particles tend to be so large it contributes significantly to mass concentration (see Section 7.4.2 for more on this). We presume for the purposes of this study that all of the non-sea-salt (nss) sulfate is fully neutralized ammonium sulfate. Although observed particles are often more acidic, this does not significantly impact the condensation calculations we will perform (observed ammonium to nss sulfate ratios range from 0.5 to 1.6 in the measurements, with the lowest ratios being present in the cleanest environments; *Quinn et al.*, 2000). Table 7.3 shows the sub-micron and super-micron sulfate mass consistent with the number distributions listed in Table 7.2 (using the central values of each distribution), as calculated using the MELAM model initialization procedure and the assumption that the aerosols are entirely ammonium sulfate. Note first that the calculated sub-micron mass agrees with observations within the listed one standard deviation variability (and often much more closely). The calculated super-micron values are minuscule, and much smaller than the observed values in all cases. This is to say that the super-micron nss sulfate particles are not well represented by the one-to-three modes of the parameterized distributions and all-sulfate assumption. *Bates et al.* (2000), from which the parameterized number distributions of Table 7.2 are taken, knowingly ignore the coarse mode particles (which includes particles with radii greater than $0.25 \mu\text{m}$) which is a minor contributor to aerosol number concentration but would include much of the super-micron sulfate mass. The vast majority of the measured mass concentration, however, is sub-micron and so we do not expect this to introduce much error. Overall, the observed number and mass distributions are in good agreement when we assume the aerosols are ammonium sulfate.

Table 7.4: O’Dowd Parameterization of Sea Salt Distributions

Mode	N_a	\bar{r}_a	σ_a
Film Drop	$10^{0.095 \text{ u} + 0.283}$	$0.1 \text{ } \mu\text{m}$	1.9
Jet Drop	$10^{0.0422 \text{ u} - 0.288}$	$1.0 \text{ } \mu\text{m}$	2.0
Spume Drop	$10^{0.069 \text{ u} - 5.81}$	$6 \text{ } \mu\text{m}$	3.0

Table 7.5: Mass Loadings of Sea Salt Aerosols: Observations and Fit to Observations

Air Mass	Calculated Wind Speed (m/s)	Sub-Micron Mass ($\mu\text{g}/\text{m}^3$)		Super-Micron Mass ($\mu\text{g}/\text{m}^3$)	
		Observed	Fit	Observed	Fit
ACE-1 Clean	14.3	1 ± 0.55	0.48	9.4 ± 5.5	11.92
ACE-2 Clean (Atlantic)	8.1	0.6 ± 0.51	0.21	6.3 ± 1.6	6.46
ACE-2 Clean (Arctic)	6.6	0.42 ± 0.28	0.18	5.1 ± 2.2	5.59
ACE-2 Coastal Portugal	12.6	0.88 ± 1.5	0.39	10 ± 3.1	10.11
ACE-2 Mediterranean	11.2	0.34 ± 0.05	0.32	4.2 ± 3.1	8.76
ACE-2 W. Europe	12.0	0.4 ± 0.28	0.36	9.4 ± 2.2	9.54

7.4.2 Sea Salt

Sea salt particles are ubiquitous in the marine environment and compete directly with sulfate aerosols for water vapor during cloud formation (*Ghan et al.*, 1998). We attempt to include realistic distributions of sea salt aerosols in our calculations by combining observed sub-micron and super-micron sea salt aerosol mass with the tri-modal parameterization of sea salt concentration to wind speed of *O’Dowd et al.* (1993); *O’Dowd and Smith* (1993); *O’Dowd et al.* (1997, 1999).

In general, the number concentration of sea salt aerosols is definable using three modes: the film drop mode centered at $0.1 \text{ } \mu\text{m}$ radius; the jet drop mode centered at $1.0 \text{ } \mu\text{m}$ radius; and the spume drop mode centered at $12 \text{ } \mu\text{m}$ radius. The flux of sea salt aerosols from the ocean surface to the atmosphere depends directly on the surface wind speed; higher winds lead to rougher seas and more drops are blown into the atmosphere and evaporate. *O’Dowd et al.* (1993); *O’Dowd and Smith* (1993) and *O’Dowd et al.* (1997) parameterize this relationship using three log-normal modes by setting the mean radius and geometric standard deviation for each mode and defining the number concentration to be a function of air speed. Table 7.4 summarizes their parameterization.

Quinn et al. (2000) report bulk aerosol mass concentrations for the sub-micron and super-micron portions of the aerosol distribution (split at $r_a = 0.55 \text{ } \mu\text{m}$ using a cascade impactor) for each of the six environments we consider. We define sea salt distributions for each of the environments by tuning the wind speed of the O’Dowd parameterization for a best fit to the central values of the *Quinn et al.* (2000) data, using least squares minimization. The results are summarized in

Table 7.6: Mode-by-Mode Soot Inclusion Rates

	Nucleation Mode	Aitken Mode	Accumulation Mode
Concentrated Mixture (C)	10%	20%	30%
Mid-Range Mixture (M)	20%	30%	40%
Broad Mixture (B)	30%	40%	50%

Table 7.5. The variability of sea salt concentrations in a given region appears to be large (*Quinn et al.*, 2000), although in the marine environments considered in this study, the expected impact of varying the distribution over the range is quite small (cf. *Ghan et al.*, 1998). We will simply use these representative distributions, fit to central values, as a way to include the impact of a sea salt distribution.

7.4.3 Black Carbon: Concentrations and Mixing State

As discussed earlier in this chapter, small soot particulates are found aggregated with sulfate particles even in remote marine environments (*Pósfai et al.*, 1999; *Hara et al.*, 2003; *Li et al.*, 2003a).

Novakov et al. (2000) reports observations of total carbon (TC) content taken during the ACE-2 campaign (and subdivides into black carbon and organic carbon content when possible); samples were taken using a cascade impactor aboard the *R.V. Vodyanitskiy* and analyzed using a thermal technique. They calculate mean sulfate / soot mass ratios in a variety of manners (noting that the two aerosol types are highly correlated in these environments), and compare their results with those obtained during the Tropospheric Aerosol Radiative Forcing Experiment (see an overview of the experiment in *Hobbs et al.*, 1996).

We will use their calculated surface-level, sub-micron, SO_4^{2-} / TC ratio of 5.3 ± 2.9 . For each environment we consider, we calculate three levels of soot using ratios of 2.4, 5.3, and 8.2 (which relate to the one standard deviation range of the observed ratio). We call these three cases Clean, Middle, and Sooty cases, respectively.

Observations of the soot mixing state must be considered to be more preliminary. *Pósfai et al.* (1999) performed limited aerosol sampling during the ACE-1, ACE-2, and ASTEX/MAGE campaigns, as discussed in Section 7.2.4, and their results are qualitatively in agreement with a number of other studies (e.g., *Hara et al.*, 2003; *Li et al.*, 2003b). Together, the observations suggested that approximately 10% to 50% of sulfate aerosols include soot particles and that larger sulfate particles are more likely to include soot than are smaller particles. As a simple first assumption based on

Table 7.7: Summary of Calculated Soot Size (C, M, S) and Mass Loadings for the Marine Environment

Concentrated Mixture							
	% Sulfate Particles with Soot Inclusions	Sub-micron Soot Mass ($\mu\text{g}/\text{m}^3$)			Soot Spherule Radius (μm)		
		Clean	Middle	Sooty	Clean	Middle	Sooty
ACE-1 Clean	17.6%	0.0232	0.036	0.0792	0.0069	0.0080	0.0104
ACE-2 Clean (Atlantic)	21.2%	0.0902	0.140	0.3083	0.0108	0.0125	0.0162
ACE-2 Clean (Arctic)	19.8%	0.0817	0.126	0.2792	0.0091	0.0105	0.0137
ACE-2 Coastal Portugal	21.1%	0.9634	1.491	3.2917	0.0120	0.0139	0.0181
ACE-2 Mediterranean	20.0%	0.8049	1.245	2.7500	0.0101	0.0117	0.0153
ACE-2 W. Europe	23.9%	0.9390	1.453	3.2083	0.0164	0.0189	0.0246

Mid-Range Mixture							
	% Sulfate Particles with Soot Inclusions	Sub-micron Soot Mass ($\mu\text{g}/\text{m}^3$)			Soot Spherule Radius (μm)		
		Clean	Middle	Sooty	Clean	Middle	Sooty
ACE-1 Clean	27.6%	0.0232	0.036	0.0792	0.0060	0.0069	0.0090
ACE-2 Clean (Atlantic)	31.2%	0.0902	0.140	0.3083	0.0095	0.0110	0.0143
ACE-2 Clean (Arctic)	29.8%	0.0817	0.126	0.2792	0.0080	0.0092	0.0120
ACE-2 Coastal Portugal	31.1%	0.9634	1.491	3.2917	0.0105	0.0122	0.0159
ACE-2 Mediterranean	30.0%	0.8049	1.245	2.7500	0.0089	0.0103	0.0133
ACE-2 W. Europe	33.9%	0.9390	1.453	3.2083	0.0146	0.0168	0.0219

Broad Mixture							
	% Sulfate Particles with Soot Inclusions	Sub-micron Soot Mass ($\mu\text{g}/\text{m}^3$)			Soot Spherule Radius (μm)		
		Clean	Middle	Sooty	Clean	Middle	Sooty
ACE-1 Clean	37.6%	0.0232	0.036	0.0792	0.0054	0.0062	0.0081
ACE-2 Clean (Atlantic)	41.2%	0.0902	0.140	0.3083	0.0086	0.0100	0.0130
ACE-2 Clean (Arctic)	39.8%	0.0817	0.126	0.2792	0.0072	0.0084	0.0109
ACE-2 Coastal Portugal	41.1%	0.9634	1.491	3.2917	0.0096	0.0111	0.0145
ACE-2 Mediterranean	40.0%	0.8049	1.245	2.7500	0.0081	0.0093	0.0121
ACE-2 W. Europe	43.9%	0.9390	1.453	3.2083	0.0134	0.0155	0.0201

these preliminary observations, we propose a simple parameterization of soot inclusion percentage that varies by mean size of sulfate mode (i.e., nucleation, Aitken, and accumulation). We propose three cases – for concentrated, mid-range, and broad mixtures of soot in the sulfate population – for which the inclusion rates are listed in Table 7.6.

We make the simplifying assumption that the soot particles are a mono-dispersion: that each is the same size. We have no information from the mixing state studies about co-variance between the sizes of soot and sulfate, and do not want to presume anything about that. We know the total soot mass and the total number of soot particles, and use that to calculate the average soot particle radius by assuming that the particles are spherical with density of 2 g cm^{-3} (*Seinfeld and Pandis, 1998*).

To summarize, we have introduced nine descriptions of atmospheric soot loading for each of

the six marine environments we are considering: three mixing states (C, M, B) each for three total soot concentrations (C, M, S). Each of these cases is detailed in Table 7.7. The table includes: the total percentage of sulfate particles that have soot inclusions (a weighted average of the mixing state percentage by the number concentrations in each mode); the soot mass loading for each of the cases; and the calculated soot radii for each of the cases. Note that the soot particles are very small, ranging from 5 nm to 25 nm in radius, and are substantially smaller than those considered in the polluted marine environments of the last section. However, these particle sizes are consistent with the observations just discussed. We have considered a broad range of soot loadings and mixing states and believe appropriately representative values to lie somewhere within the range considered. Following the discussion in Section 7.3.3, it is unclear how to calculate appropriate spherical particle radii from the data that we have; the sizes we cite are accurate if all of the sooty material was formed into the appropriate number of spherical particles, but the aggregated structures observed in the environment (see, for example, *Pósfai et al.*, 1999) may be better represented by assuming a less dense sphere or require some other correction to their size. Many of the aggregated chains of soot that are internally mixed with ammonium sulfate in the TEM images of *Pósfai et al.* (1999) (their Figure 1A), appear to have radii of about $0.05\ \mu\text{m}$, larger than even the largest particles cited in the examples in Table 7.7. The shapes of these particles, however, are extremely irregular, and may well displace an equivalent amount of a growing solution embryo as would a smaller spherical equivalent (the critical parameter of the Gorbunov model). Here we reach the limits of our observational and theoretical knowledge.

7.4.4 Results

Each of the model runs are conducted using the MELAM updraft model. All of the distributions begin in equilibrium with the environment at 1000 mb pressure, 298.15 K temperature, and 98% \mathcal{RH} , and are then lifted 1000 m adiabatically. Each mode of sulfate or mixed soot / sulfate particles are represented in a 75 bin full sectional distribution with edges ranging from $0.005\ \mu\text{m}$ to $2.5\ \mu\text{m}$ (for a total of two, four, or six sectional distributions, depending on how many modes are present). Each is populated by equilibrating a structured representative sample to the local environment and then placing the aerosols in to the appropriate size bins. Sea salt is represented in a 20 bin full sectional distribution with edges ranging from $0.005\ \mu\text{m}$ to $2.5\ \mu\text{m}$, although it is populated through appropriate inversion of the log-normal cumulative distribution function. (Refer to Section 3.3.5 for a discussion of the various aerosol representations and methods used to calculate them.)

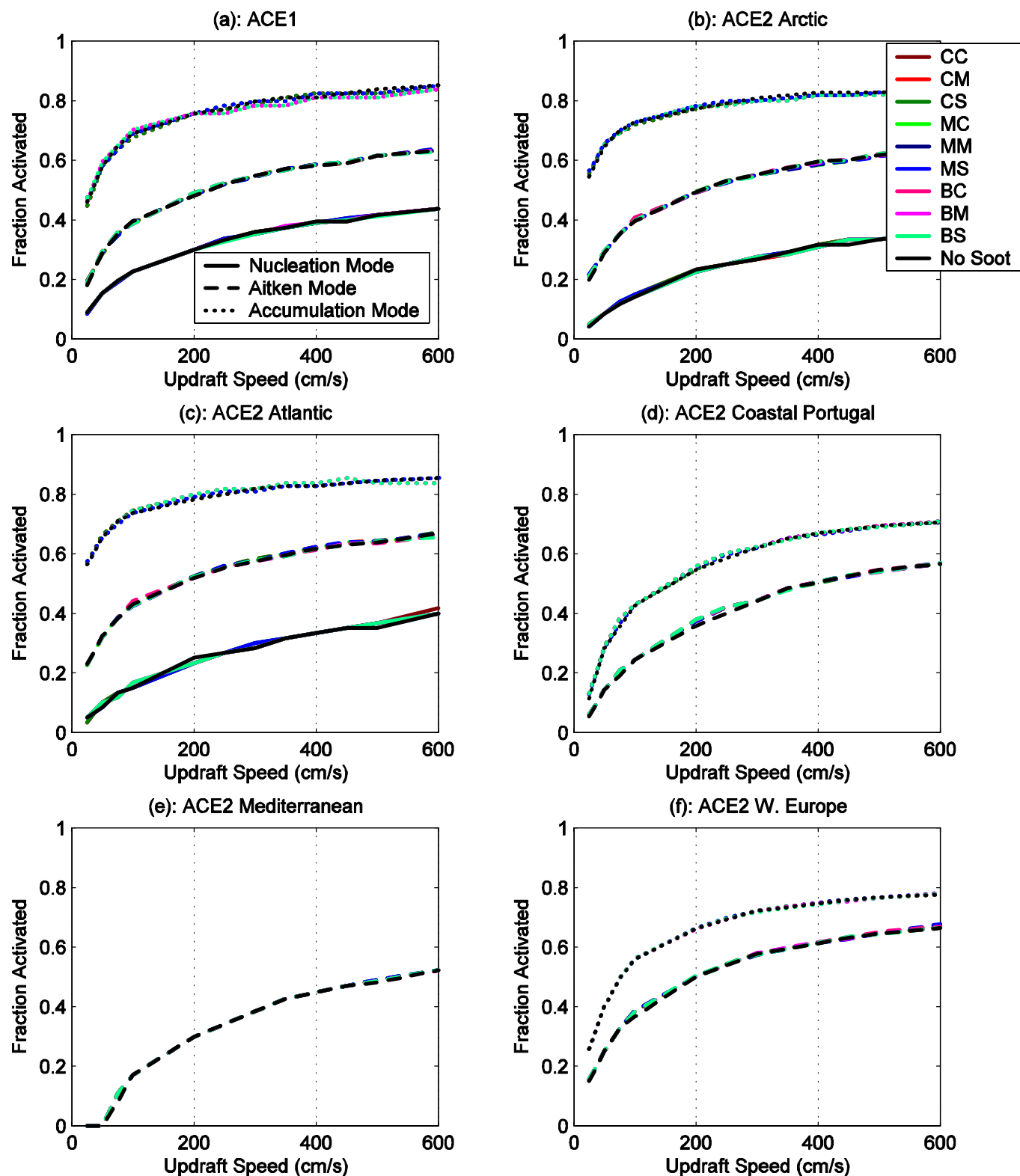


Figure 7-5: Activation fraction as a function of updraft speed for each of the six case-study environments considered; each of up to three modes are plotted separately but on the same axes, and the line type (dotted, dashed, or solid) indicates mode type; ten mixing states are drawn on the same axes: a no-soot limit and then nine cases coded using two letters (the first letter indicates the mixing state – concentrated, mid-range, and broad – and the second letter indicates the soot mass loading – clean, middle, and sooty); $\theta = 135^\circ$ for all of the results shown

As described above, there are ten proposed distributions for each of the six marine environments under consideration. Each of the samples is adiabatically lifted a number of times using the MELAM updraft model over a variety of updraft speeds and three contact angles corresponding to the three values observed by *Zuberi* (2003) (reviewed earlier in Section 7.2.1).

Figure 7-5 shows the activation fraction as a function of updraft speed for each of the six case-study environments. Each mode of the size distribution is plotted separately: nucleation mode as a solid line; Aikten mode as a dashed line; and accumulation mode as a dotted line. Ten mixing states are drawn on the same axes for each mode: a no-soot limit in black and then nine sooty cases in color, coded in the Figure's legend using two letters: the first letter (C, M, or B) indicates the mixing state (concentrated, mid-range, and broad) and the second letter (C, M, or S) indicates the soot mass loading (clean, middle, and sooty). Refer to Table 7.7 and the accompanying discussion in Section 7.4.3 for details about how the sooty cases differ. The results shown are for $\theta = 135^\circ$; the other two contact angles are not shown but have essentially identical results.

In each of the example environments, the activation fraction increases with increasing updraft speed. In each, modes of larger mean size activate more readily than those with smaller mean size; more accumulation mode particles activate than Aitken mode particles, and more Aitken mode particles activate than nucleation mode particles. And in each, the activation fraction increases more rapidly with updraft speed in weaker updrafts than in stronger, although none of the distributions appear to saturate as the Maldives example did in Section 7.3. These behaviors all agree with what should have been expected from the results of Section 7.4.4.

Remarkable in Figure 7-5, however, is that the lines for each of the ten mixing states lie on top of one another and that the activation fraction curves do not change with the contact angle of soot (not shown). Simply put: the presence of soot does not appear to affect aerosol activation in any of these clean and moderately polluted marine environments, regardless of how hydrophilic it is. This is almost certainly related to the relatively small size of soot particles included in the model (as cited in the rightmost columns of Figure 7.7), which range from $0.0054 \mu\text{m}$ radius to $0.0246 \mu\text{m}$ radius. We saw in the Section 7.3, in which we considered the more polluted environments represented by the INDOEX measurements, that decreasing the size of the soot spherules apparently decreases the magnitude of the activation enhancement. We had evidence to indicate that the soot particulates were substantially larger in that environment. And we feel that the range of soot particulate size calculated in this section is broad and reasonable, as discussed in Section 7.4.3.

7.4.5 Summary and Discussion

In the introduction to this chapter, we asked three questions about the role of internally mixed soot / sulfate particles in cloud formation in marine environments. In Section 7.3, we addressed two of those questions, and in Section 7.4 we addressed the third: Does the ubiquitous soot found in clean marine environments affect cloud formation?

In order to answer this question, we drew upon the observations of the ACE-1 and ACE-2 field campaigns, which are representative respectively of pristine and moderately polluted marine environments worldwide. For each of the environments, we formulated several distributions of ammonium sulfate aerosols, a fraction of which are internally mixed with soot particulates, to be representative of the uncertain range of mixing states and soot loadings from these two campaigns. We then used the MELAM updraft model to calculate how many of the aerosols activate during an adiabatic ascent of 1000 m. In answer to the above question, our modeling results indicate that activation in these environments is unaffected by the presence of soot.

In contrast to the results of our studies of more polluted marine environments in Section 7.3, which found that large amounts of soot substantially affects the activation of internally mixed soot / inorganic aerosols, the widespread presence of internally mixed sulfate / soot particles in cleaner marine environments apparently has a negligible effect because the soot particles are too small. In these relatively clean marine environments, aerosol activation may be determined via consideration solely of the inorganic material as has generally been done.

This is an important conclusion, but it must bear the caveat that we are unsure whether we calculate the effective size of the soot spheres for use in the Gorbunov model correctly (as discussed at the end of Section 7.4.3). Test studies using even larger particles reveal that considerably larger soot particles are required to impact aerosol activation in these environments with the observed amount of sulfate (not shown); particles comparable to the $0.1\ \mu\text{m}$ to $0.2\ \mu\text{m}$ radius particles that we showed in Section 7.3 to have an impact in polluted environments.

The recent observations of the mixing state of soot and sulfate in the marine atmosphere, which we have discussed throughout this section, indicate that soot is preferentially associated with larger particles that are more likely to form cloud droplets. This has implications for wet deposition of soot, as the fraction of mixed sulfate / soot particles that form cloud droplets relates to the amount of soot that falls from the atmosphere in precipitation. There is some debate about whether wet deposition or volatilization is the major sink of soot in the remote environment (e.g., *Molina et al.*, 2004). Deepening our understanding of the mean mixing state of soot and sulfate in

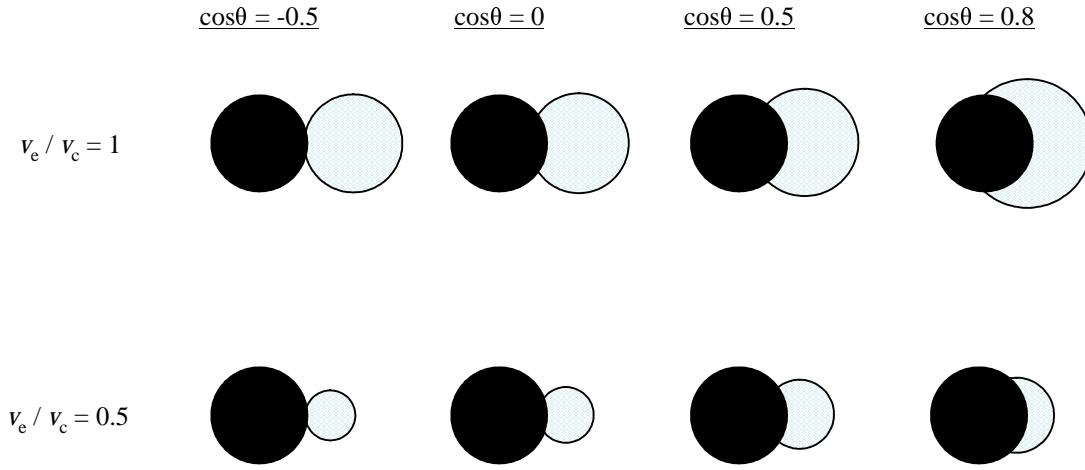


Figure 7-6: Schematic of mixed soot / sulfate aerosols; the aerosols in the top row have equal volumes of soot (v_c) and sulfate solution (v_e) and those in the bottom row have eight times more soot than sulfate by volume; each column shows the aerosols for a different contact angle (θ)

these environments will allow greater access to the mean wet deposition rates.

7.5 The Relationship Between the Size of the Soot Core and Aerosol Activation

As the activation of mixed soot / sulfate aerosols apparently hinges on the size of the soot particles, let us consider why the size of these particles is important in the context of the Gorbunov model. (Recall that the Gorbunov model was discussed in Section 5.8.2, where we paid particular attention to the calculation of the equilibrium saturation ratio, S'). Simply put, insoluble cores make the effective size of the growing solution aerosol larger. An increase in effective size affects condensation in two ways: first, it reduces the critical super-saturation at which the particle will activate; and second, it accelerates condensation onto the aerosol by increasing the transfer rate to the surface in the diffusion model and by reducing the curvature of the embryo and thus reducing the vapor concentration that is in equilibrium with the surface.

The solution embryo is characterized by an effective radius (r_e) and volume (v_e); r_e and v_e are related through a complex equation that accounts for the displacement of some volume of the otherwise spherical embryo by the attached insoluble core (*Gorbunov and Hamilton, 1997*):

$$v_e = \frac{\pi r_c^3}{3} \left\{ \frac{2}{X^3} - 2 + \frac{3(1 - X \cos \theta)}{X^3 Y} + \frac{3(X - \cos \theta)}{Y} - \left(\frac{1 - X \cos \theta}{XY} \right)^3 - \left(\frac{X - \cos \theta}{Y} \right)^3 \right\} \quad (7.1)$$

Here, X is the ratio of the radius of the insoluble core (r_c) to the radius of the solution embryo,

and Y is a function of X . Restating equation (5.58):

$$X = \frac{r_c}{r_e} \quad ; \quad Y = \sqrt{1 + X^2 - 2X \cos \theta}$$

Figure 7-6 is a schematic of mixed soot / sulfate aerosols. The aerosols in the top row have equal volumes of soot (v_c) and sulfate solution (v_e) and those in the bottom row have eight times more soot than sulfate by volume. Each column shows the aerosols for a different value of $\cos\theta$. Note that for higher values of $\cos\theta$ the solution embryo engulfs a larger fraction of the soot core and r_e (the radius from the center of the solution embryo to the solution / air interface per Figure 5-8) effectively increases.

Let us define $r_e^{\text{effective}}$ to be the radius of a spherical solution droplet with volume v_e . Equation (7.1), as expected, states that $r_e = r_e^{\text{effective}}$ when $\cos\theta = -1$ (i.e., when the soot sphere is entirely hydrophobic) or when the r_c is zero (i.e., there is no attached soot particle). Table 7.8 shows $r_e / r_e^{\text{effective}}$ (which we call the “inflation factor”) for several values of $\cos\theta$ and r_e / r_c . All of the cited embryo radii are normalized by r_c ; what matters to this calculation is the relative size of r_e to r_c , not absolute values. Note that $r_e \approx r_e^{\text{effective}}$ when the soot particle is quite hydrophobic (as represented by the $\cos\theta = -0.5$ cases) or is significantly smaller than the solution embryo. However, the inflation factor can become significantly larger than one when the soot sphere is of equal size to, or larger than, the solution embryo and when the soot sphere is hydrophilic. As we said above, this increases the condensation rate in two ways: by increasing the rate of condensation onto the particle due to the diffusive model and by decreasing the inhibiting effects of curvature of the surface. It also reduces the super-saturation required for the particle to activate. Note that r_e / r_c changes as water condenses upon the aerosol because the embryo grows while the insoluble core does not; both of these effects influence the particle’s behavior before it has activated but not afterwards (by which point the embryo has grown significantly).

Consider why the condensation rate increases as the inflation factor grows. The quasi-stationary equation, presented originally as equation (5.31), governs condensation of species i onto spherical solution aerosol droplets, as discussed in Section 5.7.1. We restate it here:

$$\frac{dm_{a,i}}{dt} = 4\pi r_a D_i [\rho_{v,i}(\infty) - \rho_{v,a,i}(r)]$$

Here, $m_{a,i}$ is the mass of species i in aerosol a , r_a is the radius of a , D_i is the molecular diffusion coefficient, and $\rho_{v,i}(\infty)$ and $\rho_{v,a,i}(r)$ are the vapor densities of species i far from the aerosol and

Table 7.8: The Relationship Between r_e and r_c

$\cos \theta$	r_e / r_c	$r_e^{\text{effective}} / r_c$	
-0.5	0.1	0.102	102%
0	0.1	0.121	121%
0.5	0.1	0.166	166%
0.8	0.1	0.263	263%
-0.5	0.5	0.510	102%
0	0.5	0.546	109%
0.5	0.5	0.637	127%
0.8	0.5	0.770	154%
-0.5	1	1.009	101%
0	1	1.039	104%
0.5	1	1.108	111%
0.8	1	1.186	119%
-0.5	2	2.005	100%
0	2	2.021	101%
0.5	2	2.050	102%
0.8	2	2.071	104%
-0.5	10	10.000	100%
0	10	10.001	100%
0.5	10	10.003	100%
0.8	10	10.003	100%

near its surface, respectively. Note that the condensation rate, $\frac{dm_{a,i}}{dt}$, is proportional to the radius of the aerosol. In the Gorbunov model, mixed soot / sulfate aerosols are not spherical; rather, such aerosols are comprised by two attached spheres with a characteristic contact angle. Water condenses upon only one of the spheres: the growing solution embryo. The condensation rate is roughly proportional to the radius of the solution embryo, although the relationship is not exact as it was for condensation upon a spherical aerosol particle because some portion of the spherical embryo's surface area is displaced by the conjoined insoluble core according to equation (7.1). Condensation onto the mixed aerosols is more rapid than it would be onto an equivalent solution aerosol of radius $r_e^{\text{effective}}$ by a multiple roughly equal to the inflation factor.

Recall the idealized Köhler theory presented in Section 5.8. In that theory, the equilibrium saturation ratio determined by the product of the solute and Kelvin (i.e., surface curvature) effects. We restate that relationship, originally presented as equation (5.49), here:

$$S' \approx \left(\frac{C'_s}{C_s} \right)_{\text{Solute}} \left(\frac{C'_s}{C_s} \right)_{\text{Kelvin}} \approx \left(\frac{C'_s}{C_s} \right)_{\text{Solute}} \exp \left(\frac{2 \sigma_{s/a} m_p}{r R^* T \rho} \right)$$

Increases in r , which is roughly equivalent to r_e in this case, reduce the solute effect and therefore

S' . Decreases in S' effectively increase the condensation rate onto the particle according to (5.46).

Consider now why the super-saturation required for the aerosol to activate changes as the r_e inflation factor increases. In Section 5.8.2, we presented the relationship between S' , $\cos\theta$, and the radii of the embryo and insoluble core as equation (5.56):

$$S' = a_w \exp \left[\frac{\sigma_{s/a}}{R^* T} \frac{M_w}{\rho} \frac{dr_e}{dv_e} \left(\frac{dA_{a/s}}{dr_e} - \cos \theta \frac{dA_{s/sd}}{dr_e} \right) \right] \quad (7.2)$$

The critical super-saturation is simply the maximum of $S' - 1$. The critical super-saturation required for a mixed soluble / insoluble aerosol to activate is decreased by increases in $\cos\theta$ or r_c (Gorbunov *et al.*, 1998). We refer the reader to Gorbunov *et al.* (1998) for a full discussion of this effect.

Mixed soot / sulfate aerosols have two advantages over pure sulfate particles when trying to activate in cloud updrafts: first, water condenses more rapidly upon them; and second, the super-saturation required for them to activate is lower. That water condenses more rapidly upon mixed aerosols than upon the equivalent pure sulfate particles implies that the mixed aerosols will grow more rapidly and activate before the pure sulfate aerosols. This may make the difference between activation and not for an aerosol particle in a particular aerosol population and updraft. Reduction of the critical super-saturation has a straight forward effect: if a particular updraft only achieves a modest super-saturation, some mixed aerosol may activate when the pure sulfate equivalents will not. Combined, these effects allow mixed aerosols to activate more readily, in many cases, than the pure sulfate equivalents.

7.6 Overview

In this chapter, we considered the the role of internally mixed soot / sulfate particles in cloud formation in marine environments. Recent observations have found significant amounts of soot in all marine environments, from the dirtiest to the very cleanest. In heavily polluted marine environments, all of the sulfate is internally mixed with soot or other insoluble aerosols. And in clean to moderately polluted marine environments, all of the soot is internally mixed with sulfate aerosols. We used observations from the ACE-1, ACE-2, and INDOEX campaigns to construct aerosol distributions representative of marine environments with various amounts of pollution and realistic mixing states. We used the Gorbunov parameterization of condensation on mixed insoluble / inorganic aerosols, introduced in Section 5.8.2, to model condensation upon the ubiquitous

soot / sulfate particles. We then used the MELAM updraft model to calculate condensation and activation.

In the introduction to this chapter, we posed three questions:

1. Do mixed soot / inorganic particles activate more or less efficiently than comparable inorganic particles?
2. What role does contact angle play in the activation of mixed soot / inorganic particles?
3. Does the ubiquitous soot found in clean marine environments affect cloud formation?

In answer to the first two questions, updraft model runs initialized using the Polluted Marine cases in Section 7.3 showed that the presence of considerable levels of soot increased the number of aerosols that activate, and that the more wettable the soot, the stronger the effect. In answer to the third question, we found in Section 7.4 that soot particles are apparently too small in clean and moderately polluted environments to influence aerosol activation. We must conclude from our results that mixed sulfate / soot aerosols ought to be explicitly represented in modeling studies of cloud activation in heavily polluted environments, but that soot may be effectively ignored when modeling activation in clean and moderately polluted marine environments. There, sulfate concentrations adequately describe the composition of these particles for the purposes of activation calculations.

We must state several caveats to these results. First, soot may become involved in cloud activation in four ways (as reviewed in the introduction to this chapter), and we have only considered one. The two mechanisms that allow condensation onto free soot particles may become important in heavily polluted environments in which free soot is present and the soot particulates are large, but are unimportant in general marine environments where no free soot is observed and the particles are small. In the heavily polluted regions, free soot may compete for water vapor with internally mixed particles during condensation. As no reasonable theory yet exists to govern condensation rates upon free soot particles, such calculations are beyond our current reach. The impact of the heating of solution droplets by internally mixed soot particles may be important in all of these environments but has not been considered.

Second, in heavily polluted environments, there are a host of competing effects that should be considered during aerosol activation, including: the impact of surfactants on surface properties of solution droplets; the impact of soluble organics on droplet surface tension; the impact of partially soluble organic species; and others. Each of these effects have been considered in one or very few

studies in the literature, and others have no doubt yet to be proposed. Issues related to indirect forcing will not be fully resolved until we are able to reduce uncertainties to do with each process and to consider all of them together; this must be considered a long term goal. We made use of recent studies that made preliminary observations of the contact angle of soot and of the mixing state of soot in marine environments to constrain the Gorbunov model. That model, however, lacks a means to translate the mass of a given soot particle (of complex structure) into an effective spherical radius. We would be more confident in these results were such a translation method available, or were the Gorbunov parameterization to be extended to include non-spherical particles and present a link between observations of soot and the structures represented.

Third, further observations could test these results. The introduction of TEM imagery and aerosol mass spectrometers allow unprecedented access to aerosol mixing state, morphology, and composition. The observational studies we used to constrain our model are either first-of-their-kind or one of a very few such studies. As more groups adopt these sophisticated measurement techniques, and more quality measurements are made, our understanding of the contact angle of soot, soot loading in various environments, the mixing state of soot, and the correlation between the size of soot and sulfate portions of internally mixed particles will grow. The prospect of these additional measurements and others drives the development of increasingly sophisticated modeling techniques that promise to, together, shed light on the indirect effect of aerosols. Climate modeling efforts should benefit from such efforts.

Chapter 8

Conclusion

8.1 Summary and Conclusions

The basic question behind all research into the indirect effects of atmospheric aerosols is: How do increasing concentrations of anthropogenic aerosol particles affect the climate by altering cloud properties? The work in this thesis focuses on the very smallest scales, appropriate for considering the uncertain physics that govern how aerosol particles become cloud condensation nuclei and cloud droplets. However, we, as scientists and as humans, are primarily interested in constraining the resulting climatic effects at the global scale. Characterizing the influence of aerosol and cloud microphysics on the global scale climate involves posing and accumulating the answers to a series of more focused questions: How do changes in aerosol composition and particle concentrations affect cloud radiative properties? How do they affect precipitation efficiency? How do they affect cloud lifetime? And what are the particular characteristics of aerosol populations that matter most? These questions, if answered in the form of adequately verified parameterizations to be used in global or meso-scale models, will lead to a much better estimate of the magnitude of the indirect effects of aerosols and may suggest strategies for control or remediation.

Underlying this thesis project is a single but important microphysical question: In a polluted air parcel, what aerosol properties and processes control activation? A new model proposed in this thesis allows investigations into the relationship between cloud drop concentrations and various properties of the aerosol populations on which they formed, and thus can help provide a physically-based answer to this question. There is a great deal of work to be done to constrain the enormously uncertain indirect effects of aerosols on climate, but a successful investigation of the microphysical processes will provide a solid foothold from which to reach for higher-level and larger scale

conclusions.

We introduce a new model of aerosol and cloud microphysics that is specifically designed to simulate the activation of complex aerosol populations: the Mixed Eulerian-Lagrangian Aerosol Model (MELAM). While formulating the model, we focused on: including physical representations that are as accurate as possible; representing the full variation of particle composition and size within aerosol populations; making the model interface as flexible as possible, and the model code as modular as possible, to facilitate altering the model for consideration of various scientific questions and inclusion of new physical models as they become available; and reconsideration of the assumptions that have underlain microphysical process models in the literature. We initialize the model with aerosol populations whose distributions of size and of composition are constrained by observations. To provide boundary conditions, we embed the model in a parcel updraft model.

Much of the thesis was devoted to the formulation of the MELAM model. In Chapter 2, we summarized the various components of model: how it represents aerosol populations, formulates various microphysical processes, and sets boundary conditions. In Chapters 3 to 5 we discussed the formulation of critical modules in MELAM and compared their behavior to data or to other models as appropriate. In Chapter 6, we presented two updraft parcel models that we used to provide boundary conditions to MELAM. And finally in Chapter 7, we considered the activation of mixed soot / sulfate aerosols. We will summarize the findings of these last two chapters, which uses MELAM to answer specific scientific questions, here.

In Chapter 6, we developed both an adiabatic constant-speed updraft parcel model, similar to others used in aerosol activation studies in the literature, and an episodically entraining, variable-updraft-speed model inspired by recent successful convective parameterizations developed in the cloud dynamics community. In the new model, updraft velocities are calculated from vertical profiles of convective available potential energy, and entrainment rates are taken from the (*Emanuel*, 1991) cloud parameterization. The method used to calculate updraft velocities is novel and, using these velocities in an updraft model, we showed that variations in updraft velocity are important to aerosol activation in cumulus convection. We compared the behaviors of the two models to investigate the importance of representing variations of updraft speed and cloud entrainment in calculations of aerosol activation. We also considered how parcel modeling efforts might eventually be integrated with convective parameterizations for use in regional or global scale models. We will summarize our findings from that chapter here:

- The updraft speed through the base of the cloud controls the relative humidity (\mathcal{RH}) maximum at the lifting condensation level (LCL). In constant-speed updraft models, the size of the \mathcal{RH} maximum just above the LCL entirely controls the fraction of aerosols that activate.
- When realistic profiles of convective updraft velocities, which generally increase with altitude, are used, a cloud may sustain increased super-saturation well above the LCL. When these super-saturations are sustained at high altitudes, aerosol particles that would not activate if only exposed to the \mathcal{RH} maximum near the LCL may activate. Note that our model did not calculate coalescence in these numerical experiments, and the presence of super-sized cloud droplets may reduce the sustained super-saturation well above the LCL.
- Episodic entrainment increases the sustained super-saturation above the LCL by reducing aerosol concentrations.
- According to the variable-speed updraft model, aerosols that activate due to the \mathcal{RH} maximum near the LCL may deactivate as the ascent velocity drops; evaporation due to the entrainment of dry air deactivates even more aerosols near the point of minimum updraft speed. These deactivated aerosols may activate again as the velocity increases above.
- The model developed here implies that it should be possible to eventually connect updraft velocities to cloud parameterizations for large scale models.

We showed that constant-speed adiabatic models are reasonable for calculating aerosol activation in very shallow clouds or near the LCL of cumulus clouds, but also that both entrainment and variations in updraft speed must be considered to simulate the development of cloud droplets in cumulus convection. The last finding above, however, may be the most important as it points towards the overall goal of this line of research. Ultimately, refining estimates of the regional and global radiative impact of the indirect effects of aerosols will require building a parameterization that relates characteristics of aerosol populations to the optical properties and behaviors of clouds using the convective parameterization.

In Chapter 7, we used the MELAM updraft model to consider how internally mixed sulfate / soot aerosols influence activation in cloud updrafts. Recent observations found this type of mixed aerosol to be ubiquitous in both polluted and very clean marine environments, which is a somewhat surprising result. Data from field campaigns suggest that these aerosols are present during the formation of most maritime clouds; this has potentially large implications for the global radiative

balance if the impact of these aerosols on activation is significant. We constrained, for the first time, the Gorbunov parameterization of condensation upon mixed soluble / insoluble aerosols (which is an appropriate analogy to the observed mixed sulfate / soot aerosols) using recent measurements of the contact angle of water on soot and TEM analyses of aerosol mixing state from several field campaigns. We defined populations of mixed sulfate / soot aerosols from observations from the ACE-1, ACE-2, and INDOEX field campaigns. We then used the MELAM updraft model to consider how these distributions behave in cloud updrafts and varied both updraft velocity and the contact angle of soot over reasonable ranges. We summarize our major findings from those studies here:

- Fresh soot, which we expect to be quite hydrophobic, has negligible impact on aerosol activation. Mixed sulfate / fresh soot aerosols activate according to their inorganic content and cloud models may therefore effectively ignore the presence of soot in these cases.
- As soot chemically ages its contact angle with water decreases, and mixed soot / sulfate particles become more likely to activate. We calculate that significantly more aerosols activate in cloud updrafts in very polluted regions when the mixed soot / sulfate particles are explicitly represented (such as in regions influenced by the pollutant outflow from the Indian sub-continent) than when soot is not explicitly included. The radiative implications in such regions may also be significant.

Many of the measurements used to constrain the Gorbunov model and the characteristics of the aerosol populations in this thesis used new observational techniques that are either first-of-their-kind or one of only a very few such studies. Additional observations, future field studies, and eventual refinement of the new measurement techniques will allow us to further improve our estimates of the role of mixed soot / sulfate aerosols in cloud formation.

In this thesis, we developed a new microphysical process model appropriate for making aerosol activation calculations. We showed that microphysical calculations of aerosol activation are sensitive to both the particulars of the composition, mixing state, and size distribution of aerosol populations and to the representation of cloud updrafts. The model we developed can be used in future studies to consider many more questions related to the indirect effects of aerosols and, ultimately, be used to develop a parameterization of aerosols' influence on cloud development appropriate for use in regional and global models.

8.2 Limitations of Data and Theory

Despite our best efforts to make the MELAM microphysics module as detailed and realistic as possible, limitations both of data and of theory limit the range of systems we can model. Furthermore, insufficient observations and observational techniques restricted our investigations of the dynamics of activation in cloud updrafts and of the activation of mixed soot / sulfate aerosols in Chapters 6 and 7. In this section, we will review the limitations of theoretical models, laboratory data, and field observations that are important to the subject of this thesis and suggest what would be necessary to improve future modeling efforts.

The model of inorganic thermodynamics used in MELAM, presented in Chapter 4, depends on very old and oftentimes inadequate data to constrain models of activity coefficients, surface tension, and density. Much of the data is more than 75 years old, considers only a limited range of temperatures and ionic strengths, and addresses only binary solutions of a single electrolyte in water. Most of the Kusik-Meissner parameters are available for only a single temperature and we are often forced to use the default value of the temperature dependence parameter. That parameter varies significantly for the electrolytes for which data is available, and our use of it in this thesis introduces unknown errors. There is apparently little incentive currently for academic or government laboratories to measure the thermodynamic properties of inorganic solutions; to solve the current problems in cloud microprocesses, this work needs to be recognized as cutting edge science. A thorough and accurate set of measurements of the solubility of electrolytes and density, surface tension, and gas-aqueous partitioning of inorganic solutions would improve aerosol modeling significantly.

Our ability to model condensation onto complex, non-spherical aerosols is poor and must be improved. We use the Gorbunov model of condensation onto soot spheres that are attached to some amount of inorganic material, but the observations we use to constrain this model are inadequate and the model itself addresses only a greatly idealized system. We used only a single study to define the contact angle of water on soot and though that pioneering study has its inadequacies it is the only one available. This study considered the contact angle of water with a flat surface of simulated soot that is chemically aged in several ways that may simulate atmospheric aging of soot aerosols. We do not expect that the contact angle of water on soot is the same for flat surfaces and curved aerosol particles, but as yet there is no means to observe the contact angle of an aerosol particle directly. The ability to observe the contact angle on actual particles would also allow us to determine how this angle in aerosols in the actual atmosphere is affected by oxidation and other

processes, how it varies within a population of particles, and how it relates to particle size; gaining this ability would be a large step forward.

Our use of the Gorbunov model is also constrained by our lack of understanding of the mixing state of soot and inorganics. The study we presented in Chapter 7 uses data from a new observational technique that allows us to determine the fraction of inorganic aerosols that have soot inclusions and the rough relationship of this fraction to the size of the entire aerosol particle. We do not, however, have any understanding of the statistics of the relationship between the amount of inorganic material and the size of the attached soot particle. Also, the Gorbunov model considers the idealized case of inorganics attached to spherical soot particles. In nature, soot aerosols often exist as agglomerations of many small soot spherules which may fold roughly into a near-spherical ball or may lengthen into a chain or other nonlinear formation; regardless of the form the particle takes, the morphology of soot aerosols is much more complicated than assumed in the Gorbunov model. Recent studies have observed that water condenses onto chains of soot spherules in a manner entirely different than it condenses upon isolated spherical particles, with condensation focusing on the indentations at junction points between spherules in chains. Initial efforts to develop mathematical models that would govern this condensational process have proven unsuccessful and have demonstrated the difficulty of the theoretical problem. Ultimately, models of condensation onto aerosol populations in real environments that contain any amount of soot need to include condensation onto chains of soot and onto chains of soot that are attached to inorganic material. These models would also need to include the ability to characterize the statistics of the spatial configurations of soot particles through direct observation.

Aerosols may contain many types of species, including a variety of inorganics, soluble and partially soluble organics, trace metals, soot and other insoluble substances, and surfactant species. And yet adequate data and theories are available for only one of these types, namely inorganics. Our inability to model aerosols containing organic species is a particularly glaring deficiency. Organic species represent perhaps half of the total atmospheric aerosol mass and yet current observational techniques can detect and quantify very few of them. Even if we knew the composition of organic aerosols, thermodynamic models of solutions containing organic species are rudimentary even when they are available. This is a recognized issue in the aerosol modeling community and there are several studies underway that seek to model the thermodynamics of simple organic systems; the results of these studies are eagerly awaited. Our use of the Gorbunov model allows us to model a second type of aerosols in addition to simple inorganic particles, namely those containing both soot and inorganics. Ultimately, process models must be able to represent all of the various prevalent

types and configurations of aerosols to advance our understanding of the indirect effects of aerosols and, eventually, better constrain their impact on the global climate.

Our understanding of cloud dynamics related to aerosol activation is also constrained by a significant lack of data and theoretical models. We showed in this thesis that aerosol activation is very sensitive to the vertical profile of updraft speed within a cloud updraft, and yet it is at present impossible to measure this profile for a single updraft or even a single cloud and no adequate model exists to define the profile. We developed a vertical profile of updraft speed that relied on convective available potential energy and a theoretical study that attempted to constrain the fraction of this potential energy that is converted into kinetic energy. This must be considered a first attempt that should yield an approximately correct profile, but much more work is required to refine this technique and validate it observationally. Calculation of updraft speed is still an open problem in the cloud dynamics community. The ability to estimate the mean updraft speed within a cloud and, eventually, the updraft speed of individual updrafts within a cloud, will greatly improve both our understanding of aerosol activation and our ability to realistically represent the indirect effects of aerosols in large scale models.

8.3 Future Directions

Future work with the MELAM model could take us in two directions: we could work to improve MELAM's ability to represent various types of aerosols; and we could use the model to answer additional scientific questions.

The following are proposals for improvements in the model:

- We could work to include organic species and organic thermodynamics in MELAM. Recent studies have highlighted the surface tension depressing effects of some dissolved organic species, and there is at least one major effort under way to build a robust organic thermodynamics model. We would like to be able to model the contributions of organic species to aerosol thermodynamics and build them into MELAM as the related techniques become available.
- We could work to include surfactant species in the model. The first microphysical process models to include aerosols with surfactants have considered only the limiting case of unbroken surfactant layers that do not interfere with the thermodynamic state of the aerosols. This simplistic model must be improved. Once it is, we can work to characterize the impact of surfactants on aerosol activation.

- We could consider condensation onto free soot particles. In this thesis, we considered the activation of mixed soot / sulfate aerosols. There is evidence that water condenses directly onto pure soot particles, and these aerosols would surely compete with mixed soot / sulfate particles for condensing water in polluted environments where free soot is present, such as those observed during INDOEX. The first attempts to model condensation onto pure soot aerosols have largely been unsuccessful. We could improve the theoretical approaches to condensation on soot and, eventually, include this in MELAM.

Beyond improvements in the model itself, there are additional ways we could use the model in the future:

- We could consider the activation of other types of aerosols, including: aerosols with surfactant layers; pure soot particles; and mixed soluble / insoluble species beyond the soot / sulfate aerosols considered in this thesis. We could also explore the impact of competition between aerosols of different types on aerosol activation.
- We could use the model to consider the in-cloud processing of complex aerosols that include insoluble cores, surfactant species, or other complexities beyond simple inorganic electrolytes. Previous studies have shown that in-cloud processing leads to the well defined Aitken aerosol modes observed in maritime environments. We could extend those studies using MELAM and include more complex aerosols to consider the role of cloud processing in creating internally mixed particles.
- We could include a simplified form of MELAM in a cloud-resolving meso-scale model to further consider the influence of cloud dynamics on aerosols activation and cloud development. Ultimately, we could characterize the relationships between aerosol populations, cloud dynamics, and cloud behavior, and build an appropriate parameterization for use in global scale models. A parameterization that relates properties of aerosol populations to the cloud cover fraction, cloud optical properties, and precipitation patterns at different vertical levels in a global model will go a great distance towards constraining the uncertainties in the impact of the indirect effects of aerosols on the global climate.

Appendix A

Definition of a Simplified Inorganic Aerosol System

In this section, we define a simple aqueous electrolytic system appropriate for use in MELAM, along with all of the related thermodynamic parameters. This system is similar to that used in SCAPE (*Kim et al.*, 1993a), ISORROPIA (*Nenes et al.*, 1998), and EQUISOLV (*Jacobson et al.*, 1996b) except that it does not allow solids to form, includes a somewhat more extensive set of electrolytes (including NH_4^+ , Na^+ , and K^+ and related sulfates, nitrates, and chlorides), and the parameters suit the numerical models used in MELAM's thermodynamic routines. We assume that sulfuric acid, nitric acid, HCl, and all solids completely dissociate in solution. Neither gas-phase nor aqueous chemical reaction sets are included, as the system is meant to drive simple thermodynamics-only aerosol simulations without chemistry or complex reaction mechanisms. As noted in Section 4.4.4, we do include bisulfate and related electrolytes but do not include letovicite ($(\text{NH}_4)_3\text{H}(\text{SO}_4)_2$).

We enumerate the species included in Table A.1. We then defined dissolution and dissociation reactions (see Section 4.3), in Tables A.2 and A.3, the Kusik-Meissner parameters (See Section 4.4.1) in Table A.4, and parameters related to surface tension and density (see Sections 4.6 and 4.7, respectively) in Table A.5.

Table A.1: Chemical Species

Gas-Phase Species
H ₂ O, NH ₃ , HNO ₃ , HCl
Liquid Species
H ₂ O, NH ₃ , HCl, HNO ₃ , H ₂ SO ₄ , H ⁺ , K ⁺ , NH ₄ ⁺ , Na ⁺ , OH ⁻ , Cl ⁻ , NO ₃ ⁻ , SO ₄ ²⁻ , HSO ₄ ⁻
Potential Solid Species
NH ₄ Cl, (NH ₄) ₂ SO ₄ , (NH ₄)HSO ₄ , NH ₄ NO ₃ , NaCl, Na ₂ SO ₄ , NaHSO ₄ , NaNO ₃ , NaOH, KCl, K ₂ SO ₄ , KHSO ₄ , KNO ₃ , KOH

Table A.2: Aqueous Phase Equilibrium Reactions

Aqueous Dissociation Reactions									
Equilibrium Reaction				$K_{eq}(298K)$	$-\frac{\Delta H_0^o}{RT_0}$	$-\frac{\Delta C_p^o}{R}$	Units	Reference	
(A1)	H ₂ O(aq)	⇌	H ⁺ (aq) + OH ⁻ (aq)	1.010×10^{-14}	-22.52	26.92	mol ² kg ⁻²	K	
(A2)	NH ₃ (aq) + H ₂ O(aq)	⇌	NH ₄ ⁺ (aq) + OH ⁻ (aq)	1.805×10^{-5}	-1.5	26.92	mol kg ⁻¹	C	
(A3)	HCl (aq)	⇌	H ⁺ (aq) + Cl ⁻ (aq)	∞					
(A4)	HNO ₃ (aq)	⇌	H ⁺ (aq) + NO ₃ ⁻ (aq)	∞					
(A5)	H ₂ SO ₄ (aq)	⇌	2 H ⁺ (aq) + SO ₄ ²⁻ (aq)	∞					
(A6)	H ⁺ (aq) + HSO ₄ ⁻ (aq)	⇌	2 H ⁺ (aq) + SO ₄ ²⁻ (aq)	1.015×10^{-2}	8.85	25.14	mol kg ⁻¹	K	
Gas - Aerosol Transfer Reactions									
Equilibrium Reaction				$K_{eq}(298K)$	$-\frac{\Delta H_0^o}{RT_0}$	$-\frac{\Delta C_p^o}{R}$	Units	Reference	α (Mass Accommodation) Reference
(A7)	NH ₃ (g)	⇌	NH ₃ (aq)	57.64	13.79	-5.39	mol kg ⁻¹ atm ⁻¹	C	0.04 L
(A8)	NH ₃ (g) + H ⁺ (aq)	⇌	NH ₄ ⁺ (aq)	1.03×10^{11}	34.81	-5.39	atm ⁻¹	J	"
(A9)	HNO ₃ (g)	⇌	H ⁺ (aq) + NO ₃ ⁻ (aq)	2.511×10^6	29.17	16.83	mol ² kg ⁻² atm ⁻¹	B	0.054 L
(A10)	HCl (g)	⇌	H ⁺ (aq) + Cl ⁻ (aq)	1.971×10^6	30.2	19.91	mol ² kg ⁻² atm ⁻¹	B	0.064 L

A reaction with equilibrium constant of ∞ exists only as the products; the reactant is not allowed to form

Of the three parameters related to the equilibrium constant, the first is the value of K_{eq} at a reference temperature of 298 K ($K_{eq}298K$), and the other two are thermodynamic quantities ($-\frac{\Delta H_0^\circ}{RT_0}$ and $-\frac{\Delta C_p^\circ}{R}$) that define a temperature-dependent K_{eq} when used in equation (4.6)

Reference B is *Brimblecombe and Clegg* (1988) and *Brimblecombe and Clegg* (1989); C is *Clegg and Brimblecombe* (1989); J is *Jacobson* (1999); K is *Kim et al.* (1993a); and L is *Leriche et al.* (2000)

Table A.3: Equilibrium Reactions

Solid Dissociation Reactions					
Equilibrium Reaction					K_{eq}
(A11)	$\text{NH}_4\text{Cl(s)}$	\rightleftharpoons	$\text{NH}_4^+(\text{aq})$	$+ \text{Cl}^-(\text{aq})$	∞
(A12)	$(\text{NH}_4)_2\text{SO}_4(\text{s})$	\rightleftharpoons	$2 \text{NH}_4^+(\text{aq})$	$+ \text{SO}_4^{2-}(\text{aq})$	∞
(A13)	$(\text{NH}_4)\text{HSO}_4(\text{s})$	\rightleftharpoons	$\text{NH}_4^+(\text{aq})$	$+ \text{HSO}_4^-(\text{aq})$	∞
(A14)	$\text{NH}_4\text{NO}_3(\text{s})$	\rightleftharpoons	$\text{NH}_4^+(\text{aq})$	$+ \text{NO}_3^-(\text{aq})$	∞
(A15)	NaCl (s)	\rightleftharpoons	$\text{Na}^+(\text{aq})$	$+ \text{Cl}^-(\text{aq})$	∞
(A16)	$\text{Na}_2\text{SO}_4(\text{s})$	\rightleftharpoons	$2 \text{Na}^+(\text{aq})$	$+ \text{SO}_4^{2-}(\text{aq})$	∞
(A17)	$\text{NaHSO}_4(\text{s})$	\rightleftharpoons	$\text{Na}^+(\text{aq})$	$+ \text{HSO}_4^-(\text{aq})$	∞
(A18)	$\text{NaNO}_3(\text{s})$	\rightleftharpoons	$\text{Na}^+(\text{aq})$	$+ \text{NO}_3^-(\text{aq})$	∞
(A19)	NaOH (s)	\rightleftharpoons	$\text{Na}^+(\text{aq})$	$+ \text{OH}^-(\text{aq})$	∞
(A20)	KCl (s)	\rightleftharpoons	$\text{K}^+(\text{aq})$	$+ \text{Cl}^-(\text{aq})$	∞
(A21)	$\text{K}_2\text{SO}_4(\text{s})$	\rightleftharpoons	$2 \text{K}^+(\text{aq})$	$+ \text{SO}_4^{2-}(\text{aq})$	∞
(A22)	$\text{KHSO}_4(\text{s})$	\rightleftharpoons	$\text{K}^+(\text{aq})$	$+ \text{HSO}_4^-(\text{aq})$	∞
(A23)	$\text{KNO}_3(\text{s})$	\rightleftharpoons	$\text{K}^+(\text{aq})$	$+ \text{NO}_3^-(\text{aq})$	∞
(A24)	KOH (s)	\rightleftharpoons	$\text{K}^+(\text{aq})$	$+ \text{OH}^-(\text{aq})$	∞

All solids are assumed to dissociate completely in solution, hence the infinite equilibrium constant.

Table A.4: Kusik-Meissner Parameters for Selected Electrolytes

Electrolyte	q_r	q_T^*	Reference
H_2O	e.g., $\gamma_{\text{H}_2\text{O}}^2 \approx \gamma_{\text{HCl}}^2 \gamma_{\text{KOH}}^2 \gamma_{\text{KCl}}^{-2}$		See discussion in Section 4.4.2 [†]
HCl	6.00	-0.0027	<i>Wexler and Seinfeld</i> (1991)
HNO_3	2.017	-0.0027	This work, Table 4.4.1
H_2SO_4	-1.10	-0.0027	<i>Kim et al.</i> (1993a)
$\text{H} - \text{HSO}_4(\text{H}^+ + \text{HSO}_4^-)$	8.00	-0.0027	<i>Kim et al.</i> (1993a)
NaOH	3.00	-0.0027	<i>Kusik and Meissner</i> (1978)
NaCl	2.290	0.00707	This work, Table 4.4.1
NaNO_3	-.39	-0.0027	<i>Kusik and Meissner</i> (1978)
Na_2SO_4	-0.19	-0.0027	<i>Kusik and Meissner</i> (1978)
NaHSO_4	e.g., $\gamma_{\text{NaHSO}_4}^3 \approx \gamma_{\text{NaCl}}^2 \gamma_{\text{H}-\text{HSO}_4}^2 \gamma_{\text{HCl}}^{-2}$		See discussion in Section 4.4.3 [†]
$\text{NH}_3 + \text{H}_2\text{O}$	e.g., $\gamma_{\text{NH}_3 + \text{H}_2\text{O}}^2 \approx \gamma_{\text{NH}_4\text{Cl}}^2 \gamma_{\text{KOH}}^2 \gamma_{\text{KCl}}^{-2}$		See discussion in Section 4.4.2 [†]
NH_4Cl	0.82	-0.0027	<i>Kusik and Meissner</i> (1978)
NH_4NO_3	-1.15	-0.0027	<i>Kusik and Meissner</i> (1978)
$(\text{NH}_4)_2\text{SO}_4$	-0.25	-0.0027	<i>Kusik and Meissner</i> (1978)
$(\text{NH}_4)\text{HSO}_4$	e.g., $\gamma_{(\text{NH}_4)\text{HSO}_4}^2 \approx \gamma_{\text{NH}_4\text{NO}_3}^2 \gamma_{\text{H}-\text{HSO}_4}^2 \gamma_{\text{HNO}_3}^{-2}$		See discussion in Section 4.4.3 [†]
KOH	4.77	-0.0027	<i>Kusik and Meissner</i> (1978)
KCl	0.92	-0.0027	<i>Kusik and Meissner</i> (1978)
KNO_3	-2.33	-0.0027	<i>Kusik and Meissner</i> (1978)
K_2SO_4	-0.25	-0.0027	<i>Kusik and Meissner</i> (1978)
KHSO_4	e.g., $\gamma_{\text{KHSO}_4}^2 \approx \gamma_{\text{NaCl}}^2 \gamma_{\text{H}-\text{HSO}_4}^2 \gamma_{\text{HCl}}^{-2}$		See discussion in Section 4.4.3 [†]

* Note that -0.0027 is the suggested reference value from *Kusik and Meissner* (1978) and is used in the absense of temperature-dependent data

[†] The particular species used when calculating composite activity coefficients are determined by MELAM at runtime, and so these are simply examples

Table A.5: Surface Tension and Density Parameters

Electrolyte	ζ_{ij} (mol m ⁻²)	K_{ij}^a (-)	$\phi_{ij}^{(0)}$	$\phi_{ij}^{(1)}$
HCl	4.12×10^{-7}	4.68×10^{-3}	1.382	0.0416
HNO ₃	8.05×10^{-7}	1.06×10^{-1}	1.455	0.0702
H ₂ SO ₄	-6.75×10^{-8}	1.65×10^3	1.696	0.0906
NaOH	-1.13×10^{-6}	1.17	1.602	0.0648
NaCl	-1.05×10^{-6}	1.20	1.728	0.0517
NaNO ₃	-1.66×10^{-6}	1.25	1.732	0.0715
Na ₂ SO ₄	-8.37×10^{-7}	7.57×10^1	1.557	0.230
NaHSO ₄	0 [*]	—	0 [†]	—
NH ₃ + H ₂ O	0 [†]	—	1.540	-0.110
NH ₄ Cl	-1.01×10^{-6}	1.30	1.190	0.0717
NH ₄ NO ₃	-3.08×10^{-6}	4.89×10^{-1}	1.353	0.0812
(NH ₄) ₂ SO ₄	-8.79×10^{-7}	3.84×10^1	1.361	0.198
(NH ₄)HSO ₄	0 [*]	—	3.204	0.0176
KOH	-5.44×10^{-7}	8.00	1.751	0.0664
KCl	-7.31×10^{-7}	4.16	2.512	0.0278
KNO ₃	-2.38×10^{-6}	1.02	1.746	0.0138
K ₂ SO ₄	-7.05×10^{-6}	9.58	1.884	0.0151
KHSO ₄	0 [*]	—	0 [†]	—

All surface tension parameter values are from *Li and Lu* (2001); all density parameters are from this work (see Section 4.7) using data from *Tang* (1980) (cf., *Stelson and Seinfeld*, 1981, 1982b) for (NH₄)HSO₄ and from *Lobo* (1989) for the other species

^{*} *Li and Lu* (2001) does not consider solids comprised of bisulfate and a cation; by assuming the surface excess is zero, we inherently presume that surface tension effects are adequately represented by the mean activities of H₂SO₄ and either Na₂SO₄, (NH₄)₂SO₄, or K₂SO₄ without further correction

[†] No value for this reaction is available, however NH₃ effectively dissociates only if it is neutralizing an acid, which means that the amount of NH₄⁺ that is associated with this “electrolyte” when calculating surface tensions is very small

[‡] Due to a lack of density data for NaHSO₄ and KHSO₄, we have assumed a default assumption that these species do not contribute to the density of the solution; recall from Section 4.7 that the density of a mixed solution is the weighted average by mean activity of the single-electrolyte densities and so setting this parameter to zero simply removes the electrolyte from consideration; in each case, the densities of H₂SO₄ and Na₂SO₄ or K₂SO₄, respectively, would contribute

Bibliography

- Abdul-Razzak, H., and S. J. Ghan (2000), A parameterization of aerosol activation - 2. multiple aerosol types, *Journal of Geophysical Research*, *105*(D5), 6837–6844.
- Abdul-Razzak, H., and S. J. Ghan (2002), A parameterization of aerosol activation - 3. sectional representation, *Journal of Geophysical Research*, *107*, 4026, doi:10.1029/2001JD000483.
- Abdul-Razzak, H., and S. J. Ghan (2004), Parameterization of the influence of organic surfactants on aerosol activation, *Journal of Geophysical Research*, *109*(D3).
- Abdul-Razzak, H., S. J. Ghan, and C. Rivera-Carpio (1998), A parameterization of aerosol activation - 1. single aerosol type, *Journal of Geophysical Research*, *103*(D6), 6123–6131.
- Abramzon, A. A., and R. D. Gaukhberg (1993a), Surface-tension of salt-solutions, *Russian Journal of Applied Chemistry*, *66*(6), 1139–1146.
- Abramzon, A. A., and R. D. Gaukhberg (1993b), Surface-tension of salt-solutions, *Russian Journal of Applied Chemistry*, *66*(7), 1315–1320.
- Abramzon, A. A., and R. D. Gaukhberg (1993c), Surface-tension of salt-solutions, *Russian Journal of Applied Chemistry*, *66*(8), 1473–1480.
- Abramzon, A. A., and R. D. Gaukhberg (1993d), Surface-tension of salt-solutions, *Russian Journal of Applied Chemistry*, *66*(9), 1643–1650.
- Abramzon, A. A., and R. D. Gaukhberg (1993e), Surface-tension of salt-solutions, *Russian Journal of Applied Chemistry*, *66*(10), 1823–1827.
- Abramzon, A. A., and R. D. Gaukhberg (1993f), Surface-tension of salt-solutions, *Russian Journal of Applied Chemistry*, *66*(11), 1985–1990.
- Ackerman, A. S., O. B. Toon, D. E. Stevens, A. J. Heymsfield, V. Ramanathan, and E. J. Welton (2000), Reduction of tropical cloudiness by soot, *Science*, *288*(5468), 1042–1047.

- Ackerman, B. (1959), The variability of the water contents of tropical cumuli, *Journal of Meteorology*, *16*, 191–198.
- Ackerman, B. (1963), Some observations of water contents in hurricanes, *Journal of the Atmospheric Sciences*, *20*, 288–298.
- Adams, P. J., and J. H. Seinfeld (2003), Disproportionate impact of particulate emissions on global cloud condensation nuclei concentrations, *Geophysical Research Letters*, *30*(5), 1239, doi: 10.1029/2002GL016303.
- Adamson, A., and A. Gast (1997), *Physical Chemistry of Surfaces*, 6th ed., 784 pp., John Wiley & Sons, Inc., New York.
- Ahr, M., A. I. Flossmann, and H. R. Pruppacher (1989), On the effect of the chemical-composition of atmospheric aerosol-particles on nucleation scavenging and the formation of a cloud interstitial aerosol, *Journal of Atmospheric Chemistry*, *9*(4), 465–478.
- Albrecht, B. A. (1989), Aerosols, cloud microphysics, and fractional cloudiness, *Science*, *245*(4923), 1227–1230.
- Alkezweeny, A. J., D. A. Burrows, and C. A. Grainger (1993), Measurements of cloud-droplet-size distributions in polluted and unpolluted stratiform clouds, *Journal of Applied Meteorology*, *32*(1), 106–115.
- Allen, A. G., R. M. Harrison, and J. W. Erisman (1989), Field-measurements of the dissociation of ammonium-nitrate and ammonium-chloride aerosols, *Atmospheric Environment*, *23*(7), 1591–1599.
- Ansari, A. S., and S. N. Pandis (1999a), An analysis of four models predicting the partitioning of semivolatile inorganic aerosol components, *Aerosol Science and Technology*, *31*(2-3), 129–153.
- Ansari, A. S., and S. N. Pandis (1999b), Prediction of multicomponent inorganic atmospheric aerosol behavior, *Atmospheric Environment*, *33*(5), 745–757.
- Ansari, A. S., and S. N. Pandis (2000), Water absorption by secondary organic aerosol and its effect on inorganic aerosol behavior, *Environmental Science & Technology*, *34*(1), 71–77.
- Arakawa, A., and W. H. Schubert (1974), Interaction of a cumulus cloud ensemble with the large-scale environment, part I, *Journal of the Atmospheric Sciences*, *31*, 674–701.

- Austin, J. M. (1948), A note on cumulus growth in a nonsaturated environment, *Journal of Meteorology*, 5, 103–107.
- Austin, J. M., and A. Fleisher (1948), A thermodynamic analysis of cumulus convection, *Journal of Meteorology*, 5, 240–243.
- Austin, P. H., M. B. Baker, A. M. Blyth, and J. B. Jensen (1985), Small-scale variability in warm continental cumulus clouds, *Journal of the Atmospheric Sciences*, 42(11), 1123–1138.
- Baker, M. B., R. G. Corbin, and J. Latham (1980), The influence of entrainment on the evolution of cloud droplet spectra - I. a model of inhomogeneous mixing, *Quarterly Journal of the Royal Meteorological Society*, 106(449), 581–598.
- Baker, M. B., R. E. Breidenthal, T. W. Choularton, and J. Latham (1984), The effects of turbulent mixing in clouds, *Journal of the Atmospheric Sciences*, 41(2), 299–304.
- Ball, W. P., R. R. Dickerson, B. G. Doddridge, J. W. Stehr, T. L. Miller, D. L. Savoie, and T. P. Carsey (2003), Bulk and size-segregated aerosol composition observed during INDOEX 1999: Overview of meteorology and continental impacts, *Journal of Geophysical Research*, 108(D10), 8001, doi:10.1029/2002JD002467.
- Barnes, G. M., J. C. Fankhauser, and W. D. Browning (1996), Evolution of the vertical mass flux and diagnosed net lateral mixing in isolated convective clouds, *Monthly Weather Review*, 124(12), 2764–2784.
- Bates, T. S., B. J. Huebert, J. L. Gras, F. B. Griffiths, and P. A. Durkee (1998), International Global Atmospheric Chemistry (IGAC) project’s first Aerosol Characterization Experiment (ACE-1): Overview, *Journal of Geophysical Research*, 103(D13), 16,297–16,318.
- Bates, T. S., P. K. Quinn, D. S. Covert, D. J. Coffman, J. E. Johnson, and A. Wiedensohler (2000), Aerosol physical properties and processes in the lower marine boundary layer: a comparison of shipboard sub-micron data from ACE-1 and ACE-2, *Tellus*, 52B(2), 258–272.
- Berner, A., C. Lurzer, F. Pohl, O. Preining, and P. Wagner (1979), Size distribution of the urban aerosol in Vienna, *Science of the Total Environment*, 13(3), 245–261.
- Bertsekas, D., and J. Tsitsiklis (2002), *Introduction to Probability*, 416 pp., Athena Scientific, Belmont, Massachusetts.

- Bessagnet, B., and R. Rosset (2001), Fractal modeling of carbonaceous aerosols - application to car exhaust plumes, *Atmospheric Environment*, *35*(28), 4751–4762.
- Bilde, M., and B. Svenningsson (2004), CCN activation of slightly soluble organics: the importance of small amounts of inorganic salt and particle phase, *Tellus*, *56B*(2), 128–134.
- Binkowski, F. S., and U. Shankar (1995), The Regional Particulate Matter Model - 1. Model description and preliminary results, *Journal of Geophysical Research*, *100*(D12), 26,191–26,209.
- Blyth, A. M., and D. J. Raymond (1988), Comparisons between observations of entrainment in Montana cumuli and results from a simple-model, *Journal of the Atmospheric Sciences*, *45*(13), 1965–1969.
- Bohren, C. F., and B. A. Albrecht (1998), *Atmospheric Thermodynamics*, 402 pp., Oxford University Press, New York.
- Boldi, R. A. (1993), A model of the ion chemistry of electrified convection, Ph.D, Massachusetts Institute of Technology.
- Bolton, D. (1980), The computation of equivalent potential temperature, *Monthly Weather Review*, *108*, 1046–53.
- Bony, S., and K. A. Emanuel (2001), A parameterization of the cloudiness associated with cumulus convection; evaluation using TOGA COARE data, *Journal of the Atmospheric Sciences*, *58*(21), 3158–3183.
- Bott, A. (1999), A numerical model of the cloud-topped planetary boundary-layer: chemistry in marine stratus and the effects on aerosol particles, *Atmospheric Environment*, *33*(12), 1921–1936.
- Boucher, O. (1999), Air traffic may increase cirrus cloudiness, *Nature*, *397*(6714), 30–31.
- Boucher, O., and U. Lohmann (1995), The sulfate-CCN-cloud albedo effect - a sensitivity study with 2 general-circulation models, *Tellus*, *47B*(3), 281–300.
- Boucher, O., S. E. Schwartz, T. P. Ackerman, T. L. Anderson, B. Bergstrom, B. Bonnel, P. Chylek, A. Dahlback, Y. Fouquart, Q. Fu, R. N. Halthore, J. M. Haywood, T. Iversen, S. Kato, S. Kinne, A. Kirkevåg, K. R. Knapp, A. Lacis, I. Laszlo, M. I. Mishchenko, S. Nemesure, V. Ramaswamy, D. L. Roberts, P. Russell, M. E. Schlesinger, G. L. Stephens, R. Wagener, M. Wang, J. Wong, and F. Yang (1998), Intercomparison of models representing direct shortwave radiative forcing by sulfate aerosols, *Journal of Geophysical Research*, *103*(D14), 16,979–16,998.

- Bower, K. N., T. W. Choularton, M. W. Gallagher, K. M. Beswick, M. J. Flynn, A. G. Allen, B. M. Davison, J. D. James, L. Robertson, R. M. Harrison, C. N. Hewitt, J. N. Cape, G. G. McFadyen, C. Milford, M. A. Sutton, B. G. Martinsson, G. Frank, E. Swietlicki, J. Zhou, O. H. Berg, B. Montes, G. Papaspiropoulos, H. Hansson, C. Leck, M. Kulmala, P. Aalto, M. Vke, A. Berner, M. Bizjak, S. Fuzzi, P. Laj, M. Facchini, G. Orsi, L. Ricci, M. Nielsen, B. J. Allan, H. Coe, G. McFiggans, J. M. C. Plane, J. Collett, K. Moore, and D. Sherman (2000), ACE2 HILLCLOUD: An overview of the ACE-2 groundbased cloud experiment, *Tellus*, 52B(1), 750–778.
- Brechtel, F. J., and S. M. Kreidenweis (2000), Predicting particle critical supersaturation from hygroscopic growth measurements in the humidified TDMA - part I: Theory and sensitivity studies, *Journal of the Atmospheric Sciences*, 57(12), 1854–1871.
- Breon, F. M., D. Tanre, and S. Generoso (2002), Aerosol effect on cloud droplet size monitored from satellite, *Science*, 295(5556), 834–838.
- Bretherton, C. S., and P. K. Smolarkiewicz (1989), Gravity-waves, compensating subsidence and detrainment around cumulus clouds, *Journal of the Atmospheric Sciences*, 46(6), 740–759.
- Brimblecombe, P., and S. L. Clegg (1988), The solubility and behavior of acid gases in the marine aerosol, *Journal of Atmospheric Chemistry*, 7(1), 1–18.
- Brimblecombe, P., and S. L. Clegg (1989), The solubility and behavior of acid gases in the marine aerosol – erratum, *Journal of Atmospheric Chemistry*, 8, 95.
- Broekhuizen, K., P. P. Kumar, and J. P. D. Abbatt (2004), Partially soluble organics as cloud condensation nuclei: Role of trace soluble and surface active species, *Geophysical Research Letters*, 31, L01107, doi:10.1029/2003GL018203.
- Bromley, L. A. (1973), Thermodynamic properties of strong electrolytes in aqueous- solutions, *AIChE Journal*, 19(2), 313–320.
- Byers, H., and R. Braham (1949), The thunderstorm project, *Tech. Rep. NTIS PB234515*, U.S. Weather Bureau, U.S. Department of Commerce.
- Capaldo, K., J. J. Corbett, P. Kasibhatla, P. Fischbeck, and S. N. Pandis (1999), Effects of ship emissions on sulphur cycling and radiative climate forcing over the ocean, *Nature*, 400(6746), 743–746.

- Cerveny, R. S., and R. C. Balling (1998), Weekly cycles of air pollutants, precipitation and tropical cyclones in the coastal NW Atlantic region, *Nature*, *394*(6693), 561–563.
- Chameides, W. L. (1984), The photochemistry of a remote marine stratiform cloud, *Journal of Geophysical Research*, *89*(ND3), 4739–4755.
- Chameides, W. L., and D. D. Davis (1982), The free-radical chemistry of cloud droplets and its impact upon the composition of rain, *Journal of Geophysical Research*, *87*(C7), 4863–4877.
- Chameides, W. L., and A. W. Stelson (1992), Aqueous-phase chemical processes in deliquescent sea-salt aerosols - a mechanism that couples the atmospheric cycles of S and sea salt, *Journal of Geophysical Research*, *97*(D18), 20,565–20,580.
- Chameides, W. L., C. Luo, R. Saylor, D. Streets, Y. Huang, M. Bergin, and F. Giorgi (2002), Correlation between model-calculated anthropogenic aerosols and satellite-derived cloud optical depths: Indication of indirect effect?, *Journal of Geophysical Research*, *107*(D10), 4085, doi: 10.1029/2000JD000208.
- Charlson, R. J., J. Langner, and H. Rodhe (1990), Sulfate aerosol and climate, *Nature*, *348*(6296), 22.
- Charlson, R. J., S. E. Schwartz, J. M. Hales, R. D. Cess, J. A. J. Coakley, J. E. Hansen, and D. J. Hofmann (1992), Climate forcing by anthropogenic aerosols, *Science*, *255*(5043), 423–430.
- Chaumerliac, N., M. Leriche, and N. Audiffren (2000), Modeling of scavenging processes in clouds: some remaining questions about the partitioning of gases among gas and liquid phases, *Atmospheric Research*, *53*(1-3), 29–43.
- Chen, J. P. (1992), Numerical simulation of the redistribution of atmospheric trace chemicals through cloud processes, Ph.D, The Pennsylvania State University.
- Chen, J. P., and D. Lamb (1994a), Simulation of cloud microphysical and chemical processes using a multicomponent framework - part I. description of the microphysical model, *Journal of the Atmospheric Sciences*, *51*(18), 2613–2630.
- Chen, J. P., and D. Lamb (1994b), The theoretical basis for the parameterization of ice crystal habits - growth by vapor-deposition, *Journal of the Atmospheric Sciences*, *51*(9), 1206–1221.

- Chen, J. P., and D. Lamb (1999), Simulation of cloud microphysical and chemical processes using a multicomponent framework - part II. microphysical evolution of a wintertime orographic cloud, *Journal of the Atmospheric Sciences*, *56*(14), 2293–2312.
- Chen, J. P., G. M. McFarquhar, A. J. Heymsfield, and V. Ramanathan (1997), A modeling and observational study of the detailed microphysical structure of tropical cirrus anvils, *Journal of Geophysical Research*, *102*(D6), 6637–6653.
- Choi, M. Y., and C. K. Chan (2002), The effects of organic species on the hygroscopic behaviors of inorganic aerosols, *Environmental Science & Technology*, *36*(11), 2422–2428.
- Choi, W., and M. T. Leu (1998), Nitric acid uptake and decomposition on black carbon (soot) surfaces: Its implications for the upper troposphere and lower stratosphere, *Journal of Physical Chemistry A*, *102*(39), 7618–7630.
- Chowdhury, Z., L. S. Hughes, L. G. Salmon, and G. R. Cass (2001), Atmospheric particle size and composition measurements to support light extinction calculations over the Indian Ocean, *Journal of Geophysical Research*, *106*(D22), 28,597–28,605.
- Chuang, C. C., and J. E. Penner (1995), Effects of anthropogenic sulfate on cloud drop nucleation and optical properties, *Tellus*, *47B*(5), 566–577.
- Chuang, C. C., J. E. Penner, K. E. Taylor, A. S. Grossman, and J. J. Walton (1997a), An assessment of the radiative effects of anthropogenic sulfate, *Journal of Geophysical Research*, *102*(D3), 3761–3778.
- Chuang, P. Y., R. J. Charlson, and J. H. Seinfeld (1997b), Kinetic limitations on droplet formation in clouds, *Nature*, *390*(6660), 594–596.
- Chughtai, A. R., M. E. Brooks, and D. M. Smith (1996), Hydration of black carbon, *Journal of Geophysical Research*, *101*(D14), 19,505–19,514.
- Chughtai, A. R., N. J. Miller, D. M. Smith, and J. R. Pitts (1999a), Carbonaceous particle hydration III, *Journal of Atmospheric Chemistry*, *34*(2), 259–279.
- Chughtai, A. R., G. R. Williams, M. M. O. Atteya, N. J. Miller, and D. M. Smith (1999b), Carbonaceous particle hydration, *Atmospheric Environment*, *33*(17), 2679–2687.
- Chughtai, A. R., J. M. Kim, and D. M. Smith (2002), The effect of air/fuel ratio on properties and reactivity of combustion soots, *Journal of Atmospheric Chemistry*, *43*(1), 21–43.

- Clegg, S. L., and P. Brimblecombe (1989), Solubility of ammonia in pure aqueous and multicomponent solutions, *Journal of Physical Chemistry*, *93*(20), 7237–7248.
- Clegg, S. L., and P. Brimblecombe (1995), Application of a multicomponent thermodynamic model to activities and thermal-properties of 0-40-mol kg⁻¹ aqueous sulfuric-acid from less-than-200 K to 328 K, *Journal of Physical Chemistry*, *40*(1), 43–64.
- Clegg, S. L., and K. S. Pitzer (1992), Thermodynamics of multicomponent, miscible, ionic-solutions - generalized equations for symmetrical electrolytes, *Journal of Physical Chemistry*, *96*(8), 3513–3520.
- Clegg, S. L., and J. H. Seinfeld (2004), Improvement of the Zdanovskii-Stokes-Robinson model for mixtures containing solutes of different charge types, *Journal of Physical Chemistry A*, *108*, 1008–1017.
- Clegg, S. L., K. S. Pitzer, and P. Brimblecombe (1992), Thermodynamics of multicomponent, miscible, ionic-solutions II: Mixtures including unsymmetrical electrolytes, *Journal of Physical Chemistry*, *96*(23), 9470–9479.
- Clegg, S. L., K. S. Pitzer, and P. Brimblecombe (1994), Thermodynamics of multicomponent, miscible, ionic-solutions - 2. mixtures including unsymmetrical electrolytes (vol 96, pg 9472, 1992), *Journal of Physical Chemistry*, *98*(4), 1368–1368.
- Clegg, S. L., P. Brimblecombe, and A. S. Wexler (1998a), Thermodynamic model of the system H⁺, NH₄⁺, Na⁺, SO₄²⁻, NO₃⁻, Cl⁻, H₂O at 298.15 K, *Journal of Physical Chemistry*, *102*(12), 2155–2171.
- Clegg, S. L., P. Brimblecombe, and A. S. Wexler (1998b), Thermodynamic model of the system H⁺, NH₄⁺, SO₄²⁻, NO₃⁻, H₂O at tropospheric temperatures, *Journal of Physical Chemistry*, *102*(12), 2137–2154.
- Clegg, S. L., J. H. Seinfeld, and P. Brimblecombe (2001), Thermodynamic modeling of aqueous aerosols containing electrolytes and dissolved organic compounds, *Journal of Aerosol Science*, *32*(6), 713–738.
- Cohen, C. (2000), A quantitative investigation of entrainment and detrainment in numerically simulated cumulonimbus clouds, *Journal of the Atmospheric Sciences*, *57*(10), 1657–1674.

- Conant, W. C., A. Nenes, and J. H. Seinfeld (2002), Black carbon radiative heating effects on cloud microphysics and implications for the aerosol indirect effect - 1. extended Köhler theory, *Journal of Geophysical Research*, *107*(D21).
- Corrigan, C. E., and T. Novakov (1999), Cloud condensation nucleus activity of organic compounds: a laboratory study, *Atmospheric Environment*, *33*(17), 2661–2668.
- Crouzet, Y., and W. H. Marlow (1995), Calculations of the equilibrium vapor-pressure of water over adhering 50-200-nm spheres, *Aerosol Science and Technology*, *22*(1), 43–59.
- Crutzen, P. J., and M. O. Andreae (1990), Biomass burning in the tropics - impact on atmospheric chemistry and biogeochemical cycles, *Science*, *250*(4988), 1669–1678.
- Cruz, C. N., and S. N. Pandis (1997), A study of the ability of pure secondary organic aerosol to act as cloud condensation nuclei, *Atmospheric Environment*, *31*(15), 2205–2214.
- Cruz, C. N., and S. N. Pandis (1998), The effect of organic coatings on the cloud condensation nuclei activation of inorganic atmospheric aerosol, *Journal of Geophysical Research*, *103*(D11), 13,111–13,123.
- Cruz, C. N., and S. N. Pandis (2000), Deliquescence and hygroscopic growth of mixed inorganic-organic atmospheric aerosol, *Environmental Science & Technology*, *34*(20), 4313–4319.
- Cziczo, D. J., and J. P. D. Abbatt (2000), Infrared observations of the response of NaCl, MgCl₂, (NH₄)HSO₄, and NH₄NO₃ aerosols to changes in relative humidity from 298 to 238 K, *Journal of Physical Chemistry*, *104*(10), 2038–2047.
- Davis, E. J. (1983), Transport phenomena with single aerosol particles, *Aerosol Science & Technology*, *2*, 121–144.
- de Reus, M., R. Krejci, J. Williams, H. Fischer, R. Scheele, and J. Strom (2001), Vertical and horizontal distributions of the aerosol number concentration and size distribution over the northern Indian Ocean, *Journal of Geophysical Research*, *106*(D22), 28,629–28,641.
- de Roode, S. R., and C. S. Bretherton (2003), Mass-flux budgets of shallow cumulus clouds, *Journal of the Atmospheric Sciences*, *60*(1), 137–151.
- Decesari, S., M. C. Facchini, S. Fuzzi, and E. Tagliavini (2000), Characterization of water-soluble organic compounds in atmospheric aerosol: A new approach, *Journal of Geophysical Research*, *105*(D1), 1481–1489.

- Decesari, S., M. C. Facchini, E. Matta, M. Mircea, S. Fuzzi, A. R. Chughtai, and D. M. Smith (2002), Water soluble organic compounds formed by oxidation of soot, *Atmospheric Environment*, *36*(11), 1827–1832.
- DeMott, P. J., Y. Chen, S. M. Kreidenweis, D. C. Rogers, and D. E. Sherman (1999), Ice formation by black carbon particles, *Geophysical Research Letters*, *26*(16), 2429–2432.
- Demou, E., and D. J. Donaldson (2002), Adsorption of atmospheric gases at the air-water interface. 4: The influence of salts, *Journal of Physical Chemistry A*, *106*(6), 982–987.
- Dentener, F. J., G. R. Carmichael, Y. Zhang, J. Lelieveld, and P. J. Crutzen (1996), Role of mineral aerosol as a reactive surface in the global troposphere, *Journal of Geophysical Research*, *101*(D17), 22,869–22,889.
- Dhaniyala, S., and A. S. Wexler (1996), Numerical schemes to model condensation and evaporation of aerosols, *Atmospheric Environment*, *30*(6), 919–928.
- Disselkamp, R. S., M. A. Carpenter, and J. P. Cowin (2000), A chamber investigation of nitric acid-soot aerosol chemistry at 298 K, *Journal of Atmospheric Chemistry*, *37*(2), 113–123.
- Djikaev, Y. S., and D. J. Donaldson (2000), Thermodynamics of heterogeneous multicomponent condensation on mixed nuclei, *Journal of Chemical Physics*, *113*(16), 6822–6830.
- Ekman, A., C. Wang, J. Wilson, and J. Ström (2004), Explicit simulation of aerosol physics in a cloud-resolving model, *Atmospheric Chemistry and Physics Discussions*, *4*, 753–803.
- Eliason, T. L., J. B. Gilman, and V. Vaida (2004), Oxidation of organic films relevant to atmospheric aerosols, *Atmospheric Environment*, *38*(9), 1367–1378.
- Emanuel, K. A. (1981), A similarity theory for unsaturated downdrafts within clouds, *Journal of the Atmospheric Sciences*, *38*(8), 1541–1557.
- Emanuel, K. A. (1991), A scheme for representing cumulus convection in large-scale models, *Journal of the Atmospheric Sciences*, *48*(21), 2313–2335.
- Emanuel, K. A. (1994), *Atmospheric Convection*, 580 pp., Oxford University Press, New York.
- Emanuel, K. A., and M. Bister (1996), Moist convective velocity and buoyancy scales, *Journal of the Atmospheric Sciences*, *53*(22), 3276–3285.

- Emanuel, K. A., and M. Zivkovic-Rothman (1999), Development and evaluation of a convection scheme for use in climate models, *Journal of the Atmospheric Sciences*, *56*(11), 1766–1782.
- Facchini, M. C., M. Mircea, S. Fuzzi, and R. J. Charlson (1999), Cloud albedo enhancement by surface-active organic solutes in growing droplets, *Nature*, *401*(6750), 257–259.
- Facchini, M. C., M. Mircea, S. Fuzzi, and R. J. Charlson (2001), Comments on “Influence of soluble surfactant properties on the activation of aerosol particles containing inorganic solute”, *Journal of the Atmospheric Sciences*, *58*(11), 1465–1467.
- Fassi-Fihri, A., K. Suhre, and R. Rosset (1997), Internal and external mixing in atmospheric aerosols by coagulation: Impact on the optical and hygroscopic properties of the sulphate-soot system, *Atmospheric Environment*, *31*(10), 1393–1402.
- Feingold, G., and P. Y. Chuang (2002a), Analysis of the influence of film-forming compounds on droplet growth: Implications for cloud microphysical processes and climate, *Journal of the Atmospheric Sciences*, *59*(12), 2006–2018.
- Feingold, G., and P. Y. Chuang (2002b), Organic films in clouds, *Bulletin of the American Meteorological Society*, *83*(8), 1137–1137.
- Feingold, G., and S. Kreidenweis (2000), Does cloud processing of aerosol enhance droplet concentrations?, *Journal of Geophysical Research*, *105*(D19), 24,351–24,361.
- Fernandez-Diaz, J. M., M. A. R. Brana, B. A. Garcia, C. G. P. Muniz, and P. J. G. Nieto (1999), The goodness of the internally mixed aerosol assumption under condensation-evaporation, *Aerosol Science and Technology*, *31*(1), 17–23.
- Ferron, G. A., and S. C. Soderholm (1990), Estimation of the times for evaporation of pure water droplets and for stabilization of salt solution particles, *Journal of Aerosol Science*, *21*(3), 415–429.
- Fick, A. E. (1855), *Ann. Phys. Lpz.*, *170*, 59.
- Fitzgerald, J. (1991), Marine aerosols: A review, *Atmospheric Environment*, *25A*, 533–545.
- Fitzgerald, J. W., and P. A. Spyers-Duran (1973), Changes in cloud nucleus concentration and cloud droplet size distribution associated with pollution from St. Louis, *Journal of Applied Meteorology*, *12*, 511–516.

- Fitzgerald, J. W., W. A. Hoppel, and F. Gelbard (1998), A one-dimensional sectional model to simulate multicomponent aerosol dynamics in the marine boundary layer - 1. model description, *Journal of Geophysical Research*, *103*(D13), 16,085–16,102.
- Fletcher, N. (1976), *The Physics of Rainclouds*, 386 pp., Cambridge University Press, Cambridge.
- Flossmann, A. I. (1993), The effect of the impaction scavenging efficiency on the wet deposition by a convective warm cloud, *Tellus*, *45B*(1), 34–39.
- Flossmann, A. I., and H. R. Pruppacher (1988), A theoretical-study of the wet removal of atmospheric pollutants - 3. the uptake, redistribution, and deposition of $(\text{NH}_4)_2\text{SO}_4$ particles by a convective cloud using a two-dimensional cloud dynamics model, *Journal of the Atmospheric Sciences*, *45*(13), 1857–1871.
- Flossmann, A. I., W. D. Hall, and H. R. Pruppacher (1985), A theoretical-study of the wet removal of atmospheric pollutants - 1. the redistribution of aerosol-particles captured through nucleation and impaction scavenging by growing cloud drops, *Journal of the Atmospheric Sciences*, *42*(6), 583–606.
- Flossmann, A. I., H. R. Pruppacher, and J. H. Topalian (1987), A theoretical-study of the wet removal of atmospheric pollutants - 2. the uptake and redistribution of $(\text{NH}_4)_2\text{SO}_4$ particles and SO_2 gas simultaneously scavenged by growing cloud drops, *Journal of the Atmospheric Sciences*, *44*(20), 2912–2923.
- Fouquart, Y., and B. Bonnel (1980), Computations of solar heating of the Earth’s atmosphere: a new parameterization, *Beitr. Phys. Atmos*, *53*, 35–62.
- Frederick, J. E., and C. Erlick (1995), Trends and interannual variations in erythemal sunlight, 1978-1993, *Photochemistry and Photobiology*, *62*(3), 476–484.
- Frolov, Y. G. (1981), Elements of the theory for mixed isoactive electrolyte solutions, *Uspekhi Khimii*, *50*(3), 429–459.
- Fuchs, N. A. (1964), *The Mechanics of Aerosols*, 408 pp., Dover Publications, Inc., New York.
- Gaffney, J. S., and N. A. Marley (1998), New directions - uncertainties of aerosol effects in global climate models, *Atmospheric Environment*, *32*(16), 2873–2874.
- Gardner, R. M., K. Adams, T. Cook, F. Deidewig, S. Ernedal, R. Falk, E. Fleuti, E. Herms, C. E. Johnson, M. Lecht, D. S. Lee, M. Leech, D. Lister, B. Masse, M. Metcalfe, P. Newton,

- A. Schmitt, C. Vandenberg, and R. VanDrimmelen (1997), The ANCAT/EC global inventory of NO_x emissions from aircraft, *Atmospheric Environment*, *31*(12), 1751–1766.
- Gaydos, T. M., B. Koo, S. N. Pandis, and D. P. Chock (2003), Development and application of an efficient moving sectional approach for the solution of the atmospheric aerosol condensation/evaporation equations, *Atmospheric Environment*, *37*(23), 3303–3316.
- Gear, C. (1971), *Numerical Initial Value Problems in Ordinary Differential Equations*, Prentice-Hall series in automatic computation, 253 pp., Prentice-Hall, Englewood Cliffs, NJ.
- Gelbard, F., and J. H. Seinfeld (1980), Simulation of multicomponent aerosol dynamics, *Journal of Colloid and Interface Science*, *78*(2), 485–501.
- Gelbard, F., Y. Tambour, and J. H. Seinfeld (1980), Sectional representations for simulating aerosol dynamics, *Journal of Colloid and Interface Science*, *76*(2), 541–556.
- Ghan, S. J., C. C. Chuang, and J. E. Penner (1993), A parameterization of cloud droplet nucleation - part I: Single aerosol type, *Atmospheric Research*, *12*(4), 198–221.
- Ghan, S. J., C. C. Chuang, and J. E. Penner (1995), A parameterization of cloud droplet nucleation - part II: Multiple aerosol types, *Atmospheric Research*, *36*(1-2), 39–54.
- Ghan, S. J., L. R. Leung, R. C. Easter, and K. Abdul-Razzak (1997), Prediction of cloud droplet number in a general circulation model, *Journal of Geophysical Research*, *102*(D18), 21,777–21,794.
- Ghan, S. J., G. Guzman, and H. Abdul-Razzak (1998), Competition between sea salt and sulfate particles as cloud condensation nuclei, *Journal of the Atmospheric Sciences*, *55*(22), 3340–3347.
- Gillani, N. V., P. H. Daum, S. E. Schwartz, W. R. Leitch, J. W. Strapp, and G. A. Isaac (1992), Fractional activation of accumulation-mode particles in warm continental stratiform clouds, in *Precipitation, Scavenging, and Atmosphere-Surface Exchange*, vol. 1, edited by S. E. Schwartz and W. G. N. Slinn, Hemisphere Publishing Corporation, Washington, D.C.
- Gillani, N. V., S. E. Schwartz, W. R. Leitch, J. W. Strapp, and G. A. Isaac (1995), Field observations in continental stratiform clouds - partitioning of cloud particles between droplets and unactivated interstitial aerosols, *Journal of Geophysical Research*, *100*(D9), 18,687–18,706.
- Gorbunov, B. (1999), Free energy of embryo formation for heterogeneous multicomponent nucleation, *Journal of Chemical Physics*, *110*(20), 10,035–10,045.

- Gorbunov, B., and R. Hamilton (1996), Water nucleation on aerosol particles containing both soluble and insoluble substances, in *Nucleation and Atmospheric Aerosols, 1996*, edited by M. Kulmala and P. E. Wagner, Elsevier Science Limited, Oxford.
- Gorbunov, B., and R. Hamilton (1997), Water nucleation on aerosol particles containing both soluble and insoluble substances, *Journal of Aerosol Science*, 28(2), 239–248.
- Gorbunov, B., R. Hamilton, N. Clegg, and R. Toumi (1998), Water nucleation on aerosol particles containing both organic and soluble inorganic substances, *Atmospheric Research*, 47-48, 271–283.
- Grandpeix, J., V. Phillips, and R. Tailleux (2004), Improving mixing representation in Emanuel’s convective scheme, *Quarterly Journal of the Royal Meteorological Society*, Submitted.
- Grassian, V. H. (2002), Chemical reactions of nitrogen oxides on the surface of oxide, carbonate, soot, and mineral dust particles: Implications for the chemical balance of the troposphere, *Journal of Physical Chemistry A*, 106(6), 860–877.
- Guazzotti, S. A., K. R. Coffee, and K. A. Prather (2001), Continuous measurements of size-resolved particle chemistry during INDOEX - Intensive Field Phase 99, *Journal of Geophysical Research*, 106(D22), 28,607–28,627.
- Guggenheim, E. A., and N. K. Adam (1933), The thermodynamics of adsorption at the surface of solutions, *Proceedings of the Royal Society (London)*, 139(837), 218–236.
- Gultepe, I., and G. A. Isaac (1999), Scale effects on averaging of cloud droplet and aerosol number concentrations: Observations and models, *Journal of Climate*, 12(5), 1268–1279.
- Hallett, J., J. G. Hudson, and C. F. Rogers (1989), Characterization of combustion aerosols for haze and cloud formation, *Aerosol Science and Technology*, 10(1), 70–83.
- Han, Q. Y., W. B. Rossow, and A. A. Lacis (1994), Near-global survey of effective droplet radii in liquid water clouds using ISCCP data, *Journal of Climate*, 7(4), 465–497.
- Hänel, G. (1970), The size of atmospheric aerosol particles as a function of the relative humidity, *Beitrage zur Physik der Atmosphäre*, 43, 119–132.
- Hänel, G. (1976), The properties of atmospheric aerosol particles as functions of the relative humidity at thermodynamic equilibrium with the surrounding moist air, *Advances in Geophysics*, 19, 73–188.

- Hansen, J., M. Sato, and R. Ruedy (1997), Radiative forcing and climate response, *Journal of Geophysical Research*, *102*(D6), 6831–6864.
- Hara, K., S. Yamagata, T. Yamanouchi, K. Sato, A. Herber, Y. Iwasaka, M. Nagatani, and H. Nakata (2003), Mixing states of individual aerosol particles in spring Arctic troposphere during ASTAR 2000 campaign, *Journal of Geophysical Research*, *108*(D7), 4209, doi: 10.1029/2002JD002513.
- Hartmann, D. L. (1994), *Global Physical Climatology*, 408 pp., Academic Press, San Diego.
- Hartmann, D. L., M. E. Ockert-Bell, and M. L. Michelsen (1993), The effect of cloud type on Earth’s energy balance: global analysis, *Journal of Climate*, *5*(11), 1281–1304.
- Hasegawa, S., and S. Ohta (2002), Some measurements of the mixing state of soot-containing particles at urban and non-urban sites, *Atmospheric Environment*, *36*(24), 3899–3908.
- Haywood, J., and O. Boucher (2000), Estimates of the direct and indirect radiative forcing due to tropospheric aerosols: A review, *Reviews of Geophysics*, *38*(4), 513–543.
- Haywood, J. M., and K. P. Shine (1995), The effect of anthropogenic sulfate and soot aerosol on the clear-sky planetary radiation budget, *Geophysical Research Letters*, *22*(5), 603–606.
- Hegg, D. A. (1990), Heterogeneous production of cloud condensation nuclei in the marine atmosphere, *Geophysical Research Letters*, *17*(12), 2165–2168.
- Hegg, D. A. (1994), Cloud condensation nucleus sulfate mass relationship and cloud albedo, *Journal of Geophysical Research*, *99*(D12), 25,903–25,907.
- Heintzenberg, J. (1989), Fine particles in the global troposphere: A review, *Tellus*, *41B*(2), 149–160.
- Heintzenberg, J., D. C. Covert, and R. Van Dingenen (2000), Size distribution and chemical composition of marine aerosols: a compilation and review, *Tellus*, *52B*(4), 1104–1122.
- Herrmann, H., B. Ervens, H. W. Jacobi, R. Wolke, P. Nowacki, and R. Zellner (2000), CAPRAM2.3: A chemical aqueous phase radical mechanism for tropospheric chemistry, *Journal of Atmospheric Chemistry*, *36*(3), 231–284.
- Hindmarsh, A., and K. Radhakrishnan (1993), Description and use of LSODE, the Livermore Solver for Ordinary Differential Equations., *Technical Report UCRL-ID-113855*, Lawrence Livermore National Laboratory.

- Hobbs, P., P. Russell, and L. Stowe (1996), Tropospheric aerosol radiative forcing observational experiment (TARFOX), in *Atmospheric aerosols: a new focus of the International Global Atmospheric Chemistry Project*, MIT Press, Cambridge, MA.
- Hobbs, P. V. (1993), Aerosol-cloud interactions, in *Aerosol-Cloud-Climate Interactions*, edited by P. V. Hobbs, International Geophysics Series, pp. 33–72, Academic Press, San Diego.
- Hobbs, P. V., J. S. Reid, R. A. Kotchenruther, R. J. Ferek, and R. Weiss (1997), Direct radiative forcing by smoke from biomass burning, *Science*, *275*(5307), 1776–1778.
- Hogan, T., J. Goerss, and R. Pauley (2001), A brief description of the emanuel convection parameterization in NOGAPS and its impact, *Tech. rep.*, Naval Research Laboratory.
- Hoppel, W. A., G. M. Frick, and R. E. Larson (1986), Effect of nonprecipitating clouds on the aerosol size distribution in the marine boundary-layer, *Geophysical Research Letters*, *13*(2), 125–128.
- Hoppel, W. A., J. W. Fitzgerald, G. M. Frick, R. E. Larson, and E. J. Mack (1990), Aerosol size distributions and optical-properties found in the marine boundary-layer over the Atlantic Ocean, *Journal of Geophysical Research*, *95*(D4), 3659–3686.
- Hori, M., S. Ohta, N. Murao, and S. Yamagata (2003), Activation capability of water soluble organic substances as CCN, *Journal of Aerosol Science*, *34*(4), 419–448.
- Houghton, J., Y. Ding, D. Griggs, M. Noguera, P. van der Linden, X. Dai, K. Maskell, and C. Johnson (Eds.) (2001), *Climate Change 2001: The Scientific Basis. Contribution of Working Group I to the Third Assessment Report of the Intergovernmental Panel on Climate Change*, 881 pp., Cambridge University Press, Cambridge, U.K.
- Houze, R. (1993), *Cloud Dynamics*, 573 pp., Academic Press, San Diego.
- Hudson, J. G., and Y. H. Xie (1999), Vertical distributions of cloud condensation nuclei spectra over the summertime northeast Pacific and Atlantic Oceans, *Journal of Geophysical Research*, *104*(D23), 30,219–30,229.
- Hudson, J. G., and S. S. Yum (2001), Maritime-continental drizzle contrasts in small cumuli, *Journal of the Atmospheric Sciences*, *58*(8), 915–926.

- Hudson, J. G., and S. S. Yum (2002), Cloud condensation nuclei spectra and polluted and clean clouds over the Indian Ocean, *Journal of Geophysical Research*, *107*(D19), 8022, doi: 10.1029/2001JD000829.
- Huebert, B. J., and R. J. Charlson (2000), Uncertainties in data on organic aerosols, *Tellus*, *52B*(5), 1249–1255.
- Ito, A., and J. E. Penner (2004), Global estimates of biomass burning emissions based on satellite imagery for the year 2000, *Journal of Geophysical Research*, *109*(D14), D14S05, doi: 10.1029/2003JD004423.
- Jacob, D. J. (1986), Chemistry of OH in remote clouds and its role in the production of formic-acid and peroxymonosulfate, *Journal of Geophysical Research*, *91*(D9), 9807–9826.
- Jacob, D. J. (2000), Heterogeneous chemistry and tropospheric ozone, *Atmospheric Environment*, *34*(12-14), 2131–2159.
- Jacobson, M. Z. (1997a), Development and application of a new air pollution modeling system - part II. aerosol module structure and design, *Atmospheric Environment*, *31*(2), 131–144.
- Jacobson, M. Z. (1997b), Development and application of a new air pollution modeling system - part III: Aerosol-phase simulations, *Atmospheric Environment*, *31*(4), 587–608.
- Jacobson, M. Z. (1997c), Numerical techniques to solve condensational and dissolutional growth equations when growth is coupled to reversible reactions, *Aerosol Science and Technology*, *27*(4), 491–498.
- Jacobson, M. Z. (1998), Studying the effects of aerosols on vertical photolysis rate coefficient and temperature profiles over an urban airshed, *Journal of Geophysical Research*, *103*(D9), 10,593–10,604.
- Jacobson, M. Z. (1999), *Fundamentals of Atmospheric Modeling*, 656 pp., Cambridge University Press, Cambridge, England.
- Jacobson, M. Z. (2001a), Strong radiative heating due to the mixing state of black carbon in atmospheric aerosols, *Nature*, *409*(6821), 695–697.
- Jacobson, M. Z. (2001b), Global direct radiative forcing due to multicomponent anthropogenic and natural aerosols, *Journal of Geophysical Research*, *106*(D2), 1551–1568.

- Jacobson, M. Z. (2002), Analysis of aerosol interactions with numerical techniques for solving coagulation, nucleation, condensation, dissolution, and reversible chemistry among multiple size distributions, *Journal of Geophysical Research*, *107*(D19), 4366, doi:10.1029/2001JD002044.
- Jacobson, M. Z. (2003), Development of mixed-phase clouds from multiple aerosol size distributions and the effect of the clouds on aerosol removal, *Journal of Geophysical Research*, *108*(D8), 4245, doi:10.1029/2002JD002691.
- Jacobson, M. Z., and R. P. Turco (1994), SMVGEAR: a sparse-matrix, vectorized Gear code for atmospheric models, *Atmospheric Environment*, *28*(2), 273–284.
- Jacobson, M. Z., and R. P. Turco (1995), Simulating condensational growth, evaporation, and coagulation of aerosols using a combined moving and stationary size grid, *Aerosol Science and Technology*, *22*(1), 73–92.
- Jacobson, M. Z., R. P. Turco, E. J. Jensen, and O. B. Toon (1994), Modeling coagulation among particles of different composition and size, *Atmospheric Environment*, *28*(7), 1327–1338.
- Jacobson, M. Z., R. Lu, and R. P. Turco (1996a), Development and application of a new air pollution modeling system - part I: Gas-phase simulations, *Atmospheric Environment*, *30*(12), 1939–1963.
- Jacobson, M. Z., A. Tabazadeh, and R. P. Turco (1996b), Simulating equilibrium within aerosols and nonequilibrium between gases and aerosols, *Journal of Geophysical Research*, *101*(D4), 9079–9091.
- Jaenicke, R. (1992), Vertical distribution of atmospheric aerosols, in *Nucleation and Atmospheric Aerosols*, edited by N. Fukuta and P. Wagner, pp. 417–425, A. DEEPAK Publishing.
- Jaenicke, R. (1993), Tropospheric aerosols, in *Aerosol-Cloud-Climate Interactions*, edited by P. V. Hobbs, International Geophysics Series, pp. 1–31, Academic Press, San Diego.
- Jang, M., R. M. Kamens, K. B. Leach, and M. R. Strommen (1997), A thermodynamic approach using group contribution methods to model the partitioning of semivolatile organic compounds on atmospheric particulate matter, *Environmental Science & Technology*, *31*(10), 2805–2811.
- Jayne, J. T., D. C. Leard, X. F. Zhang, P. Davidovits, K. A. Smith, C. E. Kolb, and D. R. Worsnop (2000), Development of an aerosol mass spectrometer for size and composition analysis of submicron particles, *Aerosol Science and Technology*, *33*(1-2), 49–70.

- Jensen, J. B., and R. J. Charlson (1984), On the efficiency of nucleation scavenging, *Tellus*, *36B*(5), 367–375.
- Jensen, J. B., P. H. Austin, M. B. Baker, and A. M. Blyth (1985), Turbulent mixing, spectral evolution and dynamics in a warm cumulus cloud, *Journal of the Atmospheric Sciences*, *42*(2), 173–192.
- Jones, A., and A. Slingo (1996), Predicting cloud-droplet effective radius and indirect sulphate aerosol forcing using a general circulation model, *Quarterly Journal of the Royal Meteorological Society*, *122*(535), 1573–1595.
- Jones, A., D. L. Roberts, and A. Slingo (1994), A climate model study of indirect radiative forcing by anthropogenic sulphate aerosols, *Nature*, *370*(6489), 450–452.
- Jorgensen, D. P., and M. A. LeMone (1989), Vertical velocity characteristics of oceanic convection, *Journal of the Atmospheric Sciences*, *46*(5), 621–640.
- Jorgensen, D. P., E. J. Zipser, and M. A. LeMone (1985), Vertical motions in intense hurricanes, *Journal of the Atmospheric Sciences*, *42*(8), 839–856.
- Kain, J. S., and J. M. Fritsch (1990), A one-dimensional entraining detraining plume model and its application in convective parameterization, *Journal of the Atmospheric Sciences*, *47*(23), 2784–2802.
- Katrinak, K. A., P. Rez, and P. R. Buseck (1992), Structural variations in individual carbonaceous particles from an urban aerosol, *Environmental Science & Technology*, *26*(10), 1967–1976.
- Kaufman, Y. J., and R. S. Fraser (1997), The effect of smoke particles on clouds and climate forcing, *Science*, *277*(5332), 1636–1639.
- Kaufman, Y. J., and D. Tanre (1994), Effect of variations in supersaturation on the formation of cloud condensation nuclei, *Nature*, *369*(6475), 45–48.
- Kerminen, V. M. (2001), Relative roles of secondary sulfate and organics in atmospheric cloud condensation nuclei production, *Journal of Geophysical Research*, *106*(D15), 17,321–17,333.
- Kessler, E. (1969), *On the Distribution and Continuity of Water Substance in Atmospheric Circulations*, *Meteorological Monographs*, vol. 32, 84 pp., American Meteorological Society, Boston.

- Khain, A. P., and M. B. Pinsky (1995), Drop inertia and its contribution to turbulent coalescence in convective clouds - 1. drop fall in the flow with random horizontal velocity, *Journal of the Atmospheric Sciences*, 52(2), 196–206.
- Kiehl, J. T., and B. P. Briegleb (1993), The relative roles of sulfate aerosols and greenhouse gases in climate forcing, *Science*, 260(5106), 311–314.
- Kim, Y. P., and J. H. Seinfeld (1995), Atmospheric gas-aerosol equilibrium III - thermodynamics of crustal elements Ca^{2+} , K^+ , and Mg^{2+} , *Aerosol Science and Technology*, 22(1), 93–110.
- Kim, Y. P., J. H. Seinfeld, and P. Saxena (1993a), Atmospheric gas aerosol equilibrium I - thermodynamic model, *Aerosol Science and Technology*, 19(2), 157–181.
- Kim, Y. P., J. H. Seinfeld, and P. Saxena (1993b), Atmospheric gas-aerosol equilibrium II - analysis of common approximations and activity-coefficient calculation methods, *Aerosol Science and Technology*, 19(2), 182–198.
- King, M. D., L. F. Radke, and P. V. Hobbs (1993), Optical-properties of marine stratocumulus clouds modified by ships, *Journal of Geophysical Research*, 98(D2), 2729–2739.
- Kirchner, U., V. Scheer, and R. Vogt (2000), FTIR spectroscopic investigation of the mechanism and kinetics of the heterogeneous reactions of NO_2 and HNO_3 with soot, *Journal of Physical Chemistry A*, 104(39), 8908–8915.
- Kleeman, M. J., G. R. Cass, and A. Eldering (1997), Modeling the airborne particle complex as a source-oriented external mixture, *Journal of Geophysical Research*, 102(D17), 21,355–21,372.
- Knopf, D. A., B. P. Luo, U. K. Krieger, and T. Koop (2003), Thermodynamic dissociation constant of the bisulfate ion from Raman and ion interaction modeling studies of aqueous sulfuric acid at low temperatures, *Journal of Physical Chemistry A*, 107(21), 4322–4332.
- Köhler, H. (1936), The nucleus in and the growth of hygroscopic droplets, *Transactions of the Faraday Society*, 32, 1152–1161.
- Koo, B. Y., A. S. Ansari, and S. N. Pandis (2003), Integrated approaches to modeling the organic and inorganic atmospheric aerosol components, *Atmospheric Environment*, 37(34), 4757–4768.
- Koren, I., Y. J. Kaufman, L. A. Remer, and J. V. Martins (2004), Measurement of the effect of Amazon smoke on inhibition of cloud formation, *Science*, 303(5662), 1342–1345.

- Kotzick, R., and R. Niessner (1999), The effects of aging processes on critical supersaturation ratios of ultrafine carbon aerosols, *Atmospheric Environment*, *33*(17), 2669–2677.
- Kotzick, R., U. Panne, and R. Niessner (1997), Changes in condensation properties of ultrafine carbon particles subjected to oxidation by ozone, *Journal of Aerosol Science*, *28*(5), 725–735.
- Kuba, N., H. Iwabuchi, K. Maruyama, T. Hayasaka, T. Takeda, and T. Fujiyoshi (2003), Parameterization of the effect of cloud condensation nuclei on optical properties of a non-precipitating water layer cloud, *Journal of the Meteorological Society of Japan*, *81*(2), 393–414.
- Kulmala, M., A. Laaksonen, P. Korhonen, T. Vesala, T. Ahonen, and J. C. Barrett (1993), The effect of atmospheric nitric-acid vapor on cloud condensation nucleus activation, *Journal of Geophysical Research*, *98*(D12), 22,949–22,958.
- Kusik, C., and H. Meissner (1978), Electrolyte activity coefficients in inorganic processing, in *Fundamental Aspects of Hydrometallurgical Processes*, *AIChE Symposium Series*, vol. 173, edited by T. Chapman, L. Taularides, G. Hubred, and R. Wellek, pp. 14–20, AIChE, New York.
- Laaksonen, A., P. Korhonen, M. Kulmala, and R. J. Charlson (1998), Modification of the Köhler equation to include soluble trace gases and slightly soluble substances, *Journal of the Atmospheric Sciences*, *55*(5), 853–862.
- Lammel, G., and T. Novakov (1995), Water nucleation properties of carbon-black and diesel soot particles, *Atmospheric Environment*, *29*(7), 813–823.
- Langmuir, I. (1918a), *Physical Review*, *12*, 368.
- Langmuir, I. (1918b), The adsorption of gases on plane surfaces of glass, mica and platinum, *Journal of the American Chemical Society*, *40*, 1361–1403.
- Lary, D. J., D. E. Shallcross, and R. Toumi (1999), Carbonaceous aerosols and their potential role in atmospheric chemistry, *Journal of Geophysical Research*, *104*(D13), 15,929–15,940.
- Leaitch, W. R., G. A. Isaac, J. W. Strapp, C. M. Banic, and H. A. Wiebe (1992), The relationship between cloud droplet number concentrations and anthropogenic pollution - observations and climatic implications, *Journal of Geophysical Research*, *97*(D2), 2463–2474.
- Lelieveld, J., and P. J. Crutzen (1991), The role of clouds in tropospheric photochemistry, *Journal of Atmospheric Chemistry*, *12*(3), 229–267.

- LeMone, M. A., and E. J. Zipser (1980), Cumulonimbus vertical velocity events in GATE - 1. diameter, intensity and mass flux, *Journal of the Atmospheric Sciences*, *37*(11), 2444–2457.
- Leriche, M., D. Voisin, N. Chaumerliac, A. Monod, and B. Aumont (2000), A model for tropospheric multiphase chemistry: application to one cloudy event during the CIME experiment, *Atmospheric Environment*, *34*(29-30), 5015–5036.
- Li, J., J. R. Anderson, and P. R. Buseck (2003a), TEM study of aerosol particles from clean and polluted marine boundary layers over the North Atlantic, *Journal of Geophysical Research*, *108*(D6), 4189, doi:10.1029/2002JD002106.
- Li, J., M. Psfai, P. V. Hobbs, and P. R. Buseck (2003b), Individual aerosol particles from biomass burning in southern Africa: 2, compositions and aging of inorganic particles, *Journal of Geophysical Research*, *108*(D13), 8484, doi:10.1029/2002JD002310.
- Li, Y. Q., P. Davidovits, Q. Shi, J. T. Jayne, C. E. Kolb, and D. R. Worsnop (2001), Mass and thermal accommodation coefficients of $\text{H}_2\text{O}(g)$ on liquid water as a function of temperature, *Journal of Physical Chemistry A*, *105*(47), 10,627–10,634.
- Li, Z. B., and B. C. Y. Lu (2001), Surface tension of aqueous electrolyte solutions at high concentrations - representation and prediction, *Chemical Engineering Science*, *56*(8), 2879–2888.
- Li, Z. B., Y. G. Li, and J. F. Lu (1999), Surface tension model for concentrated electrolyte aqueous solutions by the Pitzer equation, *Industrial & Engineering Chemistry Research*, *38*(3), 1133–1139.
- Li, Z. D., A. L. Williams, and M. J. Rood (1998), Influence of soluble surfactant properties on the activation of aerosol particles containing inorganic solute, *Journal of the Atmospheric Sciences*, *55*(10), 1859–1866.
- Liao, H., and J. H. Seinfeld (1998), Effect of clouds on direct aerosol radiative forcing of climate, *Journal of Geophysical Research*, *103*(D4), 3781–3788.
- Liao, H., Y. L. Yung, and J. H. Seinfeld (1999), Effects of aerosols on tropospheric photolysis rates in clear and cloudy atmospheres, *Journal of Geophysical Research*, *104*(D19), 23,697–23,707.
- Linke, W. F., and S. Atherton (1965), *Solubilities: Inorganic and Metal-Organic Compounds*, 4th ed., 1914 pp., American Chemical Society, Washington D.C.

- Liousse, C., H. Cachier, and S. G. Jennings (1993), Optical and thermal measurements of black carbon aerosol content in different environments - variation of the specific attenuation cross-section, *Atmospheric Environment*, 27A(8), 1203–1211.
- List, R. J. (1984), *Smithsonian Meteorological Tables*, 6th ed., 527 pp., Smithsonian Institution Press, Washington, DC.
- Liu, X. H., and W. Seidl (1998), Modeling study of cloud droplet nucleation and in-cloud sulfate production during the Sanitation of the Atmosphere (SANA) 2 campaign, *Journal of Geophysical Research*, 103(D13), 16,145–16,158.
- Lobo, V. M. M. (1989), *Handbook of Electrolyte Solutions, Physical Sciences Data*, vol. 41, 1168 pp., Elsevier Science Publishing Company, Inc., New York.
- Loehe, J. R., and M. D. Donohue (1997), Recent advances in modeling thermodynamic properties of aqueous strong electrolyte systems, *AIChE Journal*, 43(1), 180–195.
- Lohmann, U., and J. Feichter (1997), Impact of sulfate aerosols on albedo and lifetime of clouds: A sensitivity study with the ECHAM4 GCM, *Journal of Geophysical Research*, 102(D12), 13,685–13,700.
- Lohmann, U., and J. Feichter (2001), Can the direct and semi-direct aerosol effect compete with the indirect effect on a global scale?, *Geophysical Research Letters*, 28(1), 159–161.
- Lohmann, U., and G. Lesins (2002), Stronger constraints on the anthropogenic indirect aerosol effect, *Science*, 298(5595), 1012–1015.
- Lohmann, U., J. Feichter, C. C. Chuang, and J. E. Penner (1999a), Prediction of the number of cloud droplets in the ECHAM GCM, *Journal of Geophysical Research*, 104(D8), 9169–9198.
- Lohmann, U., J. Feichter, C. C. Chuang, and J. E. Penner (1999b), Prediction of the number of cloud droplets in the ECHAM GCM (vol 104, pg 9169, 1999), *Journal of Geophysical Research*, 104(D20), 24,557–24,563.
- Lohmann, U., J. Feichter, J. Penner, and R. Leaitch (2000), Indirect effect of sulfate and carbonaceous aerosols: A mechanistic treatment, *Journal of Geophysical Research*, 105(D10), 12,193–12,206.

- Lohmann, U., K. Broekhuizen, R. Leaitch, N. Shantz, and J. Abbatt (2004), How efficient is cloud droplet formation of organic aerosols?, *Geophysical Research Letters*, *31*(5), L05108, doi: 10.1029/2003GL018999.
- Lucas, C., E. J. Zipser, and M. A. LeMone (1994), Vertical velocity in oceanic convection off tropical Australia, *Journal of the Atmospheric Sciences*, *51*(21), 3183–3193.
- Lucas, D. D. (1999), Process model studies of the atmospheric dimethyl sulfide cycle, Thesis proposal, Massachusetts Institute of Technology.
- Lucas, D. D. (2003), Mechanistic, sensitivity, and uncertainty studies of the atmospheric oxidation of dimethylsulfide, Ph.D, Massachusetts Institute of Technology.
- Lurmann, F. W., A. S. Wexler, S. N. Pandis, S. Musarra, N. Kumar, and J. H. Seinfeld (1997), Modelling urban and regional aerosols II - application to California's south coast air basin, *Atmospheric Environment*, *31*(17), 2695–2715.
- Madronich, S., and J. Calvert (1990), NCAR master mechanism of the gas phase chemistry-version 2.0, *NCAR Technical Note TN-333 + SRT*, National Center for Atmospheric Research.
- Mahowald, N. M., P. J. Rasch, and R. G. Prinn (1995), Cumulus parameterizations in chemical transport models, *Journal of Geophysical Research*, *100*(D12), 26,173–26,189.
- Mallet, M., J. C. Roger, S. Despiaud, J. P. Putaud, and O. Dubovik (2004), A study of the mixing state of black carbon in urban zone, *Journal of Geophysical Research*, *109*(D4), D04202, doi: 10.1029/2003JD003940.
- Marshall, J. S., and W. M. Palmer (1948), The distribution of raindrops with size, *Journal of Meteorology*, *5*, 165–166.
- Martin, G. M., D. W. Johnson, and A. Spice (1994), The measurement and parameterization of effective radius of droplets in warm stratocumulus clouds, *Journal of the Atmospheric Sciences*, *51*(13), 1823–1842.
- Matthews, W. H. (Ed.) (1970), *Man's impact on the global environment; assessment and recommendations for action; report of the Study of Critical Environmental Problems (SCEP)*, 319 pp., MIT Press, Cambridge, MA.
- Maxwell, J. (1990), *Scientific Papers of James Clerk Maxwell*, Niven, W.D., Cambridge University Press, Cambridge.

- McQuarrie, D., and J. Simon (1997), *Physical Chemistry: A Molecular Approach*, 1360 pp., University Science Books, Sausalito, CA.
- McRae, G. J., W. R. Goodin, and J. H. Seinfeld (1982), Development of a second generation mathematical model for urban air pollution: I. model formulation, *Atmospheric Environment*, *16*, 679–696.
- Meissner, H. (1980), Prediction of activity coefficients of strong electrolytes in aqueous systems, in *Thermodynamics of Aqueous Systems with Industrial Applications*, edited by S. Newman, pp. 495–511, American Chemical Society, Washington D.C.
- Meissner, H. P., C. L. Kusik, and J. Tester (1972), Activity coefficients of strong electrolytes in aqueous solution – effect of temperature, *AIChE Journal*, *18*(3), 661–662.
- Meng, Z. Y., and J. H. Seinfeld (1996), Time scales to achieve atmospheric gas-aerosol equilibrium for volatile species, *Atmospheric Environment*, *30*(16), 2889–2900.
- Meng, Z. Y., J. H. Seinfeld, P. Saxena, and Y. P. Kim (1995), Atmospheric gas-aerosol equilibrium: IV thermodynamics of carbonates, *Aerosol Science and Technology*, *23*(2), 131–154.
- Meng, Z. Y., D. Dabdub, and J. H. Seinfeld (1998), Size-resolved and chemically resolved model of atmospheric aerosol dynamics, *Journal of Geophysical Research*, *103*(D3), 3419–3435.
- Meszaros, A., and E. Meszaros (1989), Sulfate formation on elemental carbon particles, *Aerosol Science and Technology*, *10*(2), 337–342.
- Middlebrook, A. M., D. S. Thomson, and D. M. Murphy (1997), On the purity of laboratory-generated sulfuric acid droplets and ambient particles studied by laser mass spectrometry, *Aerosol Science and Technology*, *27*(3), 293–307.
- Middlebrook, A. M., D. M. Murphy, and D. S. Thomson (1998), Observations of organic material in individual marine particles at Cape Grim during the First Aerosol Characterization Experiment (ACE 1), *Journal of Geophysical Research*, *103*(D13), 16,475–16,483.
- Miller, R. L., I. Tegen, and J. Perlwitz (2004), Surface radiative forcing by soil dust aerosols and the hydrologic cycle, *Journal of Geophysical Research*, *109*(D4), D04203, doi:10.1029/2003JD004085.
- Ming, Y., and L. M. Russell (2002), Thermodynamic equilibrium of organic-electrolyte mixtures in aerosol particles, *AIChE Journal*, *48*(6), 1331–1348.

- Molina, M., A. Ivanov, S. Trakhtenberg, and L. Molina (2004), Atmospheric evolution of organic aerosols, *Geophysical Research Letters*, (Submitted).
- Moorthi, S., and M. J. Suarez (1992), Relaxed Arakawa-Schubert - a parameterization of moist convection for general-circulation models, *Monthly Weather Review*, *120*(6), 978–1002.
- Morcrette, J. J. (1990), Impact of changes to the radiation transfer parameterizations plus cloud optical-properties in the ECMWF model, *Monthly Weather Review*, *118*(4), 847–873.
- Morcrette, J. J. (1991), Radiation and cloud radiative properties in the European Center for Medium Range Weather Forecasts forecasting system, *Journal of Geophysical Research*, *96*(D5), 9121–9132.
- Moya, M., S. N. Pandis, and M. Z. Jacobson (2002), Is the size distribution of urban aerosols determined by thermodynamic equilibrium? an application to Southern California, *Atmospheric Environment*, *36*(14), 2349–2365.
- Müller, F. (2001), Splitting error estimation for micro-physical-multiphase chemical systems in meso-scale air quality models, *Atmospheric Environment*, *35*(33), 5749–5764.
- Muller, H. (1928), Zur allgemeinen theorie der raschem koagulation. die koagulation von stabchen- und blattchen-oloiden; die theorie beliebig polydisperser system und der stromungskoagulation., *Kolloidbeihfte*, *27*, 223–50.
- Murphy, D. M., D. S. Thomson, A. M. Middlebrook, and M. E. Schein (1998), In situ single-particle characterization at Cape Grim, *Journal of Geophysical Research*, *103*(D13), 16,485–16,491.
- Murthy, A. S. V., and R. S. Nanjundiah (2000), Time-splitting errors in the numerical integration of semilinear systems of ordinary differential equations, *Monthly Weather Review*, *128*(11), 3921–3926.
- Myhre, G., F. Stordal, K. Restad, and I. S. A. Isaksen (1998), Estimation of the direct radiative forcing due to sulfate and soot aerosols, *Tellus*, *50B*(5), 463–477.
- Nath, S. (1999), Surface tension of nonideal binary liquid mixtures as a function of composition, *Journal of Colloid and Interface Science*, *209*(1), 116–122.
- Nenes, A., and J. H. Seinfeld (2003), Parameterization of cloud droplet formation in global climate models, *Journal of Geophysical Research*, *108*(D14), 4415, doi:10.1029/2002JD002911.

- Nenes, A., S. N. Pandis, and C. Pilinis (1998), ISORROPIA: A new thermodynamic equilibrium model for multiphase multicomponent inorganic aerosols, *Aquatic Geochemistry*, *4*(1), 123–152.
- Nenes, A., S. N. Pandis, and C. Pilinis (1999), Continued development and testing of a new thermodynamic aerosol module for urban and regional air quality models, *Atmospheric Environment*, *33*(10), 1553–1560.
- Nenes, A., S. Ghan, H. Abdul-Razzak, P. Y. Chuang, and J. H. Seinfeld (2001), Kinetic limitations on cloud droplet formation and impact on cloud albedo, *Tellus*, *53B*(2), 133–149.
- Nenes, A., R. J. Charlson, M. C. Facchini, M. Kulmala, A. Laaksonen, and J. H. Seinfeld (2002), Can chemical effects on cloud droplet number rival the first indirect effect?, *Geophysical Research Letters*, *29*(17), 1848, doi:10.1029/2002GL015295.
- Noble, C. A., and K. A. Prather (1996), Real-time measurement of correlated size and composition profiles of individual atmospheric aerosol particles, *Environmental Science & Technology*, *30*(9), 2667–2680.
- Noble, C. A., and K. A. Prather (1998), Single particle characterization of albuterol metered dose inhaler aerosol in near real-time, *Aerosol Science and Technology*, *29*(4), 294–306.
- Novakov, T., and J. E. Penner (1993), Large contribution of organic aerosols to cloud-condensation-nuclei concentrations, *Nature*, *365*(6449), 823–826.
- Novakov, T., C. Rivera-Carpio, J. E. Penner, and C. F. Rogers (1994), The effect of anthropogenic sulfate aerosols on marine cloud droplet concentrations, *Tellus*, *46B*(2), 132–141.
- Novakov, T., T. S. Bates, and P. K. Quinn (2000), Shipboard measurements of concentrations and properties of carbonaceous aerosols during ACE-2, *Tellus*, *52B*(2), 228–238.
- O’Dowd, C. D., and M. H. Smith (1993), Physicochemical properties of aerosols over the northeast Atlantic - evidence for wind-speed-related submicron sea-salt aerosol production, *Journal of Geophysical Research*, *98*(D1), 1137–1149.
- O’Dowd, C. D., M. H. Smith, and S. G. Jennings (1993), Submicron particle, radon, and soot carbon characteristics over the northeast Atlantic, *Journal of Geophysical Research*, *98*(D1), 1123–1135.
- O’Dowd, C. D., M. H. Smith, I. E. Consterdine, and J. A. Lowe (1997), Marine aerosol, sea-salt, and the marine sulphur cycle: A short review, *Atmospheric Environment*, *31*(1), 73–80.

- O'Dowd, C. D., J. A. Lowe, M. H. Smith, and A. D. Kaye (1999), The relative importance of non-sea-salt sulphate and sea-salt aerosol to the marine cloud condensation nuclei population: An improved multi-component aerosol-cloud droplet parametrization, *Quarterly Journal of the Royal Meteorological Society*, *125*(556), 1295–1313.
- Okada, K. (1985), Number-size distribution and formation process of submicrometer sulfate-containing particles in the urban atmosphere of Nagoya, *Atmospheric Environment*, *19*(5), 743–757.
- Parungo, F., C. Nagamoto, G. Herbert, J. Harris, R. Schnell, P. Sheridan, and N. Zhang (1993), Individual particle analyses of arctic aerosol samples collected during AGASP-III, *Atmospheric Environment*, *27A*(17-18), 2825–2837.
- Parungo, F., C. Nagamoto, M. Y. Zhou, A. D. A. Hansen, and J. Harris (1994), Aeolian transport of aerosol black carbon from China to the ocean, *Atmospheric Environment*, *28*(20), 3251–3260.
- Patwardhan, V. S., and A. Kumar (1986a), A unified approach for prediction of thermodynamic properties of aqueous mixed-electrolyte solutions - part 1: Vapor-pressure and heat of vaporization, *AIChE Journal*, *32*(9), 1419–1428.
- Patwardhan, V. S., and A. Kumar (1986b), A unified approach for prediction of thermodynamic properties of aqueous mixed-electrolyte solutions - part 2: Volume, thermal, and other properties, *AIChE Journal*, *32*(9), 1429–1438.
- Patwardhan, V. S., and A. Kumar (1993), Thermodynamic properties of aqueous-solutions of mixed electrolytes - a new mixing rule, *AIChE Journal*, *39*(4), 711–714.
- Pauluis, O., and I. M. Held (2002a), Entropy budget of an atmosphere in radiative-convective equilibrium. Part II: Latent heat transport and moist processes, *Journal of the Atmospheric Sciences*, *59*(2), 140–149.
- Pauluis, O., and I. M. Held (2002b), Entropy budget of an atmosphere in radiative-convective equilibrium. Part I: Maximum work and frictional dissipation, *Journal of the Atmospheric Sciences*, *59*(2), 125–139.
- Pauluis, O., V. Balaji, and I. M. Held (2000), Frictional dissipation in a precipitating atmosphere, *Journal of the Atmospheric Sciences*, *57*(7), 989–994.

- Penner, J. E., H. Eddleman, and T. Novakov (1993), Towards the development of a global inventory for black carbon emissions, *Atmospheric Environment*, *27A*(8), 1277–1295.
- Penner, J. E., R. J. Charlson, J. M. Hales, N. S. Laulainen, R. Leifer, T. Novakov, J. Ogren, L. F. Radke, S. E. Schwartz, and L. Travis (1994), Quantifying and minimizing uncertainty of climate forcing by anthropogenic aerosols, *Bulletin of the American Meteorological Society*, *75*(3), 375–400.
- Penner, J. E., C. C. Chuang, and K. Grant (1998), Climate forcing by carbonaceous and sulfate aerosols, *Climate Dynamics*, *14*(12), 839–851.
- Penner, J. E., S. Y. Zhang, and C. C. Chuang (2003), Soot and smoke aerosol may not warm climate, *Journal of Geophysical Research*, *108*(D21), 4657, doi:10.1029/2003JD003409.
- Penner, J. E., X. Q. Dong, and Y. Chen (2004), Observational evidence of a change in radiative forcing due to the indirect aerosol effect, *Nature*, *427*(6971), 231–234.
- Phinney, L. A., U. Lohmann, and W. R. Leaitch (2003), Limitations of using an equilibrium approximation in an aerosol activation parameterization, *Journal of Geophysical Research*, *108*(D12), 4371, doi:10.1029/2002JD002391.
- Pilinis, C., and J. H. Seinfeld (1987), Continued development of a general equilibrium-model for inorganic multicomponent atmospheric aerosols, *Atmospheric Environment*, *21*(11), 2453–2466.
- Pinsky, M., and A. Khain (1995), A model of a homogeneous isotropic turbulent flow and its application for the simulation of cloud drop tracks, *Geophysical and Astrophysical Fluid Dynamics*, *81*(1-2), 33–55.
- Pinsky, M., A. Khain, and M. Shapiro (2000), Stochastic effects of cloud droplet hydrodynamic interaction in a turbulent flow, *Atmospheric Research*, *53*(1-3), 131–169.
- Pinsky, M. B., and A. P. Khain (1996), Simulations of drop fall in a homogeneous isotropic turbulent flow, *Atmospheric Research*, *40*(2-4), 223–259.
- Pinsky, M. B., and A. P. Khain (1997), Turbulence effects on droplet growth and size distribution in clouds - a review, *Journal of Aerosol Science*, *28*(7), 1177–1214.
- Pitzer, K. S. (1973), Thermodynamics of electrolytes. 1. theoretical basis and general equations, *Journal of Physical Chemistry*, *77*(2), 268–277.

- Pitzer, K. S. (1975), Thermodynamics of electrolytes. 5. effects of higher-order electrostatic terms, *Journal of Solution Chemistry*, 4(3), 249–265.
- Pitzer, K. S., and J. J. Kim (1974), Thermodynamics of electrolytes. 4. activity and osmotic coefficients for mixed electrolytes, *Journal of the American Chemical Society*, 96(18), 5701–5707.
- Pitzer, K. S., and G. Mayorga (1973), Thermodynamics of electrolytes. 2. activity and osmotic coefficients for strong electrolytes with one or both ions univalent, *Journal of Physical Chemistry*, 77(19), 2300–2308.
- Pitzer, K. S., and J. M. Simonson (1986), Thermodynamics of multicomponent, miscible, ionic systems - theory and equations, *Journal of Physical Chemistry*, 90(13), 3005–3009.
- Pitzer, K. S., R. N. Roy, and L. F. Silvester (1977), Thermodynamics of electrolytes. 7. sulfuric-acid, *Journal of the American Chemical Society*, 99(15), 4930–4936.
- Podgorny, I. A., W. Conant, V. Ramanathan, and S. K. Satheesh (2000), Aerosol modulation of atmospheric and surface solar heating over the tropical Indian Ocean, *Tellus*, 52B(3), 947–958.
- Pósfai, M., J. R. Anderson, P. R. Buseck, and H. Sievering (1999), Soot and sulfate aerosol particles in the remote marine troposphere, *Journal of Geophysical Research*, 104(D17), 21,685–21,693.
- Pósfai, M., R. Simonics, J. Li, P. V. Hobbs, and P. R. Buseck (2003), Individual aerosol particles from biomass burning in southern Africa: 1. compositions and size distributions of carbonaceous particles, *Journal of Geophysical Research*, 108(D13), 8483, doi:10.1029/2002JD002291.
- Prather, K. A., T. Nordmeyer, and K. Salt (1994), Real-time characterization of individual aerosol-particles using time-of-flight mass-spectrometry, *Analytical Chemistry*, 66(9), 1403–1407.
- Prince, A. P., J. L. Wade, V. H. Grassian, P. D. Kleiber, and M. A. Young (2002), Heterogeneous reactions of soot aerosols with nitrogen dioxide and nitric acid: atmospheric chamber and Knudsen cell studies, *Atmospheric Environment*, 36(36-37), 5729–5740.
- Pruppacher, H. R., and J. D. Klett (1997), *Microphysics of Clouds and Precipitation*, 2nd ed., 954 pp., Kluwer Academic Publishers, Dordrecht.
- Pueschel, R. F., C. C. Vanvalin, R. C. Castillo, J. A. Kadlecsek, and E. Ganor (1986), Aerosols in polluted versus nonpolluted air masses - long-range transport and effects on clouds, *Journal of Climate and Applied Meteorology*, 25(12), 1908–1917.

- Quinn, P. K., T. S. Bates, D. J. Coffman, T. L. Miller, J. E. Johnson, D. S. Covert, J. P. Putaud, C. Neususs, and T. Novakov (2000), A comparison of aerosol chemical and optical properties from the 1st and 2nd Aerosol Characterization Experiments, *Tellus*, *52B*(2), 239–257.
- Raes, F., T. Bates, F. McGovern, and M. Van Liedekerke (2000), The 2nd Aerosol Characterization Experiment (ACE-2): general overview and main results, *Tellus*, *52B*(2), 111–125.
- Ramanathan, V., P. J. Crutzen, J. T. Kiehl, and D. Rosenfeld (2001a), Atmosphere - aerosols, climate, and the hydrological cycle, *Science*, *294*(5549), 2119–2124.
- Ramanathan, V., P. J. Crutzen, J. Lelieveld, A. P. Mitra, D. Althausen, J. Anderson, M. O. Andreae, W. Cantrell, G. R. Cass, C. E. Chung, A. D. Clarke, J. A. Coakley, W. D. Collins, W. C. Conant, F. Dulac, J. Heintzenberg, A. J. Heymsfield, B. Holben, S. Howell, J. Hudson, A. Jayaraman, J. T. Kiehl, T. N. Krishnamurti, D. Lubin, G. McFarquhar, T. Novakov, J. A. Ogren, I. A. Podgorny, K. Prather, K. Priestley, J. M. Prospero, P. K. Quinn, K. Rajeev, P. Rasch, S. Rupert, R. Sadourny, S. K. Satheesh, G. E. Shaw, P. Sheridan, and F. P. J. Valero (2001b), Indian Ocean Experiment: An integrated analysis of the climate forcing and effects of the great Indo-Asian haze, *Journal of Geophysical Research*, *106*(D22), 28,371–28,398.
- Raymond, D. J. (1995), Regulation of moist convection over the west Pacific warm pool, *Journal of the Atmospheric Sciences*, *52*(22), 3945–3959.
- Raymond, D. J., and A. M. Blyth (1986), A stochastic mixing model for nonprecipitating cumulus clouds, *Journal of the Atmospheric Sciences*, *43*(22), 2708–2718.
- Raymond, D. J., and A. M. Blyth (1992), Extension of the stochastic mixing model to cumulonimbus clouds, *Journal of the Atmospheric Sciences*, *49*(21), 1968–1983.
- Raymond, T. M., and S. N. Pandis (2002), Cloud activation of single-component organic aerosol particles, *Journal of Geophysical Research*, *107*(D24), 4787, doi:10.1029/2002JD002159.
- Raymond, T. M., and S. N. Pandis (2003), Formation of cloud droplets by multicomponent organic particles, *Journal of Geophysical Research*, *108*(D15), 4469, doi:10.1029/2003JD003503.
- Rennó, N. O., and A. P. Ingersoll (1996a), Natural convection as a heat engine: A theory for CAPE, *Journal of the Atmospheric Sciences*, *53*(4), 572–585.
- Rennó, N. O., and A. P. Ingersoll (1996b), Natural convection as a heat engine: A theory for CAPE (vol 53, pg 572, 1996), *Journal of the Atmospheric Sciences*, *53*(9), 1355–1355.

- Resch, T. J. (1995), A framework for the modeling of suspended multicomponent particulate systems with applications to atmospheric aerosols, Ph.D., Massachusetts Institute of Technology.
- Rivera-Carpio, C. A., C. E. Corrigan, T. Novakov, J. E. Penner, C. F. Rogers, and J. C. Chow (1996), Derivation of contributions of sulfate and carbonaceous aerosols to cloud condensation nuclei from mass size distributions, *Journal of Geophysical Research*, *101*(D14), 19,483–19,493.
- Robinson, R., and R. Stokes (1959), *Electrolyte solutions, the measurement and interpretation of conductance, chemical potential, and diffusion in solutions of simple electrolytes*, 571 pp., Butterworths, London.
- Roeckner, E., L. Bengtsson, J. Feichter, J. Lelieveld, and H. Rodhe (1999), Transient climate change simulations with a coupled atmosphere-ocean GCM including the tropospheric sulfur cycle, *Journal of Climate*, *12*(10), 3004–3032.
- Rogers, C. F., J. G. Hudson, J. Hallett, and J. E. Penner (1991), Cloud droplet nucleation by crude-oil smoke and coagulated crude-oil wood smoke particles, *Atmospheric Environment*, *25*(11), 2571–2580.
- Rogers, R. R., and M. K. Yau (1989), *A Short Course in Cloud Physics*, 3rd ed., 290 pp., Butterworth-Heinemann, Woburn, MA.
- Rood, M. J., and A. L. Williams (2001), Comments on “influence of soluble surfactant properties on the activation of aerosol particles containing inorganic solute” - reply, *Journal of the Atmospheric Sciences*, *58*(11), 1468–1473.
- Rotstayn, L. D., and J. E. Penner (2001), Indirect aerosol forcing, quasi forcing, and climate response, *Journal of Climate*, *14*(13), 2960–2975.
- Rotstayn, L. D., B. F. Ryan, and J. E. Penner (2000), Precipitation changes in a GCM resulting from the indirect effects of anthropogenic aerosols, *Geophysical Research Letters*, *27*(19), 3045–3048.
- Russell, A. G., G. J. McRae, and G. R. Cass (1983a), Mathematical-modeling of the formation and transport of ammonium-nitrate aerosol, *Atmospheric Environment*, *17*(5), 949–964.
- Russell, A. G., G. J. McRae, and G. R. Cass (1983b), Aerosol nitrate dynamics in an urban basin, *Aerosol Science and Technology*, *2*(2), 179–179.

- Russell, A. G., G. J. McRae, and G. R. Cass (1985), The dynamics of nitric-acid production and the fate of nitrogen-oxides, *Atmospheric Environment*, 19(6), 893–903.
- Russell, L. M., and J. H. Seinfeld (1998), Size- and composition-resolved externally mixed aerosol model, *Aerosol Science and Technology*, 28(5), 403–416.
- Russell, L. M., J. H. Seinfeld, R. C. Flagan, R. J. Ferek, D. A. Hegg, P. V. Hobbs, W. Wobrock, A. I. Flossmann, C. D. O’Dowd, K. E. Nielsen, and P. A. Durkee (1999), Aerosol dynamics in ship tracks, *Journal of Geophysical Research*, 104(D24), 31,077–31,095.
- Russell, L. M., K. J. Noone, R. J. Ferek, R. A. Pockalny, R. C. Flagan, and J. H. Seinfeld (2000), Combustion organic aerosol as cloud condensation nuclei in ship tracks, *Journal of the Atmospheric Sciences*, 57(16), 2591–2606.
- San Martini, F. (2004), Decision support tools for urban air quality management, Ph.D, Massachusetts Institute of Technology.
- Sander, R. (1999), Compilation of Henry’s Law constants for inorganic and organic species of potential importance in environmental chemistry, *Tech. rep.*, Max-Planck Institute of Chemistry.
- Saxena, P., L. M. Hildemann, P. H. McMurry, and J. H. Seinfeld (1995), Organics alter hygroscopic behavior of atmospheric particles, *Journal of Geophysical Research*, 100(D9), 18,755–18,770.
- Schwartz, S. (1986), Mass-transport considerations pertinent to aqueous phase reactions of gases in liquid-water clouds, in *Chemistry of Multiphase Atmospheric Systems*, edited by W. Jaeschke, pp. 415–471, Springer-Verlag, Berlin.
- Schwartz, S. E. (1996), The whitehouse effect - shortwave radiative forcing of climate by anthropogenic aerosols: An overview, *Journal of Aerosol Science*, 27(3), 359–382.
- Schwartz, S. E., and A. Slingo (1996), Enhanced shortwave cloud radiative forcing due to anthropogenic aerosols, in *Clouds, Chemistry and Climate, NATO ASI Series*, vol. 35, edited by P. J. Crutzen and V. Ramanathan, Springer-Verlag, Berlin.
- Scorer, R. (1957), Experiments on convection of isolated masses of buoyant fluid, *Journal of Fluid Mechanics*, 2, 583–594.
- Seigneur, C. (1982), A model of sulfate aerosol dynamics in atmospheric plumes, *Atmospheric Environment*, 16(9), 2207–2228.

- Seigneur, C., A. B. Hudischewskyj, J. H. Seinfeld, K. T. Whitby, E. R. Whitby, J. R. Brock, and H. M. Barnes (1986), Simulation of aerosol dynamics - a comparative review of mathematical models, *Aerosol Science and Technology*, 5(2), 205–222.
- Seinfeld, J. H., and R. H. Flagan (1999), Aerosol-cloud interactions and indirect forcing, *IGACtivities Newsletter*, 17.
- Seinfeld, J. H., and S. N. Pandis (1998), *Atmospheric Chemistry and Physics*, 1326 pp., John Wiley & Sons, Inc., New York.
- Shah, J., and J. Rau (1990), Carbonaceous species methods comparison study, interlaboratory round robin: Interpretation of results., *Tech. Rep. A832-154*, California Air Resources Board.
- Shantz, N. C., W. R. Leaitch, and P. F. Caffrey (2003), Effect of organics of low solubility on the growth rate of cloud droplets, *Journal of Geophysical Research*, 108(D5), 4168, doi: 10.1029/2002JD002540.
- Shi, Q., P. Davidovits, J. T. Jayne, D. R. Worsnop, and C. E. Kolb (1999), Uptake of gas-phase ammonia. 1. uptake by aqueous surfaces as a function of pH, *Journal of Physical Chemistry A*, 103(44), 8812–8823.
- Shulman, M. L., M. C. Jacobson, R. J. Carlson, R. E. Synovec, and T. E. Young (1996), Dissolution behavior and surface tension effects of organic compounds in nucleating cloud droplets, *Geophysical Research Letters*, 23(3), 277–280.
- Skatskii, V. (1965), Some results from experimental study of the liquid water content in cumulus clouds, *Izvestiya, Atmospheric and Oceanic Physics*, 1, 479–487.
- Smith, D. M., and A. R. Chughtai (1995), The surface-structure and reactivity of black carbon, *Colloids and Surfaces*, 105A(1), 47–77.
- Smith, D. M., and A. R. Chughtai (1996), Reaction kinetics of ozone at low concentrations with *n*-hexane soot, *Journal of Geophysical Research*, 101(D14), 19,607–19,620.
- Squires, P. (1958a), Penetrative downdraughts in cumuli, *Tellus*, 10(3), 381–389.
- Squires, P. (1958b), The spatial variation of liquid water and droplet concentration in cumuli, *Tellus*, 10, 372–380.

- Squires, P. (1958c), The microstructure and colloidal stability of warm clouds, II, the causes of the variations in microstructure, *Tellus*, *10*, 262–271.
- Squires, P., and J. Turner (1962), An entraining jet model for cumulonimbus updraughts, *Tellus*, *14*, 422–434.
- Staples, B. R. (1981), Activity and osmotic coefficients of aqueous sulfuric-acid at 298.15-K, *Journal of Physical and Chemical Reference Data*, *10*(3), 779–798.
- Steele, H. D. (2000), The indirect radiative forcing effect of atmospheric aerosols, *Research paper for general examination*, Massachusetts Institute of Technology.
- Steele, H. D., and R. G. Prinn (2002), Modeling the activation of externally mixed inorganic aerosol populations: the effects of competition and its sensitivity to mixing state, *EOS Transactions, American Geophysical Union*, *83*(47), Abstract A61A–0054.
- Steinfeld, J. I., J. S. Francisco, and W. L. Hase (1999), *Chemical Kinetics and Dynamics*, 2nd ed., 518 pp., Prentice Hall, Upper Saddle River, New Jersey.
- Stelson, A., M. Bassett, and J. Seinfeld (1984), Thermodynamic equilibrium properties of aqueous solutions of nitrate, sulfate, and ammonium, in *Chemistry of Particles: Fogs and Rain, Acid Precipitation Series*, vol. 3, Butterworth Publishers, Boston.
- Stelson, A. W., and J. H. Seinfeld (1981), Prediction of the density of ammonium bisulfate solutions, *Journal of Physical Chemistry*, *85*(24), 3730–3733.
- Stelson, A. W., and J. H. Seinfeld (1982a), Thermodynamic prediction of the water activity, NH_4NO_3 dissociation-constant, density and refractive-index for the NH_4NO_3 , $(\text{NH}_4)_2\text{SO}_4$, H_2O system at 25° C, *Atmospheric Environment*, *16*(10), 2507–2514.
- Stelson, A. W., and J. H. Seinfeld (1982b), On the densities of aqueous sulfate-solutions, *Atmospheric Environment*, *16*(2), 355–357.
- Stelson, A. W., S. K. Friedlander, and J. H. Seinfeld (1979), Note on the equilibrium relationship between ammonia and nitric-acid and particulate ammonium-nitrate, *Atmospheric Environment*, *13*(3), 369–371.
- Stockwell, W. R., P. Middleton, J. S. Chang, and X. Y. Tang (1990), The 2nd generation regional acid deposition model chemical mechanism for regional air-quality modeling, *Journal of Geophysical Research*, *95*(D10), 16,343–16,367.

- Stokes, R., and R. Robinson (1966), Interactions in aqueous nonelectrolyte solutions. I. solute-solvent equilibria, *Journal of Physical Chemistry*, *70*, 2126–2130.
- Stommel, H. (1947), Entrainment of air into a cumulus cloud, *Journal of Meteorology*, *4*, 91–94.
- Stommel, H. (1951), Entrainment of air into a cumulus cloud, II, *Journal of Meteorology*, *8*, 127–129.
- Suck, S. H., and J. R. Brock (1979), Evolution of atmospheric aerosol particle size distributions via Brownian coagulation: Numerical simulation, *Journal of Aerosol Science*, *10*, 581–590.
- Sun, Q., and A. S. Wexler (1998a), Modeling urban and regional aerosols - condensation and evaporation near acid neutrality, *Atmospheric Environment*, *32*(20), 3527–3531.
- Sun, Q., and A. S. Wexler (1998b), Modeling urban and regional aerosols near acid neutrality - application to the 24-25 June SCAQS episode, *Atmospheric Environment*, *32*(20), 3533–3545.
- Svenningsson, I. B., H. C. Hansson, A. Wiedensohler, J. A. Ogren, K. J. Noone, and A. Hallberg (1992), Hygroscopic growth of aerosol-particles in the Po Valley, *Tellus*, *44B*(5), 556–569.
- Tabor, K., L. Gutzwiller, and M. J. Rossi (1994), Heterogeneous chemical-kinetics of NO₂ on amorphous-carbon at ambient-temperature, *Journal of Physical Chemistry*, *98*(24), 6172–6186.
- Tang, I. N. (1980), On the equilibrium partial pressures of nitric-acid and ammonia in the atmosphere, *Atmospheric Environment*, *14*(7), 819–828.
- Tang, I. N. (1997), Thermodynamic and optical properties of mixed-salt aerosols of atmospheric importance, *Journal of Geophysical Research*, *102*(D2), 1883–1893.
- Taylor, G. R., and M. B. Baker (1991), Entrainment and detrainment in cumulus clouds, *Journal of the Atmospheric Sciences*, *48*(1), 112–121.
- Tegen, I., P. Hollrig, M. Chin, I. Fung, D. Jacob, and J. Penner (1997), Contribution of different aerosol species to the global aerosol extinction optical thickness: Estimates from model results, *Journal of Geophysical Research*, *102*(D20), 23,895–23,915.
- Telford, J. (1975), Turbulence, entrainment, and mixing in cloud dynamics, *Pure and Applied Geophysics*, *113*, 1067–1084.
- Tester, J., and M. Modell (1997), *Thermodynamics and Its Applications*, 3rd ed., 936 pp., Prentice-Hall.

- Tett, S. F. B., G. S. Jones, P. A. Stott, D. C. Hill, J. F. B. Mitchell, M. R. Allen, W. J. Ingram, T. C. Johns, C. E. Johnson, A. Jones, D. L. Roberts, D. M. H. Sexton, and M. J. Woodage (2002), Estimation of natural and anthropogenic contributions to twentieth century temperature change, *Journal of Geophysical Research*, *107*(D16), 4306, 10.1029/2000JD000,028.
- Toon, O. B. (2000), Atmospheric science - how pollution suppresses rain, *Science*, *287*(5459), 1763.
- Tsang, T. H., and J. R. Brock (1983), Simulation of condensation aerosol growth by condensation and evaporation, *Aerosol Science and Technology*, *2*, 311–320.
- Tsang, T. H., and J. R. Brock (1986), Dynamics of ostwald ripening with coalescence for aerosols with continuum diffusive growth laws, *Aerosol Science and Technology*, *5*, 385–388.
- Turpin, B. J., P. Saxena, and E. Andrews (2000), Measuring and simulating particulate organics in the atmosphere: problems and prospects, *Atmospheric Environment*, *34*(18), 2983–3013.
- Twohy, C. H., and J. G. Hudson (1995), Measurements of cloud condensation nuclei spectra within maritime cumulus cloud droplets - implications for mixing processes, *Journal of Applied Meteorology*, *34*(4), 815–833.
- Twohy, C. H., P. A. Durkee, B. J. Huebert, and R. J. Charlson (1995), Effects of aerosol-particles on the microphysics of coastal stratiform clouds, *Journal of Climate*, *8*(4), 773–783.
- Twohy, C. H., J. G. Hudson, S. S. Yum, J. R. Anderson, S. K. Durlak, and D. Baumgardner (2001), Characteristics of cloud-nucleating aerosols in the Indian Ocean region, *Journal of Geophysical Research*, *106*(D22), 28,699–28,710.
- Twomey, S. (1959), The nuclei of natural cloud formation - II. the supersaturation in natural clouds and the variation of cloud droplet concentrations, *Geofis. Pura Appl.*, *43*, 243–249.
- Twomey, S. (1974), Pollution and the planetary albedo, *Atmospheric Environment*, *33*, 1251–1256.
- Twomey, S. (1977a), *Atmospheric Aerosols*, 302 pp., Elsevier Scientific Publishing Company, Amsterdam.
- Twomey, S. (1977b), The influence of pollution on the shortwave albedo of clouds, *Journal of the Atmospheric Sciences*, *34*, 1149–1152.
- Twomey, S. (1991), Aerosols, clouds and radiation, *Atmospheric Environment*, *25*(11), 2435–2442.

- Twomey, S., and J. Warner (1967), Comparison of measurements of cloud droplets and cloud nuclei, *Journal of the Atmospheric Sciences*, *24*, 702–703.
- Tzivion, S. T., G. Feingold, and Z. Levin (1987), An efficient numerical-solution to the stochastic collection equation, *Journal of the Atmospheric Sciences*, *44*(21), 3139–3149.
- Van Dingenen, R., F. Raes, and N. R. Jensen (1995), Evidence for anthropogenic impact on number concentration and sulfate content of cloud-processed aerosol-particles over the north-Atlantic, *Journal of Geophysical Research*, *100*(D10), 21,057–21,067.
- Vandoren, J. M., L. R. Watson, P. Davidovits, D. R. Worsnop, M. S. Zahniser, and C. E. Kolb (1990), Temperature-dependence of the uptake coefficients of HNO_3 , HCl , and N_2O_5 by water droplets, *Journal of Physical Chemistry*, *94*(8), 3265–3269.
- Varoglu, E., and W. D. L. Finn (1980), Finite-elements incorporating characteristics for one-dimensional diffusion-convection equation, *Journal of Computational Physics*, *34*(3), 371–389.
- Verver, G., F. Raes, D. Voegelezang, and D. Johnson (2000), The 2nd Aerosol Characterization Experiment (ACE-2): meteorological and chemical context, *Tellus*, *52B*(2), 126–140.
- Villars, D. (1959), A method of successive approximations for computing combustion equilibria on a high speed digital computer, *Journal of Physical Chemistry*, *63*, 521–5.
- Wang, C. (2004), A modeling study on the climate impacts of black carbon aerosols, *Journal of Geophysical Research*, *109*(D3), D03106, doi:10.1029/2003JD004084.
- Wang, C., and J. Chang (1993a), A three-dimensional numerical model of cloud dynamics, microphysics, and chemistry - 1: Concepts and formulation, *Journal of Geophysical Research*, *98*(D8), 14,827–14,844.
- Wang, C., and J. Chang (1993b), A three-dimensional numerical model of cloud dynamics, microphysics, and chemistry - 3: Redistribution of pollutants, *Journal of Geophysical Research*, *98*(D9), 16,787–16,798.
- Wang, C., and R. G. Prinn (1998), Impact of the horizontal wind profile on the convective transport of chemical species, *Journal of Geophysical Research*, *103*(D17), 22,063–2071.
- Wang, C., and R. G. Prinn (2000), On the roles of deep convective clouds in tropospheric chemistry, *Journal of Geophysical Research*, *105*(D17), 22,269–22,297.

- Warner, J. (1955), The water content of cumuliform clouds, *Tellus*, 7, 449–457.
- Warner, J. (1969), The microstructure of cumulus cloud, *Journal of the Atmospheric Sciences*, 26, 1272–1282.
- Warner, J. (1970a), The microstructure of cumulus cloud. part III. the nature of the updraft, *Journal of the Atmospheric Sciences*, 27(4), 682–688.
- Warner, J. (1970b), On steady-state one-dimensional models of cumulus convection, *Journal of the Atmospheric Sciences*, 27(4), 1035–1040.
- Warner, J., and P. Squires (1958), Liquid water content and the adiabatic model of cumulus development, *Tellus*, 10, 390–394.
- Warner, J., and S. Twomey (1967), The production of cloud nuclei by cane fires and the effect on cloud droplet concentration, *Journal of the Atmospheric Sciences*, 24, 704–706.
- Warren, D. R., and J. H. Seinfeld (1985), Prediction of aerosol concentrations resulting from a burst of nucleation, *Journal of Colloid and Interface Science*, 105(1), 136–142.
- Weingartner, E., U. Baltensperger, and H. Burtscher (1995), Growth and structural-change of combustion aerosols at high relative-humidity, *Environmental Science & Technology*, 29(12), 2982–2986.
- Weingartner, E., H. Burtscher, and U. Baltensperger (1997), Hygroscopic properties of carbon and diesel soot particles, *Atmospheric Environment*, 31(15), 2311–2327.
- Wexler, A. S., and S. L. Clegg (2002), Atmospheric aerosol models for systems including the ions H^+ , NH_4^+ , Na^+ , SO_4^{2-} , NO_3^- , Cl^- , Br^- , and H_2O , *Journal of Geophysical Research*, 107(D14), 4207, doi:10.1029/2001JD000451.
- Wexler, A. S., and J. H. Seinfeld (1990), The distribution of ammonium-salts among a size and composition dispersed aerosol, *Atmospheric Environment*, 24(5), 1231–1246.
- Wexler, A. S., and J. H. Seinfeld (1991), 2nd-generation inorganic aerosol model, *Atmospheric Environment*, 25(12), 2731–2748.
- Wexler, A. S., F. W. Lurmann, and J. H. Seinfeld (1994), Modeling urban and regional aerosols - 1. model development, *Atmospheric Environment*, 28(3), 531–546.

- Whitby, K. T. (1981), Determination of aerosol growth-rates in the atmosphere using lumped mode aerosol dynamics, *Journal of Aerosol Science*, *12*(3), 173–178.
- Wigley, T. M. L. (1991), Could reducing fossil-fuel emissions cause global warming, *Nature*, *349*(6309), 503–506.
- Wilson, C. L. (Ed.) (1970), *Study of Man’s Impact on Climate: Inadvertent Climate Modification*, 308 pp., MIT Press, Stockholm.
- Wright, D. L., R. McGraw, C. M. Benkovitz, and S. E. Schwartz (2000), Six-moment representation of multiple aerosol populations in a sub-hemispheric chemical transformation model, *Geophysical Research Letters*, *27*(7), 967–970.
- Wright, D. L., P. S. Kasibhatla, R. McGraw, and S. E. Schwartz (2001), Description and evaluation of a six-moment aerosol microphysical module for use in atmospheric chemical transport models, *Journal of Geophysical Research*, *106*(D17), 20,275–20,291.
- Wu, X. A., C. Seigneur, and R. W. Bergstrom (1996), Evaluation of a sectional representation of size distributions for calculating aerosol optical properties, *Journal of Geophysical Research*, *101*(D14), 19,277–19,283.
- Yamasoe, M. A., P. Artaxo, A. H. Miguel, and A. G. Allen (2000), Chemical composition of aerosol particles from direct emissions of vegetation fires in the Amazon Basin: water-soluble species and trace elements, *Atmospheric Environment*, *34*(10), 1641–1653.
- Yu, S. C., P. S. Kasibhatla, D. L. Wright, S. E. Schwartz, R. McGraw, and A. J. Deng (2003), Moment-based simulation of microphysical properties of sulfate aerosols in the eastern United States: Model description, evaluation, and regional analysis, *Journal of Geophysical Research*, *108*(D12), 4353, doi:10.1029/2002JD002890.
- Yum, S. S., J. G. Hudson, and Y. H. Xie (1998), Comparisons of cloud microphysics with cloud condensation nuclei spectra over the summertime Southern Ocean, *Journal of Geophysical Research*, *103*(D13), 16,625–16,636.
- Zemaitis, J. F., D. Clark, M. Rafal, and N. Scrivner (1986), *Handbook of Aqueous Electrolyte Thermodynamics*, 852 pp., Design Institute for Physical Property Data (DIPPR), New York.
- Zhang, Y., C. Seigneur, J. H. Seinfeld, M. Z. Jacobson, and F. S. Binkowski (1999), Simulation

- of aerosol dynamics: A comparative review of algorithms used in air quality models, *Aerosol Science and Technology*, 31(6), 487–514.
- Zhang, Y., C. Seigneur, J. H. Seinfeld, M. Jacobson, S. L. Clegg, and F. S. Binkowski (2000), A comparative review of inorganic aerosol thermodynamic equilibrium modules: similarities, differences, and their likely causes, *Atmospheric Environment*, 34(1), 117–137.
- Zhang, Y., R. C. Easter, S. J. Ghan, and H. Abdul-Razzak (2002), Impact of aerosol size representation on modeling aerosol-cloud interactions, *Journal of Geophysical Research*, 107(D21), 4558, doi:10.1029/2001JD001549.
- Zipser, E. J., and M. A. LeMone (1980), Cumulonimbus vertical velocity events in GATE - 2. synthesis and model core structure, *Journal of the Atmospheric Sciences*, 37(11), 2458–2469.
- Zuberi, B. (2003), Microphysics of atmospheric aerosols: Phase transitions and cloud formation mechanisms, Ph.D, Massachusetts Institute of Technology.

74. Investigations of Cloud Altering Effects of Atmospheric Aerosols using a New Mixed Eulerian-Lagrangian Aerosol Model, *H.D. Steele* (9/04)
73. Estimation of Methane and Carbon Dioxide Surface Fluxes using a 3-D Global Atmospheric Chemical Transport Model, *Y.-H. Chen* (12/03)
72. The Equilibration of an Adjoint Model on Climatological Scales, *V. Bugnion & C. Hill* (6/03)
71. Mechanistic, Sensitivity, and Uncertainty Studies of the Atmospheric Oxidation of Dimethylsulfide, *D. Lucas* (6/03)
70. Box Modeling of the Eastern Mediterranean Sea, *Y. Ashkenazy & P.H. Stone* (5/03)
69. The 41 kyr World: Milankovitch's Other Unsolved Mystery, *M. Raymo & K. Nisancioglu* (9/02)
68. Reorganization of Miocene Deep Water Circulation in Response to the Shoaling of the Central American Seaway, *K.H. Nisancioglu et al.* (8/02)
67. Snowpack Model Estimates of the Mass Balance of the Greenland Ice Sheet and its Changes Over the 21st Century, *V. Bugnion & P.H. Stone* (1/02)
66. The Production of Non-Methane Hydrocarbons by Marine Plankton, *S. Shaw* (9/01)
65. Optimal Determination of Global Tropospheric OH Concentrations Using Multiple Trace Gases, *J. Huang* (1/00)
64. Measurement and Deduction of Emissions of Short-lived Atmospheric Organo-chlorine Compounds, *G. Kleiman* (9/99)
63. Construction of the Adjoint MIT Ocean GCM and Application to Atlantic Heat Transport Sensitivity, *J. Marotzke et al.* (5/99)
62. Terrestrial Sources and Sinks of Atmospheric Methyl Bromide: 3D Modeling of Tropospheric Abundance and Sensitivities, *C. Jensen* (4/99)
61. Inverse Modeling of Seasonal Variations in the North Atlantic Ocean, *L. Yu & P. Malanotte-Rizzoli* (8/98)
60. Interhemispheric Thermohaline Circulation in a Coupled Box Model, *J. Scott, J. Marotzke & P. Stone* (7/98)
59. Seasonal Measurements of Nonmethane Hydrocarbons in a Sub-tropical Evergreen Forest in Southern China, *J. Graham* (7/98)
58. Temporal Changes in Eddy Energy of the Oceans, *D. Stammer & C. Wunsch* (6/98)
57. On Convective Mixing and the Thermohaline Circulation, *J. Marotzke* (6/98)
56. The Importance of Open-Boundary Estimation for an Indian Ocean GCM-Data Synthesis, *Q. Zhang & J. Marotzke* (5/98)
55. Boundary Mixing and Equatorially Asymmetric Thermohaline Circulation, *J. Marotzke & B.A. Klinger* (4/98)
54. Impact of the Horizontal Wind Profile on the Convective Transport of Chemical Species, *C. Wang & R. Prinn*, (3/98)
53. Adjusting to Policy Expectations in Climate Change Modeling, *S. Shackley et al.* (3/98)
52. Open-Ocean Convection: Observations, Theory and Models, *J. Marshall & F. Schott* (1/98)
51. Global Thermohaline Circulation: Parts I and II, *X. Wang, P. Stone & J. Marotzke* (10/97)
50. Destabilization of the Thermohaline Circulation by Atmospheric Transports: An Analytic Solution, *Y. Krasovskiy & P. Stone* (7/97)
49. The Global Ocean Circulation Estimated from TOPEX/POSEIDON Altimetry and the MIT GCM, *D. Stammer, et al.* (7/97)
48. Trapped Methane Volume and Potential Effects on Methane Ebullition in a Northern Peatland, *E. Fechner-Levy & H. Hemond* (5/97)
47. Seasonal Cycles of Meridional Overturning and Heat Transport of the Indian Ocean, *T. Lee & J. Marotzke* (3/97)
46. Analysis of the North Atlantic Climatologies Using a Combined OGCM/Adjoint Approach, *L. Yu & P. Malanotte-Rizzoli* (12/96)
45. Tracer Applications of Anthropogenic Iodine-129 in the North Atlantic Ocean, *H.N. Edmonds* (11/96)
44. Boundary Mixing and the Dynamics of Three-Dimensional Thermohaline Circulations, *J. Marotzke* (8/96)
43. The Role of Aerosols in the Troposphere: Radiative Forcing, Model Response, and Uncertainty Analysis, *W. Pan* (5/96)
42. Development of a 3D Chemical Transport Model Based on Observed Winds and Use in Inverse Modeling of CFC₁₂ Sources, *N. Mahowald* (4/96)
41. The Role of Vegetation in the Dynamics of West African Monsoons, *X. Zheng & E. Eltahir* (3/96)
40. Inferring Meridional Mass and Heat Transports of the Indian Ocean by Fitting a GCM to Climatological Data, *T. Lee & J. Marotzke* (2/96)
39. Analysis of Thermohaline Feedbacks, *J. Marotzke* (12/95)
38. The Iron Hypothesis: Basic Research Meets Environmental Policy, *S.W. Chisholm* (12/95)
37. Hydrostatic, Quasi-Hydrostatic and Non-Hydrostatic Ocean Modeling, *J. Marshall et al.* (9/95)

36. A Finite-Volume, Incompressible Navier Stokes Model for Studies of the Ocean on Parallel Computers, *J. Marshall et al.* (9/95)
35. A Case Study of the Adequacy of GCM Simulations for Assessing Regional Climate Changes, *J. Risbey & P. Stone* (3/95)
34. On the Role of Vegetation in Sustaining Large Scale Atmospheric Circulations in the Tropics, *E. Eltahir* (2/95)
33. Sprites, Q-Bursts and Positive Ground Strokes, *D. Boccippio, E. Williams et al.* (2/95)
32. Subduction of Carbon in the Subtropical Gyre of the North Atlantic, *M. Follows et al.* (10/94)
31. The Growth of Convective Plumes at Seafloor Hot Springs, *K. Speer & J. Marshall* (10/94)
30. The CMPO/MIT TOPEX/POSEIDON Altimetric Data Set, *C. King, D. Stammer & C.I. Wunsch* (8/94)
29. Atmospheric Transports, the Thermohaline Circulation, and Flux Adjustments in a Simple Coupled Model, *J. Marotzke & P. Stone* (4/94)
28. Climate Dynamics and Global Change, *R. Lindzen* (3/94)
27. Effects of Atmospheric Coupling on the Stability of the Thermohaline Circulation, *M. Nakamura, P. Stone & J. Marotzke* (1/94)
26. Poleward Heat Transport in a Barotropic Ocean Model, *X. Wang, P.H. Stone & J. Marotzke* (12/93)
25. An EPV View of the Zonal Mean Distribution of Temperature and Wind in the Extra-tropical Troposphere, *D. Sun & R. Lindzen* (12/93)
24. Laboratory Experiments of Chemical Reactions on Polar Stratospheric Cloud Particles, *K. Beyer* (11/93)
23. A Model of the Ion Chemistry of Electrified Convection, *R. Boldi* (5/93)
22. Destabilization of the Thermohaline Circulation by Atmospheric Feedback, *M. Nakamura et al.* (3/93)
21. Global Circuit Response to Seasonal Variations in Global Surface Air Temperature, *E. Williams* (3/93)
20. Precipitation Recycling in the Amazon Basin, *E. Eltahir & R.L. Bras* (1/93)
19. On the Response of the Tropical Atmosphere to Large-Scale Deforestation, *E. Eltahir & R.L. Bras* (1/93)
18. On the Feasibility of Determining Surface Emissions of Trace Gases Using an Inverse Method in a 3D Transport Model, *D. Hartley & R. Prinn* (11/92)
17. Deducing Trace Gas Emissions Using an Inverse Method in 3D Chemical Transport Models, *D. Hartley* (11/92)
16. An Active Titration Method for the Local Measurement of Tropospheric Hydroxyl Radical, *M. Sprengnether* (10/92)
15. A Description of Rainfall Interception over Large Areas; and, On the Estimation of the Coverage of Rainfall in Climate Models, *E. Eltahir & R. Bras* (8/92)
14. The Schumann Resonance: A Global Tropical Thermometer, *E. Williams* (5/92)
13. The Heterogeneous Reaction $\text{HOCl} \rightarrow \text{HCl}_2 + \text{H}_2\text{O}$ on Ice and Nitric Acid Trihydrate, *J. Abbatt & M.J. Molina* (4/92)
12. Forecast Cloudy: The Limits of Global Warming Models, *P.H. Stone* (3/92)
11. The Implementation and Validation of Improved Landsurface Hydrology in an Atmospheric GCM, *K. Johnson et al.* (2/92)
10. Inferring the Annual-mean Subduction Rate Over the North Atlantic, *J. Marshall et al.* (1/92)
9. The Role of Ice in the Conditional Instability of the Tropical Atmosphere, *E. Williams & N. Renno* (11/91)
8. Nonmethane Hydrocarbon Chemistry in the Remote Marine Atmosphere, *N. Donahue* (7/91)
7. Global-Scale Sea Surface Variability from Combined Altimetric and Tide Gauge Measurements, *C.I. Wunsch* (1/91)
- 5/6. Non-linear Dynamics of Soil Moisture at Climate Scales: Stochastic and Chaotic Analyses, *I. Rodriguez-Iturbe, et al.* (11/90)
4. Atmospheric Emissions and Trends of Nitrous Oxide Deduced from Ten Years of ALE-GAGE Data, *R. Prinn et al.* (6/90)
3. A Scheme for Representing Cumulus Convection in Large-Scale Models, *K.A. Emanuel* (4/90)
2. On the Limitations of General Circulation Climate Models, *P.H. Stone & J. Risbey* (3/90)
1. An Annotated Bibliography on Greenhouse Effect Change, *M. Handel & J. Risbey* (4/92)